SISSA

Investigations on structure and functional properties of CNG channels

Thesis submitted for the degree of Doctor Philosophiae

Neuroscience area
PhD in Neurobiology
October 2015

Candidate   **Supervisor**

Manuel Arcangeletti   **Vincent Torre**

Scuola Internazionale Superiore di Studi Avanzati - Trieste

Investigations on structure and functional properties of CNG channels

Thesis submitted for the degree of Doctor Philosophiae

Neuroscience area
PhD in Neurobiology
October 2015

Candidate   **Supervisor**

Manuel Arcangeletti   **Vincent Torre**

SISSA – Via Bonomea 265 – 34136 TRIESTE - Italy

"E da allora sono perché tu sei.

E da allora sei, sono e siamo.

E per amore sarò, sarai, saremo."

Pablo Neruda

Grazie di tutto…..

INDEX

DECLARATION

All the work described in this thesis arises exclusively from my own experiments, with exception made for the parts regarding x-ray crystallography, molecular dynamic simulations and single molecule force spectroscopy, and was carried out at the International School for Advanced Studies, SISSA, between November 2011 and October 2015, under the supervision of Professor Vincent Torre.

LIST OF PUBLICATIONS

Published or accepted papers

Arcangeletti, M., Marchesi, A., Mazzolini, M., and Torre, V. (2013). Multiple mechanisms underlying rectification in retinal cyclic nucleotide-gated (CNGA1) channels. Physiological Reports.

Marchesi, A., Arcangeletti, M., Mazzolini, M., and Torre, V. (2015). Proton transfer unlocks inactivation in CNGA1 channels. The Journal of Physiology *593*, 857–870.

Maity, S., Mazzolini, M., Arcangeletti, M., Valbuena, A., Fabris, P., Lazzarino, M., and Torre, V. (2015). Conformational rearrangements in the transmembrane domain of CNGA1 channels revealed by single-molecule force spectroscopy. Nature Communications *6*, 7093.

Napolitano, L.M.R., Bisha, I., De March, M., Marchesi, A., Arcangeletti, M., Demitri, N., Mazzolini, M., Rodriguez, A., Magistrato, A., Onesti, S., Laio A., and Torre, V. (2015). A structural, functional, and computational analysis suggests pore flexibility as the base for the poor selectivity of CNG channels. Proceedings of the National Academy of Sciences *112*, E3619–E3628.

Papers in preparation

Arcangeletti, M., Mazzolini, M., Anselmi, C., Grosa, D., Maity, S., Marchesi, A., Napolitano, L., and Torre, V. Interactions between the C-linker and the S4-S5 linker mediate gating in CNGA1 channels.

ABSTRACT

Ion channels are allosteric proteins that play a fundamental role for cells; they regulate ion fluxes across biological membranes by residing in any of three functionally distinct states: deactivated (closed), activated (open) or inactivated (closed). In addition to selecting permeant ions, channels undergo conformational changes that open and close their ion-permeable pores, a process referred to as gating.

On the basis of their primary structure the ion channels are classified into a relatively small number of discrete gene families. Cyclic nucleotide gated (CNG) and hyperpolarization-activated, cyclic nucleotide-gated (HCN), together with K^+, Na^+, Ca^{2+} and transient receptor potential (TRP) channels belong to the superfamily of voltage gated channels. All members of this family are tetrameric or pseudotetrameric and share a common pore domain that contains two transmembrane (TM) segments - referred to as M1 and M2, or S5 and S6.

As in all the voltage-gated channels, CNG channels have four additional TM segments per subunit: S1–S4 that, correspond to the sensor for the allosteric modulation of gating by membrane voltage. CNG channels are mainly activated by binding of cyclic nucleotides, but, in the presence of symmetrical ionic conditions, current-voltage (I-V) relationship depends, in a complex way, on the radius of permeating ion and has been suggested that both the pore and S4 helix contribute to the observed rectification.

CNG channels are essential for visual and olfactory transduction: in rod photoreceptors CNG channels open in dark conditions and are responsible for a steady inward current that flows through them keeping the membrane depolarized. In vertebrates, seven members of the CNG channel gene family have been identified that, according to sequence similarity, are grouped into two subtypes, CNGA (CNGA1-CNGA5) and CNGB (CNGB1 and CNGB3). Only CNGA subunits - except the A4 subunit - can form cyclic nucleotide-activated homomeric channels, while CNGB1 and CNGB3 are modulatory and cannot form functional homomeric channels.

CNG channels are only slightly voltage-dependent and, for opening, require the binding of cGMP or cAMP to a receptor site located in their C-terminal. In the presence of a saturating agonist, CNG channel gating is voltage independent and it is not known why CNG channels are voltage-insensitive despite harbouring the S4-type voltage sensor. Moreover, unlike many K^+ channels, cyclic nucleotide-gated (CNG) channels are known not to inactivate. While electrophysiology combined with mutagenesis have identified the channel pore and the binding

domain for cyclic nucleotides (CNs), conformational changes associated with gating have remained elusive.

During my PhD course I focused my energies on investigating the structural and functional properties of different domains of the CNGA1 channels, combining results from different techniques like homology modelling, single molecule force spectroscopy (SMFS), molecular dynamics (MD) simulations, and X-ray crystallography with my own data from electrophysiology and site-directed mutagenesis in order to get better insights of fundamental properties of the channels, like permeation and channel gating. The main findings of my PhD thesis are the following:

I. I showed that current rectification, in presence of large organic cations, like ethylammonium and dimethylammonium, strongly depends on two voltage-dependent transitions, of which, only the first, is sensible to mutation of charge residues in the S4 helix. These results indicate the existence of at least two distinct mechanisms underlying rectification in CNG channels: a restricted motion of the S4 helix, together with an inefficient coupling to the channel gate that render CNGA1 channels poorly sensitive to voltage in the presence of physiological Na^+ and K^+.

II. has been demonstrated that, contrary to previous belief, when extracellular pH is decreased from 7.4 to 6 or lower, wild-type CNGA1 channels inactivate in a voltage-dependent manner. This mechanism is reminiscent of the C-type inactivation observed in K^+ channels. Low pH inactivation may represent an unrecognized endogenous mechanism that regulate CNG physiological functions in diverse tissues.

III. combining electrophysiology with molecular dynamics (MD) simulations, and X-ray crystallography has been demonstrated that the pore of CNG channels is highly flexible and, mainly due to the side chain of Glu66 in the selectivity filter and to the prolines in the outer vestibule, capable to coordinate different ionic species. This flexibility underlies the coupling between gating and permeation and the poor ionic selectivity of CNG channels.

IV. by mean of electrophysiology combined with single-molecule force spectroscopy (SMFS), mutagenesis and bioinformatics have been obtained better insights about conformational changes associated with gating and, in particular, about the mechanical coupling between the voltage sensor and the binding domain. We revealed putative electrostatic interactions between an aspartate in the C-linker and an arginine in the S4-

S5 linker. We hypothesized a possible mechanism, possibly shared with HCN channels, by which these electrostatic interactions determine the motion of S5, leading to conformational rearrangements of residues flanking the pore so that the lumen of the pore widens and the channel opens.

INTRODUCTION

Cyclic nucleotide-gated (CNG) channels are membrane proteins that play a fundamental role in a variety of physiological processes. They were first discovered 30 years ago when it was shown that cGMP directly activates a current in isolated patches of outer segment (OS) membrane of retinal rods (Fesenko *et al.*, 1985). Similar channels were also found in cone photoreceptors and lately, in 1987, in the cilia of olfactory receptor neurons (ORNs) was detected a similar ionic current, directly activated by cGMP or cAMP (Nakamura and Gold, 1987); they have also been found in other neuronal and non-neuronal tissues but, while in rod and cone photoreceptors and in ORNs their function has been strongly established (Stryer, 1986; Menini, 1995), in these tissues their specific functions are yet to be assessed carefully (Zufall *et al.*, 1997; Kaupp and Seifert, 2002; Togashi *et al.*, 2008).

Even though CNG channels are directly activated by the binding of cyclic nucleotides to a specific intracellular site on the channel protein, they belong to the superfamily of voltage-gated ion channels, whose gating, *i.e.* the transition between the open and closed conformation, depends on the membrane voltage. Most likely, four molecules of the ligand are required to fully open the channels (Kaupp and Seifert, 2002). All CNG channels are sensible, to some extent, to both cAMP and cGMP (Kaupp and Seifert, 2002).

CNG channels are non-selective cation channels that have a very important role in sensory transduction (Kohl *et al.*, 1998) as well as in cellular development (Podda and Grassi, 2013). They poorly discriminate between alkali monovalent cations and even allow the passage of some divalent cations, in particular Ca^{2+}. The entry of Ca^{2+} through these channels has a very important physiological role for both excitation and adaptation of sensory cells. The study and the complete understanding of CNG channels are relevant also to prevent some human diseases, indeed mutations in CNG channel genes give rise to retinal degeneration and color blindness; in particular, mutations in the A and B subunits of the CNG channel expressed in human cones cause various forms of complete and incomplete achromatopsia (Kaupp and Seifert, 2002; Biel and Michalakis, 2007; Remmer *et al.*, 2015). Furthermore, CNG channel activity can be also regulated by other factors such as the concentration of the external pH (pH_o) and changes in the external pH have been also observed in several physiological and pathophysiological conditions in the brain; for instance, localized pH changes have been suggested to occur in the brain during normal function (Magnotta *et al.*, 2012); variation in the concentration of pH has also been demonstrated in the rabbit retina, where a circadian clock regulates the pH so that the proton concentration is

lower at night and higher during the day (Dmitriev and Mangel, 2001). Moreover, the influence of intracellular and extracellular acidosis on neuronal viability and the effect of acidosis on neuronal damage progressing under brain ischemia/hypoxia have been widely investigated (Isaev *et al.*, 2008).

The role of CNG channels in visual phototransduction

Phototransduction is the process by which light, captured by a visual pigment molecule, generates an electrical response (Stavenga *et al.*, 2000). It takes place at level of rod and cone photoreceptor cells that are specialized type of neurons found in the retina. These cells are organized in two principal parts: the outer segment (OS) and the inner segment (IS). The former is the site in which the phototransduction takes place and contains the rhodopsin molecule, that is made of a chromophore (retinal) and a protein component (opsin), the cyclic nucleotide-gated (CNG) channels and the Na^+/Ca^{2+}-K^+ exchangers (Kaupp and Seifert, 2002; O'Brien, 1982; Papermaster and Dreyer, 1974). It is organized with a structure that consists of a stack of membranous discs containing the visual pigment rhodopsin; in rods, the discs are enclosed by the surface membrane, whereas in cones they consist of folding of the surface membrane. Even if the OS is considered an homogeneous system, a recent study - carried out by Mazzolini *et al.*, in which they developed a methodology based on special tapered optical fibers (TOFs) to deliver highly localized light stimulations - demonstrated that the efficacy of the transduction machinery is not uniform along the OS and is higher at the base respect to the tip (Mazzolini *et al.*, 2015). The IS contains the nucleus as well as mitochondria and the endoplasmic reticulum; in addition it includes Na^+/K^+ pumps (Kaupp and Seifert, 2002; O'Brien, 1982). Rods and cones, with the synaptic terminals, are connected to bipolar and horizontal cells (**Fig.1**).
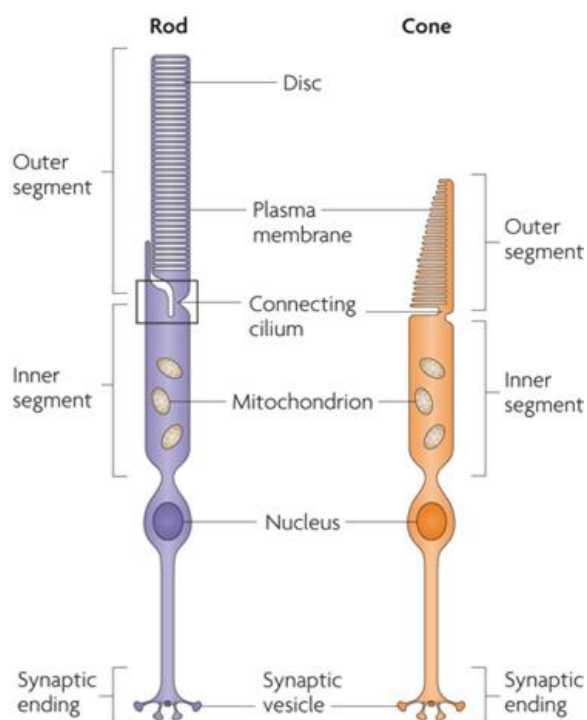

Fig.1: Schematic diagram of photoreceptor cells (Wright et al., 2010).

CNG are the main channels involved in the generation of the so called light-regulated or cGMP-activated conductance that is the ionic conductance that generates the electrical response to light in rods and cones of the vertebrate retina (Yau and Baylor, 1989). In rods the arrival of the light stimulus generates a cascade that leads to a brief hyperpolarization of the rods mediated by the closure of the CNG channels located in the surface membrane of the OS (Yau and Baylor, 1989). The actors that play this piece are the rhodopsin (R), the G protein transducin (T), and the phosphodiesterase (PDE). In the dark, CNG channels are typically activated and therefore a steady cation current flows into the OS. In particular, the absorption of a photon by a rhodopsin molecule causes the photoisomerization of the retinal from its 11-cis stereoisomer to its all-trans form (Yoshizawa and Wald, 1963; Baylor, 1996), leading to the conversion of rhodopsin to its active metarhodopsin state (Emeis *et al.*, 1982). This form of rhodopsin exchanges the guanosine diphosphate (GDP) which is bound to the α subunit of the transducin, for guanosine triphosphate (GTP). Consequently to this exchange, the GTP-Tα complex moves toward one of the inhibitory γ subunit of the PDE. This enzyme is then able to hydrolyze cyclic GMP (cGMP) to GMP determining the closure of the channels. As a result of the closure, the inward current ceases and the cell hyperpolarizes (**Fig.2**). The sensitivity of the CNG channel has been optimized to detect and signal the drop in cGMP concentration resulting from the absorption of a single photon of light (Baylor *et al.*, 1979). The channel's relatively low affinity for cGMP leads to a fast off rate for ligand and allows the channel to close quickly in response to light (Cobbs and Pugh, 1987). The nature of the interaction between cyclic nucleotide and the CNBD has been revealed by molecular modeling and mutagenesis studies that predicted 10 different interactions between cGMP and the binding pocket involving 8 amino acid residues, 5 with the purine ring and 5 with the ribofuranose; interactions with the common ribofuranose moiety are largely similar for all cyclic nucleotides and include an arginine (Arg559 in CNGA1, Arg591 in HCN2 and Arg538 in HCN1) located in the CNBD region of both CNG and HCN channels. Mutations in this residue appear to strongly affect the specificity of CNG and HCN channels for cyclic nucleotides. On the other hand, differential interaction with the purine ring controls ligand selectivity; diverse interaction of cAMP and cGMP with Asp604 in the C-helix of the cNMP-binding domain has been proposed to underlie ligand discrimination in CNG channels (Kaupp and Seifert, 2002; Matulef and Zagotta, 2003).

To ensure that photoreceptors remain functional, all the proteins involved in the above mentioned reactions have to be regenerated. Rhodopsin is restored after several enzymatic steps in which 11-cis retinal is reconstituted. Also the transducin molecule is regenerated thanks to an

endogenous GTPase activity of the α subunit which subsequently permits the reunion to the βγ complex (Yau and Baylor, 1989). During a prolonged light stimulation the cytoplasmic Ca^{2+} concentration ($[Ca^{2+}]_i$) decreases, this is a very important physiological process for at least two aspects: first, it initiates the recovery from the light response by enhancing the synthesis of new cGMP molecules and second, it gives rise to the light adaptation, a process that determines the adjustment of the sensitivity of the transduction machinery. These processes are mediated by three reactions that help to restore the dark state and to adjust the light sensitivity of the cell (Stavenga *et al.*, 2000). First, the decline in $[Ca^{2+}]_i$, stimulates the activity of the guanylyl cyclase (GC) that synthesizes cGMP relying on two small Ca^{2+}-binding proteins, designated GC-activating proteins (GCAP1 and GCAP2) (Koch, 1992; Palczewski *et al.*, 2000). Second, the lifetime of active PDE is shortened through the phosphorylation of light-activated rhodopsin (R*) by the rhodopsin kinase (Koch, 1992). Finally, the ligand sensitivity of the CNG channel increases as $[Ca^{2+}]_i$ decreases due to the action of a Ca^{2+}-modulated (CaM) protein (Hsu and Molday, 1993; Molday, 1996). In rods, CNG channel is fundamental because it provides the only source for Ca^{2+} influx into the OS and in these cells between 10 and 18% of the dark current (~30 pA) is carried by Ca^{2+} (Nakatani and Yau, 1988; Lagnado *et al.*, 1992; Gray-Keller and Detwiler, 1994; Younger *et al.*, 1996).
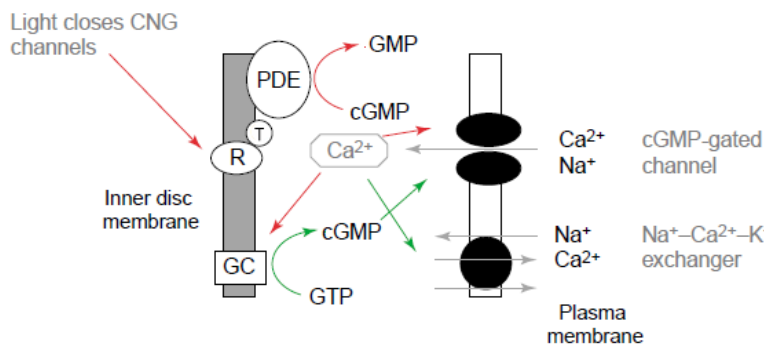

Fig.2: Signal transduction pathways in photoreceptors. Color refers to processes that act to promote opening (green) or closing (red). Rhodopsin (R), transducin (T), phosphodiesterase (PDE), guanylyl cyclase (GC) (Bradley et al., 2005).

A similar transduction scheme exists in cones, the photoreceptors responsible for vision in bright light. However, the light sensitivity of cones is 30- to 100-fold lower than that of rods, and cones adapt over a wider range of light intensities than rods (Stavenga *et al.*, 2000). Several observations demonstrate that the cGMP sensitivity (Hackos, 1997), its modulation by $[Ca^{2+}]_i$ (Nakatani *et al.*, 1995; Rebrik, 1998), and the Ca^{2+} permeation (Picones and Korenbrot, 1995; Wells and Tanaka, 1997) are profoundly different in CNG channels of rods and cones, supporting the notion that the CNG channel is an essential determinant of the dynamics of Ca^{2+} homeostasis in vertebrate photoreceptor cells.

The role of CNG channels in the olfactory transduction

In vertebrates, olfactory sensory neurons are bipolar neurons with a single dendrite from which several cilia - where the olfactory transduction occurs - protrude. The cilia are embed in the mucus that lines the superior portion of the nasal cavity. In this place volatile odorant molecules interact with odorant receptors, and give rise to an enzymatic cascade that conducts to an increase in the intraciliary concentration of cAMP that, in turn, causes the opening of the CNG channels that allows an influx of Na^+ and Ca^{2+} inside the cilia, resulting in the depolarization and then in the generation of action potentials that are conducted along the axon to the olfactory bulb (Firestein, 2001; Menini, 2004; Pifferi *et al.*, 2006). Going into details, the enzymatic cascade starts with the binding of the odorant directly to one of many receptor molecules located in the membranes of the cilia and the consequent activation of an odorant-specific G-protein (G_{olf}, a G_s-like G protein) that, in turn, activates an adenylate cyclase, resulting in the generation of cyclic AMP (cAMP). One of many targets of the cAMP is the CNG channel that, opening and permitting the influx of Na^+ and Ca^{2+}, determines the depolarization of the membrane. The increase in intracellular Ca^{2+} opens Ca^{2+}-gated Cl^- channels that, due to the unusually high intracellular Cl^- concentration, produce the outflow of Cl^-, contributing to the inward current (Frings *et al.*, 2000). The role of Ca^{2+} is not only important for the excitatory, but also for the inhibitory effects; a Ca^{2+}–calmodulin complex, indeed, binds to the channel, reducing its affinity for cAMP and activates a phosphodiesterase (PDE1C2) that, in turn, hydrolyzes cAMP (Borisy *et al.*, 1992; Yan *et al.*, 1995) giving rise to a negative feedback effect on the CNG channel itself, that mediate olfactory adaptation (Menini, 1999). Finally, Ca^{2+} is extruded through the Ca^{2+}/Na^+ exchange pathway (Purves *et al.*, 2001) (**Fig.3**).
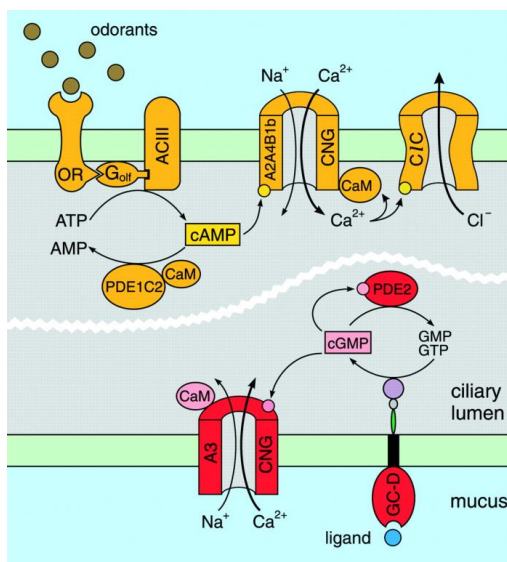

Fig.3: Signal transduction pathways in olfactory sensory neurons. Odorant receptor (OR), G protein (G_{olf}), calmodulin (CaM), Cl^--channels (ClC), CaM-dependent phosphodiesterase (PDE1C2), cGMPregulated phosphodiesterase (PDE2), guanylyl cyclase type D (GC-D), Ca2+-dependent denylyl cyclase type III (ACIII) (Kaupp and Seifert, 2002).

CNG channels structure

Up to now, only few structural information on CNG channels are accessible; Higgins *et al.* in 2002 obtained the low-resolution electron microscopy map for the CNG channel from bovine retina at 35 Å resolution, suggesting that the cyclic nucleotide-binding domains 'hang' below the pore-forming part of the channel only attached by narrow linkers and that the four subunits of the CNG channels are arranged as a pair of dimers; In 2011 Lolicato *et al.* obtained a partial crystal structure for the C-terminal domain of HCN1, HCN2 and HCN4, providing structural information about the intracellular cyclic nucleotide-binding domain and the tetramerization mechanisms in presence of the ligand. Moreover, in 2011 Derebe *et al.* obtained the crystal structure of a chimeric channel (NaK2CNG) constituted by the selectivity-filter of the CNG channel engineered into a bacterial NaK channel, that resembles for some aspects the CNG channels and lately in 2015 Napolitano *et al.* crystallized this chimeric channel in presence of a variety of monovalent cations shedding new light on the characteristics of the selectivity filter. (Derebe *et al.*, 2011; Higgins *et al.*, 2002; Lolicato *et al.*, 2011; Napolitano *et al.*, 2015). It seems logical, therefore, to resort to new techniques, that permit to obtain more tractable results and in a easier way. Single molecule force spectroscopy (SMFS) uses atomic force microscopy (AFM) to measure the force (F) required to unfold a protein or a polymer while the distance (D) between the AFM cantilever tip and the sample is measured as the coordinate reaction. In a force-distance (F-D) curve, each force peak represents the unfolding of a structured segment while an unstructured segment unfolds with almost no force (Engel and Gaub, 2008; Müller *et al.*, 2008; Rief, 1997). With this technique it is possible not only to visualize the sample at the nanoscale resolution but also to obtain measurements of sample mechanics and can be used for the analysis of molecular interactions in order to have structural information about the protein under investigation (Engel and Gaub, 2008; Hoffmann and Dougan, 2012; Müller *et al.*, 2008; Rief, 1997).

CNG channels are considered members of a gene superfamily of cation channels, which evolved from a common primordial ancestor (Heginbotham *et al.*, 1992; Jan, 1990). The first CNG channel was identified through protein purification (Cook *et al.*, 1987) and subsequent cloning of the gene from a cDNA library from bovine retina (Kaupp *et al.*, 1989). The advent of molecular cloning has uncovered a huge number of genes from various species encoding different CNG channel subunits. In vertebrates, seven members of the CNG channel gene family have been identified (Kaupp and Seifert, 2002; Tetreault *et al.*, 2006) and can be distinguished into two subtypes, CNGA and CNGB (Bradley, 2001; Tetreault *et al.*, 2006). Each type of subunit can assemble in a variety of

combinations to produce tetrameric channels. Only, CNGA1, CNGA2, and CNGA3 and CNGA5 can form, on their own, homomeric channels, with properties similar but not identical to native CNG channels, in heterologous expression systems and have been referred to as "principal" subunits; the other subtypes do not form functional homomeric channels but, assembling with other subunits, form functional heteromeric channels and have been designated "modulatory" subunits. Native channels are generally composed by different type of subunits, the combination of which give each tissue-specific CNG channel unique properties to perform its physiological role (Craven and Zagotta, 2006) (**Fig.4A**). Despite some differences in the sequence, CNG subunits share the same prototype of secondary structure with six membrane-spanning segments, designated S1-S6, with an intracellular N and C termini, in which there is a cyclic nucleotide binding (CNB) domain and in all of them we can distinguish common functional domains: a voltage-sensor motif, a pore region, an inner helix and two terminal ends. (Biel *et al.*, 1999; Kaupp and Seifert, 2002; Mazzolini *et al.*, 2010). CNG channels of rod photoreceptors contain three CNGA1 subunits and one CNGB1 subunit while those of cone photoreceptors are composed by two CNGA3 and two CNGB3 subunits. CNG channels of olfactory neurons are even different (**Fig.4B**). The A1 subunit, that is the subunit that we have been using in our study, is a polypeptide of 63 kDa, composed of 690 amino acids while B1 subunits are 1394 aa long (Weitz *et al.*, 2002; Zheng *et al.*, 2002; Zhong *et al.*, 2002). The two subunits differ principally at the N-terminus, where there is a glutamic acid and proline rich domain (GARP) found only in the B1 subunit (Higgins *et al.*, 2002). This domain interacts with the peripherin-2 complex in the disc membrane and is responsible of the link between the plasma and the disc membranes and it is important for the structure of the rod OS (Poetsch *et al.*, 2001).
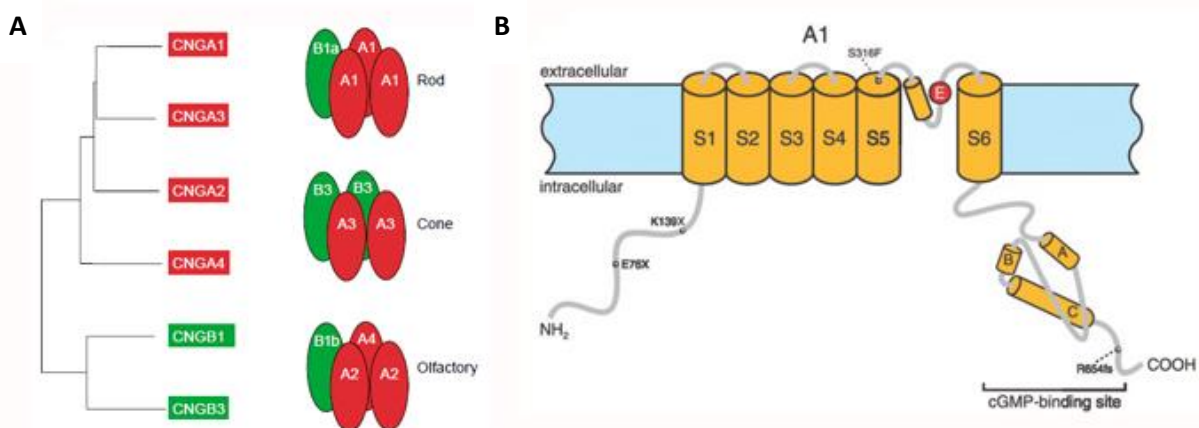

Fig.4: Transmembrane topology and subunits stoichiometry in photoreceptors and ORNs. A. Stoichiometry and subunit composition of rod, cone and olfactory CNG transduction channels (Bradley et al., 2005). B. The proposed topology of CNGA1 subunit in the membrane. The cylinders (S1-S6) indicate the transmembrane segments (Kaupp and Seifert, 2002).

The A1 subunits have a conserved glutamate (Glu363) residue within the pore-forming region that is thought to be fundamental for selectivity as well as affinity for extracellular divalent cations (Derebe *et al.*, 2011; Eismann *et al.*, 1994; Root and MacKinnon, 1994); this residue is replaced with an aspartate and a glycine residue in A4 and B1, respectively. Moreover the B1 subunit has two calmodulin-binding sites (CaM1 and CaM2) that are lacking in the A1 subunit (Kaupp and Seifert, 2002).

The "voltage-sensing" S4 segment in voltage-gated K^+, Na^+, and Ca^{2+} channels is characterized by a repeated charged sequence motif, with positively charged residues (Arg or Lys) at every third position. This segment, in voltage-gated channels, has been proposed to serve as sensor of membrane voltage (Kaupp and Seifert, 2002). According to a previous model when the membrane potential changes from hyperpolarized to depolarized, segment S4 rotates 180°, changes its tilt by about 30° and moves towards the extracellular side by about 6.5 Å. This movement is then transmitted through the S4–S5 linker to the intracellular part of S6 and to the channel pore (Bezanilla, 2008). Recent investigations, instead, suggest that this process may occur via the helical conversion of the entire S4 segment between α and 3_{10} conformations (Kubota *et al.*, 2014). In CNG channels S4 resembles the one of voltage-gated ion channels (VGICs), even if the net charge is reduced by the presence of negatively charged residues and thus, although CNG channels show a very mild voltage dependency, a similar mechanism has been proposed for CNG channels (Marchesi *et al.*, 2012). Moreover has been demonstrated that, even with the S4 motif of the rat olfactory CNG channel, the Drosophila mutant ether-â-gogo (eag) channel was able to maintain significant sensitivity to voltage changes (Moreau *et al.*, 2014; Tang and Papazian, 1997). Certainly, more work is needed to eventually understand the role of the S4 segment of CNG channels. In voltage-gated channels, S4 is connected to S5 by a linker, called S4–S5; in Kv1.2 this linker is composed of about 14 residues forming an α-helix (Long *et al.*, 2005a, 2005b). This linker has been proposed to have a major role in the gating of K^+ channels as a downward displacement of the S4 helix pushes down the S4–S5 linker, which is rigid enough to compress the C-terminal end of S6, leading to the channel closure (Long *et al.*, 2005b). In CNG and HCN channels the S4–S5 linker sequences are slightly different respect to Kv1.2; CNG channels have a shorter linker composed of about 11 residues, with a well conserved in almost all CNGA subunits proline in the middle; in addition, in this region, CNG channels lack many of the residues with a high α-helical interface propensity. Secondary structure predictions show that the S4–S5 linker of CNGA1 channels could

be, instead of being in a α-helix conformation, a flexible loop, decoupling, therefore, S4 from S6 (Anselmi *et al.*, 2007).

The pore region (~20–30 amino acids long) is located between S5 and S6 and comprises the fifth transmembrane domain (S5), a reentrant pore loop that does not completely traverse the membrane (P-helix), and the sixth transmembrane domain (S6) and is thought to be structurally similar to those of other P-loop containing ion channels (Flynn and Zagotta, 2003). The structure for the pore of this family of channels was revealed by the crystal structure of a KcsA, a bacterial potassium channel and is described like an inverted cone made of the P loops of the four subunits that form the channel (Doyle *et al.*, 1998). The pore region of all Shaker-like K$^+$ channels and other K$^+$ selective ion channels contains two residues, a tyrosine and a glycine (YG motif), that are always present. In CNG channel this motif is absent and, interestingly, when the same motif is removed from the Shaker pore region, the channel is converted into a non-selective ion channel suggesting that these residues belongs to the selectivity filter (**Fig.5**).
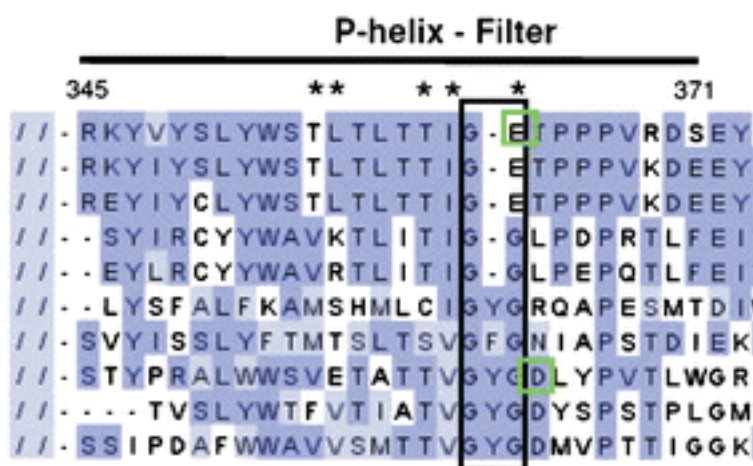

Fig.5: Sequence alignment of K$^+$ and CNG channels for the P-helix and the filter region. Green boxes indicate the negatively charged residues in the outer vestibule in CNGA1 channels (Glu363) and in KcsA channels (Asp80). In black box the conserved signature of K+ channels and correspondent residues of CNGs (Mazzolini et al., 2010).

The S6 helix of all functional voltage-gated K$^+$ channels contains the PXP motif (Ottschytsch *et al.*, 2005); this motif introduces a kink in S6 helix, as seen in the crystal structure of Kv1.2 (Long *et al.*, 2005a, 2005b). The S6 segment of HCN and CNG channels shares an high degree of sequence similarity with KcsA and lacks the PXP motif; it features instead two highly conserved glycines that could be the hinges around which the motion of S6 occurs during gating (Anselmi *et al.*, 2007). The existence of a strong coupling between the upper portion of S6 and the P-helix provides a straightforward molecular mechanism for the gating in K$^+$ selective channels, in which it is thought to be controlled by the bundle crossing at the intracellular side. The current view assumes that the selectivity filter of K$^+$ channels is a relatively rigid structure with the gating and the permeation that are considered independent processes with distinct structural basis (Doyle *et al.*, 1998;

Morais-Cabral *et al.*, 2001; Zhou *et al.*, 2001). This relies on two main experimental evidences: first, the crystal structure in the open channel conformation of the MthK channel, in which the inner helices are curved of approximately 30 degrees and stay open creating a wide (12 Å) entryway; second, the crystal structure of the KcsA in the closed conformation, in which the pore-lining inner helices are in a straight conformation and form a bundle that closes the pore (Jiang *et al.*, 2002). In contrast to K^+ channels, the primary gate in CNG channels is located at the selectivity filter (Contreras *et al.*, 2008), suggesting that the same protein region controls both ion permeation and gating, indeed, in CNG channels, ions that permeate influence channel gating, although the nature of this coupling is not well understood (Gamel and Torre, 2000; Hackos and Korenbrot, 1999; Holmgren, 2003; Kusch *et al.*, 2004).

The intracellular N-terminal region is different between various HCN and CNG subunits; in CNG channels, the N-terminus is ~ 162 aa long and can be autoexcitatory and contributes to calmodulin modulation (Maity *et al.*, 2015; Trudeau and Zagotta, 2003). The intracellular C-terminus contains a ligand-binding domain called the cyclic nucleotide–binding domain (CNBD) (~ 109 aa) that is connected to the end of the S6 by the C-linker, *i.e.* a segment of about 90 amino acids. Some of its residues are shown to play a very important role in mediating the coupling between the ligand binding and the channel gating (Paoletti *et al.*, 1999; Zong *et al.*, 1998). Moreover in HCN channels has been shown that the coupling between the voltage sensing and the intracellular gate formed by the S6 domain could arise from interaction between specific residues present in the S4–S5 linker and in the C-linker. In their study Decher *et al.* suggested a specific electrostatic interaction between Arg339 of the S4–S5 linker and Asp443 of the C-linker that could participate in this coupling (Decher *et al.*, 2004).

The CNBD of CNG channels shares 20% sequence identity with other CNB proteins, such as the CNB domain of HCN channels (**Fig.6**) and MlotiK1 potassium channels (Lolicato *et al.*, 2011; Mari *et al.*, 2011; Zagotta *et al.*, 2003) and has a conserved 3D structure. It is constistuted by a short N-terminal α-helix (A-helix), eight-stranded antiparallel β-roll and other two C-terminal α-helices (B- and C-helix). The binding of ligand to the CNBD favors channel opening owing to a conformational change in the CNBD, which may be conferred to the pore through movement in the C-linker.

Subsequently to the CNBD (post-CNBD region), there is a region that is proposed to be important in subunit assembly of CNG channels (Zhong *et al.*, 2002, 2003).
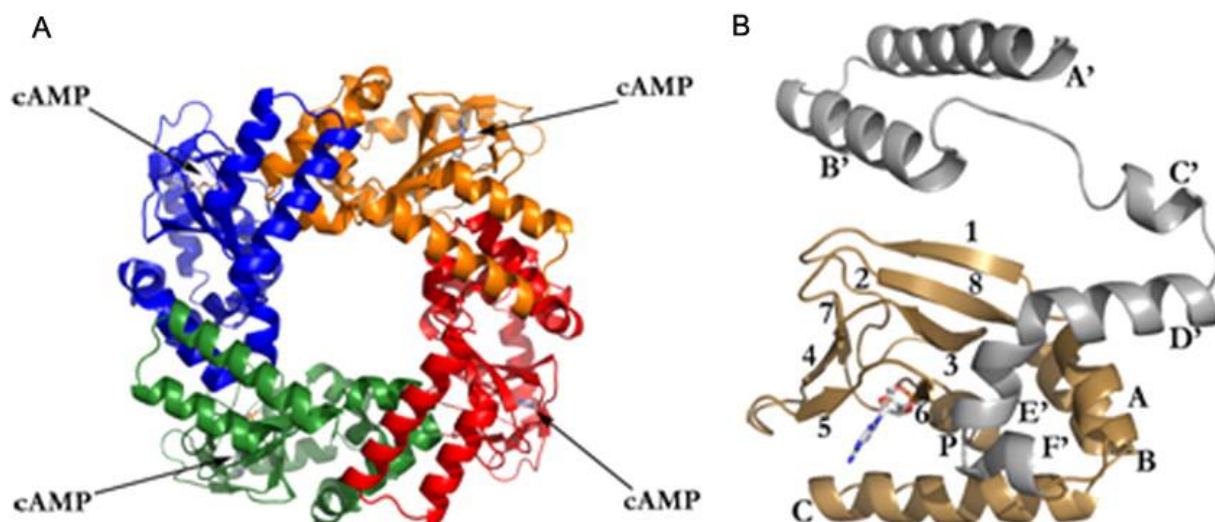
Fig.6: Crystal structure of the soluble portion CB (C-linker plus CNBD) of HCN1 bound to cAMP. A. HCN1CB tetramer viewed parallel to the 4-fold axis. Each subunit is shown in a different color. B. HCN1CB with cAMP. The C-linker, helices A'–F', is in gray; the CNBD, β-sheets 1–8 and helices A, B, P, and C, is in gold.

Biophysical properties of CNG channels

Although CNG channels belong to the superfamily of voltage-gated ion channels, they are only barely modulated by membrane voltage (Craven and Zagotta, 2006; Hille, 1992; Kaupp and Seifert, 2002; Mazzolini *et al.*, 2010; Yu *et al.*, 2005). Moreover they are known not to inactivate or to desensitize in the presence of a steady CN concentration (Craven and Zagotta, 2006; Kaupp and Seifert, 2002).

As mentioned before, CNG channels strongly select cations over anions but do not discriminate among monovalent cations as has been demonstrated previously in intact retinal rods (Menini *et al.*, 1988) and secondarily in excised patches (Colamartino *et al.*, 1991; Furman and Tanaka, 1990; Menini, 1990). CNG channels commonly carry an inward Na^+ and Ca^{2+} current but are almost equally permeable to all the monovalent cations. The following sequence of permeability ratios was determined from recordings under bi-ionic conditions in excised patches obtained for the channel from salamander rods: $Li^+ > Na^+ \sim K^+ > Rb^+ > Cs^+$ = 1.14:1:0.98:0.84:0.58 (Menini, 1990). Nevertheless, respect to the native channel, the homomeric CNGA1 channel is more selective for Na^+ than for Li^+ ions (Kaupp and Seifert, 2002), but, in conclusion, permeability ratios are very similar in various isoforms of CNG channels and across species. Also divalent cations can permeate the channel and despite the importance of their physiological role, these ions can also block the channel at high concentrations (Colamartino *et al.*, 1991; Yau and Baylor, 1989). This is due to an

acidic residue in the outer mouth of CNG channels that replaces the two residues of the GYG signature sequence of K^+ channels (Eismann *et al.*, 1994; Sesti *et al.*, 1995). Also the proton concentration affects the CNG channels biophysical properties; indeed lowering the external pH, a subconductance state, due to a blocking effect, is observed (Root and MacKinnon, 1994). Ionic selectivity of CNG channels for non-physiological cations has also been investigated in order to give an estimation of the size of the pore and what came out is that they are permeable to, at least, thirteen organic cations. Thus, considering that the cross section of the narrowest part of the pore must be at least as large as 0.38 x 0.5 nm, the pore should be not bigger than the one of the Ca^{2+} channel of skeletal muscle and not smaller than the ones of Na^+ and K^+ channels (Picco and Menini, 1993).

The macroscopic biophysical properties of CNG channels are generally studied using the patch-clamp technique, either using photoreceptors or different heterologous expression systems. When an inside-out patch excised from the membrane expressing CNG channels is exposed to micromolar concentrations of cyclic-nucleotide, the current elicited by many channels can be recorded and the current observed is obviously dependent on the cGMP concentration and can be described as:

$$I = I_{max} [g^n / (g^n + K^n)]$$

where I_{max} is the maximal current activated by cGMP, g is the cGMP concentration, K the cGMP concentration activating half of the maximal current and n the Hill coefficient. Experimentally, n is between 1.7 and 3.5 and K has a value of 10 μM to 50 μM (Kaupp and Seifert, 2002; Yau and Baylor, 1989; Zimmerman and Baylor, 1992). This indicate that the channel activation is steeply dependent on cGMP concentration and that several cGMP molecules bind to the channel in a cooperative manner (Kaupp and Seifert, 2002).

CNG channel activation also exhibits evidence for a mild voltage-dependence: hyperpolarization appears to increase the rate constant of channel closing (Karpen *et al.*, 1988). The analysis of single channel activity at positive and negative voltages indicates that the outward rectification observed in the presence of low cGMP concentration is primarily due to an increase in the open probability at positive voltages (Sesti *et al.*, 1994). Moreover even if the gating of the wild-type CNGA1 and native CNG channels is voltage independent, it is highly voltage-dependent in the presence of Rb^+, Cs^+ and organic cations (Marchesi *et al.*, 2012).

Albeit all cyclic nucleotides are thought to open the same activation gate in CNG channels, located in the pore loop, the affinity of each of them is not the same, indeed, the open probability of CNG is increased dramatically by the binding of cGMP and less by the other. (Craven and Zagotta, 2006). The common view is that the greater agonist efficacy of cGMP in CNG channels is due to the absence of a Ile636, present in the HCN2 C-terminal, that is thought to interacts with cAMP. In CNG channels instead of the Ile636 there is an aspartate (Asp604) and when this residue is mutated into a neutral amino acid, do not still prefer cGMP instead of cAMP (Sunderman and Zagotta, 1999; Varnum *et al.*, 1995). Additionally, also Thr560 of CNGA1 is thought to stabilize the syn configuration of cGMP during initial binding (Altenhofen *et al.*, 1991).

REFERENCES

Altenhofen, W., Ludwig, J., Eismann, E., Kraus, W., Bönigk, W., and Kaupp, U.B. (1991). Control of ligand specificity in cyclic nucleotide-gated channels from rod photoreceptors and olfactory epithelium. Proc. Natl. Acad. Sci. U. S. A. *88*, 9868–9872.

Anselmi, C., Carloni, P., and Torre, V. (2007). Origin of functional diversity among tetrameric voltage-gated channels. Proteins *66*, 136–146.

Baylor, D. (1996). How photons start vision. Proc. Natl. Acad. Sci. U. S. A. *93*, 560–565.

Baylor, D.A., Lamb, T.D., and Yau, K.W. (1979). Responses of retinal rods to single photons. J. Physiol. *288*, 613–634.

Bezanilla, F. (2008). How membrane proteins sense voltage. Nat. Rev. Mol. Cell Biol. *9*, 323–332.

Biel, M., and Michalakis, S. (2007). Function and dysfunction of CNG channels: insights from channelopathies and mouse models. Mol. Neurobiol. *35*, 266–277.

Biel, M., Zong, X., Ludwig, A., Sautter, A., and Hofmann, F. (1999). Structure and function of cyclic nucleotide-gated channels. Rev. Physiol. Biochem. Pharmacol. *135*, 151–171.

Borisy, F.F., Ronnett, G.V., Cunningham, A.M., Juilfs, D., Beavo, J., and Snyder, S.H. (1992). Calcium/calmodulin-activated phosphodiesterase expressed in olfactory receptor neurons. J. Neurosci. Off. J. Soc. Neurosci. *12*, 915–923.

Bradley, J. (2001). Nomenclature for Ion Channel Subunits. Science *294*, 2095–2096.

Cobbs, W.H., and Pugh, E.N. (1987). Kinetics and components of the flash photocurrent of isolated retinal rods of the larval salamander, Ambystoma tigrinum. J. Physiol. *394*, 529–572.

Colamartino, G., Menini, A., and Torre, V. (1991). Blockage and permeation of divalent cations through the cyclic GMP-activated channel from tiger salamander retinal rods. J. Physiol. *440*, 189.

Contreras, J.E., Srikumar, D., and Holmgren, M. (2008). Gating at the selectivity filter in cyclic nucleotide-gated channels. Proc. Natl. Acad. Sci. *105*, 3310–3314.

Cook, N.J., Hanke, W., and Kaupp, U.B. (1987). Identification, purification, and functional reconstitution of the cyclic GMP-dependent channel from rod photoreceptors. Proc. Natl. Acad. Sci. U. S. A. *84*, 585–589.

Craven, K.B., and Zagotta, W.N. (2006). CNG AND HCN CHANNELS: Two Peas, One Pod. Annu. Rev. Physiol. *68*, 375–401.

Decher, N., Chen, J., and Sanguinetti, M.C. (2004). Voltage-dependent Gating of Hyperpolarization-activated, Cyclic Nucleotide-gated Pacemaker Channels MOLECULAR COUPLING BETWEEN THE S4–S5 AND C-LINKERS. J. Biol. Chem. *279*, 13859–13865.

Derebe, M.G., Zeng, W., Li, Y., Alam, A., and Jiang, Y. (2011). Structural studies of ion permeation and Ca2+ blockage of a bacterial channel mimicking the cyclic nucleotide-gated channel pore. Proc. Natl. Acad. Sci. *108*, 592–597.

Dmitriev, A.V., and Mangel, S.C. (2001). Circadian clock regulation of pH in the rabbit retina. J. Neurosci. Off. J. Soc. Neurosci. *21*, 2897–2902.

Doyle, D.A., Cabral, J.M., Pfuetzner, R.A., Kuo, A., Gulbis, J.M., Cohen, S.L., Chait, B.T., and MacKinnon, R. (1998). The Structure of the Potassium Channel: Molecular Basis of K+ Conduction and Selectivity. Science *280*, 69–77.

Eismann, E., Müller, F., Heinemann, S.H., and Kaupp, U.B. (1994). A single negative charge within the pore region of a cGMP-gated channel controls rectification, Ca2+ blockage, and ionic selectivity. Proc. Natl. Acad. Sci. U. S. A. *91*, 1109.

Emeis, D., Kühn, H., Reichert, J., and Hofmann, K.P. (1982). Complex formation between metarhodopsin II and GTP-binding protein in bovine photoreceptor membranes leads to a shift of the photoproduct equilibrium. FEBS Lett. *143*, 29–34.

Engel, A., and Gaub, H.E. (2008). Structure and Mechanics of Membrane Proteins. Annu. Rev. Biochem. *77*, 127–148.

Fesenko, E.E., Kolesnikov, S.S., and Lyubarsky, A.L. (1985). Induction by cyclic GMP of cationic conductance in plasma membrane of retinal rod outer segment. Nature *313*, 310–313.

Firestein, S. (2001). How the olfactory system makes sense of scents. Nature *413*, 211–218.

Flynn, G.E., and Zagotta, W.N. (2003). A Cysteine Scan of the Inner Vestibule of Cyclic Nucleotide–gated Channels Reveals Architecture and Rearrangement of the Pore. J. Gen. Physiol. *121*, 563–583.

Frings, S., Reuter, D., and Kleene, S.J. (2000). Neuronal Ca2+-activated Cl– channels — homing in on an elusive channel species. Prog. Neurobiol. *60*, 247–289.

Furman, R.E., and Tanaka, J.C. (1990). Monovalent selectivity of the cyclic guanosine monophosphate-activated ion channel. J. Gen. Physiol. *96*, 57–82.

Gamel, K., and Torre, V. (2000). The interaction of Na(+) and K(+) in the pore of cyclic nucleotide-gated channels. Biophys. J. *79*, 2475.

Gray-Keller, M.P., and Detwiler, P.B. (1994). The calcium feedback signal in the phototransduction cascade of vertebrate rods. Neuron *13*, 849–861.

Hackos, D.H. (1997). Calcium Modulation of Ligand Affinity in the Cyclic GMP-gated Ion Channels of Cone Photoreceptors. J. Gen. Physiol. *110*, 515–528.

Hackos, D.H., and Korenbrot, J.I. (1999). Divalent Cation Selectivity Is a Function of Gating in Native and Recombinant Cyclic Nucleotide–gated Ion Channels from Retinal Photoreceptors. J. Gen. Physiol. *113*, 799–818.

Heginbotham, L., Abramson, T., and MacKinnon, R. (1992). A functional connection between the pores of distantly related ion channels as revealed by mutant K+ channels. Science *258*, 1152–1155.

Higgins, M.K., Weitz, D., Warne, T., Schertler, G.F.X., and Kaupp, U.B. (2002). Molecular architecture of a retinal cGMP-gated channel: the arrangement of the cytoplasmic domains. EMBO J. *21*, 2087–2094.

Hille, B. (1992). Ionic Channels of Excitable Membranes (Mass.).

Hoffmann, T., and Dougan, L. (2012). Single molecule force spectroscopy using polyproteins. Chem. Soc. Rev. *41*, 4781–4796.

Holmgren, M. (2003). Influence of Permeant Ions on Gating in Cyclic Nucleotide–gated Channels. J. Gen. Physiol. *121*, 61.

Hsu, Y.T., and Molday, R.S. (1993). Modulation of the cGMP-gated channel of rod photoreceptor cells by calmodulin. Nature *361*, 76–79.

Isaev, N.K., Stelmashook, E.V., Plotnikov, E.Y., Khryapenkova, T.G., Lozier, E.R., Doludin, Y.V., Silachev, D.N., and Zorov, D.B. (2008). Role of acidosis, NMDA receptors, and acid-sensitive ion channel 1a (ASIC1a) in neuronal death induced by ischemia. Biochem. Biokhimi͡ia *73*, 1171–1175.

Jan, L.Y. (1990). A superfamily of ion channels. Nature *345*, 672–672.

Jiang, Y., Lee, A., Chen, J., Cadene, M., Chait, B.T., and MacKinnon, R. (2002). The open pore conformation of potassium channels. Nature *417*, 523–526.

Karpen, J.W., Zimmerman, A.L., Stryer, L., and Baylor, D.A. (1988). Gating kinetics of the cyclic-GMP-activated channel of retinal rods: flash photolysis and voltage-jump studies. Proc. Natl. Acad. Sci. U. S. A. *85*, 1287.

Kaupp, U.B., and Seifert, R. (2002). Cyclic nucleotide-gated ion channels. Physiol. Rev. *82*, 769–824.

Kaupp, U.B., Niidome, T., Tanabe, T., Terada, S., Bönigk, W., Stühmer, W., Cook, N.J., Kangawa, K., Matsuo, H., Hirose, T., *et al.* (1989). Primary structure and functional expression from complementary DNA of the rod photoreceptor cyclic GMP-gated channel. Nature *342*, 762–766.

Koch, K.W. (1992). Biochemical mechanism of light adaptation in vertebrate photoreceptors. Trends Biochem. Sci. *17*, 307–311.

Kohl, S., Marx, T., Giddings, I., Jägle, H., Jacobson, S.G., Apfelstedt-Sylla, E., Zrenner, E., Sharpe, L.T., and Wissinger, B. (1998). Total colourblindness is caused by mutations in the gene encoding the alpha-subunit of the cone photoreceptor cGMP-gated cation channel. Nat. Genet. *19*, 257–259.

Kubota, T., Lacroix, J.J., Bezanilla, F., and Correa, A.M. (2014). Probing α-3(10) transitions in a voltage-sensing S4 helix. Biophys. J. *107*, 1117–1128.

Kusch, J., Nache, V., and Benndorf, K. (2004). Effects of permeating ions and cGMP on gating and conductance of rod-type cyclic nucleotide-gated (CNGA1) channels. J. Physiol. *560*, 605.

Lagnado, L., Cervetto, L., and McNaughton, P.A. (1992). Calcium homeostasis in the outer segments of retinal rods from the tiger salamander. J. Physiol. *455*, 111–142.

Lolicato, M., Nardini, M., Gazzarrini, S., Möller, S., Bertinetti, D., Herberg, F.W., Bolognesi, M., Martin, H., Fasolini, M., Bertrand, J.A., *et al.* (2011). Tetramerization Dynamics of C-terminal Domain Underlies Isoform-specific cAMP Gating in Hyperpolarization-activated Cyclic Nucleotide-gated Channels. J. Biol. Chem. *286*, 44811–44820.

Long, S.B., Campbell, E.B., and MacKinnon, R. (2005a). Crystal Structure of a Mammalian Voltage-Dependent Shaker Family K+ Channel. Science *309*, 897–903.

Long, S.B., Campbell, E.B., and Mackinnon, R. (2005b). Voltage sensor of Kv1.2: structural basis of electromechanical coupling. Science *309*, 903–908.

Magnotta, V.A., Heo, H.-Y., Dlouhy, B.J., Dahdaleh, N.S., Follmer, R.L., Thedens, D.R., Welsh, M.J., and Wemmie, J.A. (2012). Detecting activity-evoked pH changes in human brain. Proc. Natl. Acad. Sci. U. S. A. *109*, 8270–8273.

Maity, S., Mazzolini, M., Arcangeletti, M., Valbuena, A., Fabris, P., Lazzarino, M., and Torre, V. (2015). Conformational rearrangements in the transmembrane domain of CNGA1 channels revealed by single-molecule force spectroscopy. Nat. Commun. *6*, 7093.

Marchesi, A., Mazzolini, M., and Torre, V. (2012). Gating of cyclic nucleotide-gated channels is voltage dependent. Nat. Commun. *3*, 973.

Mari, S.A., Pessoa, J., Altieri, S., Hensen, U., Thomas, L., Morais-Cabral, J.H., and Müller, D.J. (2011). Gating of the MlotiK1 potassium channel involves large rearrangements of the cyclic nucleotide-binding domains. Proc. Natl. Acad. Sci. U. S. A. *108*, 20802–20807.

Matulef, K., and Zagotta, W.N. (2003). Cyclic Nucleotide-Gated Ion Channels. Annu. Rev. Cell Dev. Biol. *19*, 23–44.

Mazzolini, M., Marchesi, A., Giorgetti, A., and Torre, V. (2010). Gating in CNGA1 channels. Pflüg. Arch. Eur. J. Physiol. *459*, 547–555.

Mazzolini, M., Facchetti, G., Andolfi, L., Proietti Zaccaria, R., Tuccio, S., Treu, J., Altafini, C., Di Fabrizio, E.M., Lazzarino, M., Rapp, G., *et al.* (2015). The phototransduction machinery in the rod outer segment has a strong efficacy gradient. Proc. Natl. Acad. Sci. U. S. A. *112*, E2715–E2724.

Menini, A. (1990). Currents carried by monovalent cations through cyclic GMP-activated channels in excised patches from salamander rods. J. Physiol. *424*, 167.

Menini, A. (1995). Cyclic nucleotide-gated channels in visual and olfactory transduction. Biophys. Chem. *55*, 185–196.

Menini, A. (1999). Calcium signalling and regulation in olfactory neurons. Curr. Opin. Neurobiol. *9*, 419–426.

Menini, A. (2004). Olfaction: From Odorant Molecules to the Olfactory Cortex. News Physiol. Sci. *19*, 101–104.

Menini, A., Rispoli, G., and Torre, V. (1988). The ionic selectivity of the light-sensitive current in isolated rods of the tiger salamander. J. Physiol. *402*, 279.

Molday, R.S. (1996). Calmodulin regulation of cyclic-nucleotide-gated channels. Curr. Opin. Neurobiol. *6*, 445–452.

Morais-Cabral, J.H., Zhou, Y., and MacKinnon, R. (2001). Energetic optimization of ion conduction rate by the K+ selectivity filter. Nature *414*, 37–42.

Moreau, A., Gosselin-Badaroudine, P., and Chahine, M. (2014). Molecular biology and biophysical properties of ion channel gating pores. Q. Rev. Biophys. *47*, 364–388.

Müller, D.J., Wu, N., and Palczewski, K. (2008). Vertebrate Membrane Proteins: Structure, Function, and Insights from Biophysical Approaches. Pharmacol. Rev. *60*, 43–78.

Nakamura, T., and Gold, G.H. (1987). A cyclic nucleotide-gated conductance in olfactory receptor cilia. Nature *325*, 442–444.

Nakatani, K., and Yau, K.-W. (1988). Calcium and light adaptation in retinal rods and cones. Nature *334*, 69–71.

Nakatani, K., Koutalos, Y., and Yau, K.W. (1995). Ca2+ modulation of the cGMP-gated channel of bullfrog retinal rod photoreceptors. J. Physiol. *484 (Pt 1)*, 69–76.

Napolitano, L.M.R., Bisha, I., De March, M., Marchesi, A., Arcangeletti, M., Demitri, N., Mazzolini, M., Rodriguez, A., Magistrato, A., Onesti, S., *et al.* (2015). A structural, functional, and computational analysis suggests pore flexibility as the base for the poor selectivity of CNG channels. Proc. Natl. Acad. Sci. U. S. A. *112*, E3619–E3628.

O'Brien, D.F. (1982). The chemistry of vision. Science *218*, 961–966.

Ottschytsch, N., Raes, A.L., Timmermans, J.-P., and Snyders, D.J. (2005). Domain analysis of Kv6.3, an electrically silent channel. J. Physiol. *568*, 737–747.

Palczewski, K., Polans, A.S., Baehr, W., and Ames, J.B. (2000). Ca(2+)-binding proteins in the retina: structure, function, and the etiology of human visual diseases. BioEssays News Rev. Mol. Cell. Dev. Biol. *22*, 337–350.

Paoletti, P., Young, E.C., and Siegelbaum, S.A. (1999). C-Linker of Cyclic Nucleotide–gated Channels Controls Coupling of Ligand Binding to Channel Gating. J. Gen. Physiol. *113*, 17–34.

Papermaster, D.S., and Dreyer, W.J. (1974). Rhodopsin content in the outer segment membranes of bovine and frog retinal rods. Biochemistry (Mosc.) *13*, 2438–2444.

Picco, C., and Menini, A. (1993). The permeability of the cGMP-activated channel to organic cations in retinal rods of the tiger salamander. J. Physiol. *460*, 741.

Picones, A., and Korenbrot, J.I. (1995). Permeability and interaction of Ca2+ with cGMP-gated ion channels differ in retinal rod and cone photoreceptors. Biophys. J. *69*, 120–127.

Pifferi, S., Boccaccio, A., and Menini, A. (2006). Cyclic nucleotide-gated ion channels in sensory transduction. FEBS Lett. *580*, 2853–2859.

Podda, M.V., and Grassi, C. (2013). New perspectives in cyclic nucleotide-mediated functions in the CNS: the emerging role of cyclic nucleotide-gated (CNG) channels. Pflüg. Arch. - Eur. J. Physiol. *466*, 1241–1257.

Poetsch, A., Molday, L.L., and Molday, R.S. (2001). The cGMP-gated channel and related glutamic acid rich proteins interact with peripherin-2 at the rim region of rod photoreceptor disc membranes. J. Biol. Chem.

Purves, D., Augustine, G.J., Fitzpatrick, D., Katz, L.C., LaMantia, A.-S., McNamara, J.O., and Williams, S.M. (2001). The Transduction of Olfactory Signals.

Rebrik, T.I. (1998). In Intact Cone Photoreceptors, a Ca2+-dependent, Diffusible Factor Modulates the cGMP-gated Ion Channels Differently than in Rods. J. Gen. Physiol. *112*, 537–548.

Remmer, M.H., Rastogi, N., Ranka, M.P., and Ceisler, E.J. (2015). Achromatopsia: a review. Curr. Opin. Ophthalmol. *26*, 333–340.

Rief, M. (1997). Reversible Unfolding of Individual Titin Immunoglobulin Domains by AFM. Science *276*, 1109–1112.

Root, M.J., and MacKinnon, R. (1994). Two identical noninteracting sites in an ion channel revealed by proton transfer. Science *265*, 1852–1856.

Sesti, F., Straforini, M., Lamb, T.D., and Torre, V. (1994). Gating, selectivity and blockage of single channels activated by cyclic GMP in retinal rods of the tiger salamander. J. Physiol. *474*, 203.

Sesti, F., Eismann, E., Kaupp, U.B., Nizzari, M., and Torre, V. (1995). The multi-ion nature of the cGMP-gated channel from vertebrate rods. J. Physiol. *487*, 17.

Stavenga, D.G., Grip, W.J. de, and Pugh, E.N. (2000). Molecular Mechanisms in Visual Transduction (Elsevier).

Stryer, L. (1986). Cyclic GMP cascade of vision. Annu. Rev. Neurosci. *9*, 87–119.

Sunderman, E.R., and Zagotta, W.N. (1999). Sequence of Events Underlying the Allosteric Transition of Rod Cyclic Nucleotide–gated Channels. J. Gen. Physiol. *113*, 621–640.

Tang, C.Y., and Papazian, D.M. (1997). Transfer of voltage independence from a rat olfactory channel to the Drosophila ether-à-go-go K+ channel. J. Gen. Physiol. *109*, 301–311.

Tetreault, M.L., Henry, D., Horrigan, D.M., Matthews, G., and Zimmerman, A.L. (2006). Characterization of a novel cyclic nucleotide-gated channel from zebrafish brain. Biochem. Biophys. Res. Commun. *348*, 441–449.

Togashi, K., von Schimmelmann, M.J., Nishiyama, M., Lim, C.-S., Yoshida, N., Yun, B., Molday, R.S., Goshima, Y., and Hong, K. (2008). Cyclic GMP-Gated CNG Channels Function in Sema3A-Induced Growth Cone Repulsion. Neuron *58*, 694–707.

Trudeau, M.C., and Zagotta, W.N. (2003). Calcium/Calmodulin Modulation of Olfactory and Rod Cyclic Nucleotide-gated Ion Channels. J. Biol. Chem. *278*, 18705–18708.

Varnum, M.D., Black, K.D., and Zagotta, W.N. (1995). Molecular mechanism for ligand discrimination of cyclic nucleotide-gated channels. Neuron *15*, 619–625.

Weitz, D., Ficek, N., Kremmer, E., Bauer, P.J., and Kaupp, U.B. (2002). Subunit Stoichiometry of the CNG Channel of Rod Photoreceptors. Neuron *36*, 881–889.

Wells, G.B., and Tanaka, J.C. (1997). Ion selectivity predictions from a two-site permeation model for the cyclic nucleotide-gated channel of retinal rod cells. Biophys. J. *72*, 127–140.

Yan, C., Zhao, A.Z., Bentley, J.K., Loughney, K., Ferguson, K., and Beavo, J.A. (1995). Molecular cloning and characterization of a calmodulin-dependent phosphodiesterase enriched in olfactory sensory neurons. Proc. Natl. Acad. Sci. U. S. A. *92*, 9677–9681.

Yau, K.W., and Baylor, D.A. (1989). Cyclic GMP-Activated Conductance of Retinal Photoreceptor Cells. Annu. Rev. Neurosci. *12*, 289–327.

Yoshizawa, T., and Wald, G. (1963). Pre-lumirhodopsin and the bleaching of visual pigments. Nature *197*, 1279–1286.

Younger, J.P., McCarthy, S.T., and Owen, W.G. (1996). Light-dependent control of calcium in intact rods of the bullfrog Rana catesbeiana. J. Neurophysiol. *75*, 354–366.

Yu, F.H., Yarov-Yarovoy, V., Gutman, G.A., and Catterall, W.A. (2005). Overview of molecular relationships in the voltage-gated ion channel superfamily. Pharmacol. Rev. *57*, 387–395.

Zagotta, W.N., Olivier, N.B., Black, K.D., Young, E.C., Olson, R., and Gouaux, E. (2003). Structural basis for modulation and agonist specificity of HCN pacemaker channels. Nature *425*, 200–205.

Zheng, J., Trudeau, M.C., and Zagotta, W.N. (2002). Rod Cyclic Nucleotide-Gated Channels Have a Stoichiometry of Three CNGA1 Subunits and One CNGB1 Subunit. Neuron *36*, 891–896.

Zhong, H., Molday, L.L., Molday, R.S., and Yau, K.-W. (2002). The heteromeric cyclic nucleotide-gated channel adopts a 3A:1B stoichiometry. Nature *420*, 193–198.

Zhong, H., Lai, J., and Yau, K.-W. (2003). Selective heteromeric assembly of cyclic nucleotide-gated channels. Proc. Natl. Acad. Sci. *100*, 5509–5513.

Zhou, Y., Morais-Cabral, J.H., Kaufman, A., and MacKinnon, R. (2001). Chemistry of ion coordination and hydration revealed by a K+ channel–Fab complex at 2.0 |[angst]| resolution. Nature *414*, 43–48.

Zimmerman, A.L., and Baylor, D.A. (1992). Cation interactions within the cyclic GMP-activated channel of retinal rods from the tiger salamander. J. Physiol. *449*, 759.

Zong, X., Zucker, H., Hofmann, F., and Biel, M. (1998). Three amino acids in the C-linker are major determinants of gating in cyclic nucleotide-gated channels. EMBO J. *17*, 353–362.

Zufall, F., Shepherd, G.M., and Barnstable, C.J. (1997). Cyclic nucleotide gated channels as regulators of CNS development and plasticity. Curr. Opin. Neurobiol. *7*, 404–412.

RESULTS

This section is the sum of several experiments carried out by different people, with expertise in different areas, that were combined with the common aim to explain a single phenomenon.

For what concerns me:

I performed all the electrophysiology experiments and corresponding data analysis and figures preparation. I also carried out part of the molecular biology. I actively participated in writing and designing these works.

Multiple mechanisms underlying rectification in retinal cyclic nucleotide-gated (CNGA1) channels.

Manuel Arcangeletti, Arin Marchesi, Monica Mazzolini, and Vincent Torre.

ORIGINAL RESEARCH

Multiple mechanisms underlying rectification in retinal cyclic nucleotide-gated (CNGA1) channels

Manuel Arcangeletti[1],*, Arin Marchesi[1],*, Monica Mazzolini[1,2] & Vincent Torre[1]

1 Neuroscience Area, International School for Advanced Studies (SISSA), Trieste, Italy
2 CBM S.c.r.l., Area Science Park, Basovizza, 34012, Trieste, Italy

Abstract

In cyclic nucleotide-gated (CNGA1) channels, in the presence of symmetrical ionic conditions, current–voltage (I-V) relationship depends, in a complex way, on the radius of permeating ion. It has been suggested that both the pore and S4 helix contribute to the observed rectification. In the present manuscript, using tail and gating current measurements from homotetrameric CNGA1 channels expressed in Xenopus oocytes, we clarify and quantify the role of the pore and of the S4 helix. We show that in symmetrical Rb^+ and Cs^+ single-channel current rectification dominates macroscopic currents while voltage-dependent gating becomes larger in symmetrical ethylammonium and dimethylammonium, where the open probability strongly depends on voltage. Isochronal tail currents analysis in dimethylammonium shows that at least two voltage-dependent transitions underlie the observed rectification. Only the first voltage-dependent transition is sensible to mutation of charge residues in the S4 helix. Moreover, analysis of tail and gating currents indicates that the number of elementary charges per channel moving across the membrane is less than 2, when they are about 12 in K^+ channels. These results indicate the existence of distinct mechanisms underlying rectification in CNG channels. A restricted motion of the S4 helix together with an inefficient coupling to the channel gate render CNGA1 channels poorly sensitive to voltage in the presence of physiological Na^+ and K^+.

Introduction

Ion channels are ubiquitous proteins playing a fundamental role in cellular functions (Hille 1992). They are grouped in superfamilies evolved from a common ancestor (Jan and Jan 1992; Jegla et al. 2009). The superfamily of voltage-gated ion channels comprises Na^+, K^+, and Ca^{2+} channels the gating of which – that is, transitions between the open and closed conformation – is highly dependent on the voltage across the membrane, as well as cyclic nucleotide-gated (CNG) channels where the gating is primarily controlled by binding of cyclic nucleotides

(CNs) (Jan and Jan 1992; Yu et al. 2005; Jegla et al. 2009).

Voltage-dependent gating in native channels and both in WT and pore mutant CNG channels have been studied, demonstrating a clear coupling between voltage gating and channel activation by cGMP (Karpen et al. 1988; Benndorf et al. 1999; Nache et al. 2006; Martínez-François et al. 2009, 2010). The current rectification observed at low cGMP concentration becomes negligible at saturating concentration of agonist and is attributed to an increase in the open probability (Karpen et al. 1988; Benndorf et al. 1999). The molecular origin underpinning this moderate voltage sensibility is still poorly understood and is possibly caused by the mobility of the selectivity filter (Nache et al. 2006; Martínez-François et al. 2009).

Up until recent years, it was believed that at saturating concentration of agonist, the gating of CNG channels was poorly controlled by voltage. This view was based on recordings of macroscopic currents and single-channel openings obtained in the presence of Li^+, Na^+, and K^+. We have recently shown that in the presence of larger alkali monovalent cations, such as Rb^+ and Cs^+ and of organic cations such as methylammonium (MA^+) and dymethylammonium (DMA^+), gating of CNGA1 channels is also powerfully controlled by voltage (Marchesi et al. 2012). If at positive voltages V the open probability P_o is higher than at negative voltages such as at -200 mV, large tail currents I_t are expected to be measured at -200 mV when they are preceded by steps at positive voltages V. In fact, ion channels which are open at positive voltages will close with delays when V returns to -200 mV, giving raise to I_t.

In the present manuscript, we aim to dissect the mechanisms underlying the observed rectification and to clarify the role of the S4 helix by analyzing I_t and gating currents (I_g) in the presence of alkali monovalent and a variety of organic cations. We show that at saturating cGMP (i) in symmetrical Rb^+ and Cs^+ open-pore rectification prevails in macroscopic currents, whereas voltage-dependent gating becomes larger in symmetrical EA^+ and DMA^+ where the open probability at positive voltages can be 10–20 times larger than at negative ones; (ii) the analysis of tail currents in DMA^+ suggests that at least two voltage-dependent reactions are at the basis of the observed rectification with an apparent valence (z) of 1.70 ± 0.10 and 1.00 ± 0.13, respectively; (iii) neutralization of the second arginine in the S4-transmembrane segments significantly affects only the steeper voltage-dependent transition; (iv) I_g measurements from giant patches containing more than 20,000 CNGA1 channels indicate that the number of elementary charges z moving per channel is not larger than 2.

Material and Methods

Ethical approval

All the studies have been approved by the SISSA's Ethics Committee according to the Italian and European guidelines for animal care (d.l. 116/92; 86/609/C.E.). All *Xenopus laevis* surgeries were performed under general anesthesia and using aseptic technique. Anesthesia was obtained by immersion in a 0.2% solution of Tricaine methane sulfonate (MS-222) for 15–20 min. The individual donor animals were used up to five times. A minimum of 1-month recovery period was ensured between ovarian lobe resection from the same animal to avoid distress.

Molecular biology

The CNGA1 channel from bovine rod consisting of 690 amino acids was used. Tandem dimer constructs were generated by the insertion of one copy of the CNGA1 DNA into a vector pGEMHE already containing another copy of CNGA1 DNA. At the end of the cloning process, two copies of the CNGA1 DNA were connected by a 10-amino acid linker, GSGGTELGST, joining the C terminus of the first CNGA1 with the N terminus of the second one. This second subunit was made by replacing the ApaI restriction site GGGCCC at the end of the CNGA1 DNA without changing the amino acid GGTCCC and adding to the start codon a new ApaI restriction site, followed by a linker using a PCR reaction. Subunits were linked after HindIII/ApaI was cut. cDNAs were linearized and were transcribed to cRNA in vitro using the mMessage mMachine kit (Ambion, Austin, TX). The RxQ and RxQ_WT nomenclature in the text refers to homotetramers and tandem dimer constructs, respectively. Rx indicates one of the first four Arginines in the S4 helix, where R1, R2, R3, and R4 refer to Arg269, Arg272, Arg275, and Arg278, respectively.

Oocyte preparation and chemicals

Mutant channel cRNAs were injected into *X. laevis* oocytes ("Xenopus express" Ancienne Ecole de Vernassal, Le Bourg 43270, Vernassal, Haute-Loire, France). Oocytes were prepared as described by Nizzari et al. (1993). Injected eggs were maintained at 18°C in a Barth solution supplemented with 50 μg/mL of gentamicin sulfate and containing (in mmol/L): 88 NaCl, 1 KCl, 0.82 $MgSO_4$, 0.33 $Ca(NO_3)_2$, 0.41 $CaCl_2$, 2.4 $NaHCO_3$, 5 TRIS-HCl (Tris (hydroxymethyl)aminomethane hydrochloride), pH_o 7.4 (buffered with NaOH). During the experiments, oocytes were kept in a Ringer solution containing (in mmol/L): 110 NaCl, 2.5 KCl, 1 $CaCl_2$, 1.6 $MgCl_2$, 10 HEPES-NaOH, pH_o 7.4 (buffered with NaOH). Usual

Recording apparatus

cGMP-gated currents from excised patches (Hamill et al. 1981) were recorded with a patch-clamp amplifier (Axopatch 200, Axon Instruments Inc., Foster City, CA), 2–6 days after RNA injection at room temperature (20–24°C). The perfusion system was as described by Sesti et al. (1995) and allowed a complete solution change in less than 1 sec. Macroscopic and single-channel current recordings obtained with borosilicate glass pipettes had resistances of 2–5 MΩ in symmetrical standard solution. The standard solution on both sides of the membrane consisted of (in mmol/L) 110 NaCl, 10 HEPES (4-(2-Hydroxyethyl)piperazine-1-ethanesulfonic acid), and 0.2 ethylenediaminetetraacetic acid (pH_o 7.4). When the cation X^+ was used as the charge carrier, NaCl in the standard solution on both sides of the membrane patch was replaced by an equimolar amount of the cation X^+ (buffered at pH_o 7.4 with tetramethylammonium hydroxide). We used Clampex 10.0, Clampfit 10.1, SigmaPlot 9.0, and MatLab 7.9.0 for data acquisition and analysis. Gating currents I_g were measured from excised patches containing at least 10^4 channels both in the absence and presence of 1 mmol/L cGMP with 110 mmol/L TEACl (tetraethylammonium chloride) or NMDG (N-Methyl-D-Glucamine) on both sides of the membrane patch (Perozo et al. 1992; Seoh et al. 1996). In the absence of cGMP, similar results were obtained with 110 mmol/L NaCl on both sides of the patch. Each trace represents the mean of 20 recordings. Patch pipettes have a resistance of 0.2–1 MΩ and a diameter of 10–20 μm (Hilgemann and Lu 1998) as determined from the internal glass opening by visual inspection under a 40× light microscope after fire polishing. Capacitive currents were reduced by parafilm–oil mixture (Hilgemann and Lu 1998) and the P/−4 protocol (Armstrong and Bezanilla 1974). If not otherwise indicated, traces were low pass filtered at 10 kHz and current signals were sampled with a 16-bit A/D converter (Digidata 1440A; Axon Instruments), using a sampling rate of 50 kHz.

Data analysis

Normalized tail currents $I_t - I_{min}/I_{+200}$ against voltage relationship in the presence of symmetrical DMA^+ were fitted with a two components Boltzmann function:

$$y(V) = \left(\frac{A}{1 + e^{(V_{mid1} - V)/K_1}} + \frac{1 - A}{1 + e^{(V_{mid2} - V)/K_2}} \right) \quad (1)$$

where A is a scaling factor for the first Boltzmann component; V_{midi} and k_i are the voltages that give the half-maximal activation and the slope factors for the i Boltzmann component, respectively. The gating charge associated with each Boltzmann component z_i can be obtained using $z_i = RT/k_iF$, where $T = 295$ K, and R and F are the gas and the Faraday constants, respectively.

If not otherwise indicated data are presented as mean ± SEM, with n indicating the number of patches. Statistical significance for parametric analysis was determined using unpaired two-tailed T-test or single-variable analysis of variance (ANOVA), as indicated. For pairwise comparisons, Bonferroni test was used as post hoc test. A value of $P < 0.01$ was considered significant. Data analysis and figures were made with Clampfit 10.1 (Molecular Devices, Sunnyvale, CA), Sigmaplot 12.0 (Systat Software, Chicago, IL) and MatLab 7.9.0 (MathWorks, Natick, MA).

Counting the number N of CNGA1 channels in excised giant membrane patches

A reliable measurement of I_g can be obtained only when excised giant membrane patches contain at least 10^4 channels as in experiments using cut-open voltage-clamp (Perozo et al. 1992) or in macro/giant membrane patches (Hilgemann and Lu 1998). In the presence of 1 mmol/L cGMP, the open probability P_o at +60 mV of CNGA1 channels is 0.8 ± 0.08 ($n = 3$) and the single-channel conductance γ_{sc} is 30 ± 3 pS ($n = 3$). The number N of CNGA1 channels is estimated as:

$$N = \frac{I(V)}{P_o \gamma_{sc} V} \quad (2)$$

where I is the macroscopic current measured at membrane voltage (V). With patch pipettes of the diameter of $1–2 -\mu$m, the current I at ±60 mV could be 1 or 2 nA (Fig. 1A) corresponding to values of N from 0.7 ± 0.1 to $1.4 \pm 0.3 \times 10^3$. Using pipettes of a diameter varying between 10 and 20 μm, the amplitude of I at ±10 mV could be ≥10 nA (Fig. 1B) indicating that $N \geq 4.2 \pm 0.8 \times 10^4$. When 110 mmol/L NaCl in the patch pipette was substituted entirely with TEACl – impermeable ions – for measuring I_g, equation 2 was substituted with:

$$N = \frac{I(V)}{\alpha(V) P_o \gamma_{sc} V} \quad (3)$$

$$\alpha = \frac{I_{TEACl}(V)}{I_{Na}(V)} \quad (4)$$

where α is the fractional blockage of the Na^+ current caused by TEACl. As shown in Figure 1C, when extracellular Na^+ was substituted with TEA^+ in outside-out
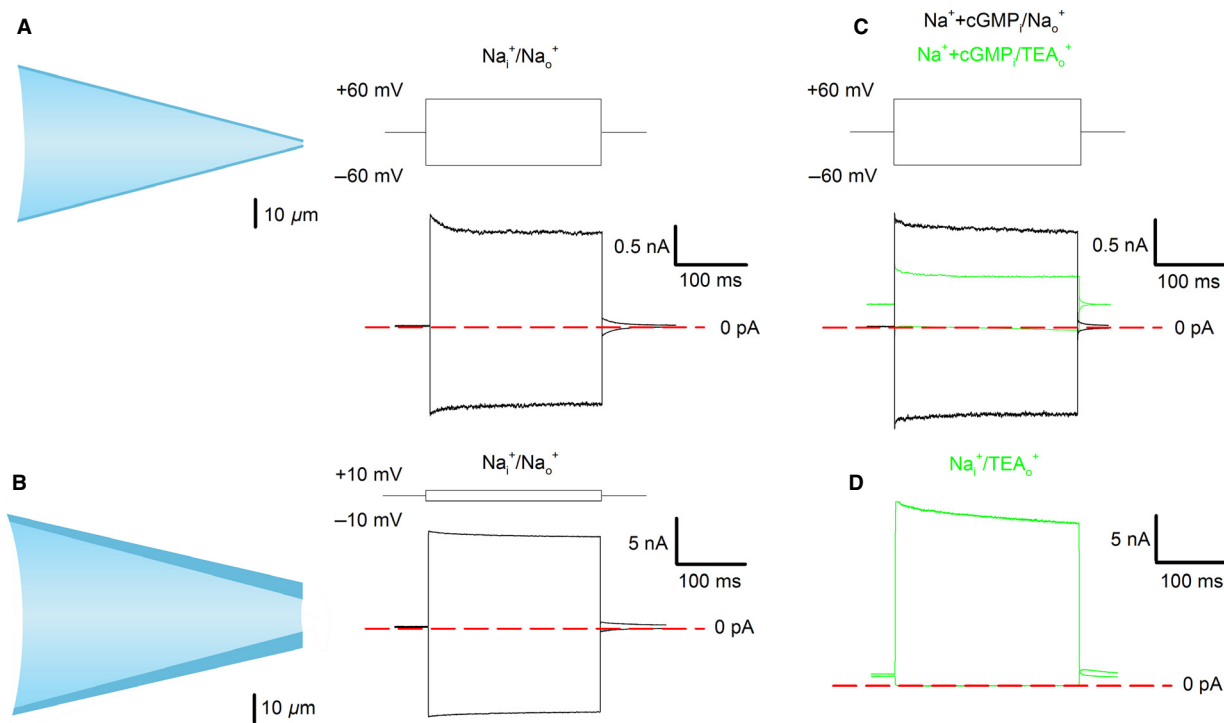
Figure 1. Counting the number of channels in excised giant membrane patches. (A) Currents recorded at ± 60 mV in the presence of 1 mmol/L cGMP in symmetrical 110 mmol/L NaCl using patch pipette with a diameter of 1–2 μm. (B) Currents recorded at ± 10 mV in the presence of 1 mmol/L cGMP in symmetrical 110 mmol/L NaCl using patch pipette with a diameter of 12 μm. (C) blockage by extracellular TEACl in outside-out patches. Black traces represent currents at ± 60 mV in symmetrical 110 mmol/L NaCl and in green the same but with TEACl in the bath solution and NaCl + 1 mmol/L cGMP inside the patch pipette. (D) Currents recorded at ± 60 mV in the presence of 1 mmol/L cGMP with 110 mmol/L NaCl in bath solution and 110 mmol/L TEACl inside a large patch pipette. A, B, and D are excised patches in inside-out configuration, whereas C is in an outside-out patch. Red broken lines indicate 0 current level.

patches at +60 mV $\alpha = 0.48 \pm 0.04$ ($n = 4$). In the presence of 110 mmol/L TEACl in the patch pipette and 110 mmol/L NaCl in the bathing medium, a cGMP-gated current of 20 nA was recorded at + 60 mV (Fig. 1D). In these experiments, the estimated value of N from equation (4) was $2.9 \pm 0.8 \times 10^4$.

Properties of gating currents of spHCN channels measured with giant membrane patches

In order to verify that our experimental conditions could measure gating currents in a reliable way, we expressed in oocytes the mRNA coding for Hyperpolarization-activated cyclic nucleotide-gated (HCN) channels from the sea urchin sperm (spHCN). Gating currents from these channels were already measured with cut-open oocyte technique (Männikkö et al. 2002). The comparison with already published data and those obtained by us with giant membrane patches represents a good test of our experimental setup. The activation curve in the spHCN

channel was determined from the isochronal tail current analysis at 50 mV following voltage steps from -10 mV to -150 mV in the presence of 1 mmol/L cAMP (Fig. 2A). Gating currents were obtained in response to voltage steps from -10 to -120 mV, from a holding potential of -10 mV, tail potential +50 mV (Fig. 2B). Figure 2C reproduces the relationship between G/G_{-150} (filled symbols) and V in symmetrical 110 mmol/L KCl conditions and the relation between Q/Q_{-120} (open symbols) and V in symmetrical 110 mmol/L TEACl conditions. The total charge Q at a given voltage V, $Q(V)$, was obtained by integrating the off-gating current (i.e., the current associated with the movement of the voltage sensor from the activated to the resting state) over time.

Membrane fluctuations

In the presence of 1 mmol/L cGMP, WT CNGA1 channels have a dominant single-channel conductance. Under these conditions, the noise variance (σ^2) is related to the amplitude of the mean current (I) by the following equation:
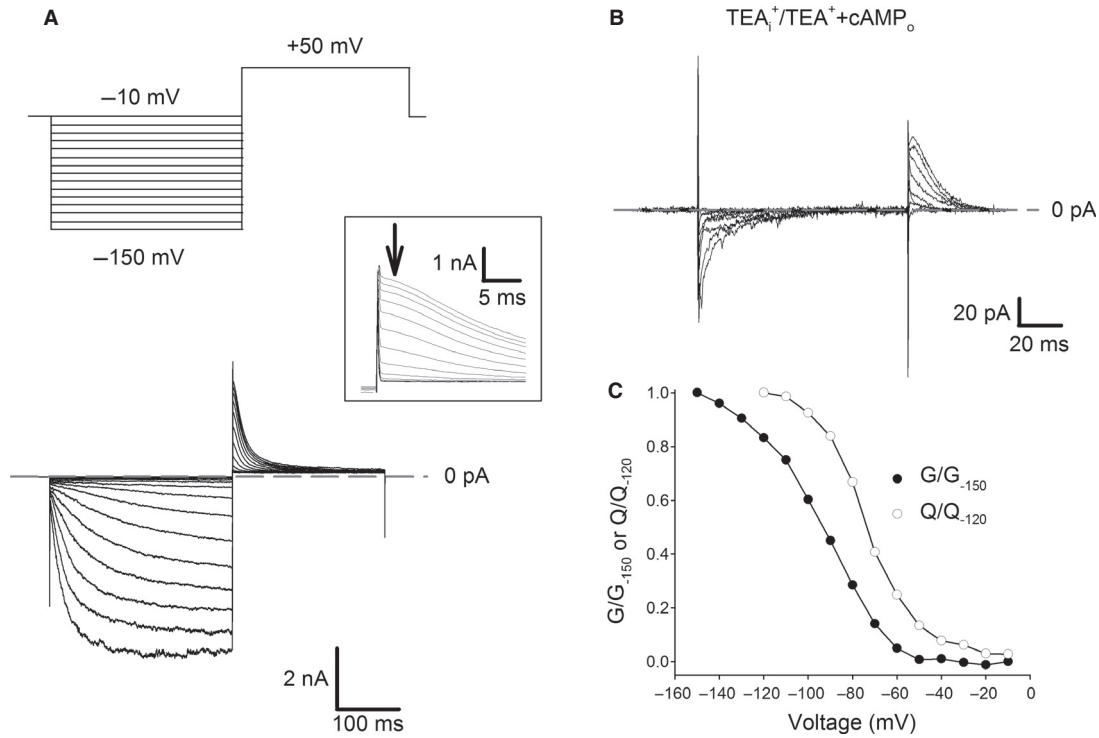
Figure 2. Comparison of the dependence of G/G_{-150} and Q/Q_{-120} on voltage in the spHCN channels. (A) Current recordings from giant patches excised from oocytes injected with the mRNA coding for the spHCN channels (lower panel). Voltage steps are shown in the upper panel. Current recordings obtained in the presence of 1 mmol/L cAMP and in symmetrical 110 mmol/L KCl conditions. The inset in the box represents the tail current (tail potential at +50 mV) and the arrow corresponds to the isochronal currents used to calculate the conductance (G). (B) Gating current for spHCN channel in response to voltage steps from −10 to −120 mV, from a holding potential of −10 mV, tail potential +50 mV. (C) Ionic conductance (G/G_{-150} filled circles) and normalized charge movement (Q/Q_{-120} open circles) for the electrical recordings in A and B; the conductance (G) was calculated from tail current (arrow in panel A) normalized as $G(V) = [I(V)-I_{min}]/(I_{max}-I_{min})$; the gating current (Fig. 2A) was integrated in time so to obtain the charge (Q). Gray broken lines in panels A and B indicate 0 current level.

$$\sigma^2 = i_{sc}I - \frac{I^2}{N} \qquad (5)$$

where i_{sc} is the amplitude of the single-channel current and N is the number of channels present in the membrane patch (Neher and Stevens 1977). At hyperpolarized membrane potentials, when voltage drives protons into the channel pore, a fast mechanism of blockage could result in an increased open-channel noise (σ_o^2) from fast, nonresolved gating transitions (Root and MacKinnon 1994). Therefore, we ask whether the open-channel noise could contribute to the differences in noise level here described. If σ_e^2 is the ensemble variance of the open-pore fluctuations and σ^2 is the noise associated with channel opening and closing, the overall amplitude of membrane fluctuations is expected to be:

$$\sigma_{tot} = \sqrt{\sigma_e^2 + \sigma^2} \qquad (6)$$

where σ_e^2 can be calculate as:

$$\sigma_e^2 = NP_o\sigma_o^2 \qquad (7)$$

The overall contribution of σ_e to σ_{tot} depends only on two independent parameters: σ_o/i_{sc} and P_o. At +100 mV σ_o/i_{sc} is around 0.1, and does not depend on the permeant ion (Kusch et al. 2004). If Cs^+ permeation is considered, at −200 mV P_o has to be less than 0.5 (Marchesi et al. 2012). Even in the unlikely scenario where σ_o/i_{sc} degrades to 0.5, σ_e is not expected to increase membrane fluctuations more than 25%, while the differences in noise levels experimentally observed between +200 and −200 mV are usually between 700 and 1000%. It is fair to conclude that the open-channel noise is not likely to explain most of the differences observed in the noise level in the present manuscript.

Molecular modeling

Sequences alignment were performed using The UniProt Consortium server-based software (available at http://www.uniprot.org/) and further visualized and edited with Jalview 2.8 (Clamp et al. 2004). Pore cartoons were prepared using known structures of K_v and NaK chimeric channels available in the Protein Data Bank (PDB) using

the DeepView module of the Swiss-PDBViewer (v4.04) software (Guex and Peitsch 1997).

Results

Ionic permeation of alkali monovalent cations through WT CNGA1 channels

Current recordings obtained under voltage clamp in symmetrical conditions of Li$^+$, Na$^+$, K$^+$, Rb$^+$, and Cs$^+$ (110 mmol/L) are shown in Figure 3.

The shape of these recordings differs – according to the permeating ion – in several aspects. First, the current–voltage *I-V* relationship depends on the permeant ion, being outwardly rectifying in the presence of K$^+$ (Fig. 3C), almost linear in the presence of Li$^+$ and Na$^+$

(Fig.3A and B), and inwardly rectifying in the presence of Rb$^+$ and Cs$^+$ (Fig. 3D and E). Second, small tail currents I$_t$ can be observed in the presence of small alkali cations, such as Li$^+$, Na$^+$, and K$^+$ (Figs. 3A–C and F–H) which become significant with the larger alkali cations Rb$^+$ and Cs$^+$ (Fig. 3D, E, I, and J). These transient currents are not likely to arise from a voltage-dependent proton blockage (Root and MacKinnon 1994), as very similar tail currents were observed when extracellular pH$_o$ was lowered to 5 (Fig. 4). In fact, Na$^+$ and Rb$^+$ currents observed at −200 mV increase from 5 to 10 times when proton concentration is decreased from pH$_o$ 5 to 7.4 (Fig. 4A, B and D, E for Na$^+$ and Rb$^+$ conditions, respectively), reflecting proton blockage. However, only a modest effect on P_o/P_{o_max} curves was observed (Fig. 4C and F), suggesting that tail currents do not arise from Glu363
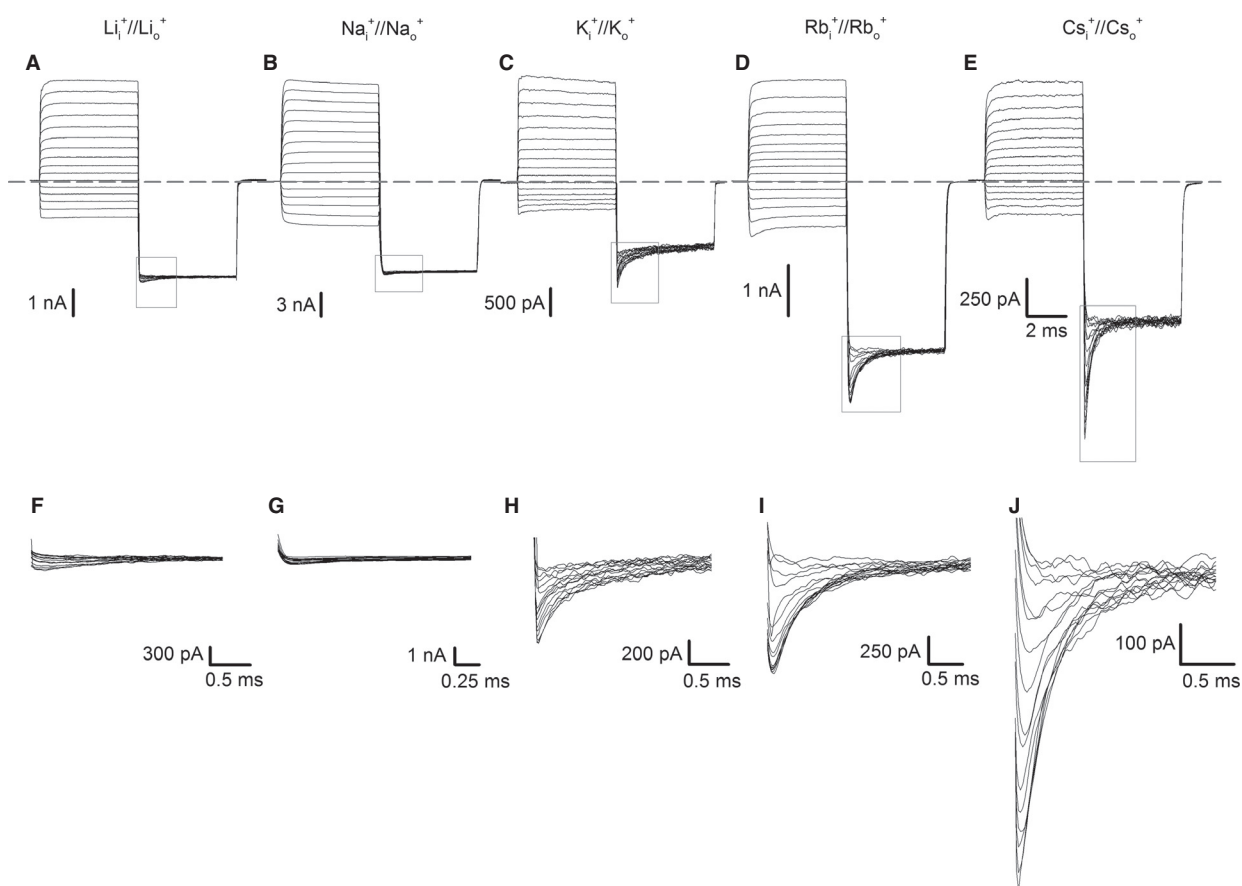

Figure 3. Macroscopic and tail currents in symmetrical Li$^+$, Na$^+$, K$^+$, Rb$^+$, and Cs$^+$ conditions. (A–E) Macroscopic currents recorded from excised patches in symmetrical solutions of Li$^+$ (A), Na$^+$ (B), K$^+$ (C), Rb$^+$ (D) , and Cs$^+$ (E) with 1 mmol/L cGMP in the intracellular medium. Leak and capacitive components were removed subtracting from the cGMP-activated current those records obtained in response to the same voltage protocol but without cGMP. The voltage commands were stepped from a holding potential of 0 mV to prepulses varying between −100 and +200 mV in 20 mV steps. At the end, the voltage command was moved to −200 mV for 5 msec in order to elicit tail currents $I_t(V)$. Gray broken line indicates 0 current level. (F–J), Enlargement of tail currents (boxed areas in A–E) in Li$^+$ (F), Na$^+$ (G), K$^+$ (H), Rb$^+$ (I), and Cs$^+$ (J). Current recordings were filtered at 10 kHz and sampled at 50 kHz to resolve rapid transients.
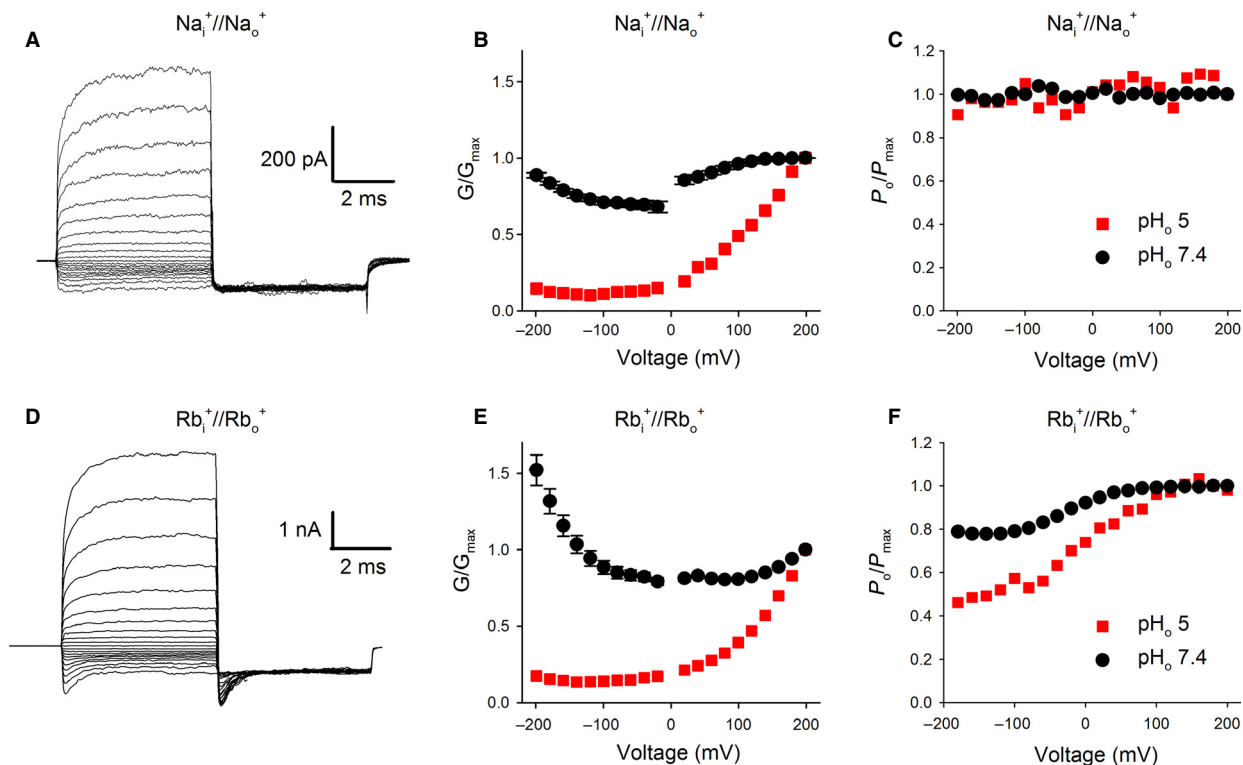
Figure 4. Macroscopic and tail currents in symmetrical Na^+ and Rb^+ conditions at low pH_o. (A) Macroscopic currents recorded from excised patches in symmetrical solutions of Na^+ with 1 mmol/L cGMP on the cytoplasmic side and pH_o 5 at the extracellular side of the membrane (pH_i = 7.4). Tail currents at −200 mV evoked by prepulses at voltages from −200 to +200 mV (ΔV=20 mV); current recordings were filtered at 10 kHz and sampled at 50 kHz to resolve rapid transients. (B) Dependence of G/G_{+200} on V for Na^+ at pH_o 7.4 (black dots) and 5 (red squares). (C) Estimation of P_o/P_{o_max} from tail currents. P_o/P_{o_max} was estimated as I_t/I_{t_max}. (D) as in A but in symmetrical solutions of Rb^+. E, as in B but for Rb^+. F, as in C but for Rb^+.

protonation/deprotonation. These recordings suggest that a fast mechanism of blockage underscore proton action in CNGA1 channels, which is not expected to result in significant measurable tail currents within the used recording bandwidth (Fig. 4). Thus, the observed current decays in response to voltage jumps are likely to reflect a voltage-dependent conformational change.

If these current recordings are not averaged over several trials, another remarkable and unexpected feature is observed: in the presence of Rb^+ and Cs^+ current recordings at negative voltages are significantly noisier than those at positive voltages, although the mean outward and inward currents are approximately similar (Marchesi et al. 2012). The relation σ^2/I against V for different ions, where σ^2 is the current variance and I the macroscopic mean current, is shown in Figure 5A–E. If channels open to a single conductance level, σ^2/I is equal to $i_{sc}(1-P_o)$, where i_{sc} is the single-channel current and P_o is the open probability (Neher and Stevens 1977). As the open-channel noise associated with the proton blockage at resting membrane potentials is not expected to contribute signifi-

cantly to the differences observed in membrane fluctuations (see Methods), if both, i_{sc} and P_o do not depend significantly on voltage the σ^2/I versus voltage relationship is expected to be approximately linear. While this seems to be so for Li^+ and Na^+ permeation (5A, B), it is not so when K^+, Rb^+, and Cs^+ (5C–E) are used as the charge carriers, suggesting that in the presence of symmetrical Rb^+ and Cs^+ – and, to a lesser extent, also in the presence of K^+ – WT CNGA1 channels have a voltage-dependent gating (Marchesi et al. 2012).

How do voltage-dependent changes in i_{sc} and P_o, as suggested from noise analysis and single-channel recordings (Marchesi et al. 2012), relate to the I–V relationship shown in Figure 3, and how do they depend on the permeant ion? To answer this basic question, we have obtained and compared the dependence from V of the normalized conductance G/G_{+200} (Fig. 5F) and the amplitude of the normalized tail current I_t/I_{t+200} (Fig. 5G). The $I_t(V)/I_{t+200}$ relationship provides a good estimate of the dependence of P_o/P_{o+200} on V, whereas $G(V)/G_{+200}$ depends on both, γ_{sc} and P_o. From the knowledge of
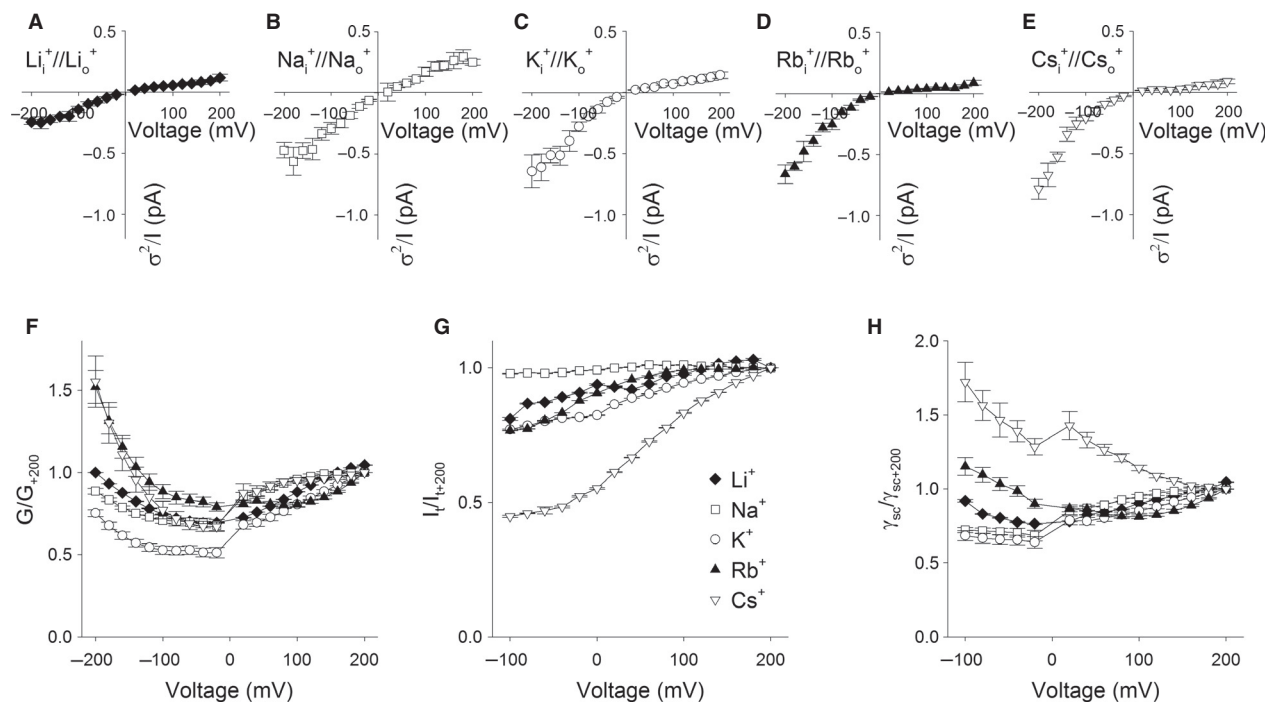
Figure 5. G/G_{+200}, P_o/P_{o+200}, γ/γ_{200} against V relationships and noise analysis in symmetrical Li^+, Na^+, K^+, Rb^+, and Cs^+ conditions. (A–E) Relationship between σ_i^2/I and V for Li^+, (A), Na^+ (B), K^+ (C), Rb^+ (D), and Cs^+ (E). The background noise observed in the absence of cGMP was subtracted; ($n \geq 6$). F, Dependence of G/G_{+200} on V for Li^+, Na^+, K^+, Rb^+, and Cs^+. G/G_{+200} is the fractional steady conductance obtained from macroscopic currents elicited by voltage commands from -200 to $+200$ mV ($\Delta V = 20$ mV). G, Dependence of P_o/P_{o+200} on V for Li^+, Na^+, K^+, Rb^+, and Cs^+ obtained from tail currents as I_t/I_{t+200}. (H) Dependence of $\gamma_{sc}/\gamma_{sc+200}$ on V for Li^+, Na^+, K^+, Rb^+, and Cs^+ ions. The $\gamma_{sc}/\gamma_{sc+200}$ relationship for various ions was computed from the G/G_{+200} and P_o/P_{o+200} plots as described in the text. Li^+ (filled diamonds), Na^+ (open squares), K^+ (open circles), Rb^+ (filled triangles), and Cs^+ (open triangles); ($n \geq 4$).

$I_t(V)/I_{t+200}$ and $G(V)/G_{+200}$ the dependency of the relative single-channel conductance $\gamma_{sc}/\gamma_{sc+200}$ on V was inferred by dividing the values of G/G_{+200} obtained at different voltages by the corresponding values of P_o/P_{o+200}. The $\gamma_{sc}(V)/\gamma_{sc+200}$ relationship thus obtained is shown in Figure 5H and illustrates the dependency of the open-pore rectification on the permeant ions.

Alternatively, when clear tail currents are observed as in the presence of Rb^+ and Cs^+, the dependency of i_{sc}/i_{sc+200} and of deactivation time constant (τ_{deact}) from V could be directly measured from a different voltage protocol (Fig. 6A and B). The voltage commands were first stepped from a holding potential of 0 mV to a prepulse at 200 mV to maximally open channels and were next followed by test voltages varying between -200 and 200 mV in 20 mV steps to induce tail currents. As expected – reflecting a voltage-dependent transition – the deactivation time constants are voltage dependent, being faster at hyperpolarized potentials, either when Rb^+ (Fig. 6C) or Cs^+ (Fig. 6D) ions are used as the charge carriers. The normalized I–V relationship obtained by plotting the instantaneous tail currents measured at the beginning of each step (see arrows in

Fig. 6A and B) versus the step voltage is shown in Figure 6E and F for Rb^+ and Cs^+, respectively (filled circles). These relationships are inwardly rectifying, and are almost identical to the relationship estimated for the $\gamma_{sc}(V)/\gamma_{sc+200}$ shown in Figure 5H (compare solid lines and filled circles in Fig. 6E and F). These results demonstrate that in symmetrical Rb^+ and Cs^+ the open-channel current strongly depends on V.

To double check the accuracy of our $P_o(V)/P_{o+200}$ and $i_{sc}(V)/i_{sc+200}$ plots, we asked whether it was possible to recapitulate the $\sigma^2/I(V)$ relationship obtained from noise analysis. First, the $i_{sc}(V)/i_{sc+200}$ plots determined from tail currents (Fig. 6E and F) were scaled to the i_{sc} experimentally measured from single-channel recordings at +160 mV in symmetrical Rb^+ and Cs^+ (Marchesi et al. 2012) in order to obtain the i_{sc} versus V relation. The P_o/P_{o+200} relationships were also scaled to the absolute P_o at +160 mV determined from noise analysis as $1 - [(\sigma^2/I)/i_{sc}]$ in order to avoid the typical variability inherent to single-channel measurements. σ_I^2/I where then computed from the single-channel parameters as $i_{sc}(1-P_o)$. Figure 6G and H illustrate the $\sigma^2/I(V)$ relationship thus extrapolated in
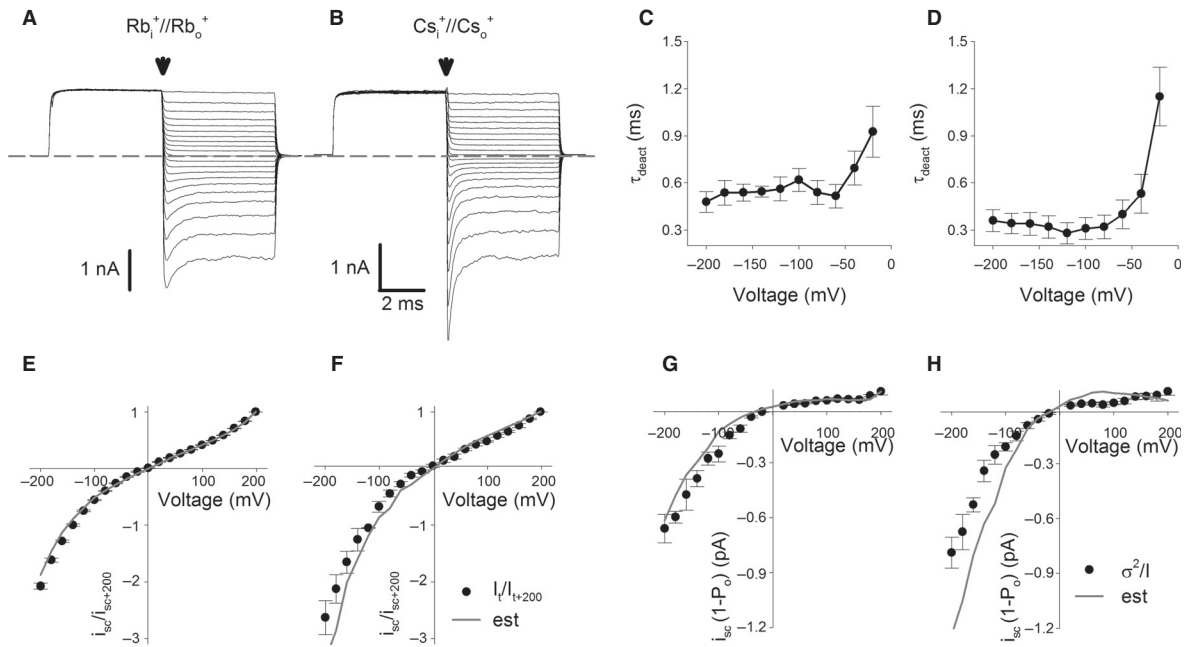
Figure 6. Tail currents, i_{sc}/i_{sc+200} against *V* relationship and predicted macroscopic current noise in symmetrical Rb$^+$ and Cs$^+$ conditions. (A,B) Macroscopic currents in symmetrical solutions of Rb$^+$ (A) and Cs$^+$ (B). Voltage prepulse held at +200 mV was followed by test potentials ranging from −200 mV to +200 mV (ΔV = 20 mV). Gray broken line indicates 0 current level. (C,D) Dependence of inward transient kinetics on *V* in symmetrical Rb$^+$ (C) and Cs$^+$ (D). These transients decay with a single time constant between 0.3 and 1.2 msec. (E,F) Dependence of i_{sc}/i_{sc+200} on *V* for Rb$^+$ (E) and Cs$^+$ (F) obtained from instantaneous *I*–*V* relationship measured immediately after the depolarizing voltage prepulse (see arrows in A,B). Solid gray lines represent the expected i_{sc}/i_{sc+200} curves from the $\gamma_{sc}/\gamma_{sc+200}$ plots in 5H; ($n \geq 4$). G,H, Dependence of $i_{sc}(1-P_o)$ on *V* for Rb$^+$ (G) and Cs$^+$ (H). In the presence of 1 mmol/L cGMP, WT CNGA1 channels have a dominant single-channel conductance (γ_{sc}). Under these conditions, the noise variance (σ_I^2) is related to the amplitude of the mean current (I) by: $\sigma_I^2 = i_{sc}I - I^2/n$. If i_{sc} is the single-channel current then the ratio σ_I^2/I of the variance of current fluctuations (σ_I^2) and of the mean current (I) is $i_{sc}(1-P_o)$. Filled circles show the experimentally observed noise (σ_I^2/I) in macroscopic currents at different voltages (see also Fig. 5A–E). Solid lines represent the expected $i_{sc}(1-P_o)$ curves computed from the P_o/P_{o+200} and i_{sc}/i_{sc+200} plots as described in the text.

symmetrical Rb$^+$ and Cs$^+$ which closely tracks the σ^2/I relationship experimentally measured in Rb$^+$ and – to a lesser extent – in Cs$^+$. The discrepancies observed in symmetrical Cs$^+$ between the observed and the predicted noise are probably due to the flickering openings and the subconductance states previously reported at hyperpolarized potentials during Cs$^+$ permeation (Marchesi et al. 2012).

These observations are consistent with significant differences in both, the single-channel conductance γ_{sc} and the open probability P_o at positive and negative voltages. In the presence of Rb$^+$ and Cs$^+$ γ_{sc} increases of ~200% and ~300% from 200 to −200 mV (Fig. 6E and F), whereas P_o decreases of ~25% and ~55% (Fig. 5G), respectively, resulting in an inwardly rectifying *I*–*V* relationship. When Li$^+$, Na$^+$, and K$^+$ are the charge carriers, the dependency of γ_{sc} and P_o on *V* is very mild (Fig. 5G and H), and the resulting *I*–*V* relationship is almost linear.

Take together, these data clearly demonstrate that the $G(V)/G_{+200}$, $I_t(V)/I_{t+200}$, and $\gamma_{sc}(V)/\gamma_{sc+200}$ relationship

depend on the ionic species, showing a profound coupling between permeation and gating in CNGA1 channels.

Ionic permeation of organic cations through WT CNGA1 channels

To further explore the linkage between voltage gating and permeation, we analyzed tail currents also in the presence of large organic cations such as MA$^+$, DMA$^+$, and EA$^+$. Figure 7 illustrates macroscopic current recordings obtained in the presence of symmetrical MA$^+$ (Fig. 7A), DMA$^+$ (Fig. 7B), and EA$^+$ (Fig. 7C) from voltage commands very similar to those described in Figure 3. The *I*–*V* relationships were outwardly rectifying for all three cations, being $|I_{+200}/I_{-200}|$ equal to 3.31 ± 0.33, 7.22 ± 1.05, and 23.25 ± 0.89 for MA$^+$, DMA$^+$, and EA$^+$, respectively (Fig. 7G), in agreement with previous findings for MA$^+$ and DMA$^+$ (Marchesi et al. 2012). Moreover, the macroscopic current traces shown in
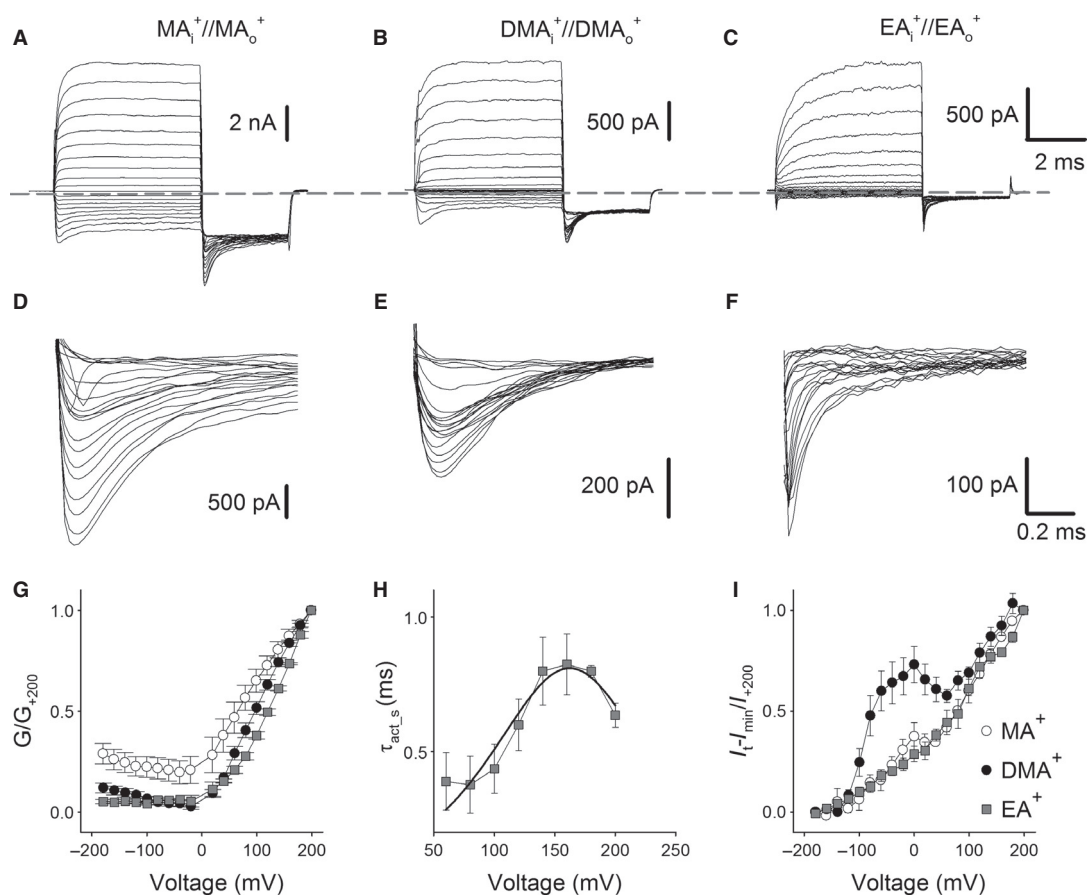
Figure 7. Macroscopic and tail currents in symmetrical MA$^+$, DMA$^+$, and EA$^+$ conditions. (A–C) Macroscopic currents recorded from excised patches in symmetrical solutions of MA$^+$ (A), DMA$^+$ (B), and EA$^+$ (C) with 1 mmol/L cGMP in the intracellular medium. Voltage prepulses from -180 to $+200$ mV ($\Delta V = 20$ mV) were followed by a tail potential at -200 mV. Gray broken line indicates 0 current level. (D–F) Enlargement of tail currents in MA$^+$ (D), DMA$^+$ (E), and EA$^+$ (F). Current recordings were filtered at 10 kHz and sampled at 50 kHz. (G) Dependence of G/G_{+200} on V for MA$^+$, DMA$^+$, and EA$^+$. MA$^+$ open circles, DMA$^+$ filled circles, EA$^+$ filled squares. (H) Dependence of the slow activation time constants (τ_{act_s}) on V in the presence of EA$^+$. The bell-shaped distribution of τ_{act_s} was fitted to the following relation: $\tau_{act\_s} = 1/[\alpha(V)+\beta(V)]$, where $\alpha(V)$ and $\beta(V)$ are the voltage-dependent forward and backward rate constants, respectively. Dependence of I_t-I_{min}/I_{+200}, obtained from tail currents, on V for MA$^+$, DMA$^+$, and EA$^+$. Symbols as in G; ($n \geq 4$).

Figure 7A–C show a time-dependent increase in current amplitude at depolarizing potentials. We have analyzed the activation time constant (τ_{act}) in the presence of EA$^+$, where it appears to be particularly slow (Fig. 7C). The time courses could be described as the sum of two exponentials, yielding a fast (τ_{act_f}) and slow (τ_{act_s}) time constant. τ_{act_f} develops in <100 μs and could not be reliably solved and measured within the used recording bandwidth; however, the dependency of τ_{act_s} on V could be studied. The $\tau_{act\_s}(V)$ relationship appears to be bell shaped (Fig. 7H), indicating that the slower activation component τ_{act_s} is associated with the translocation of 0.88 equivalent charges.

Furthermore the analysis of tail currents reveals an unconventional behavior (Fig. 7D–F). In the presence of

DMA$^+$ (Fig. 7E), and – to a lesser extent – also in the presence of MA$^+$ (Fig. 7D) and EA$^+$ (Fig. 7F), tail currents exhibit a plateau before further increasing with the prepulse amplitude. These observations are reflected in the prominent hunch observed around 0 mV for DMA$^+$ in the I_t-I_{min}/I_{+200} versus V plot (Fig. 7I, filled circles), indicating the possibility that two different charge systems underlie voltage gating.

The $G(V)/G_{+200}$ relationship for DMA$^+$ does not mirror the I_t-I_{min}/I_{+200} versus V plot between -200 and 0 mV (Fig. 7G, filled circles) and unexpectedly, the slope of the $G(V)/G_{+200}$ curve is negative within this voltage range (compare Fig. 7G and 7I, filled circles). Whereas the amplitude of tail currents observed at -200 mV depends only on the P_o at the preceding voltage

commands, and hence the $I_t - I_{min}/I_{+200}$ versus V plot depends solely on P_o, the $G(V)/G_{+200}$ relationship depends on both γ_{sc} and P_o. It is therefore conceivable that in the $G(V)/G_{+200}$ relationship a nonlinearity of i_{sc} effectively covers the early voltage-dependent transitions observed at negative voltages in the $I_t - I_{min}/I_{+200}$ versus V plot.

In this view, the negative slope of the $G(V)/G_{+200}$ relationship observed between -200 and 0 mV (Fig. 7G) is due to a decrease in single-channel conductance that has overcome the voltage-dependent increase in P_o. This hypothesis leads to the prediction that macroscopic current noise decreases more than linearly with voltage. Figure 8A illustrates current recordings obtained from the same inside-out membrane patch at -200, -150, and -100 mV in the presence of symmetrical DMA$^+$. Indeed, current r.m.s. increases more than six times from -100 mV to -200 mV, being 8.7 and 1.5 pA at -200 and -100 mV, respectively (Fig. 8A). Figure 8B shows the $\sigma^2/I(V)$ relationship which is equivalent to $i_{sc}(1-P_o)$ as discussed above. Since between -200 and -100 mV P_o is almost constant (Fig. 7I), the ratio σ^2/I is expected to be driven by changes in the i_{sc} within this voltage range. An estimate of the dependency of the relative single-channel current i_{sc}/i_{-200} on V was inferred by dividing the values of G/G_{+200} obtained at different voltages by the corresponding values of P_o/P_{o+200}. The $i_{sc}(V)/i_{-200}$ relationship thus obtained is shown in Figure 8C (solid line) and closely matches the measured normalized noise (filled circles).

To further substantiate the notion that the single-channel conductance is inversely related to the membrane potential at hyperpolarized voltages, we analyzed the properties of single-channel currents in the presence of DMA$^+$. Figure 8D and E show electrical recordings obtained from an inside-out patch containing only two CNGA1 channels (Fig. 9) in symmetrical DMA$^+$ at -200, -150, and -100 mV. At 5 kHz bandwidth (Fig. 8D, left traces) clear openings of variable amplitude could be observed only at -200 mV. Further filtering at 1 kHz (Fig. 8D, right traces) reveals flickering openings also at -150 mV, but no electrical signal detaching from membrane noise could be reliably measured at -100 mV. In the corresponding amplitude histogram, flickering openings appear as a one-sided tail spreading out from the closed state noise which rapidly reduces as membrane voltage depolarizes (Fig. 8E). Estimates of single-channel currents obtained from peak analysis (Marchesi et al. 2012) show that the single-channel conductance is almost halved from -200 to -100 mV (Fig. 8E).

These results clearly demonstrate that: (i) permeation of large organic cations is associated with outward rectification; (ii) two voltage-dependent transitions are at the basis of the observed voltage gating; (iii) early voltage-dependent transitions occurring at hyperpolarized potentials are covered by the voltage dependency of γ_{sc} in the $G(V)/G_{+200}$ relationship.

The role of positive charges in S4 in voltage sensing

If the movement of S4 is responsible for voltage sensing, replacement of Arg269, Arg272, Arg275, and Arg278 in S4 (here referred to as R1, R2, R3, and R4) with a neutral amino acid such as Glutamine is expected to alter gating. None of the RxQ mutant channels give rise to appreciable currents when expressed in oocytes; however, clear cGMP currents could be measured from tandem constructs RxQ_WT where one mutant channel was attached to a WT CNGA1 subunit with an appropriate linker (Marchesi et al. 2012). A significant effect was previously reported in the presence of large cations such as Cs$^+$ only when Arg272 (R2) of the CNGA1 channels was neutralized. This observation prompted us to analyze voltage gating in the R2Q_WT construct in the presence of symmetrical DMA$^+$ where tail current analysis indicates the existence of two voltage-dependent transitions (Fig. 7). Figure 10A and B illustrate current recordings obtained in the presence of symmetrical DMA$^+$ for the WT and the R2Q_WT construct, respectively. Current rectification and the $G(V)/G_{+200}$ relationship were very similar for both channels, although not identical (Fig. 10A, B, and G). However, a closer inspection of current traces revealed an altered gating in the R2Q_WT mutant channel: the steady-state current was reached more slowly in the R2Q_WT mutants being the activation time constant at 200 mV equal to 0.3 and 0.5 msec for the WT and R2Q_WT channels, respectively. Figure 10C and D show an enlargement of tail currents observed at -200 mV after prepulses varying between -180 and 200 mV for both channels. In the R2Q_WT construct the early voltage-dependent transition is markedly reduced compared to the WT channel and similar results were obtained from five additional patches (Fig. 10E and F). Fitting the normalized tail currents versus voltage relationship with a two components Boltzmann function (Fig. 10H) provides a lower estimate to the gating charge associated with early (z_1) and late (z_2) voltage-dependent reactions. These results show that neutralization of R2 affects only the steeper early voltage-dependent transition (z_1 equal to 1.70 ± 0.10 and 1.00 ± 0.20 for WT and R2Q_WT constructs, respectively; T-test, $P < 0.01$, $n \geq 5$) and further substantiate the notion that S4 helix contributes to voltage gating in CNG channels. The voltage-dependent activation above 100 mV is very similar in both channels (z_2 equal to
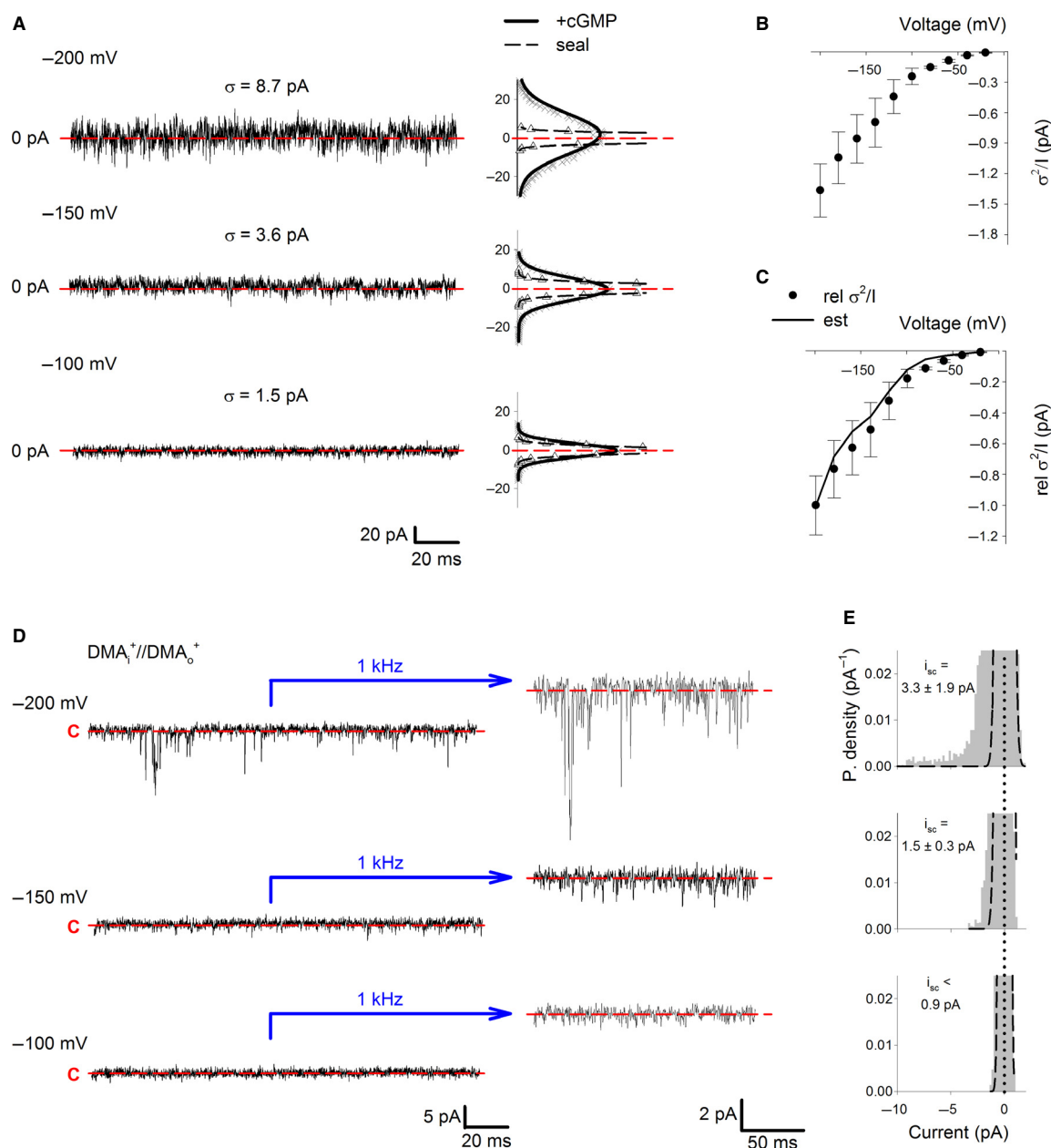
Figure 8. Noise analysis and single-channel recordings in symmetrical DMA$^+$ conditions. (A) Macroscopic currents fluctuations in symmetrical solutions of DMA$^+$ at -200, -150, and -100 mV from the same excised patch. Current r.m.s. (σ) were obtained after background noise subtraction as $\sigma_{cGMP} - \sigma_{seal}$, where σ_{cGMP} and σ_{seal} indicate the r.m.s recorded in the presence and absence of 1 mmol/L cGMP, respectively. The corresponding current amplitude histogram after mean current subtraction is shown on the right. Crosses and open triangles refer to traces obtained in the presence and absence of cGMP, respectively. Data were fitted with a Gaussian distribution yielding σ_{cGMP} and σ_{seal} (solid and dashed lines, respectively). Red broken line indicates 0 current level. (B) Relationship between σ_I^2/I and V for DMA$^+$ ($n = 3$). (C) Relationship between the expected relative single-channel current (i_{sc}/i_{sc-200}) and V. Filled circles show the experimentally observed normalized noise (rel σ_I^2/I) at different voltages. Solid line represents the $i_{sc}(V)/i_{sc-200}$ curve (est) computed as described in the text. (D) Single-channel recordings at -200, -150, and -100 mV from the same patch in the presence of symmetrical DMA$^+$. Current records were acquired at 50 kHz, and filtered at 10 kHz. For presentation purposes, traces were digitally filtered at 5 kHz and 1 kHz (left and right panels, respectively). Dashed lines in single-channel recordings indicate the closed state (C) of the channel. (E) All-point amplitude histograms from recordings as in (D) after offline digital filtering at 1 kHz. Dashed lines refer to all-point amplitude histograms Gaussian fit from records obtained in the same experimental conditions as in (D) but in the absence of cGMP. Single-channel current amplitude that were estimated from the peak current analysis procedure are indicated (Marchesi et al. 2012). The vertical dotted line indicates 0 current level.
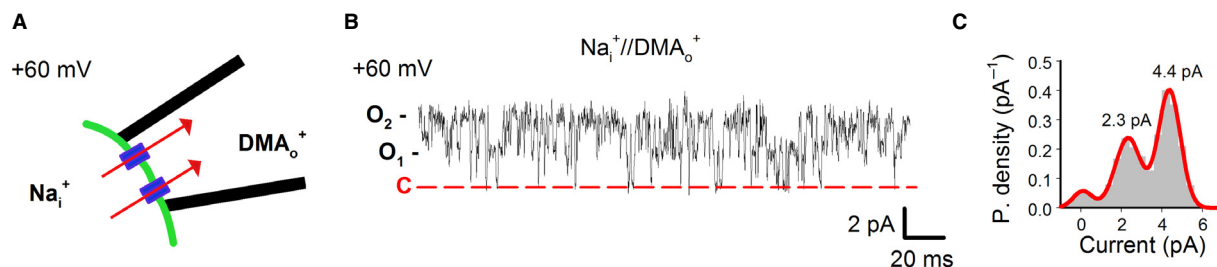
Figure 9. Estimating the number of channels underlying current fluctuations in symmetric DMA$^+$ (A) Schematic depicting an excised patch in bi-ionic conditions of intracellular Na$^+$ (Na$_i^+$) and extracellular DMA$^+$ (DMA$_o^+$) with two CNGA1 channels present in the membrane patch. The arrows indicate the direction of the electrochemical driving force at +60 mV. In bi-ionic conditions, the cGMP-activated current at +60 mV was carried almost by Na$^+$ ions moving from the bath solution toward the patch pipette. (B) Single-channel recording from the experimental conditions shown in A. Well-resolved openings slightly larger than those usually observed in symmetrical Na$^+$ could be detected. Dashed line indicates the closed (C) state of the channel; O$_1$ and O$_2$ refer to the two open states. (C) All-point amplitude histogram from the electrical recording shown in B. Data were fitted with a three component Gaussian function (solid red line) indicating that two CNGA1 channels were present in the membrane patch.
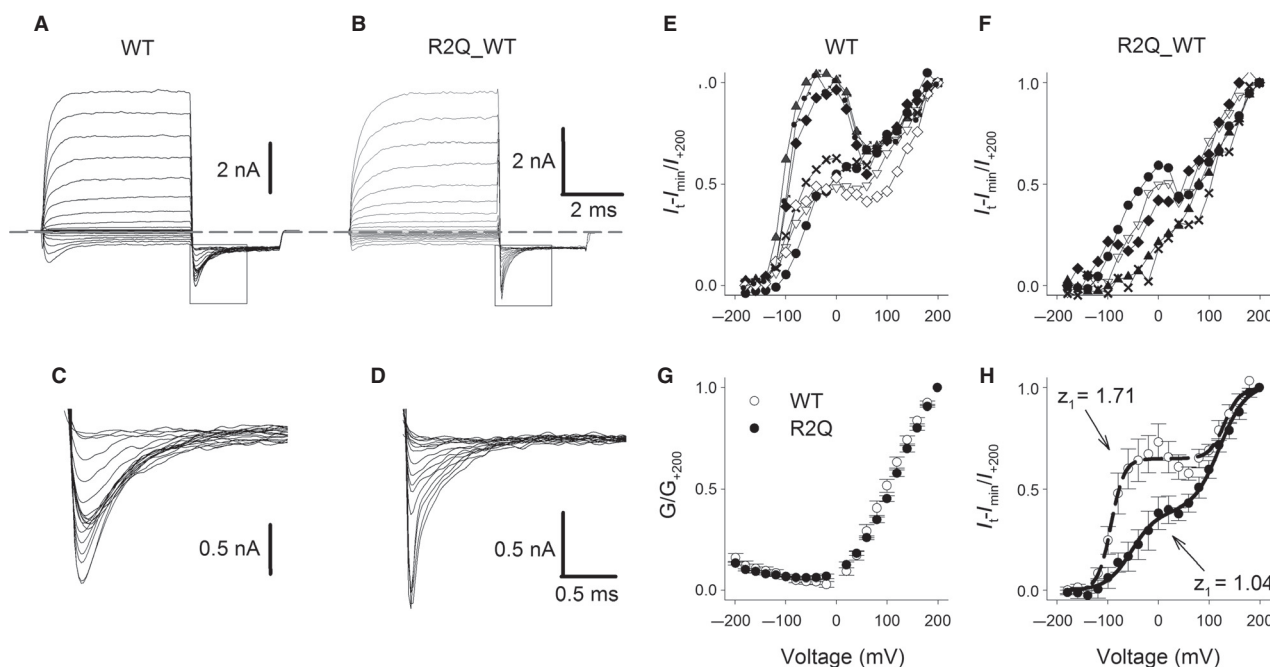

Figure 10. Macroscopic and tail currents in symmetrical DMA$^+$ conditions for WT and the R2Q_WT construct. (A, B) Macroscopic currents recorded from excised patches in symmetrical solutions of the DMA$^+$ for WT channel (A) and for the R2Q_WT mutant channel (B) with 1 mmol/L cGMP in the intracellular medium. Voltage prepulses from −180 to +200 mV (ΔV = 20 mV) were followed by a tail potential at −200 mV. Gray broken line indicates 0 current level. (C–D) Enlargement of tail currents (boxed areas in A,B) in DMA$^+$ for WT channel (C) and for the R2Q_WT mutant channel (D). Current recordings were filtered at 10 kHz and sampled at 50 kH. (E,F) Dependence of $I_t - I_{min}/I_{+200}$ on V for DMA$^+$ in WT channel (E) and in the R2Q_WT mutant channel (F). Recordings from different patches are shown in different symbols. (G) Dependence of G/G_{+200} on V in symmetrical DMA$^+$ solutions for the WT channel and for the R2Q_WT mutant channel. WT (open circles), R2Q_WT (filled circles); ($n \geq 5$). (H) Dependence of $I_t - I_{min}/I_{+200}$ on V in DMA$^+$ for WT channel and for the R2Q_WT mutant channel. WT (open circles), R2Q (filled circles); ($n \geq 5$). Data were fitted with a modified two components Boltzmann function (see Methods) yielding the following activation parameters: z_1 = 1.71, 1.04; V_{mid1} = −93.64, −53.01; z_2 = 1.07, 0.98; V_{mid2} = +130.73, +120.37; for the WT and the R2Q_WT channels, respectively.

1.00 ± 0.13 and 1.04 ± 0.03 for the WT and R2Q_WT constructs, respectively; T-test, $P = 0.84$, $n \geq 5$) suggesting the possibility that it could reflect a different underlying molecular mechanism.

Gating currents in WT CNGA1 channels

In Na^+, K^+, and Ca^{2+} channels, the motion of the S4 helix can be detected by measuring gating currents (I_g). Therefore, we attempted to measure I_g in WT CNGA1 channels (Fig. 11).

Let us suppose we have N ion channels and for each of them, if z elementary charges (in units of e_0 equal to 1.6×10^{-19} C) translocate across the membrane in the time Δt, a gating current I_g approximately equal to $ze_0N/\Delta t$ can be measured. In K^+ channels z is around 12–13 (Aggarwal and MacKinnon 1996; Seoh et al. 1996) and Δt is about 10^{-3} sec, so that in excised patches containing 4–5×10^3 channels I_g is about 7 pA. The determination of I_g requires the reduction in all contaminating currents, primarily ionic, and capacitive currents (Armstrong and Bezanilla 1977). A reliable measurement of I_g in CNG channels can be obtained only when N is at least 10^4 as in experiments using cut-open voltage-clamp technique or in macro/giant membrane patches (Perozo et al. 1992; Hilgemann and Lu 1998). In order to rapidly change the ionic medium, instead of using cut-open oocytes, we opted for patch pipettes with a diameter of 10–20 μm, where N could be larger than 2×10^4 (see Meth-

ods and Fig. 1) and cGMP can be added and removed within 10^{-1} sec.

In order to verify that our experimental conditions could measure I_g, we expressed in oocytes the mRNA coding for HCN channels from the sea urchin sperm (spHCN). We measured I_g with an amplitude of 40–50 pA from excised patches containing spHCN channels (see Methods) with kinetics and voltage dependence similar to those already described (Fig. 2). The r.m.s. of our current recordings is about 1 pA (at a bandwidth of 10 kHz) and the lowest measurable I_g is 5 pA, that is, five times the r.m.s. Assuming that I_g has an exponential decay (τ is 1–2 msec) and if N is about 3×10^4, I_g produced by a z as low as 2 could be detected (Fig. 11B). However, when the voltage was stepped from -120 to $+180$ mV only capacitive artifact lasting no longer than 300 μsec was recorded (Fig. 11A). Similar results were obtained in five additional giant patches containing at least 3×10^4 WT channels both in the absence and in the presence of 1 mmol/L cGMP (Fig. 11A). Therefore, based on the number of CNG channels present in the membrane patch (see Methods), we estimated that in the WT channels, either the value of z is about or less than 2 or I_g is too slow – and cannot be resolved because of uncertainties and noise of the baseline (Fig. 11B). In all these circumstances, the voltage sensor in CNGA1 channels does not move as in K^+ channels. As the voltage sensor of CNG channels is capable of sustaining voltage-dependent gating, (Tang and Papazian 1997; Xu et al.
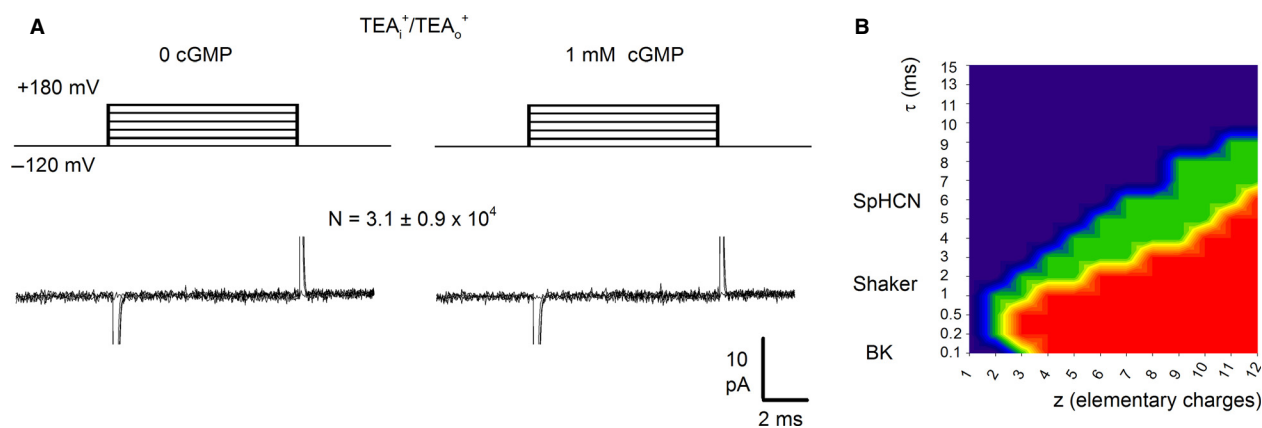

Figure 11. Gating currents measurements in WT CNGA1 channels. (A) Gating currents measurements in the presence of symmetrical TEA^+ (110 mmol/L) and in the absence (left panels) and presence (right panels) of 1 mmol/L cGMP from a representative membrane patch, containing $\approx 30,000$ ion channels. Only fast (<300 μsec) nonlinear capacitive artifacts were visible after P/−4 procedure, similar to those recorded in uninjected oocytes. Voltage commands P were as shown in the upper panels. Similar results were observed in five additional giant patches. (B) Contour plot depicting the predicted gating currents color-coded signal-to-noise ratio (S/N < 4, blue; $4 \leq S/N \leq 6$, green, S/N > 6, red) as a function of z and gating currents time constant τ for a membrane patch containing approximately 3×10^4 ion channels. Off-gating currents for a simple two state model representing two possible states of a voltage sensor (resting and activated) were simulated. S/N was measured at the peak of the simulated off-gating currents. Background r.m.s. was assumed to be 1 pA.

2010) the voltage sensor in WT CNGA1 channels moves much less than in K^+ channels, in agreement with the estimate of z lower than 2 obtained from measurements of gating currents and from the analysis of the voltage gating in Cs^+, MA^+, and DMA^+.

Discussion

The present manuscript, by using tail and gating current measurements, clarifies the role of the pore and of the S4 helix toward the asymmetries in the *I–V* relationship observed in symmetrical conditions with different ionic species. Voltage gating highly depends on the permeating ion: for small monovalent alkali cations, such as Li^+, Na^+, and K^+ gating is weakly voltage dependent, but gating is progressively voltage dependent for larger alkali cations, such as Rb^+ and Cs^+ and for organic cations such as EA^+ and DMA^+.

Voltage sensing in the WT CNGA1 channels is the result of a translocation of the usual voltage sensor, constituted by the S1–S4 domains and by voltage-dependent rearrangements of charged and polar groups within the pore region, primarily of Glu363. Measurements of I_g indicate that the voltage sensor in CNG channels moves much less than in K^+ channels. Let us see now more in detail how P_o and γ_{sc} depend on V and which molecular structures could underlie this voltage sensing.

Dependence of P_o and γ_{sc} on voltage in alkali and organic cations

Analysis of tail currents demonstrates that gating of CNG channels is voltage dependent in the presence of larger monovalent alkali cations Rb^+ and Cs^+, and of a variety of organic cations such as MA^+, DMA^+, and EA^+. By means of noise, tail and macroscopic current analysis, we show that in the presence of all these cations, P_o increases with voltage – although with different magnitude and steepness – while macroscopic currents might be either inwardly rectifying (Rb^+ and Cs^+) or outwardly rectifying (MA^+, DMA^+, and EA^+). This apparent contradiction could be easily disentangled if it is considered that the final shape of the *I–V* and $G(V)/G_{+200}$ relationship depends not only on P_o, but on both P_o and γ_{sc}. A well-established way to discriminate between the open-pore rectification (voltage-dependent changes in γ_{sc}) and channel voltage gating (voltage-dependent changes in P_o) is to use a proper sequence of voltage commands in order to induce tail currents. After a perturbation (sudden change in membrane potential) tail currents arise from the kinetic of ion channels redistribution toward a new equilibrium (Hille 1992). Thus, tail currents are thought to reflect changes in P_o from a previous condition of equi-

librium, whereas changes in γ_{sc} are believed to develop almost instantaneously. It was therefore possible to show with appropriate voltage protocols that in the presence of Rb^+ and Cs^+ γ_{sc} decreases of ~50% and ~70% from -200 to $+200$ mV, whereas P_o increases of ~25% and ~120%, respectively. In the presence of Rb^+ and Cs^+ γ_{sc} decreases more powerfully with V then what P_o increases, while the opposite occurs in symmetrical conditions of MA^+, DMA^+, and EA^+. Therefore, the *I–V* relationship is inwardly rectifying in Rb^+ and Cs^+ – being driven by changes in γ_{sc} – while it is outwardly rectifying in the presence of MA^+, DMA^+, and EA^+ – being mainly driven by changes in P_o.

The S4 voltage sensor in CNG channels and K^+ channels

CNG channels belong to the superfamily of K^+ voltage-gated channels but in the presence of small alkali cations such as Li^+, Na^+, or K^+ exhibit little inherent sensitivity to voltage (Kaupp and Seifert 2002; Matulef and Zagotta 2003; Craven and Zagotta 2006). Studies with chimeric channels where the S4 transmembrane segment or the CNG voltage sensor paddle have been transplanted into different K^+ channels have led to the notion that CNG channels harbor a potentially functional voltage-sensing domain (Tang and Papazian 1997; Xu et al. 2010). In the light of current understanding of voltage sensor operation, two distinct although not mutually exclusive mechanisms, effectively disabling channel voltage-dependent gating, can be considered. First of all the S4 helix, although functional, might be partially or almost completely impeded in its movements by the specific surrounding protein scaffolding (Tang and Papazian 1997). Alternatively, while S4 could move as much as in K_v channels, a loose electromechanical coupling between the S1–S4 voltage-sensing domain and the pore gate could result in channels with an altered gating and a reduced voltage sensitivity (Lu et al. 2002). To discriminate between these two different basic mechanisms, we analyzed capacitative transients in the presence of non-permeant ions, such as TEA^+ and $NMDA^+$, and the effect of charges neutralization in the S4 helix.

Voltage sensor movement can be detected as nonlinear capacitive transients – known as gating currents – caused by the rearrangement of its electrostatic charges with respect to the electric field (Armstrong and Bezanilla 1974). If it is assumed that S4 freely moves in CNG channels as it does in usual K_v channels, 12–13 e_0 per channel are expected to translocate through the electric field (Schoppa et al. 1992; Aggarwal and MacKinnon 1996; Seoh et al. 1996). Gating currents measurements in CNG channels provided us an upper bound on the number of elementary charges associated with voltage sensor movements, indicating that no more than 2 e_0 per channel tra-

verse the electric field. These results strongly suggest that although potentially functional, the S4 helix is constrained in its operation by the surrounding protein environment.

The analysis of tail currents in the presence of a variety of permeant cations indicates that a residual motion of the S4 transmembrane segment may still contribute to voltage gating in CNG channels. Indeed, when the second Arginine in the S4 segment is neutralized, voltage gating in the presence of large permeant ions is altered (Marchesi et al. 2012). In the present manuscript, we show that an early voltage-dependent transition associated with channel gating is affected in the R2Q_WT tandem construct, leaving almost unaltered voltage gating above 100 mV (Fig. 10). These results suggested the intriguing possibility that the two voltage-dependent transitions observed in the $I_t(V)/I_{+200}$ relationship might be controlled by different underlying molecular mechanisms: the steeper Boltzmann component developing at hyperpolarized potentials ($z_1 = 1.70 \pm 0.10$; $V_{mid1} = -88.36 \pm 5.99$) is likely associated with conformational rearrangements in the S4-type voltage sensor, whereas the second component occurring at depolarized potentials ($z_2 = 1.00 \pm 0.13$; $V_{mid2} = 140.18 \pm 5.97$) might reflect an inherent pore voltage sensitivity, as recently suggested for some pore mutant channels (Martínez-François et al. 2009; Sauer et al. 2011).

Our results indicate that in the presence of physiological ions, such as Na$^+$ and K$^+$, the additive contributions of two distinct mechanisms are at the basis of the reduced voltage sensitivity in CNG channels: (i) a reduced motion of the S4 transmembrane segment, which could be restricted by specific molecular interactions with neighbor residues; (ii) an inefficient coupling between the voltage-sensing domain and the channel gate which is modulated by the permeant ion.

Flexibility at the selectivity filter in CNG and K$^+$ channels

Although several studies have examined voltage gating in CNG channels and the linkage between gating and permeation (Karpen et al. 1988; Benndorf et al. 1999; Gamel and Torre 2000; Holmgren 2003; Kusch et al. 2004; Nache et al. 2006; Martínez-François et al. 2009), the relation between the permeation-gating coupling and voltage has so far been neglected. In the present manuscript, we show that membrane voltage powerfully controls gating and permeation properties in CNG channels (Fig. 12A). Although novel, these findings are not entirely unexpected in the light of the so far available structural data and basic differences in the amino acidic sequences among the K+ and CNG channels (Fig. 12B). A comparison between the crystal structure of KcsA (Fig. 12C) and

the CNG NaK chimera (Fig. 12D) shows that the KcsA selectivity filter is stabilized by extensive hydrogen bonding and Van Der Waals interactions with the pore helix, while this network of interactions is less developed in CNG channels (Fig. 12C and D). Indeed, the ring of Tyrosines which is thought to provide the putative rigidity and the network of hydrogen bonding (Fig. 12C) necessary to stabilize the structure of K+ channels selectivity filter (Doyle et al. 1998; Zhou et al. 2001; Bernèche and Roux 2005; Sauer et al. 2011) is replaced by a ring of Glutamates in CNG channels (Fig. 12B and D). Moreover, a wealth of crystallographic, electrophysiological, and MD simulations data indicate that in K$^+$ channels one of the microscopic factors influencing pore stability is the occupancy of specific cations binding sites within the selectivity filter (López-Barneo et al. 1993; Shrivastava and Sansom 2000; Loboda et al. 2001; Zhou et al. 2001; Bernèche and Roux 2005; Piskorowski and Aldrich 2006). In this view, it is conceivable that the contribution of a permeating ion to the overall filter stability is enhanced in ion channels where the selectivity filter is loosely attached to the surrounding structures, establishing the molecular rational for the gating-permeation coupling. Membrane voltage, acting on specific charged and polar residues within the pore, is expected to further tune this coupling.

Over the last two decades, several functional studies have documented the linkage between gating and permeation in CNG channels (Ruiz and Karpen 1997; Hackos and Korenbrot 1999; Gamel and Torre 2000; Holmgren 2003; Kusch et al. 2004). For instance, it has been shown that ions that pass more slowly through CNG channels stabilize the open state of the channels (Kusch et al. 2004). We have recently shown that this linkage is powerfully controlled by voltage; the low-conductance long-lasting openings observed in symmetrical Rb$^+$ and Cs$^+$ single-channel recordings at positive voltages are readily converted into high-conductance flicker openings by membrane hyperpolarization (Marchesi et al. 2012). Interestingly, several evidences suggest that Glu363 is at the basis of these differences in ion conduction (Root and MacKinnon 1994; Marchesi et al. 2012). We believe that the heterogeneity of channel openings observed at hyperpolarized voltages arise from small conformational fluctuations of the selectivity filter which can be triggered by local rearrangements of Glu363 side chain. Because (i) the selectivity filter stability is expected to be sensitive to the local electrostatic as well as to the protonation state of ionizable groups (such as Glu363 side chain) and (ii) the main chain carbonyl oxygens interact directly with permeating ions, these conformational changes are expected to be strongly affected by the nature of the permeant ion, as well as local proton concentration and membrane voltage. In other words, the permeation of larger cations such as Rb$^+$ and
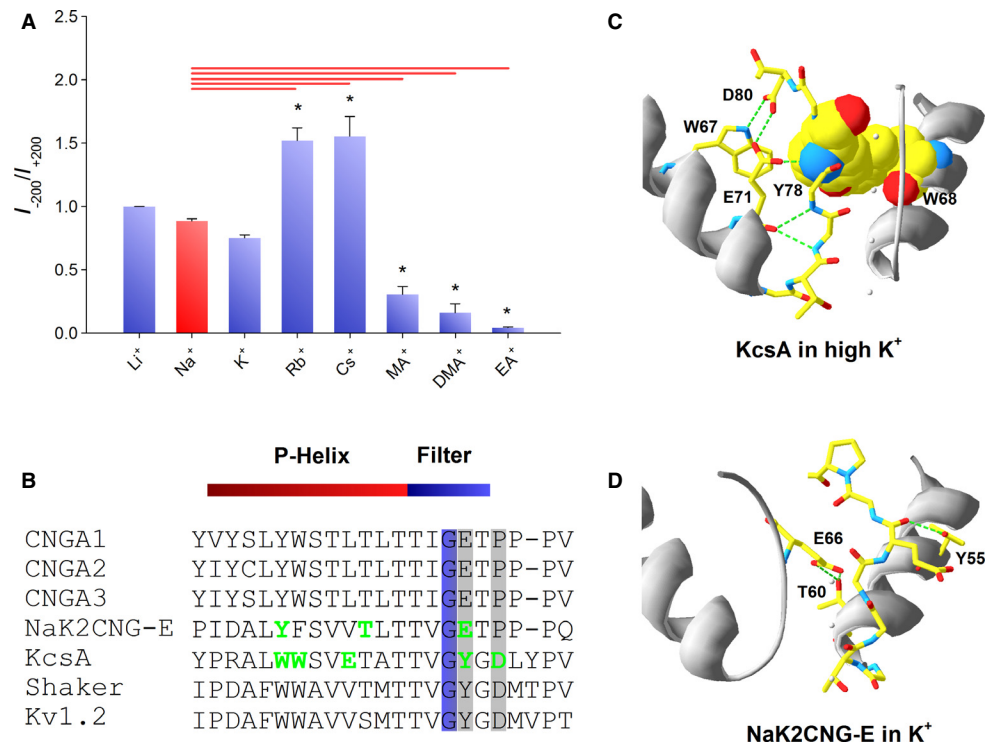
Figure 12. Partial sequence alignment among different ion channels and molecular structures of the KcsA and CNG mimicking NaK chimera featuring the interactions within the selectivity filter and surrounding scaffolding. (A) Dependence of I_{-200}/I_{+200} on the permeating ions. ANOVA and Bonferroni post hoc tests were performed to compare each ion against Na^{+}. Asterisks point out a statistical significance with a $P < 0.01$ ($n \geq 4$.). (B) Partial sequence alignment in the pore region of the bovine alfa subunits (CNGA1-CNGA3), CNG mimicking NaK chimera (NaK2CNG-E) and K^{+} channels (KcsA, Shaker, Kv1.2). The conserved Glycine residue in the selectivity filter is highlighted in blue. The Tyrosine of the K+ selective channels signature sequence is replaced by a ring of Glutamate residues in CNG channels, while the aspartate immediately following the filter is substituted by a proline; highlighted in light gray. Residues involved in H-bonding in the KcsA and CNG chimera structures are marked in green. (C, D) Partial molecular structure of the KcsA channel (C) and NaK2CNG-E channel (D) as deposited in the Protein Data Bank (PDB entry code 1K4C and 3K0D, respectively) featuring the selectivity filter and the P-helix in two adjacent subunits. Crucial intersubunit and intrasubunit H bonds stabilizing the selectivity filter architecture are shown in both structures as dashed green lines. Residues side chains involved in H bonds are shown in ball-and-stick format while aromatic residues constraining the pore structure are shown in space-filling format. The K^{+} ions in the selectivity filter are shown as white spheres. The selectivity filter of the NaK2CNG-E chimera is stabilized by fewer hydrogen's bonds compared to KcsA channel.

Cs^{+} unveils the operation of a pore voltage sensor controlling voltage-dependent asymmetries in single-channel conductance. The action of this pore voltage sensor is at the basis of the inward rectification in macroscopic currents here described when Rb^{+} and Cs^{+} permeate.

Thus, structural and electrophysiological evidence indicates that the selectivity filter of the CNG channels is an intrinsically dynamic structure possibly capable of fine structural rearrangements. This flexibility is necessary for the selectivity filter in order to act as the primary gate of the channel.

Acknowledgment

We thank M. Lough for checking the English.

Conflict of Interest

None declare.

References

Aggarwal, S. K., and R. MacKinnon. 1996. Contribution of the S4 segment to gating charge in the Shaker K^{+} channel. Neuron 16:1169–1177.

Armstrong, C. M., and F. Bezanilla. 1974. Charge movement associated with the opening and closing of the activation gates of the Na channels. J. Gen. Physiol. 63:533–552.

Armstrong, C. M., and F. Bezanilla. 1977. Inactivation of the sodium channel. II Gating current experiments.. J. Gen. Physiol. 70:567–590.

Benndorf, K., R. Koopmann, E. Eismann, and U. B. Kaupp. 1999. Gating by cyclic GMP and voltage in the alpha subunit of the cyclic GMP-gated channel from rod photoreceptors. J. Gen. Physiol. 114:477–490.

Bernèche, S., and B. Roux. 2005. A gate in the selectivity filter of potassium channels. Struct. Lond. Engl. 1993:591–600.

Clamp, M., J. Cuff, S. M. Searle, and G. J. Barton. 2004. The Jalview Java alignment editor. Bioinforma. Oxf. Engl. 20:426–427.

Craven, K. B., and W. N. Zagotta. 2006. CNG and HCN channels: two peas, one pod. Annu. Rev. Physiol. 68:375–401.

Doyle, D. A., J. Morais Cabral, R. A. Pfuetzner, A. Kuo, J. M. Gulbis, S. L. Cohen, et al. 1998. The structure of the potassium channel: molecular basis of K+ conduction and selectivity. Science 280:69–77.

Gamel, K., and V. Torre. 2000. The interaction of Na$^+$ and K$^+$ in the pore of cyclic nucleotide-gated channels. Biophys. J. 79:2475–2493.

Guex, N., and M. C. Peitsch. 1997. SWISS-MODEL and the Swiss-PdbViewer: an environment for comparative protein modeling.. Electrophoresis 18:2714–2723.

Hackos, D. H., and J. I. Korenbrot. 1999. Divalent cation selectivity is a function of gating in native and recombinant cyclic nucleotide-gated ion channels from retinal photoreceptors. J. Gen. Physiol. 113:799–818.

Hamill, O. P., A. Marty, E. Neher, B. Sakmann, and F. J. Sigworth. 1981. Improved patch-clamp techniques for high-resolution current recording from cells and cell-free membrane patches. Pflügers Arch. Eur. J. Physiol. 391:85–100.

Hilgemann, D. W., and C. C. Lu. 1998. Giant membrane patches: improvements and applications. Methods Enzymol. 293:267–280.

Hille, B. 1992. Ionic Channels of Excitable Membranes. 2 Sub. Sinauer Associates Inc, Sunderland, MD.

Holmgren, M. 2003. Influence of permeant ions on gating in cyclic nucleotide-gated channels. J. Gen. Physiol. 121:61–72.

Jan, L. Y., and Y. N. Jan. 1992. Tracing the roots of ion channels. Cell 69:715–718.

Jegla, T. J., C. M. Zmasek, S. Batalov, and S. K. Nayak. 2009. Evolution of the human ion channel set. Comb. Chem. High Throughput Screen 12:2–23.

Karpen, J. W., A. L. Zimmerman, L. Stryer, and D. A. Baylor. 1988. Gating kinetics of the cyclic-GMP-activated channel of retinal rods: flash photolysis and voltage-jump studies. Proc. Natl Acad. Sci. USA 85:1287–1291.

Kaupp, U. B., and R. Seifert. 2002. Cyclic nucleotide-gated ion channels. Physiol. Rev. 82:769–824.

Kusch, J., V. Nache, and K. Benndorf. 2004. Effects of permeating ions and cGMP on gating and conductance of rod-type cyclic nucleotide-gated (CNGA1) channels. J. Physiol. 560:605–616.

Loboda, A., A. Melishchuk, and C. Armstrong. 2001. Dilated and defunct K channels in the absence of K$^+$. Biophys. J. 80:2704–2714.

López-Barneo, J., T. Hoshi, S. H. Heinemann, and R. W. Aldrich. 1993. Effects of external cations and mutations in the pore region on C-type inactivation of Shaker potassium channels. Receptors Channels 1:61–71.

Lu, Z., A. M. Klem, and Y. Ramu. 2002. Coupling between voltage sensors and activation gate in voltage-gated K$^+$ channels. J. Gen. Physiol. 120:663–676.

Männikkö, R., F. Elinder, and H. P. Larsson. 2002. Voltage-sensing mechanism is conserved among ion channels gated by opposite voltages. Nature 419:837–841.

Marchesi, A., M. Mazzolini, and V. Torre. 2012. Gating of cyclic nucleotide-gated channels is voltage dependent. Nat. Commun. 3:973.

Martínez-François, J. R., Y. Xu, and Z. Lu. 2009. Mutations reveal voltage gating of CNGA1 channels in saturating cGMP. J. Gen. Physiol. 134:151–164.

Martínez-François, J. R., Y. Xu, and Z. Lu. 2010. Extracellular protons titrate voltage gating of a ligand-gated ion channel. J. Gen. Physiol. 136:179–187.

Matulef, K., and W. N. Zagotta. 2003. Cyclic nucleotide-gated ion channels. Annu. Rev. Cell Dev. Biol. 19: 23–44.

Nache, V., J. Kusch, V. Hagen, and K. Benndorf. 2006. Gating of cyclic nucleotide-gated (CNGA1) channels by cGMP jumps and depolarizing voltage steps. Biophys. J. 90:3146–3154.

Neher, E., and C. F. Stevens. 1977. Conductance fluctuations and ionic pores in membranes. Annu. Rev. Biophys. Bioeng. 6:345–381.

Nizzari, M., F. Sesti, M. T. Giraudo, C. Virginio, A. Cattaneo, and V. Torre. 1993. Single-channel properties of cloned cGMP-activated channels from retinal rods. Proc. Biol. Sci. 254:69–74.

Perozo, E., D. M. Papazian, E. Stefani, and F. Bezanilla. 1992. Gating currents in Shaker K$^+$ channels. Implications for activation and inactivation models. Biophys. J. 62:160–168. discussion 169–171.

Piskorowski, R. A., and R. W. Aldrich. 2006. Relationship between pore occupancy and gating in BK potassium channels. J. Gen. Physiol. 127:557–576.

Root, M. J., and R. MacKinnon. 1994. Two identical noninteracting sites in an ion channel revealed by proton transfer. Science 265:1852–1856.

Ruiz, M. L., and J. W. Karpen. 1997. Single cyclic nucleotide-gated channels locked in different ligand-bound states. Nature 389:389–392.

Sauer, D. B., W. Zeng, S. Raghunathan, and Y. Jiang. 2011. Protein interactions central to stabilizing the K$^+$ channel selectivity filter in a four-sited configuration for selective K$^+$ permeation. Proc. Natl Acad. Sci. USA 108:16634–16639.

Schoppa, N. E., K. McCormack, M. A. Tanouye, and F. J. Sigworth. 1992. The size of gating charge in wild-type and mutant Shaker potassium channels. Science 255:1712–1715.

Seoh, S. A., D. Sigg, D. M. Papazian, and F. Bezanilla. 1996. Voltage-sensing residues in the S2 and S4 segments of the Shaker K^+ channel. Neuron 16:1159–1167.

Sesti, F., E. Eismann, U. B. Kaupp, M. Nizzari, and V. Torre. 1995. The multi-ion nature of the cGMP-gated channel from vertebrate rods. J. Physiol. 487(Pt 1):17–36.

Shrivastava, I. H., and M. S. Sansom. 2000. Simulations of ion permeation through a potassium channel: molecular dynamics of KcsA in a phospholipid bilayer. Biophys. J. 78:557–570.

Tang, C. Y., and D. M. Papazian. 1997. Transfer of voltage independence from a rat olfactory channel to the Drosophila ether-à-go-go K^+ channel. J. Gen. Physiol. 109:301–311.

Xu, Y., Y. Ramu, and Z. Lu. 2010. A shaker K^+ channel with a miniature engineered voltage sensor. Cell 142:580–589.

Yu, F. H., V. Yarov-Yarovoy, G. A. Gutman, and W. A. Catterall. 2005. Overview of molecular relationships in the voltage-gated ion channel superfamily. Pharmacol. Rev. 57:387–395.

Zhou, Y., J. H. Morais-Cabral, A. Kaufman, and R. MacKinnon. 2001. Chemistry of ion coordination and hydration revealed by a K^+ channel-Fab complex at 2.0 A resolution. Nature 414:43–48.

Proton transfer unlocks inactivation in CNGA1 channels.

Arin Marchesi, Manuel Arcangeletti, Monica Mazzolini and Vincent Torre.

Neuroscience

The Journal of Physiology

JPn

Proton transfer unlocks inactivation in cyclic nucleotide-gated A1 channels

Arin Marchesi, Manuel Arcangeletti, Monica Mazzolini and Vincent Torre

Neurobiology Sector, International School for Advanced Studies (SISSA), Trieste, Italy

Key points

- Desensitization and inactivation provide a form of short-term memory controlling the firing patterns of excitable cells and adaptation in sensory systems.
- Unlike many of their cousin K^+ channels, cyclic nucleotide-gated (CNG) channels are thought not to desensitize or inactivate.
- Here we report that CNG channels do inactivate and that inactivation is controlled by extracellular protons.
- Titration of a glutamate residue within the selectivity filter destabilizes the pore architecture, which collapses towards a non-conductive, inactivated state in a process reminiscent of the usual C-type inactivation observed in many K^+ channels.
- These results indicate that inactivation in CNG channels represents a regulatory mechanism that has been neglected thus far, with possible implications in several physiological processes ranging from signal transduction to growth cone navigation.

Abstract Ion channels control ionic fluxes across biological membranes by residing in any of three functionally distinct states: deactivated (closed), activated (open) or inactivated (closed). Unlike many of their cousin K^+ channels, cyclic nucleotide-gated (CNG) channels do not desensitize or inactivate. Using patch recording techniques, we show that when extracellular pH (pH_o) is decreased from 7.4 to 6 or lower, wild-type CNGA1 channels inactivate in a voltage-dependent manner. pH_o titration experiments show that at $pH_o < 7$ the *I–V* relationships are outwardly rectifying and that inactivation is coupled to current rectification. Single-channel recordings indicate that a fast mechanism of proton blockage underlines current rectification while inactivation arises from conformational changes downstream from protonation. Furthermore, mutagenesis and ionic substitution experiments highlight the role of the selectivity filter in current decline, suggesting analogies with the C-type inactivation observed in K^+ channels. Analysis with Markovian models indicates that the non-independent binding of two protons within the transmembrane electrical field explains both the voltage-dependent blockage and the inactivation. Low pH, by inhibiting the CNGA1 channels in a state-dependent manner, may represent an unrecognized endogenous signal regulating CNG physiological functions in diverse tissues.

Abbreviations BS, binding site; CN, cyclic nucleotide; CNG, cyclic nucleotide-gated; VGIC, voltage-gated ion channel.

Introduction

Cyclic nucleotide-gated (CNG) channels conduct a Ca^{2+}-permeable non-selective cation current mediating

signal transduction in photoreceptor and olfactory sensory neurons (Hille, 1992; Kaupp & Seifert, 2002; Craven & Zagotta, 2006). Although CNG channels belong to the superfamily of voltage-gated ion channels (VGICs), they open in response to binding of cyclic nucleotides

A. Marchesi and M. Arcangeletti contributed equally to this work.

(CNs) and are only barely modulated by membrane voltage (Hille, 1992; Kaupp & Seifert, 2002; Yu *et al.* 2005; Craven & Zagotta, 2006; Mazzolini *et al.* 2010). CNG channel activity is also regulated by a variety of molecules and ions, including protons. Changes in extracellular hydrogen ion concentration (pH_o) occur in a variety of physiological and pathophysiological conditions, such as neuronal activity, ischaemia and inflammation (Kellum et al. 2004; Isaev *et al.* 2008; Magnotta *et al.* 2012). In the retina, pH_o follows a circadian rhythm (Dmitriev & Mangel, 2001), and pH changes could play a role in adaptation of the retinal response to different light intensities. Moreover, acidosis has been associated with changes in cell excitability in vascular tissues as well as in the CNS (Tolner et al. 2011; Pavlov *et al.* 2013), in which CNG channels are widely expressed (Zufall et al. 1997; Kaupp & Seifert, 2002; Leung *et al.* 2010; Lopez-Jimenez *et al.* 2012). Therefore, determining the effect of pH_o on CNG channel gating has great clinical and physiological significance.

It is well established that extracellular protons inhibit CNG currents, although conflicting mechanisms have been proposed (Root & MacKinnon, 1994; Rho & Park, 2013; Morrill & MacKinnon, 1999; Martínez-François *et al.* 2010). For instance, the outward rectification observed at low pH_o has been attributed to a voltage-dependent proton blockage (Rho & Park, 2013) and more recently to an enhancement of the wild-type (WT) channel inherent mild voltage-dependent gating (Martínez-François et al. 2010). Here we show that when pH_o is decreased from 7.4 to 6 or lower, WT CNGA1 channels inactivate or desensitize. The term 'desensitization' usually refers to a mechanism of activity attenuation following sustained exposure to a chemical messenger, such as a neurotransmitter in ligand-gated channels, whereas inactivation is commonly used for VGICs. In the present investigation, mutagenesis and ionic substitution experiments indicated that the current decline is reminiscent of the usual C-type inactivation observed in K_v channels and consequently we refer to the observed loss of conduction as inactivation. A simple kinetic model in which two protons bind within the selectivity filter provides a conceptual framework to rationalize both voltage-dependent proton block and inactivation. Inactivation thus represents a novel regulatory mechanism of CNG channels that has been neglected.

Methods

Ethical approval

Molecular biology

The CNGA1 channel from bovine rods consisting of 690 amino acids was used (Kaupp et al. 1989). Selected residues were replaced as described (Becchetti et al. 1999) using the Quick Change Site-Directed Mutagenesis kit (Stratagene, La Jolla, CA, USA). Point mutations were confirmed by sequencing, using a LI-COR sequencer (4000 l; LI-COR Biosciences, Lincoln, NE, USA). cDNAs were linearized and were transcribed to cRNA *in vitro* using the mMessage mMachine kit (Ambion, Austin, TX, USA).

Oocyte preparation and chemicals

Mutant channel cRNAs were injected into *X. laevis* oocytes ('Xenopus express' Ancienne Ecole de Vernassal, Le Bourg 43270, Vernassal, Haute-Loire, France). Oocytes were prepared as described (Nizzari et al. 1993). Injected eggs were maintained at 18°C in a Barth solution supplemented with 50 μg ml^{-1} gentamycin sulfate and containing (in mM): 88 NaCl, 1 KCl, 0.82 $MgSO_4$, 0.33 $Ca(NO_3)_2$, 0.41 $CaCl_2$, 2.4 $NaHCO_3$ and 5 Tris-HCl, pH 7.4 (buffered with NaOH). During the experiments, oocytes were kept in a Ringer solution containing (in mM): 110 NaCl, 2.5 KCl, 1 $CaCl_2$, 1.6 $MgCl_2$ and 10 Hepes, pH 7.4 (buffered with

NaOH). Usual salts and reagents were purchased from Sigma Chemicals (St Louis, MO, USA).

Recording apparatus

cGMP-gated currents from excised patches (Hamill *et al.* 1981) were recorded with a patch-clamp amplifier (Axopatch 200; Axon Instruments Inc., Foster City, CA, USA), 2–6 days after RNA injection, at room temperature (20–24°C). The perfusion system was as described (Sesti et al. 1995) and allowed a complete solution change in less than 0.1 s. Macroscopic and single-channel current recordings were obtained with borosilicate glass pipettes which had resistances of 2–5 MΩ in symmetrical standard solution. The standard solution on both sides of the membrane consisted of (in mM) 110 NaCl, 10 Hepes and 0.2 EDTA (pH 7.4). For solutions buffered at pH lower than 7, 10 mM MES instead of 10 mM Hepes was used and for solution at pH 9, 10 mM CHES was used. Solutions were buffered with tetramethylammonium hydroxide at the desired pH. When the cation X^+ was used as the charge carrier, NaCl in the standard solution on both sides of the membrane patch was replaced by an equimolar amount of the cation X^+. We used Clampex version 10.0 for data acquisition. Recordings from macroscopic currents to elicit *I–V* relationships (Figs 2*A*, *B*, *G* and 4*I*) and to perform noise analysis (Fig. 2*D*) were low-pass filtered at 10 kHz. Current signals were sampled with a 16-bit A/D converter (Digidata 1440A; Axon Instruments), using a sampling rate of 50 kHz. All other macroscopic current recordings were low-pass filtered at 1 kHz and sampled at 2.5 kHz if not otherwise indicated. Single-channel recordings were low-pass filtered at 2 kHz and sampled at 5 kHz.

Data analysis

Inactivation time constants (τ) were obtained from fitting cGMP activated currents with one-component exponential functions. Single-channel currents (i) were estimated from patches containing only one CNGA1 channel and fitting normalized all-point histograms with two-component Gaussian functions as previously described (Bucossi et al. 1997). The dependency of the fraction of unblocked channels ($P_{unblocked}/P_{max}$, Fig. 2*I*) on voltage at different pH_o was determined from the ratios of the normalized conductance G/G_{+200} at the indicated pH_o and at $pH_o = 9$. If not otherwise indicated, data are presented as mean ± SEM, with n indicating the number of patches. Statistical significance for parametric analysis was determined using unpaired two-tailed *t*-test or single-variable ANOVA, as indicated. For pairwise comparisons, a Holm–Sidak test was used as *post hoc* test. $P < 0.01$ or $P < 0.05$ were considered significant,

as indicated. Data analysis and figures were made with Clampfit version 10.1 (Molecular Devices, Sunnyvale, CA, USA) and Sigmaplot 12.0 (Systat Software, Chicago, IL, USA). Kinetic models were generated and evaluated using MatLab 7.9.0 (MathWorks, Natick, MA, USA). The voltage-dependent association constant for protons shown in Fig. 6 was assumed to be of the form:

$$X(V) = X(0)e^{z\delta VF/RT}$$

where $X(0)$ is the association constant at 0 mV, z is the valence ($+1$), V is the voltage across the membrane, δ is the fraction of the membrane voltage at the binding site (the electrical distance) and $F/RT = 25.5$ mV at 23°C.

Results

Extracellular protons induce inactivation and outward rectification

WT CNG channels are known not to inactivate or to desensitize in the presence of a steady CN concentration. Rather unexpectedly, when CNGA1 channels were exposed to a low pH_o, they inactivated (Fig. 1*A*). We filled the patch pipette with the usual concentration of 110 mM NaCl buffered at pH_o 5 and stepped the voltage command to −50 mV (Fig. 1*A*). After a few seconds we added 1 mM cGMP to the medium bathing the cytoplasmic side of the membrane patch (indicated by solid blue bars in Fig. 1*A*) and very quickly the expected cGMP-gated current appeared (Fig. 1*A*). This current, however, was not stable and declined to a much lower level corresponding to approximately 25% of the current initially observed. After 30–40 s of exposure to cGMP, the CN was removed from the medium and we monitored the current amplitude by exposing the membrane patch to brief pulses of cGMP. The amplitude of the cGMP-activated current recovered to its original level, provided that cGMP was removed for at least 60–90 s from the bathing medium.

Inactivation was not observed when pH_o was reduced from 7.4 to 7 (Fig. 1*C*) or when increased to 8 (Fig. 1*B*). When pH_o was reduced to 6, an appreciable inactivation was observed only at negative voltages (Fig. 1*D*). At pH_o 5, CNG channels inactivate significantly also at positive voltages (Fig. 1*E*). At steady state, currents declined to 72 ± 6 and 28 ± 2% ($n = 4$) of their initial values at +60 and −60 mV, respectively. When inactivation fully developed, after a steady exposure to cGMP for 1–2 min, the *I–V* relationships were clearly outward rectifying at pH_o 5 (Fig. 2*A*), in agreement with previous observations (Martínez-François *et al.* 2010). Thus, extracellular acidification not only induces current rectification (Rho & Park, 2013; Martínez-François *et al.* 2010) but is also responsible for a slow, state-dependent loss of conduction modulating CNG channel activity.

The effect of extracellular acidification is best seen in outside-out membrane patches where different proton concentrations could be assessed during the same experiment (Fig. 1*F*). Mg^{2+} at 20 mM was used (indicated by solid red bars in Fig. 1*F*) to block CNG channels – which are continuously exposed to 1 mM cGMP present in the patch pipette – and estimate the leak current (Liu & Siegelbaum, 2000). Upon pH_o switch to 5, a current corresponding to approximately 20% of the current at pH_o 7.4 is observed (Fig. 1*F*). Notably, this current is not stable

and exhibits a slow run-down as observed in inside-out patches at the same pH_o (Fig. 1*E*). The current decline is fully reversible when pH_o was reverted from 5 to 7.4 (Fig. 1*F*, right panel).

As inactivation appears to be stronger at negative potentials (Fig. 1*E*) and both inactivation and rectification depend on pH_o (Fig. 1*B–E* and *G*), the observed outward rectification (Fig. 2*A*) could arise from the voltage and pH dependency of the current decline. However, several observations suggest that this is not the case. First, while
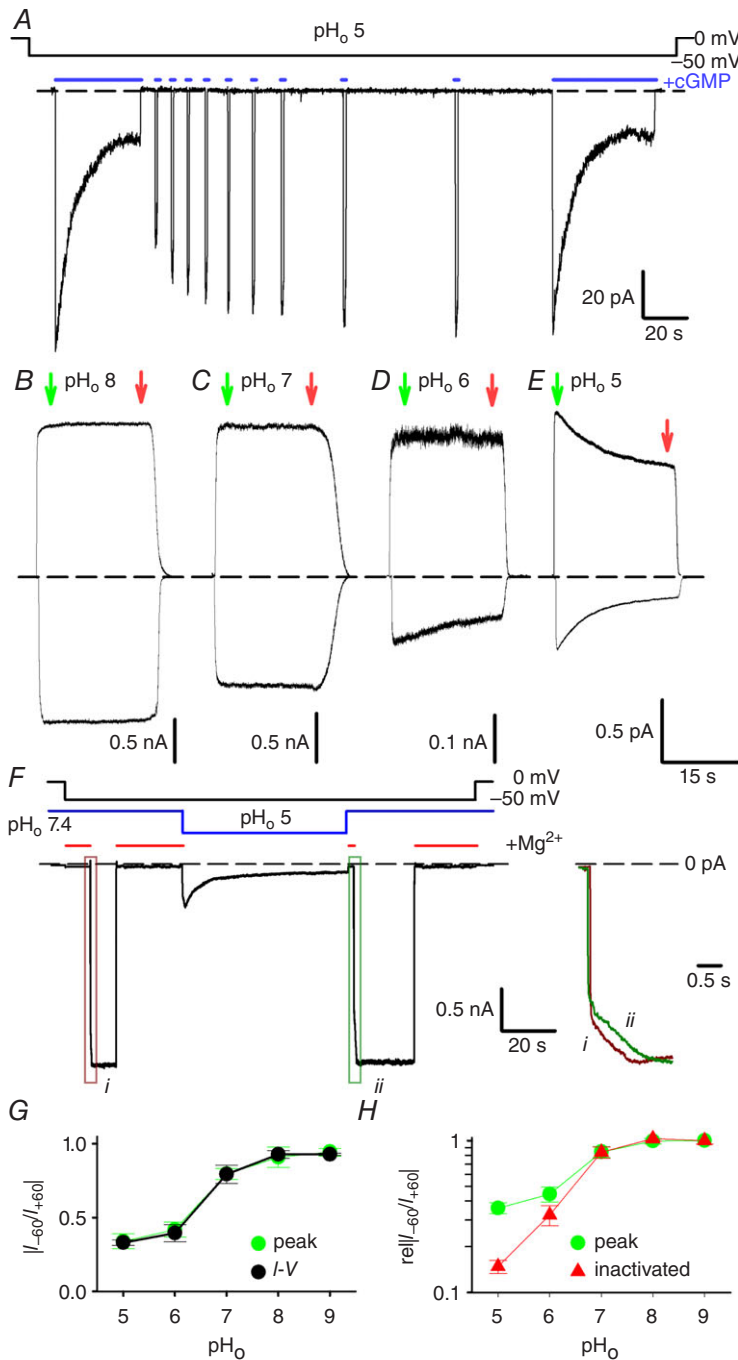

Figure 1. Properties of macroscopic currents at different pH_o in WT CNGA1 channel
A, current recording during a voltage step at −50 mV at pH_o 5 (pH_i 7.4) in symmetrical 110 mM Na^+ solutions. Currents were evoked by the application of 1 mM cGMP as indicated by solid blue bars. Brief cGMP pulses were used to monitor channel recovery from inactivation. A second prolonged application of cGMP after recovery produced an almost identical time-dependent current decline. *B–E*, current recordings during voltage steps at +60 and −60 mV evoked by 1 mM cGMP jumps at pH_o 8 (*B*), 7 (*C*), 6 (*D*) and 5 (*E*). *F*, current recording obtained from a representative outside-out patch, during a prolonged voltage step at −50 mV, in symmetrical 110 mM Na^+ solutions. The experiment was performed varying pH_o from 7.4 to 5 and back to 7.4 (solid blue line). CNG channels were continuously activated by 1 mM cGMP present in the patch pipette. Reference current was obtained by adding 20 mM Mg^{2+} to the bath solution as indicated (solid red lines). Kinetics of current activation at pH_o 7.4 prior to (*i*) and after inactivation at pH_o 5 (*ii*) are shown to the right. The areas in the green and red boxes are expanded along the time scale and superimposed for comparison. *G*, dependence of current rectification at +60 and −60 mV ($|I_{−60}/I_{+60}|$) on pH_o determined before inactivation onset (green circles) and from *I–V* relationships such as in Fig. 2*A* (black circles). *H*, dependence of relative current rectification (rel$|I_{−60}/I_{+60}|$) on pH_o before (green circles) and after (red circles) current inactivation. rel$|I_{−60}/I_{+60}|$ was determined from the ratio of $I_{−60}/I_{+60}$ at the indicated pH_o and $I_{−60}/I_{+60}$ at pH_o 9. Green and red arrows in *B–E* refer to the currents prior to and after inactivation development. Dashed black lines indicate the 0 current level.

rectification develops almost instantaneously (Fig. 2*A*), inactivation occurs within several seconds (Fig. 1*D*, *E*), and thus within the 20 ms voltage steps used to elicit the *I–V* relationship there would not be enough time for a significant inactivation to develop. Indeed, the

rectification measured at +60 and −60 mV (L_{-60}/I_{+60}) from the *I–V* relationships (Fig. 1*G*, black circles) is very similar to the rectification observed before the current decline onset (Fig. 1*G*, green circles). Second, inactivation and rectification appear to have a different pH

Figure 2. Proton block and current rectification in WT CNGA1 channel
A and *B*, macroscopic current recordings in the inactivated state obtained 2 min after the addition of 1 mM cGMP at 0 mV elicited by voltage steps from −200 to +200 mV ($\Delta V = 20$ mV) at pH$_o$ 5 (*A*) and 7.4 (*B*). Leak and capacitative components were removed by subtracting from the cGMP-activated current those records obtained in response to the same voltage protocol but without cGMP. *C*, single-channel *i–V* (black circles) and macroscopic *I–V* relationships (red circles) obtained from noise analysis (*D*) and from the recording in *A*, respectively. The *I–V* relationship was scaled to the *i* flowing at +180 mV. *D*, stationary fluctuation analysis at the indicated positive (upper panels) and negative (lower panels) voltages. A linear regression fit throughout each dataset provided the indicated unitary current *i*. Currents were evoked by 30 μM intracellular cGMP and leak currents and variance observed in the absence of cGMP subtracted. Each point indicates the mean current (*I*) and the variance of the corresponding mean current (σ^2) measured from one independent excised membrane patch. Recordings for each patch were of duration between 0.5 and 2 s. *E*, single-channel current recordings at +100 mV at the indicated pH$_o$. Amplitude histogram from recordings at pH$_o$ 5 is shown at the right (grey area). Dashed brown and blue lines represent a two-component Gaussian fit to histograms obtained at pH$_o$ 5 and 7.4, respectively. Black dashed lines indicate the 0 current level. C, O$_b$ and O refer to the closed, blocked and open states respectively; *i* indicates the unitary current. *F*, as in *E* but at −100 mV. *G*, macroscopic current recording in the inactivated state elicited by a voltage prepulse held at +200 mV followed by test potentials ranging from −200 to +200 mV ($\Delta V = 20$ mV). No tail currents were observed at negative membrane potentials, suggesting a fast mechanism of proton block. Black dashed line indicates the 0 current level. *H*, a sketch of the energy landscape for a symmetrical two-barrier Woodhull model of block. $U_{\pm i}$, $k(0)_{\pm i}$ and δ indicate the heights of energy barriers, rate constants at 0 mV and the electrical distance, respectively. *I*, dependence of the fraction of unblocked channels (see Methods) on *V* at different pH$_o$ (filled circles, open circles, filled triangles, open triangles, open squares and filled squares refer to pH$_o$ 9, 8, 7, 6, 5 and 4, respectively). The red lines represent simultaneous fits of all the data with the model shown in *F* with $k(0)_1$, $k(0)_{-1}$, $k(0)_2$, $k(0)_{-2}$ and δ equal to 7.3×10^7 M^{-1} s^{-1}, 40.8 s^{-1}, 8.9 s^{-1}, 1.6×10^7 M^{-1} s^{-1} and 0.41, respectively.
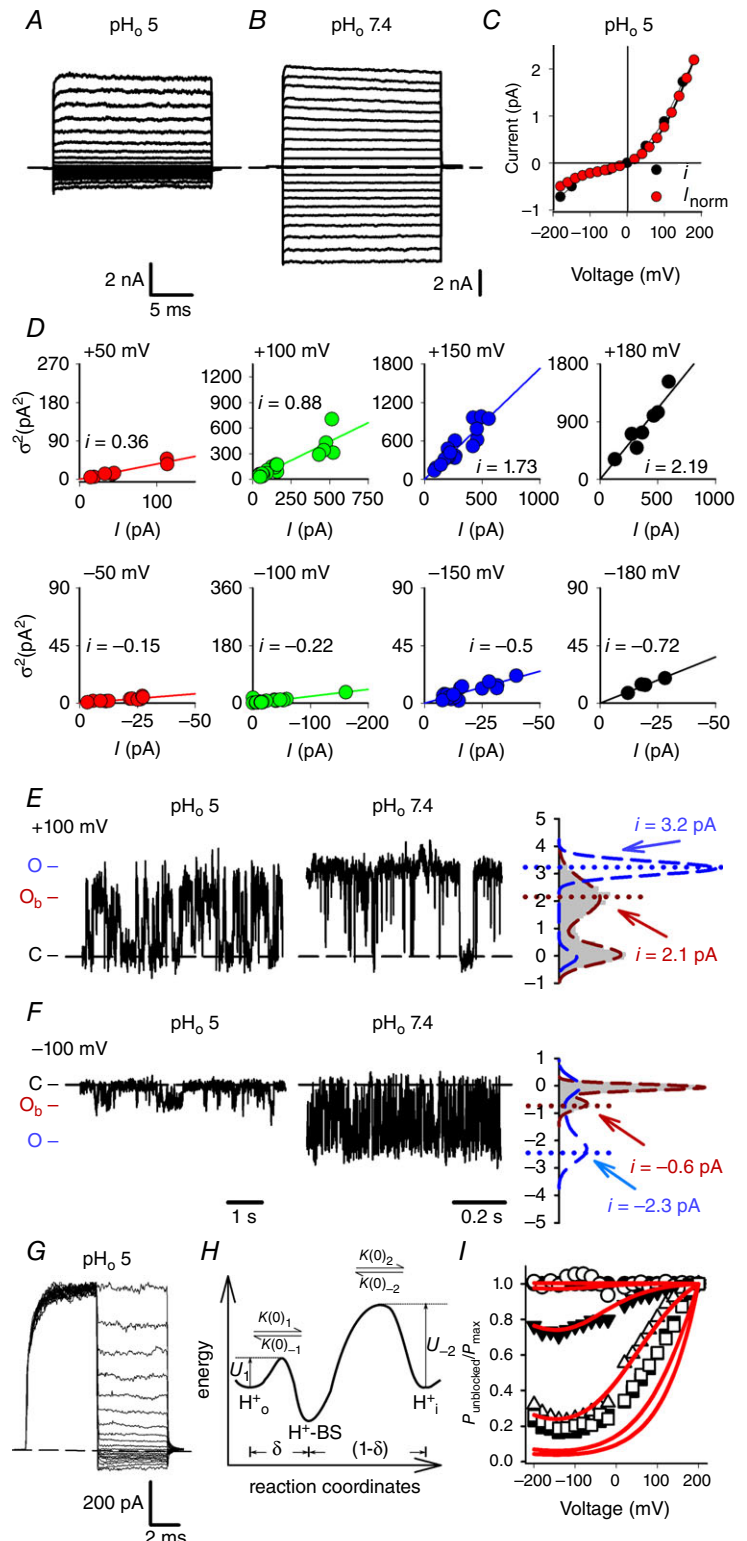
dependency: while a significant increase in rectification was already observed when pH_o is lowered from 8 to 7 (Fig. 1*B*, *C*, *G*), an appreciable inactivation was not detected until pH_o was lowered to 6 (Fig. 1*B*–*D*). Lastly, the voltage dependency of inactivation adds to the instantaneous rectification resulting in an enhancement of the steady-state current rectification (Fig. 1*H*). Thus, the voltage- and time-dependent loss of conductance is not at the origin of the outward rectification observed in the *I*–*V* relationship, and the two processes of rectification and inactivation could have different underlying molecular mechanisms.

Outward rectification arises from voltage dependency of proton blockage

The almost instantaneous rectification at pH_o 5 (Fig. 2*A*) was substantially relieved at the usual pH_o 7.4 (Fig. 2*B*) and could reflect obstruction of the permeation pathway by protons within the transmembrane electrical field. Indeed, at hyperpolarized membrane potentials, protons are expected to be driven into the channel pore, enhancing the block and resulting in an outward rectification. To confirm

this mechanism, we estimated the single-channel current *i* by noise analysis of macroscopic currents at different voltages (Fig. 2*D*). Estimates of the corresponding *i* thus obtained are plotted as a function of voltage in Fig. 2*C* (black dots). As with the macroscopic *I*–*V* relationship (Fig. 2*C*, red dots), the *i*–*V* plot is outwardly rectifying and the two curves are almost overlapping. Indeed, the ratio of the macroscopic and unitary currents flowing at +180 and −180 mV (I_{+180}/I_{180} and i_{+180}/i_{180}) were 4.5 and 3, respectively, suggesting that the voltage dependency of proton blockage is responsible for a large fraction of the observed rectification.

Estimates of single-channel currents based on stationary fluctuation analysis could be biased by filtering settings (Hille, 1992), and therefore we also attempted to measure single-channel events from membrane patches containing possibly only one channel. Such electrical recordings are shown in Fig. 2*E* and *F* and have been obtained at +100 (Fig. 2*E*) and −100 mV (Fig. 2*F*) at the usual pH_o of 7.4 (right traces) and when pH_o was lowered to 5 (left traces). Proton elevation resulted in a reduction of the single-channel amplitude that was more prominent at negative voltages (Fig. 2*F*). At −100 mV, amplitude histograms indicate that the *i* reduced from
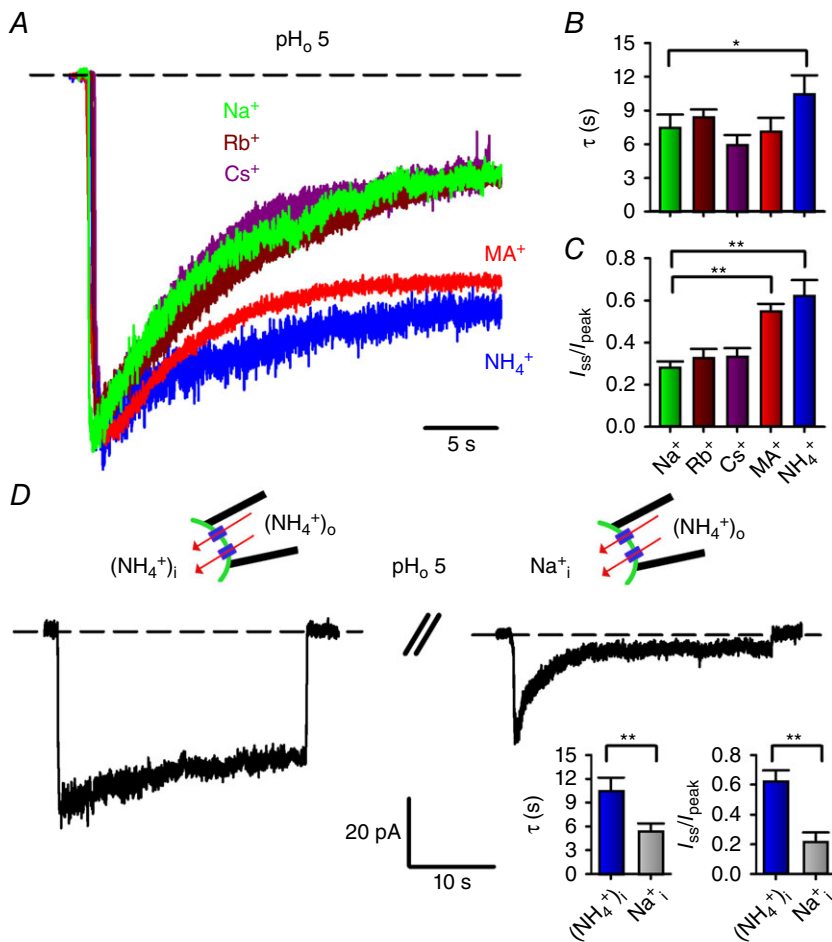
Figure 3. Properties of inactivation under different ionic conditions in WT CNGA1 channel
A, current recordings during a voltage step at −60 mV at pH_o 5 in symmetrical 110 mM Na^+ (green trace), Rb^+ (brown trace), Cs^+ (purple trace), MA^+ (red trace) and NH_4^+ (blue trace) solutions. Currents were evoked by 1 mM cGMP and scaled for comparison. *B* and *C*, inactivation time constant τ (*B*) and residual fractional current I_{ss}/I_{peak} (*C*) in the presence of Na^+, Rb^+, Cs^+, MA^+ and NH_4^+. ANOVA and Holm–Sidak *post hoc* tests were performed to compare each ion against each other (*$P < 0.05$, **$P < 0.01$). *D*, current recordings during a prolonged voltage step at −60 mV at pH_o 5 in symmetrical NH_4^+ (left trace) and when intracellular NH_4^+ was replaced by an equimolar amount of Na^+ (right trace). A 2 min wash-out between the two recordings was performed to ensure complete recovery from inactivation. Currents were evoked by 1 mM cGMP. Inactivation time constant τ and residual fractional current I_{ss}/I_{peak} in the presence of symmetrical NH_4^+ and when intracellular NH_4^+ was replaced by an equimolar amount of Na^+ are shown in the right insets. An unpaired two-tailed *t*-test was performed to compare Na^+_i to $(NH_4^+)_i$ (**$P < 0.01$). Dashed lines in *A* and *D* indicate the 0 current level.

−2.3 to −0.58 pA when pH_o was lowered from 7.4 to 5 (Fig. 2*F*), and a substantial relief of block was observed at +100 mV (Fig. 2*E*, left trace). Indeed, the ratio of the single-channel conductance at +100 and −100 mV

($\gamma_{+100}/\gamma_{-100}$) is equal to 3.6 at pH_o 5. These data suggest that a fast mechanism of proton blockage is the leading cause of the current rectification, a notion that is further substantiated by the lack of tail currents when classical

Figure 4. Properties of inactivation in pore mutant channels

A and *B*, current recordings during a voltage step at −60 mV at pH_o 5 and 7.4, in symmetrical 110 mM Na^+ for the WT (*A*) and for the E363A mutant (*B*) channels. Currents were evoked by 1 mM cGMP and scaled for comparison. *C* and *D*, inactivation time constant τ (*C*) and residual fractional current I_{ss}/I_{peak} (*D*) for the E363A mutant channel at pH_o 5 and 7.4. An unpaired two-tailed *t*-test was performed to compare the two conditions. No statistically significant differences were found. *E*, current recording during a voltage step at −50 mV at pH_o 7.4 in symmetrical Na^+ for the E363A mutant channel. Currents were evoked by the application of 1 mM cGMP as indicated by solid black bars. The inset shows the fractional recovery I_t/I_{max} for the E363A mutant channel at pH_o 7.4 (black circles) and WT channel at pH_o 5 (green circles) plotted as a function of the cumulative interpulse interval. Data were fitted to a single exponential function providing the indicated time constants τ. *F*, current recordings during a voltage step at −60 mV in symmetrical 110 mM Na^+ for E363A (black trace), WT (green trace), T360A (blue trace) and T359A (red trace) channels, at pH_o 5. Currents were evoked by 1 mM cGMP and scaled for comparison. *G* and *H*, inactivation time constant τ (*G*) and residual fractional current I_{ss}/I_{peak} (*H*) for WT, E363A, T359A and T360A channels. ANOVA and Holm–Sidak *post hoc* tests were performed to compare each ion against each other (*$P < 0.05$; **$P < 0.01$). *I*, macroscopic current recording in symmetrical 110 mM Na^+, evoked by 1 mM cGMP and elicited by voltage steps from −200 to +200 mV ($\Delta V = 20$ mV) at pH_o 5 for the T359A mutant channel. *J*, dependence of G/G_{+200} on *V* for WT (black dots) and T359A mutant (red squares) channels at pH_o 5. While abolishing desensitization (*F*), Thr359 replacement with an alanine does not affect voltage dependency of proton blockage (*J*). Dashed black lines in *A*, *B*, *E* and *F* indicate the 0 current level.

voltage jump experiments are considered to uncover the voltage dependency of channel deactivation (Fig. 2*G*).

Like divalent cations, protons appear to reduce unitary currents by acting inside the conduction pathway of the channel (Dzeja *et al.* 1999; Seifert *et al.* 1999), and therefore we examined whether the Woodhull model (Woodhull, 1973) describes proton blockage (Fig. 2*H*). We assumed that H^+ binds to a binding site (BS) located at a certain electrical distance δ from the extracellular side of the membrane (Fig. 2*H*). Figure 2*I* illustrates the normalized G/G_{+200} relationship recorded at different pH$_o$, the shape of which could be described by the Woodhull model, yielding a δ of ~0.41. In this framework, the negative slope of the conductance observed at negative voltages (Fig. 2*I*) reflects the punch-through of H^+ from the pore. The model, however, does not satisfactorily fit the data at a pH$_o$ equal to or lower than 5 (filled and open squares, respectively, in Fig. 2*I*), in which the predicted proton

blockage is consistently larger than effectively measured. A very similar model has been described to explain extracellular divalent cation blockage and the blocking site is located at almost the same electrical distance δ of 0.45 (Seifert *et al.* 1999). It is thus conceivable that protons and divalent cations compete for the same BS within the selectivity filter of CNG channels.

The inactivation gate is located at the selectivity filter

In K^+ channels, the intimate relationship between the so-called C-type inactivation and the selectivity filter is illustrated by the substantial effects of the permeant ions on inactivation gating (López-Barneo *et al.* 1993; Starkus *et al.* 1997). Therefore, we examined whether ionic substitution could also affect the extent and the rate of inactivation in CNGA1 channels. Current decline was observed in the presence of Na^+, NH_4^+
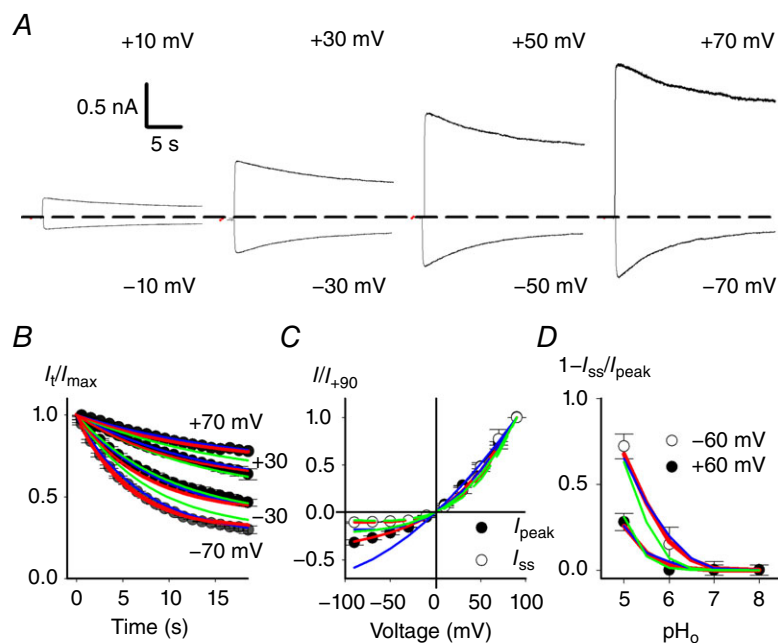

Figure 5. Voltage dependency of inactivation in WT CNGA1 channel
A, current recordings at pH$_o$ 5 from the same inside-out patch at the indicated membrane potentials in symmetrical Na^+. Currents were evoked by 1 mM cGMP. Dashed line indicates the 0 current level. *B*, time course of inactivation I_t/I_{max} at pH$_o$ 5 for the indicated membrane potentials from experiments as in *A* where sampling points were averaged every 500 μs. Each current decay was obtained from at least three independent experiments. I_{max} was measured at the peak of the cGMP current. *C*, dependence of the cGMP-activated current on membrane voltage prior to current decline (black circles) and after completion of inactivation (white circles). Current was scaled to the current flowing at +90 mV. *D*, dependence of fractional inactivation $(1 - I_{ss})/I_{peak}$ at + 60 mV (white dots) and −60 mV (black dots) on pH$_o$. I_{peak} and I_{ss} were measured at the beginning and termination of the cGMP pulse, respectively. Blue, green and red lines refer to simultaneous fits of all the data with schemes *i*, *ii*, and *iii* shown in Fig. 6*A*, respectively. For scheme *i* association constant $B(0)$ was 1.59×10^4 M^{-1} (pK$_a$ 4.2). The electrical distance δ_B was 0.37. The forward (i_+) and backward (i_-) inactivation rate constants were 0.41 and 0.05 s^{-1}, respectively. For scheme *ii* association constants $B(0)_1$ and $B(0)_2$ were 2.8×10^5 M^{-1} (pK$_a$ 5.44) and 2.5×10^4 M^{-1} (pK$_a$ 4.4), respectively. The electrical distance δ_B was 0.22. The forward (i_+) and backward (i_-) inactivation rate constants were 0.51 and 0.035 s^{-1}, respectively. For scheme *iii* association constants $P(0)$, $B(0)_1$ and $B(0)_2$ were 1.59×10^4 M^{-1} (pK$_a$ 4.2), 1.25×10^6 M^{-1} (pK$_a$ 6.1) and 5×10^4 M^{-1} (pK$_a$ 4.7), respectively. The electrical distances δ_P and δ_{Bi} were 0.37 and 0.45, respectively. The forward (i_+) and backward (i_-) inactivation rate constants were 0.41 and 0.05 s^{-1}, respectively.

and methylammonium (MA^+) (Fig. 3A), although inactivation was appreciably slower in the presence of NH_4^+ ($\tau = 10.5 \pm 1.7$ s, $n = 5$) compared to Na^+ ($\tau = 7.5 \pm 1.2$ s, $n = 5$) and MA^+ ($\tau = 7.2 \pm 1.2$ s, $n = 3$) conditions (Fig. 3B). Moreover, in the presence of either NH_4^+ or MA^+ ions, current decline was significantly less complete (Fig. 3C). When Na^+ ions were replaced with Rb^+ and Cs^+, inactivation properties did not differ among the different conditions (Fig. 3A–C). Thus, the pore occupancy of specific ions appears to be one of the microscopic factors controlling inactivation. Recently we showed that the presence of large cations such as Rb^+ and Cs^+ in the bathing medium inhibits the Na^+ inward current by interacting with Thr359 and Thr360 at the intracellular mouth of the selectivity filter. Indeed, the ring of these threonines contributes to an ion binding site at the intracellular entrance of the selectivity filter, and cations present in the intracellular medium could potentially interact with this site and affect channel gating and permeation (Marchesi et al. 2012). Therefore, we investigated whether occupancy of this binding site by certain ions compared to others could affect inactivation properties. When NH_4^+ ions in the bathing medium were replaced by an equimolar amount of Na^+, the NH_4^+ current not only appeared to be inhibited by the presence of intracellular Na^+ as the NH_4^+ peak current reduced by 32% in the presence of intracellular Na^+ ($I(NH_4^+)_i/I(Na^+)_i = 0.68 \pm 0.06; n = 4$), but inactivation also proceeded faster ($\tau = 5.38 \pm 0.98$ s, $n = 4$) and was more complete (Fig. 3D). It is therefore conceivable that Na^+ occupancy of this intracellular site, signalled by the NH_4^+ current blockage, prompted channel collapse towards the non-conductive, inactivated state.

Previous studies identified the Glu363 residue at the outer mouth of the selectivity filter as the major proton and divalent cation target (Root & MacKinnon, 1993, 1994; Eismann et al. 1994; Rho & Park, 2013; Morrill & MacKinnon, 1999). Therefore, we evaluated whether besides current rectification, proton binding to Glu363 also controls the time- and voltage-dependent loss of conductance discussed earlier. Similar to WT channels when pH_o was reduced to 5, mutant E363A channels inactivated at the usual pH_o of 7.4 (Fig. 4A, B, E), as previously described (Mazzolini et al. 2009). Moreover, the current decline observed at pH_o 7.4 and pH_o 5 is almost identical in this mutant (Fig. 4B); the inactivation time constant τ is equal to 3.1 ± 0.1 and 2.9 ± 0.2 s, respectively, and the residual steady-state current to 0.04 ± 0.01 and 0.05 ± 0.01 (Fig. 4C, D; $n \geq 4$). Thus, neutralization of Glu363 abolishes the pH dependency of inactivation, indicating that proton binding to Glu363 is also responsible for the slow current decline. Remarkably, compared to the WT channel, the onset rate of current decline was faster (Fig. 4F, G) and inactivation was more pronounced in the E363A mutant channel (Fig. 4F, H),

while the time course of recovery did not significantly differ in the two channels (Fig. 4E, inset). Inactivation kinetics is from two to three orders of magnitude slower than the gating transitions: indeed CNGA1 channels open in a few milliseconds in response to cGMP concentration jumps (Nache et al. 2006). Relying on this separation of timescales, the onset rate of inactivation depends on both the forward and the backward inactivation rate constants, while the recovery process depends solely on the backward rate constant. As the current decline onset in the E363A mutant is faster but recovery from this effect is not different from the WT channel, the mutation appears to affect only the forward inactivation rate constant, i.e. mutation of Glu363 destabilizes the open conformation of the pore.

To further substantiate the notion that the occupancy of an ion binding site in close proximity to the central cavity controls inactivation, we studied the current decline in Thr359 and Thr360 mutant channels (Marchesi et al. 2012). Inactivation kinetics for WT, T359A and T360A at pH_o 5 are shown in Fig. 4F. Current decline developed significantly more slowly in the T360A mutant channel ($\tau = 19.0 \pm 1.9$ s, $n = 3$, Fig. 4G) compared to the WT channel ($\tau = 7.5 \pm 1.2$ s, $n = 5$, Fig. 4G). When Thr359 at the intracellular entrance of the selectivity filter was mutated to an alanine, a significant inactivation was not observed within 20 s (Fig. 4F, H). The lack of current decline observed in T359A channels is unlikely to arise from a decreased affinity to protons, as the outward rectification at pH_o 5 is very similar in WT and T359A channels (Fig. 4I, J).

Voltage dependency of inactivation is expected from proton binding within the electrical transmembrane field

We studied the effect of membrane potential on inactivation kinetics by eliciting currents in response to 1 mM cGMP at different voltages (Fig. 5A). Two key differences among these records are the amplitude of steady-state currents and the rate of inactivation: the former increases as the membrane is made more depolarized, while the latter decreases. This finding is best illustrated in Fig. 5B, in which current decays obtained at different voltages were normalized to the current measured and compared immediately after addition of cGMP. Fitting the time course of inactivation at +70 and −70 mV with a single exponential yields a τ of inactivation equal to 16.3 and 6.7 s, respectively, and a residual steady-state current (I_t/I_{max}) equal to 0.63 and 0.27. The I–V relationships measured immediately after exposure to cGMP (filled circles) and after development of current decline (open circles) are shown in Fig. 5C and had a different degree of rectification. Indeed, at steady state,

the outward rectification increased due to the additional contribution of the inactivation (Fig. 5*C*). Finally, the pH dependency of inactivation at +60 mV (open circles) and −60 mV (solid circles) is shown in Fig. 5*D*. The fraction of channels residing in the inactivated state appears to be larger at negative membrane potentials and low pH (Figs 1*H* and 5*D*).

The slow time course of current decline described here might reflect a reduced accessibility of Glu363 carboxylate to extracellular protons. Indeed, previous

structure–function studies suggested that this residue is not directly accessible to extracellular solvent (Sun *et al.* 1996; Mazzolini *et al.* 2009; Martínez-François *et al.* 2009). Yet, this simple interpretation is hard to reconcile with several experimental observations. First, according to this idea, the disruption of the proton binding site should have resulted in a non-inactivating phenotype at pH$_o$ 5. This is in contrast to the finding that neutralization of Glu363 results in inactivating currents at the usual pH$_o$ of 7.4 (Fig. 4*E*). Indeed, the inactivation onset and recovery in the E363A mutant are still slow and comparable to those observed in the WT channel (Fig. 4*E*, *F*). Second, recovery from inactivation is fast – less than 1 s as no obvious kinetics could be resolved – when pH$_o$ is reverted from 5 to 7.4 in outside-out patches (Fig. 1*F*, right panel). If the slow current run-down reflected the low accessibility of Glu363 to protons, then one would have expected a similar slow recovery upon pH$_o$ switch to 7.4. Therefore, we suggest that current decline reflects proton-induced conformational changes, of which the kinetics are limited by a transition downstream from protonation. In this view, protons first bind
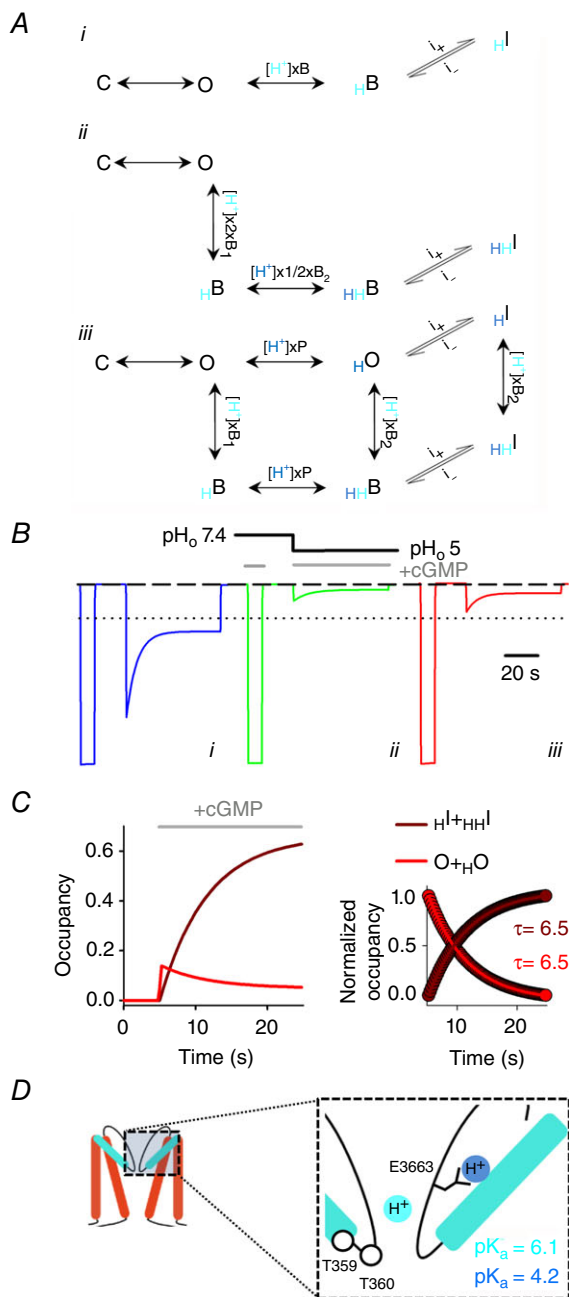

A, schemes showing the proposed mechanisms for proton binding and inactivation with one proton binding site (*i*), two equivalent proton binding sites (*ii*) and two non-equivalent and non-independent binding sites (*iii*). In *iii* columns depict protons (cyan circle and symbols) binding within permeation pathway and blocking ion conduction (*D*). A second proton (blue circle and symbols) binds to E363 carboxylate, possibly impairing an electrostatic interaction between E363 side chain and neighbouring residues in the P-helix (*D*) (Mazzolini *et al.* 2009; Martínez-François *et al.* 2010). The open conformation of the pore is now metastable and collapses to inactivated states $_H$I and $_{HH}$I. C, O, B and I indicate closed, open, blocked and inactivated states, respectively. H subscripts indicate proton transfer to the pore. *P* and B_i are the association constants for protons to the two non-equivalent binding sites within the pore lumen. i_+ and i_- are the forward and backward inactivation rate constants. *B*, simulated currents with schemes *i* (blue trace), *ii* (green trace) and *iii* (red trace) shown in *A* in response to a pH$_o$ step from 7.4 to 5 (black line) at −50 mV. The dotted black line indicates the mean fractional peak current observed in outside-out patches at pH$_o$ 5 (I(pH$_o$5)/I(pH$_o$7.4) = 0.21 ± 0.02, $n = 3$; Fig. 1*F*). The dashed black line indicates the 0 current level. Rate constants are listed in the legend to Fig. 5. *C*, time course of occupancies for the conductive states (O + $_H$O; solid red line) and inactivated states ($_H$I + $_{HH}$I; solid brown line). The occupancies were calculated from the scheme *iii* shown in *A* at −50 mV and pH$_o$ 5 after a step in cGMP concentration from 0 to 1 m$_M$. The inset at the right shows the decaying and rising phase of these occupancies, highlighting the same time constants ($\tau = 6.5$ s). cGMP application in *B* and *C* is indicated by the solid grey lines. *D*, cartoon illustrating CNGA1 pore domain. The inset shows an enlargement of the selectivity filter region. Residues E363, T359 and T360 are shown. Cyan and blue circles represent two protons binding, respectively, within the permeation pathway and to the E363 side chain. The logarithmic acidic dissociation constants (pK$_a$) for the two binding sites were determined from P(0) and B_1(0) association constants by fitting the model in *A* to the data shown in Fig. 5.

Figure 6. Proposed mechanism for proton action in CNGA1 channels

to Glu363 within the electrical transmembrane field, quickly blocking ion conduction and destabilizing the pore, which subsequently undergoes a slow structural collapse leading to a virtually closed channel. This molecular picture is captured by the simple linear scheme shown in Fig. 6*Ai*, involving transitions among an open, blocked and inactivated state, which could successfully describe the pH and voltage dependency of inactivation, yielding a pK$_a$ of 4.2 (Fig. 5*B, D* blue lines). Although we could not rule out the possibility that membrane voltage might affect the conformation of charged residues and/or structures located within the electrical field as suggested for bacterial K$^+$ channel KcsA (Cordero-Morales *et al.* 2006), the properties of the observed current decline are well accounted by the voltage-dependent concentration of H$^+$ within the electrical field alone, without the necessity of taking explicitly into account a voltage-dependent conformational change. The fraction of the membrane voltage at the binding site thus obtained ($\delta \sim 0.37$) is consistent with the expected location of Glu363 within the electrical field (Contreras *et al.* 2010). This scheme, however, appears to be critically deficient in reproducing the instantaneous and steady-state *I–V* relationship (Figs 5*C* and 6*B*, blue lines). The basis of this shortcoming is the different pH dependency of proton blockage and inactivation. Indeed, proton blockage has been associated with an apparent acidic dissociation constant (pK$_a$) between 6 and 7 in several reports (Root & MacKinnon, 1994; Seifert *et al.* 1999). It is therefore possible that the binding of at least two protons underlines proton blockage and inactivation in CNGA1 channels.

Discussion

Desensitization and inactivation are widespread phenomena in ion channels, in which they modulate the amplitude, duration and frequency of electrical signalling within and between cells. Unlike many of their cousin K$^+$ channels and other membrane receptors, CNG channels do not desensitize or inactivate at physiological pH when a network of chemical interactions between residues in the pore region is maintained (Mazzolini *et al.* 2009). We have shown that in response to changes of extracellular pH, CNG channels also inactivate, representing a possible novel regulatory mechanism that has so far been neglected.

Previous studies suggested the presence of multiple H$^+$-binding sites in the CNG channel pore. Single-channel current analysis in olfactory CNG channels indicated that the binding of two protons is required to model the proton monovalent current inhibition (Root & MacKinnon, 1994). Moreover, Seifert *et al.* (1999, fig. 5*B, C*) showed that a Hill coefficient of ~ 2 describes the pH dependency of divalent cation blockage in CNGA1 channels, suggesting

the binding of at least two protons. In agreement with these earliest observations we were unable to describe the experimental data when the binding of only one proton was considered (Fig. 5). Similarly, a linear scheme assuming two equivalent proton binding sites (Fig. 6*Aii*) failed to satisfactory reproduce the experimental data as it overestimates the current inhibition observed at low pH$_o$ (compare Figs 1*F* and 6*B*, green trace). Therefore, we evaluated a more general kinetic scheme in which two non-equivalent and non-independent proton binding reactions were modelled (Fig. 6*Aiii*). This model appears to adequately describe key features of the reported current decline, such as the time course of inactivation (Fig. 5*B*, red lines), its pH dependency (Fig. 5*D*, red lines), the instantaneous and steady-state rectification (Fig. 5*C*, red lines) and the fractional current blockage observed at pH$_o$ 5 (Fig. 6*B*, red trace). As we were unable to resolve the kinetics of H$^+$ unbinding in outside-out patches (Fig. 1*F*) as well as the kinetics of proton blockage from voltage jump experiments (Fig. 2*G*), the proton binding reactions are not likely to contribute to the observed slow current relaxation kinetics and the two binding reactions are therefore assumed to be diffusion limited in this model. Once protons have bound, the slow current decline reflects the very slow inactivation rate constants, which are the rate-limiting reactions in the scheme. Indeed, the time courses of the occupancies for the conductive states (O + $_H$O, red lines) and the inactivated states ($_H$I + $_{HH}$I, brown lines) are symmetrical (Fig. 6*C*), yielding at -50 mV the same time constant τ of 6.5 s. Thus, we propose that the non-equivalent binding of two protons within the transmembrane electrical field underlies voltage-dependent blockage and inactivation.

It has also been suggested that voltage-dependent gating contributes to the rectification of the macroscopic currents at very low pH$_o$ (pH$_o$ = 4) as a consequence of Glu363 side chain titration (Martínez-François *et al.* 2010). Based on noise analysis (Fig. 2*C, D*), single-channel recordings (Fig. 2*E, F*) and voltage-jump experiments (Fig. 2*G*), this mechanism does not appear to significantly contribute to the outward rectification observed at higher pH$_o$ (pH$_o \geq 5$) and has therefore not been included (Fig. 6*A*).

How could the proposed kinetic mechanism be interpreted in the light of the available structural and functional data? The crystal structure of a recently solved bacterial channel mimicking the CNG channel pore (Derebe *et al.* 2011) suggests that Ca^{2+} ions are chelated by backbone carbonyl oxygens and not by the Glu363 side chain, which is engaged in hydrogen bonding interactions with its neighbouring residues and buried underneath the external surface of the protein. The authors of this study suggested that the Glu363 carboxylate negative charge could perturb the electron shell distribution along the backbone of the filter residues, making certain carbonyl oxygen atoms, such as those of Gly65, more electronegative and suited

for Ca^{2+} binding (Derebe *et al.* 2011). These observations are consistent with several recent structure–function studies, suggesting that interactions between the Glu363 side chain and residues in the P-helix are necessary for normal gating in CNG channels (Mazzolini *et al.* 2009; Martínez-François *et al.* 2009, 2010). In this view proton blockage could arise from the high-affinity binding to the main chain carbonyl oxygens within the selectivity filter (Fig. 6*D*, $pK_a = 6.1$). A second, low-affinity binding site for protons could be constituted by the Glu363 side chain ($pK_a = 4.2$), titration of which results in the neutralization of the negatively charged carboxylate and in the weakening of key interactions anchoring the selectivity filter to the surrounding channel moiety (Fig. 6*D*) (Mazzolini *et al.* 2009; Martínez-François *et al.* 2009, 2010). After Glu363 protonation, glycine carbonyl oxygen specificity for protons and divalent cations is lost – the pK_a of the proton high-affinity binding site reduces from 6.1 to 4.7 – and thus a substantial relief from blockage is observed at low extracellular pH_o (Fig. 2*I*). It then follows a slow pore collapse toward a non-conductive, inactivated state. These observations suggest that the two binding sites are non-independent, and explain why neutralization of the same residue (Glu363) affects both proton blockage (Root & MacKinnon, 1994) and the pH dependency of inactivation (Fig. 4).

One of the hallmarks of the C-type inactivation is its intimate dependence on the permeant ion. Indeed, it has long been known that the rate and extent of C-type inactivation is governed by the occupancy of an ion binding site near the external mouth of the pore via a foot-in-the-door mechanism (Yellen, 1998; Kurata & Fedida, 2006). Our results indicate that such a relationship between the permeant ion and inactivation also exists in CNG channels (Fig. 3), although the underlying mechanism appears to be somewhat different. In fact, inactivation appears to be primarily modulated by the nature of the intracellular cation, being faster in the presence of intracellular Na^+ (Fig. 3*D*). Furthermore, inactivation is abolished when the intracellular ion binding site is disrupted (Fig. 4*F*), thus suggesting that the occupancy of an ion binding site possibly equivalent to the fourth ion binding site within the selectivity filter (S4 site) of the K^+ channel might control the rate and extent of inactivation in CNG channels. Therefore, it is conceivable that the pore collapse triggered by the protonation of Glu363 implies fine conformational changes also of the intracellular vestibule involving the two threonines Thr359 and Thr360. Although the molecular basis underpinning the C-type inactivation is still of debate (Devaraneni *et al.* 2013; Armstrong & Hoshi, 2014), according to the predominant view inactivation is associated with a conformational change close to the external mouth of the K^+ channel pore

(Yellen, 1998; Kurata & Fedida, 2006; Hoshi & Armstrong, 2013). Nonetheless, rearrangements near the intracellular face of the selectivity filter have been implied as well. Indeed, Posson *et al.* (2013) demonstrated that the binding affinity of certain intracellular blockers depends on the conformational state of the selectivity filter (open-conductive versus closed-inactivated). The authors of this study argued that the observed state-dependent affinities reflect a conformational change at the intracellular face of the selectivity filter upon inactivation. These rearrangements close to the intracellular end of the selectivity filer could be more pronounced during the CNG channel inactivation process as they may reflect the allosteric connection between the CN-binding domain and the selectivity filter gate. In this view, residues Thr359 and Thr360 might play an important role in the observed current decline. Overall, inactivation appears to be associated with a local remodelling confined to the selectivity filter and neighbouring regions in CNG as well as K^+ channels (Roncaglia & Becchetti, 2001; Kurata & Fedida, 2006; Mazzolini *et al.* 2009).

In the present study, we demonstrate that the outward rectification observed at $pH_o \geq 5$ at stationary conditions (i.e. after a steady exposure to cGMP for 1–2 min) is mainly caused by asymmetries in the unitary current (Fig. 2). This finding is consistent with several earlier studies suggesting that proton elevation is associated with the stabilization of low conductance states primarily at negative voltages (Root & MacKinnon, 1994; Rho & Park, 2013; Morrill & MacKinnon, 1999). We propose that a Woodhull model of block, alongside divalent cation blockage (Seifert *et al.* 1999), underlies proton block in CNG channels. This is directly opposite to the conclusions reached by a recent report suggesting that the outward rectification is due to an inherent channel voltage-dependent gating (Martínez-François *et al.* 2010). The reasons for these discrepancies are not clear. Several of the Glu363 mutants display voltage-dependent gating in addition to inactivation (Bucossi *et al.* 1996; Martínez-François *et al.* 2009). It is thus likely that voltage gating additively contributes to the observed rectification when extracellular pH is further lowered to 4 and slow activation kinetics are observed (Martínez-François *et al.* 2010). Determining the extent that such a mechanism contributes to the outward rectification at very low pH_o will require further experimentation. Nonetheless, demonstration of common gating features (inactivation and voltage gating) as the result of pore mutation and protonation further illustrates the gating role of the outer pore in CNG channels.

Changes in pH_o can arise in a variety of physiological and pathophysiological conditions, such as neuronal activity, ischaemia and inflammation (Kellum *et al.* 2004; Isaev *et al.* 2008; Magnotta *et al.* 2012). Low pH

acts as a negative feedback mechanism that inhibits the CNGA1 channel in a state-dependent manner and may represent an unrecognized endogenous signal regulating CNG physiological functions in diverse tissues.

References

Armstrong CM & Hoshi T (2014). K$^+$ channel gating: C-type inactivation is enhanced by calcium or lanthanum outside. *J Gen Physiol* **144**, 221–230.

Becchetti A, Gamel K & Torre V (1999). Cyclic nucleotide-gated channels. Pore topology studied through the accessibility of reporter cysteines. *J Gen Physiol* **114**, 377–392.

Bucossi G, Eismann E, Sesti F, Nizzari M, Seri M, Kaupp UB & Torre V (1996). Time-dependent current decline in cyclic GMP-gated bovine channels caused by point mutations in the pore region expressed in *Xenopus* oocytes. *J Physiol* **493**, 409–418.

Bucossi G, Nizzari M & Torre V (1997). Single-channel properties of ionic channels gated by cyclic nucleotides. *Biophys J* **72**, 1165–1181.

Contreras JE, Chen J, Lau AY, Jogini V, Roux B & Holmgren M (2010). Voltage profile along the permeation pathway of an open channel. *Biophys J* **99**, 2863–2869.

Cordero-Morales JF, Cuello LG & Perozo E (2006). Voltage-dependent gating at the KcsA selectivity filter. *Nat Struct Mol Biol* **13**, 319–322.

Craven KB & Zagotta WN (2006). CNG and HCN channels: two peas, one pod. *Annu Rev Physiol* **68**, 375–401.

Derebe MG, Zeng W, Li Y, Alam A & Jiang Y (2011). Structural studies of ion permeation and Ca^{2+} blockage of a bacterial channel mimicking the cyclic nucleotide-gated channel pore. *Proc Natl Acad Sci USA* **108**, 592–597.

Devaraneni PK, Komarov AG, Costantino CA, Devereaux JJ, Matulef K & Valiyaveetil FI (2013). Semisynthetic K$^+$ channels show that the constricted conformation of the selectivity filter is not the C-type inactivated state. *Proc Natl Acad Sci USA* **110**, 15698–15703.

Dmitriev AV & Mangel SC (2001). Circadian clock regulation of pH in the rabbit retina. *J Neurosci* **21**, 2897–2902.

Dzeja C, Hagen V, Kaupp UB & Frings S (1999). Ca^{2+} permeation in cyclic nucleotide-gated channels. *EMBO J* **18**, 131–144.

Eismann E, Müller F, Heinemann SH & Kaupp UB (1994). A single negative charge within the pore region of a cGMP-gated channel controls rectification, Ca^{2+} blockage, and ionic selectivity. *Proc Natl Acad Sci USA* **91**, 1109–1113.

Hamill OP, Marty A, Neher E, Sakmann B & Sigworth FJ (1981). Improved patch-clamp techniques for high-resolution current recording from cells and cell-free membrane patches. *Pflügers Arch* **391**, 85–100.

Hille B (1992). *Ionic Channels of Excitable Membranes*, 2 Sub. Sinauer Associates Inc., Sunderland, MA.

Hoshi T & Armstrong CM (2013). C-type inactivation of voltage-gated K$^+$ channels: pore constriction or dilation? *J Gen Physiol* **141**, 151–160.

Isaev NK, Stelmashook EV, Plotnikov EY, Khryapenkova TG, Lozier ER, Doludin YV, Silachev DN & Zorov DB (2008). Role of acidosis, NMDA receptors, and acid-sensitive ion channel 1a (ASIC1a) in neuronal death induced by ischemia. *Biochemistry (Mosc)* **73**, 1171–1175.

Kaupp UB, Niidome T, Tanabe T, Terada S, Bönigk W, Stühmer W, Cook NJ, Kangawa K, Matsuo H & Hirose T (1989). Primary structure and functional expression from complementary DNA of the rod photoreceptor cyclic GMP-gated channel. *Nature* **342**, 762–766.

Kaupp UB & Seifert R (2002). Cyclic nucleotide-gated ion channels. *Physiol Rev* **82**, 769–824.

Kellum JA, Song M & Li J (2004). Science review: extracellular acidosis and the immune response: clinical and physiologic implications. *Crit Care* **8**, 331–336.

Kurata HT & Fedida D (2006). A structural interpretation of voltage-gated potassium channel inactivation. *Prog Biophys Mol Biol* **92**, 185–208.

Leung YK, Du J, Huang Y & Yao X (2010). Cyclic nucleotide-gated channels contribute to thromboxane A2-induced contraction of rat small mesenteric arteries. *PLoS ONE* **5**, e11098.

Liu J & Siegelbaum SA (2000). Change of pore helix conformational state upon opening of cyclic nucleotide-gated channels. *Neuron* **28**, 899–909.

López-Barneo J, Hoshi T, Heinemann SH & Aldrich RW (1993). Effects of external cations and mutations in the pore region on C-type inactivation of Shaker potassium channels. *Receptors Channels* **1**, 61–71.

Lopez-Jimenez ME, González JC, Lizasoain I, Sánchez-Prieto J, Hernández-Guijo JM & Torres M (2012). Functional cGMP-gated channels in cerebellar granule cells. *J Cell Physiol* **227**, 2252–2263.

Magnotta VA, Heo H-Y, Dlouhy BJ, Dahdaleh NS, Follmer RL, Thedens DR, Welsh MJ & Wemmie JA (2012). Detecting activity-evoked pH changes in human brain. *Proc Natl Acad Sci USA* **109**, 8270–8273.

Marchesi A, Mazzolini M & Torre V (2012). A ring of threonines in the inner vestibule of the pore of CNGA1 channels constitutes a binding site for permeating ions. *J Physiol* **590**, 5075–5090.

Martínez-François JR, Xu Y & Lu Z (2009). Mutations reveal voltage gating of CNGA1 channels in saturating cGMP. *J Gen Physiol* **134**, 151–164.

Martínez-François JR, Xu Y & Lu Z (2010). Extracellular protons titrate voltage gating of a ligand-gated ion channel. *J Gen Physiol* **136**, 179–187.

Mazzolini M, Anselmi C & Torre V (2009). The analysis of desensitizing CNGA1 channels reveals molecular interactions essential for normal gating. *J Gen Physiol* **133**, 375–386.

Mazzolini M, Marchesi A, Giorgetti A & Torre V (2010). Gating in CNGA1 channels. *Pflügers Arch* **459**, 547–555.

Morrill JA & MacKinnon R (1999). Isolation of a single carboxyl-carboxylate proton binding site in the pore of a cyclic nucleotide-gated channel. *J Gen Physiol* **114**, 71–83.

Nache V, Kusch J, Hagen V & Benndorf K (2006). Gating of cyclic nucleotide-gated (CNGA1) channels by cGMP jumps and depolarizing voltage steps. *Biophys J* **90**, 3146–3154.

Nizzari M, Sesti F, Giraudo MT, Virginio C, Cattaneo A & Torre V (1993). Single-channel properties of cloned cGMP-activated channels from retinal rods. *Proc Biol Sci* **254**, 69–74.

Pavlov I, Kaila K, Kullmann DM & Miles R (2013). Cortical inhibition, pH and cell excitability in epilepsy: what are optimal targets for antiepileptic interventions? *J Physiol* **591**, 765–774.

Posson DJ, McCoy JG & Nimigean CM (2013). The voltage-dependent gate in MthK potassium channels is located at the selectivity filter. *Nat Struct Mol Biol* **20**, 159–166.

Rho SH & Park CS (2013). Extracellular proton alters the divalent cation binding affinity in a cyclic nucleotide-gated channel pore. *FEBS Lett* **440**, 199–202.

Roncaglia P & Becchetti A (2001). Cyclic-nucleotide-gated channels: pore topology in desensitizing E19A mutants. *Pflügers Arch* **441**, 772–780.

Root MJ & MacKinnon R (1993). Identification of an external divalent cation-binding site in the pore of a cGMP-activated channel. *Neuron* **11**, 459–466.

Root MJ & MacKinnon R (1994). Two identical noninteracting sites in an ion channel revealed by proton transfer. *Science* **265**, 1852–1856.

Seifert R, Eismann E, Ludwig J, Baumann A & Kaupp UB (1999). Molecular determinants of a Ca^{2+}-binding site in the pore of cyclic nucleotide-gated channels: S5/S6 segments control affinity of intrapore glutamates. *EMBO J* **18**, 119–130.

Sesti F, Eismann E, Kaupp UB, Nizzari M & Torre V (1995). The multi-ion nature of the cGMP-gated channel from vertebrate rods. *J Physiol* **487**, 17–36.

Starkus JG, Kuschel L, Rayner MD & Heinemann SH (1997). Ion conduction through C-type inactivated Shaker channels. *J Gen Physiol* **110**, 539–550.

Sun ZP, Akabas MH, Goulding EH, Karlin A & Siegelbaum SA (1996). Exposure of residues in the cyclic nucleotide-gated channel pore: P region structure and function in gating. *Neuron* **16**, 141–149.

Tolner EA, Hochman DW, Hassinen P, Otáhal J, Gaily E, Haglund MM, Kubová H, Schuchmann S, Vanhatalo S & Kaila K (2011). Five percent CO_2 is a potent, fast-acting inhalation anticonvulsant. *Epilepsia* **52**, 104–114.

Woodhull AM (1973). Ionic blockage of sodium channels in nerve. *J Gen Physiol* **61**, 687–708.

Yellen G (1998). The moving parts of voltage-gated ion channels. *Q Rev Biophys* **31**, 239–295.

Yu FH, Yarov-Yarovoy V, Gutman GA & Catterall WA (2005). Overview of molecular relationships in the voltage-gated ion channel superfamily. *Pharmacol Rev* **57**, 387–395.

Zufall F, Shepherd GM & Barnstable CJ (1997). Cyclic nucleotide gated channels as regulators of CNS development and plasticity. *Curr Opin Neurobiol* **7**, 404–412.

Additional Information

Competing interests

The authors declare that there are no competing interests.

Author contributions

M.A. and A.M. performed experiments on oocytes. M.M. performed mutagenesis. All authors participated in designing experiments, and analysing and interpreting the data. A.M. wrote the paper, which was revised by all authors in collaboration. A.M. and V.T. supervised the project. All authors approved the final version of the manuscript.

Funding

Conformational rearrangements in the transmembrane domain of CNGA1 channels revealed by single-molecule force spectroscopy.

Sourav Maity, Monica Mazzolini, Manuel Arcangeletti, Alejandro Valbuena, Paolo Fabris, Marco Lazzarino, and Vincent Torre.

ARTICLE

OPEN

Conformational rearrangements in the transmembrane domain of CNGA1 channels revealed by single-molecule force spectroscopy

Sourav Maity[1], Monica Mazzolini[1,2], Manuel Arcangeletti[1], Alejandro Valbuena[1], Paolo Fabris[1], Marco Lazzarino[2,3] & Vincent Torre[1]

Cyclic nucleotide-gated (CNG) channels are activated by binding of cyclic nucleotides. Although structural studies have identified the channel pore and selectivity filter, conformation changes associated with gating remain poorly understood. Here we combine single-molecule force spectroscopy (SMFS) with mutagenesis, bioinformatics and electrophysiology to study conformational changes associated with gating. By expressing functional channels with SMFS fingerprints in *Xenopus laevis* oocytes, we were able to investigate gating of CNGA1 in a physiological-like membrane. Force spectra determined that the S4 transmembrane domain is mechanically coupled to S5 in the closed state, but S3 in the open state. We also show there are multiple pathways for the unfolding of the transmembrane domains, probably caused by a different degree of α-helix folding. This approach demonstrates that CNG transmembrane domains have dynamic structure and establishes SMFS as a tool for probing conformational change in ion channels.

---

[1] International School for Advanced Studies (SISSA) Neuroscience Area, via Bonomea 265, Trieste 34136, Italy. [2] CBM S.c.r.l., Area Science Park, Basovizza, Trieste 34149, Italy. [3] IOM-CNR, Area Science Park, Basovizza, Trieste 34149, Italy. Correspondence and requests for materials should be addressed to V.T. (email: torre@sissa.it).

1

Atomic force microscopy (AFM) is a powerful technique used for surface imaging, measurements of sample mechanics and for the analysis of molecular interactions. Single-molecule force spectroscopy (SMFS) uses an atomic force microscope to apply a force to unfold a molecule or a polymer[1–4]. The obtained force–distance (F–D) curves characterize the stretching of the molecule; the resulting sequence of unfolding force peaks and their magnitude allows for the identification of folded and unfolded regions, thus providing insight into the interactions between and within domains of the molecule that stabilize secondary structures[1–5]. SMFS has been used to identify the conformational changes of membrane proteins belonging to the rhodopsin family[6–8] and other proteins, such as the Na$^+$/H$^+$ antiporter, the BetP symporter, the KpOmpA transmembrane protein, the β2-adrenergic receptor, T4 lysozyme and the leucine-binding protein[9–14].

Ion channels are membrane proteins that play a major functional role and they are grouped in superfamilies[15,16]: the superfamily of voltage-gated ion channels comprises Na$^+$, K$^+$ and Ca^{2+} channels, whose gating (transitions between the open and closed conformation) depends on the membrane voltage. This superfamily also includes cyclic nucleotide-gated (CNG) channels[17–21] that are voltage dependent[21] but are opened by the binding of cyclic nucleotides to the cyclic nucleotide-binding (CNB) domain[17,19,20].

In vertebrates, seven members of the CNG channel gene family have been identified[19,22] and are grouped into two subtypes, CNGA (CNGA1–CNGA5) and CNGB (CNGB1 and CNGB3). CNGA1, CNGA2, CNGA3 and CNGA5 (but not CNGA4) can form cyclic nucleotide-activated homotetrameric channels, while CNGB1 and CNGB3 are modulatory subunits that cannot form functional homomeric channels. Hydropathicity and biochemical analyses of CNGA1 channels[17]—690 amino acid residues (a.a.) long—have revealed six transmembrane α-helices (known as S1, S2, S3, S4, S5 and S6) that span the lipid bilayer (see Supplementary Fig. 1a); these helices are linked by non-spanning loops, which are either extracellular or intracellular. Ion permeation occurs through a pore region between S5 and S6, and electrophysiological experiments have identified 20 a.a. that form the P-helix (V348-L358) and the selectivity filter (T359-P367)[23–28]. The amino- and carboxy-terminal ends are both cytoplasmic, and the C-terminal end (N400-D690) is a large domain composed of the C-linker (N400-E482) and the CNB domain (A483-N610)[29,30]. The CNB domain shares 20% sequence identity with other CNB proteins, such as the CNB domain of HCN channels[31] and MlotiK1 potassium channels (originally referred as mlCNG channels)[32], and it consists of three α-helices and eight stranded anti-parallel β-rolls. The functional properties of CNG channels have been investigated extensively[19,33,34], and a low-resolution architecture[35], partial crystal structures of the CNB domain[31,36,37], a crystal structure of the isolated C-terminal end from L621 to D690 (ref. 38) and a mimic of the pore[39] are available. However, the full-length channel has never been crystallized and the conformational changes that are associated with gating are poorly understood.

In this study, we demonstrate how SMFS can be used to examine the gating of CNGA1 channels that are overexpressed in membranes from X. laevis oocytes[21,40,41] (that is, almost in situ); the plasma membrane of these oocytes contains few native membrane proteins[41–44]. We identify F–D curves using bioinformatics analysis and by engineering proteins that are composed of CNGA1 channels linked at their C-termini to an SMFS marker, that is, a protein with a known unfolding pattern that act as a fingerprint. Our results provide new insights on the structure of the transmembrane domain of CNGA1 channels: first, the S4 domain shows different interactions between S3 and S5 in the closed and open state. Second, there are multiple pathways for the unfolding of the transmembrane domain probably caused by a different degree of folding of α-helices.

Results

CNGA1 channel constructs. Several constructs were designed to identify the F–D curves obtained from the unfolding of CNGA1 channels, to explore different pulling configurations and to validate a hypothesis of the molecular mechanisms. All these constructs had cGMP-activated currents that were measured using electrophysiological experiments (Supplementary Fig. 1 and Supplementary Note 1). We performed SMFS experiments in the presence and the absence of cGMP, that is, in the open and closed states of these channels. We performed SMFS experiments using both uninjected oocytes and oocytes injected with the messenger RNA coding for CNGA1 channels.

SMFS of the CNGA1 channels. In our SMFS experiments, the obtained F–D curves could not only represent the unfolding of the full CNGA1 channel but also the unfolding of endogenous proteins and/or of the partial unfolding of CNGA1 channels. To identify the F–D curves obtained from the unfolding of the full CNGA1 channels, we have designed a method that analyses the F–D curves obtained using CNGA1 channels with appropriate mutations and/or channels that bear specific fingerprints.

The N- and C- termini and some loops between the transmembrane helices of the CNGA1 channels are cytoplasmic, and the AFM tip could attach to all a.a. in these different positions. If the tip starts the unfolding from residue D690 (that is, from the C-terminal)—assuming that the length of a single residue is 0.4 nm (ref. 1)—the complete stretch corresponds to a contour length (Lc) of ~240 nm (from the end of the C-terminal to the beginning of S1); if the AFM tip started the unfolding from residue M1 (that is, from the N-terminal), the complete stretch corresponds to an Lc of 180 nm (from the N-terminal to the end of S6). Therefore, we have restricted our analysis to those F–D curves that had the last peak with an Lc value larger than 220 nm and only ~1% of the F–D curves passed this filtering step (see Methods and Supplementary Fig. 2). These F–D curves were too diverse to be ascribed to the unfolding of the same protein. To identify the F–D curves obtained from the unfolding of CNGA1 channels, we developed a two-step method based on the following criteria: first, these F–D curves must be distinguishable and must be found only in SMFS experiments performed using membranes extracted from injected oocytes expressing CNGA1 channels at a high level; these F–D curves must stand out from the other F–D curves and must form a cluster of F–D curves with similar features (identification). Second, these F–D curves are 'good' candidates as F–D curves from the unfolding of CNGA1 channels, but they must be further validated by an appropriate fingerprint that is clearly visible in the F–D curves (validation).

The bioinformatics analysis (see Methods) was based on the coding of the F–D curves (Fig. 1a). From the analysis of the corresponding (F,Lc) plot (Fig. 1b)[45], three different coding schemes were obtained (Fig. 1c–e). Once the F–D curves were coded in appropriate strings of symbols, clustering methods developed in Computer Science were used (see Methods and Supplementary Figs 3 and 4). At the end of the bioinformatics analysis, we identified three major clusters of similar F–D curves that were obtained only from the membranes extracted from injected oocytes (Supplementary Fig. 5). To validate these clusters as clusters obtained from the unfolding of CNGA1 channels in the closed state, we used the construct CNGA1-N2B-HisTag and we selected those F–D curves that exhibited an N2B fingerprint (black curves in Fig. 1f) that showed an initial segment of
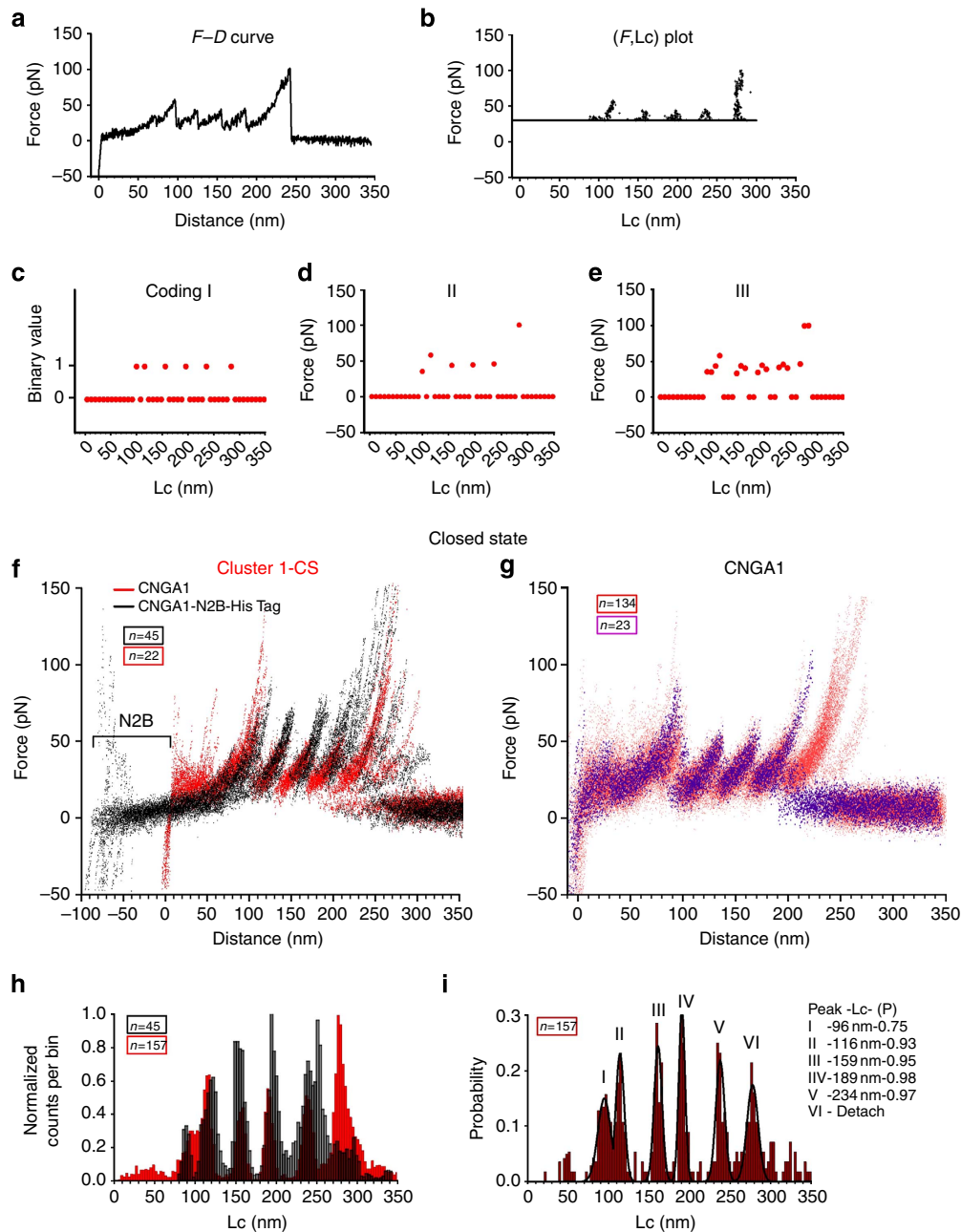
Figure 1 | F–D curves from CNGA1 and CNGA1-N2B-HisTag in the closed state. (**a**) An example of an F–D curve. (**b**) Transformation of the F–D curve in **a** into an (F,Lc) plot; if the F–D curve fits well in a piecewise manner using the WLC model, the resulting (F,Lc) plot is composed of a series of almost vertical segments located at the corresponding value of Lc and the upper value of each of these segments corresponds to the value of the force peak F. (**c–e**) Three different coding schemes of increasing complexity that are all based on the processing of the (F,Lc) plot in **b**; coding scheme I (**c**) considers only the location of the force peak (the corresponding value of Lc) and is a binary coding; coding II (**d**) considers the location and the amplitude of the force peak and is not a binary coding; coding III (**e**) fits all sample values of F above 30 pN. Red dots represent the final coding of the F–D curves. (**f**) 22 F–D curves from Cluster 1-CS of CNGA1 (red) detected using bioinformatics analysis and 45 F–D curves from the construct CNGA1-N2B-HisTag (black) in the closed state. The construct with N2B has an initial flat region of 85 nm, followed by force peaks matching the unfolding events observed with the CNGA1 construct. (**g**) Superimposition of 157 F–D curves obtained from injected oocytes showing the peak force location of CNGA1. The 23F–D curves (violet) end with a force peak with an Lc of ~234 nm; 134 F–D curves (red) have an additional force peak with an Lc of ~276 nm. (**h**) Superimposition of histograms of normalized counts/bin against Lc from the 157 F–D curves of **b** (now all in red) and 45 F–D curves from the CNGA1-N2B-HisTag construct (black). (**i**) Histogram of Lc values of force peak (with Gaussian fit for the different peaks) from the F–D curves in **g** with five peaks located at 96 ± 3 (mean ± s.d., n = 117), 116 ± 3 (mean ± s.d., n = 146), 159 ± 3 (mean ± s.d., n = 157), 189 ± 5 (mean ± s.d., n = 157), 234 ± 6 (mean ± s.d., n = 157) nm and the detachment with the probability (P) of 0.75, 0.93, 0.95, 0.98 and 0.97, respectively.

~85 nm (in Lc) without unfolding events, which are typical characteristics of the N2B construct[46–48]. This initial segment was followed by an additional segment resembling the peaks obtained for the CNGA1 channel construct (red curves in Fig. 1f). F–D

curves, obtained from the unfolding of CNGA1 channels, were identified by an initial filtering (Step 1 and 2 described in the Methods) of F–D curves from experiments using injected and uninjected oocytes followed by a clusterization aimed to identify

clusters of *F–D* curves obtained only from injected oocytes (Step 3 and 4 in the Methods).

When these curves were displaced by Lc of 85 nm, the resulting curves superimposed precisely with the curves present in the Cluster 1-CS (Fig. 1f and Supplementary Fig. 5a). This cluster was identified using the bioinformatics analysis and was therefore validated as representing the *F–D* curves obtained from the C-terminal unfolding of the CNGA1 channels. These last *F–D* curves were used as a template to find additional *F–D* curves (Fig. 1g), which when shifted by < ±5 nm aligned properly with those of Fig. 1f and include also *F–D* curves from Cluster 2-CS (Supplementary Fig. 5b) and additional *F–D* curves from injected oocytes (see Methods).

Some *F–D* curves (violet curves in Fig. 1g) ended with a force peak that had an Lc of ∼234 nm, whereas the remaining *F–D* curves (red curves in Fig. 1g) were longer and had an additional force peak with an Lc of ∼276 nm, which exactly correspond to 690 a.a. This behaviour is attributed to the variability of the final detachment. We computed the corresponding value of Lc (see Methods) for each point of the *F–D* curves, to compare the Lc histograms for the selected curves from the CNGA1 channel (Fig. 1h in red) and for the curves from the construct CNGA1-N2B-HisTag (Fig. 1h in black). When the Lc histogram that was obtained from the construct CNGA1-N2B-HisTag is shifted by 85 nm (the closeness between the two sets of *F–D* curves was quantified using the inter-cluster similarity described in Methods), the histogram of Lc values at force peaks from the CNGA1 channels has five common peaks (Fig. 1i).

We performed SMFS in the open state (Fig. 2), to determine the conformational changes that occur upon gating[19,33,34]. Clustering procedures identified two major groups of *F–D* curves that were found only from membranes extracted from injected oocytes. The last force peak of the first cluster (Cluster 1-OS) had an Lc of < 300 nm (blue curves in Fig. 2a), which was similar to that for Cluster 1-CS (Fig. 1f). However, we found another cluster (Cluster 2-OS) of *F–D* curves in which the last force peak had an Lc that was > 350 nm (cyan curves in Fig. 2a); these curves appeared to be the sequential unfolding of the longer protein. The use of the N2B fingerprint (green curves in Fig. 2a) validated that Cluster 1-OS resulted from the unfolding of a single CNGA1 channel and suggested that Cluster 2-OS was obtained from the unfolding of two CNGA1 channel subunits that interact via the N-terminal of one subunit and the C-terminal of its neighbour[49,50]. The Lc histogram from the *F–D* curves of these two clusters superimpose very precisely up to 250 nm (Supplementary Fig. 6a). We found other *F–D* curves that could be ascribed to the unfolding of CNGA1 channels in the open state (Fig. 2b) when we used Cluster 1-OS as the template. Lc histograms that were obtained in both the closed and open states from the construct CNGA1-N2B-HisTag, and similar histograms that were shifted by 85 nm and obtained from the CNGA1 channels have common peaks (Fig. 2c). The histogram of the Lc that was obtained from the CNGA1 *F–D* curves in the open state has eight peaks (Fig. 2d) and was noticeably different from those obtained for the closed state (Figs 1i and 2d, and Supplementary Fig. 6b): first, there is a force peak with an Lc of
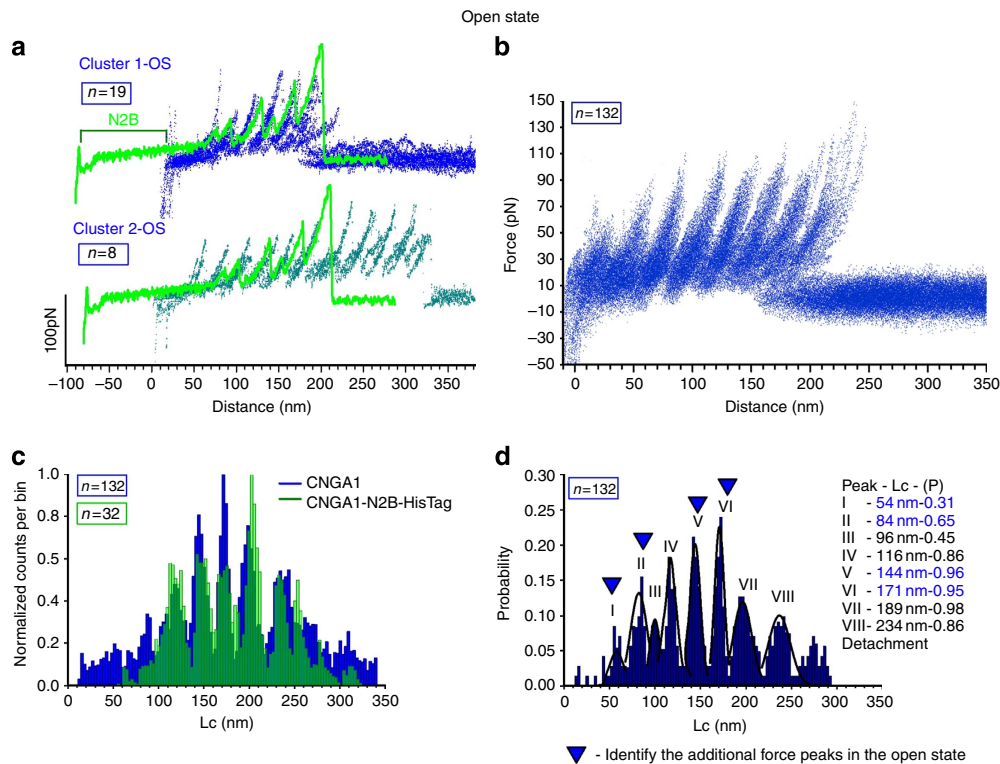

Figure 2 | Unfolding of CNGA1 and CNGA1-N2B-HisTag in the open state. (**a**) Example of *F–D* curves obtained from the unfolding of single CNGA1 (blue and cyan) and CNGA1-N2B-HisTag (green) constructs in the open state (19 curves for cluster 1-OS, 8 curves for cluster 2-OS and 1 curve for CNGA1-N2B-HisTag). The construct with N2B has an initial flat region of 85 nm, followed by peaks that correspond to the unfolding events that were observed in the CNGA1 construct. (**b**) Superimposition of 132 *F–D* curves that were obtained from injected oocytes in the open state using the curves of Cluster 1-OS as a template. (**c**) Superimposition of the histograms of normalized counts/bin against Lc from the *F–D* curves of **b** (blue) and 32 *F–D* curves from the CNGA1-N2B-HisTag (green) constructs in the open state. (**d**) Histogram of Lc values of force peak (with Gaussian fit for the different peaks) from the *F–D* curves in **d** with eight peaks located at 54 ± 3 (mean ± s.d., *n* = 41), 84 ± 3 (mean ± s.d., *n* = 86), 96 ± 3 (mean ± s.d., *n* = 59), 116 ± 3 (mean ± s.d., *n* = 114), 144 ± 3 (mean ± s.d., *n* = 132), 171 ± 3 (mean ± s.d., *n* = 132), 189 ± 5 (mean ± s.d., *n* = 132), 234 ± 6 (mean ± s.d., *n* = 132) nm and the detachment; the probabilities of the unfolding are 0.31, 0.65, 0.45, 0.86, 0.96, 0.95, 0.98 and 0.86, respectively.

84 ± 3 nm (mean $\pm$ s.d., $n = 85$) and a mean force of 60 ± 15 pN (mean $\pm$ s.d., $n = 85$), which was rarely observed in the Lc histogram that was obtained from the closed state channel. Second, the force peak with an Lc of 159 ± 3 nm (50 ± 12 pN) (mean $\pm$ s.d., $n = 149$) that was observed from the closed state channel is replaced by two force peaks with Lc values of 144 ± 3 nm (mean force of 65 ± 22 pN) (mean $\pm$ s.d., $n = 126$) and 171 ± 3 nm (mean force of 80 ± 18 pN) (mean $\pm$ s.d., $n = 126$). All the other force peaks that are present in the closed state are also observed in the open state (Supplementary Figs 6b and 7).

For a further validation of the identification of F–D curves of Figs 1 and 2 as obtained from the unfolding of CNGA1 channels, we performed SMFS on the CNGA1–CNGA1 tandem[51] construct (Supplementary Fig. 8 and Supplementary Note 3) and the F380C construct[52] (Supplementary Fig. 9 and Supplementary Note 4). The results of the experiments with the CNGA1–CNGA1 tandem show that in the open state CNGA1 channels can be unfolded as a sequence of two linked subunits. The unique repetitive unfolding pattern of the F–D curves obtained from identical experiments also confirms that the F–D curves of Figs 1 and 2 represent the unfolding of the CNGA1 channel from the C-terminal end in the closed and open states, respectively. In the open state, the mutant channel F380C is known to form a disulfide bond between the exogenous C380 and the endogenous C314 (ref. 52), and the F–D curves obtained from its unfolding are expected to be 26.4 nm shorter than those obtained from the CNGA1 channels, in agreement with the experimentally observed gap of 26 ± 2 nm (mean $\pm$ s.d., $n = 28$; Supplementary Fig. 9).

The comparison of the F–D curves of Figs 1 and 2 also demonstrates that the unfolding pathway of CNGA1 channels is different in the open and closed states, and that the unfolding of CNGA1 channels in the open state is characterized by the presence of three additional peaks.

Identification of the cytoplasmic domain. The Lc histograms in the closed (Fig. 1) and open (Fig. 2) states show force peaks with values of Lc ranging from 50 to 250 nm. It is important to identify the part of the F–D curves that corresponds to the unfolding of the cytoplasmic and transmembrane domains. This question can be answered by having F–D curves that represent the unfolding of only the cytoplasmic domain of CNGA1 channels in which the extracellular loop of S6 is strongly anchored to the substrate and the other portion of the transmembrane domain cannot be unfolded (Fig. 3a,b). Therefore, we constructed the mutant channel P366C-HisTag, in which we inserted a cysteine at position P366 on the extracellular loop of S6 (ref. 28). If this exogenous cysteine forms a covalent bond with a gold substrate—with a breaking force of 1.4 nN (ref. 53)—the transmembrane domain cannot be unfolded, and only the region from D690 to P366 will be unfolded, corresponding to ~ 130 nm (Fig. 3c). To identify these shorter F–D curves, we inserted a fingerprint at the C-terminal end of the mutant channel P366C; this finger was composed of two I27 modules[1,46,54] and we performed SMFS experiments with the construct P366C-(I27)$_2$-HisTag. If the cantilever tip attaches to the HisTag and because CNGA1 unfolds with forces below 200 pN, we expect[4] to unfold initially the cytoplasmic domain and S6 from D690 up to P366 and then the two I27 modules (Fig. 3a,b).

We found that many of F–D curves obtained from membranes extracted from oocytes injected with the construct P366C-(I27)$_2$-HisTag exhibited the expected fingerprint (Fig. 3b and black curve in Fig. 3c). In the closed state, we observed a force peak with an Lc of 96 ± 3 nm (mean $\pm$ s.d., $n = 117$; curve I in Fig. 3d). In the open state, we observed two additional force peaks with Lc values of 54 ± 3 (mean $\pm$ s.d., $n = 41$) and 84 ± 3 nm (mean $\pm$ s.d.,

$n = 86$; curves III and IV, respectively, in Fig. 3d). All these force peaks were observed in CNGA1 channels (red and blue curves in Fig. 3d) and in the construct P366C-(I27)$_2$-HisTag (black and green curves in Fig. 3d). In the closed state, the F–D curves from the construct P366C-HisTag (cyan curve in Fig. 3c) had two peaks with Lc values of 96 ± 3 (mean $\pm$ s.d., $n = 18$) and 116 ± 3 nm (mean $\pm$ s.d., $n = 18$), followed by a detachment. For both constructs, these features were preceded by a less frequent and lower force peak with an Lc that varied between 80 and 100 nm (Fig. 3e). When the same experiments were repeated in the open state, the force peaks had similar values for both the CNGA1 channel and the construct P366C-(I27)$_2$-HisTag (Fig. 3f). The F–D curves for the P366C-(I27)$_2$-HisTag and CNGA1 constructs can be closely superimposed for the portions of the curve up to the force peaks with Lc values of 116 ± 3 nm in both the closed and open states, which indicates that the cytoplasmic domain of the CNGA1 channels unfolds before the transmembrane segments S1–S6. These results show that the portion of the F–D curves with tip-sample separation (TSS) values < 116 nm (corresponding to ~ 290 a.a.) represents the unfolding of the cytoplasmic domain comprising both the CNB domain and the C-linker (from D690 to N400). The assignment of force peaks, in this region of the F–D curves, to the unfolding of specific molecular domains is more difficult.

Conformational changes upon gating in the cytoplasmic domain. Our results indicate three conformational changes that occur in three regions upon gating in CNGA1 channels: the cytoplasmic domain, the transmembrane domain and at the C and N termini. The assignment of the secondary structure of CNGA1 channels corresponding to the observed force peaks in the closed and open states (Figs 1 and 2) is reported in Fig. 4.

The unfolding of the cytoplasmic segment up to an Lc of 80 nm in the closed state usually requires forces below 25–35 pN, consistent with the notion that these domains do not have a well-defined conformation[30] and with their problematic crystallization[31,35–37]. In the open state, there is a peak, which appears with a probability of ~ 0.31, that has an Lc of 54 ± 3 nm (mean $\pm$ s.d., $n = 41$) with a force of 55 ± 10 pN (mean $\pm$ s.d., $n = 41$); this peak is either absent or present with a very low force in the closed state. The force peak with an Lc of 84 ± 3 nm (mean $\pm$ s.d., $n = 86$), a force of 60 ± 15 pN (mean $\pm$ s.d., $n = 86$) and probability of 0.65 is only present in the open state, whereas the force peak with an Lc of 96 ± 3 nm (mean $\pm$ s.d., $n = 117$) is present both in the open and closed states with a probability of 0.45 and 0.75, respectively.

Conformational changes upon gating in the membrane domain. The force peaks with an Lc between 120 and 250 nm appear with a probability close to 1 and correspond to the unfolding of the transmembrane domains that unfold sequentially according to the a.a. sequence of the protein[3,55], with force peaks corresponding to unstructured regions, such as the connecting loops[11]; these force peaks can be reliably assigned to specific domains of CNGA1 channels (Fig. 5a,b).

In the closed state (Fig. 5a,b), three peaks with Lc equal to 159 ± 3 (mean $\pm$ s.d., $n = 157$), 189 ± 3 (mean $\pm$ s.d., $n = 157$) and 234 ± 3 nm (mean $\pm$ s.d., $n = 157$) are observed requiring forces varying between 50 and 60 pN (Fig. 1 and Supplementary Fig. 7). The peak at 159 ± 3 nm (mean $\pm$ s.d., $n = 157$) corresponds to the unfolding of S6-P-helix-S5 segments (S399-L301) followed by an unstructured loop (N300-N291) that causes a drop in the pulling force; the second peak at 189 ± 3 nm (mean $\pm$ s.d., $n = 157$) corresponds to the unfolding of S4 and S3 (N291-V215), and the last peak at 234 ± 3 nm (mean $\pm$ s.d., $n = 157$)—before
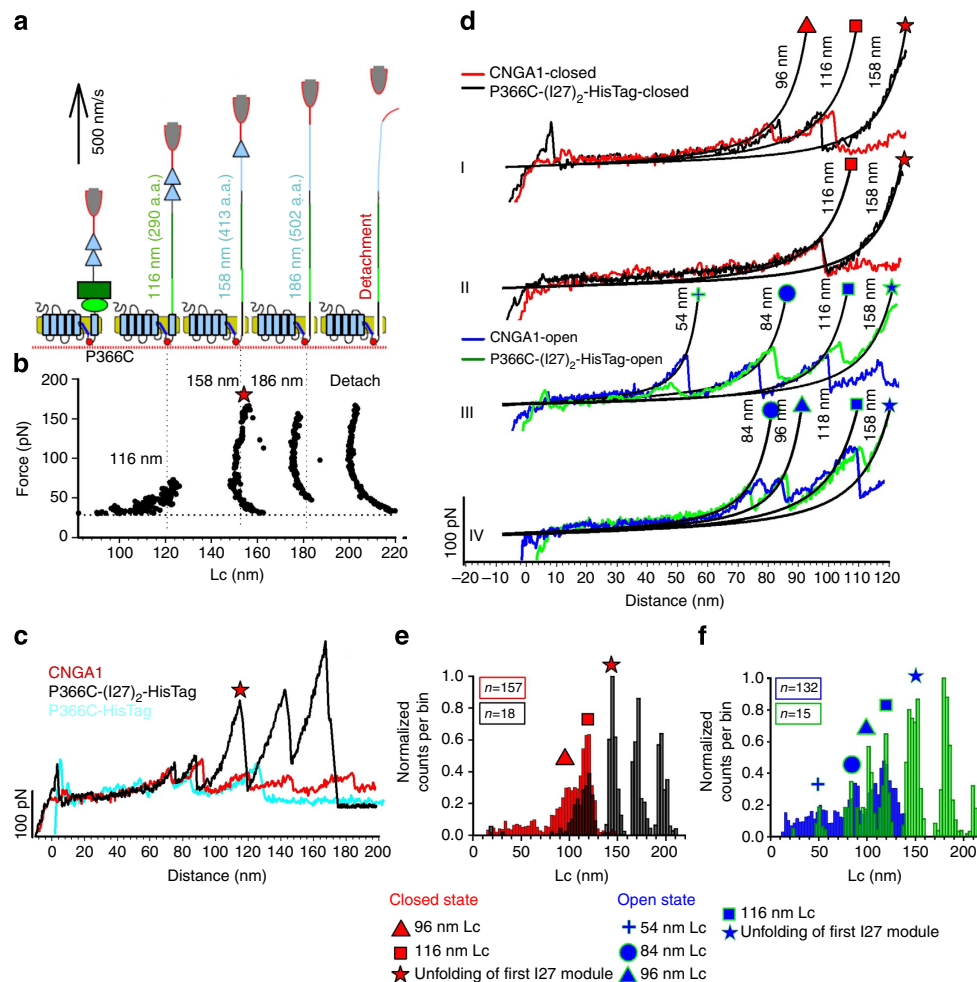
Figure 3 | Unfolding of CNB domain. (**a**) Schematic representation of the unfolding sequence, with the expected Lc values and the relative a.a. length in parenthesis and single module of I27 (cyan triangle), CNB domain (green rectangle), C-linker (green oval), transmembrane domains (cyan rectangles) and mutation P366C (red dots). (**b**) (F,Lc) plot from a typical curve of P366C-(I27)$_2$-HisTag. The finger print is composed by two force peaks of ~ 200 pN separated by ~ 28 nm with the detachment peak, with a value of Lc corresponding to unfolding of the cytoplasmic domain from D690 to P366 and the two I27 modules (that is, $(D690 - P366) \cdot 0.4$ nm $+ 2 \cdot 28$ nm) $= 186$ nm. (**c**) Superimposition of the F–D curves of CNGA1 (red), P366C-HisTag (cyan) and P366C-(I27)$_2$-HisTag (black). The F–D curves from the construct P366C-HisTag are shorter than those from CNGA1 and have a detachment event at 120–140 nm. Force peaks with Lc values at 96 and 116 nm are present in the F–D curves from the CNGA1, P366C-HisTag and P366C-(I27)$_2$-HisTag constructs. (**d**) Different unfolding pathways in the open and closed states; I and II: superposition of the F–D curves from CNGA1 channels (red) and from the construct P366C-(I27)$_2$-HisTag (black) in the closed state. In I, there are two force peaks with Lc values of 96 and 116 nm, but there is only one force peak in II; III and IV: superposition of the F–D curves from CNGA1 channels (blue) and from the constructs P366C-(I27)$_2$-HisTag (green) in the open state. In III there are three force peaks with Lc values of 54, 84 and 116 nm, and in IV there are three force peaks with Lc values of 84, 96 and 118 nm. The force peak with an Lc of 158 is only present in the construct P366C-(I27)$_2$-HisTag. (**e**) Superimposition of histograms of normalized counts/bin against Lc from the F–D curves obtained from P366C-(I27)$_2$-HisTag (black) and from CNGA1 channels (red) in the closed state (**f**) same as in **e** for P366C-(I27)$_2$-HisTag (green) and from CNGA1 channels (blue) in the open state. The data in **e,f** are from CNGA1 channels as described in Figs 1 and 2.

detachment—corresponds to the unfolding of S2 and S1 (R216-E100). The force peak that has an Lc of 159 ± 3 nm (mean $\pm$ s.d., $n = 157$) for the closed state (corresponding to a residue near P293) splits into two force peaks for the open state with Lc of 144 ± 3 (mean $\pm$ s.d., $n = 132$) (~ 360 a.a.) and 171 ± 3 (mean $\pm$ s.d., $n = 132$) (~ 428 a.a.) nm; these peaks have higher forces of 65 ± 22 (mean $\pm$ s.d., $n = 132$) and 80 ± 18 pN (mean $\pm$ s.d., $n = 132$), respectively (Figs 2 and 5a, and Supplementary Fig. 7). This splitting reveals an important conformational change in the transmembrane domain that could be controlled by the S4–S5 linker via the helix-breaker proline P293: in the open state, the unfolding of S6-P-helix-S5 occurs in two steps. The first step consists of the unfolding of S6 and the P-helix (V348-S399); this unfolding is followed by a drop in the force at an unstructured loop (F325-Y347). In the second step, S5

is unfolded together with S4 (Y265-F324). Therefore, in the open state S5 is mechanically coupled to S4, whereas in the closed state S5 is more strongly connected to the P-helix and S6, as suggested by the obtained F–D curves (Fig. 5b).

Homology modelling of the structure of CNGA1 channels based on the Kv1.2 channel[56,57] and the use of an improved algorithm for predicting α-helix folding suggest that the stretch of a.a. from Y265 to F324, corresponding to the region comprising the S4 and S5 transmembrane domains, has a good propensity to have an α-helix fold and the three-dimensional (3D) structure is shown in Fig. 5c (inset). To validate this interpretation of the SMFS data (Figs 4 and 5a,b), we performed electrophysiological experiments using CNGA1 mutant channels with the following rationale: if S4 in the open state is mechanically coupled by the S4–S5 linker to S5 (Fig. 5c), point mutations in the S4–S5 linker

Feature key	Description	Secondary structure	Polypeptide segment	Length (a.a.)	Average Lc ± s.d. (nm)[a]		ΔLC (nm (a.a.))[b]		Average unfolding force ± s.d. (pN)[c]	
					Closed	Open	Closed	Open	Closed	Open
Topological domain	Cytoplasmic*	C terminal	D690 - I611	80						
Binding site	Cytoplasmic CNBD*	Helix C	N610 - D588	23						
		Helix B	E585 - K576	10		54±3		54 (135)		55±10
		β Strands 7, 8	S575 - I562	14		87±3		31 (78)		60±15
		Helix P	N549 - I545	5						
		β Strands 1 – 6	F542 -Q494	49						
		Helix A	V490 - A483	8	96±3	96±3	96 (240)	10 (25)	55±15	65±15
C-linker	Cytoplasmic (C-linker)*	Helices A' - F'	E482 - N400	83	116(N400)±3	116(N400)±3	20 (50)	17 (43)	60±16	60±17
Transmembrane	Helical	Helix S6	S399 -F375	29						
Pore region	Extracellular	Selectivity filter	T359-P367	9						
		P-helix	L358-V348	11						
		Loop P-helix-S5	Y347-F325	23		144(W330)±3		28 (70)		65±22
Transmembrane	Helical	Helix S5	F324-I298	27						
Topological domain	Cytoplasmic	Loop S5-S4	R297-E287	11	159(P293)±3		43 (108)		50±12	
Transmembrane	Helical	Helix S4	T286-Y265	22						
Topological domain	Extracellular	Loop S4-S3	Y264-Y258	7		171(G262)±3		27 (68)		80±18
Transmembrane	Helical	Helix S3	L257-Y238	20						
Topological domain	Cytoplasmic	Loop S3-S2	K237-R216	22	189(R218)±5	189(R218)±5	30 (75)	18 (45)	55±15	85±20
Transmembrane	Helical	Helix S2	V215-Y197	19						
Topological domain	Extracellular	Loop S2-S1	E196-R184	13						
Transmembrane	Helical	Helix S1	A183-Y163	21	234(K105)±6	234(K105)±6	45 (113)	45 (113)	60±18	80±28
Topological domain	Cytoplasmic	N Terminal	Y162-M1	162	273(T8)±7	276(M1)±9	39(98)	42 (105)	80±30	90±30

Figure 4 | Assignment of secondary structure and different domains of CNGA1 channels to the observed force peaks in the closed and open states. The first and second columns show the key features of the functional domains identified in CNGA1 channels according to the available literature[23-30]; the third column reports the presumed secondary structure[17,31]; the fourth and fifth columns contain the corresponding polypeptide segments and the associated a.a. number; the remaining columns indicate the Lc, ΔLc and force values of the corresponding force peaks in the closed and open states. The length and the polypeptide segments are obtained from the results of Figs 1 and 2. The number of a.a. for the transmembrane domains has been calculated by considering the membrane thickness ($\sim$5 nm or $\sim$13 a.a.)[3,44]. The initial and final a.a. of each polypeptide segment are only indicative (**a**) average Lc values of the force peaks with s.d. in nanometres, with the number inside the brackets representing the average position of the force peaks in the a.a. sequence. (**b**) Average ΔLc in nanometres and the corresponding number of a.a. (in brackets). (**c**) Average value of the unfolding force with the corresponding s.d. in pN. *The unfolding of the cytoplasmic segments in the C-terminal cannot be exactly determined.

are expected to propagate to the pore region and affect ionic permeation in the open state. We have identified a specific residue in the S4–S5 linker that corresponds to a conserved proline (P293 in the CNGA1 channel), which—when inserted into an α-helix— is expected to modify the ideal helical structure; therefore, we constructed the mutant channel P293A, in which P293 is substituted by the α-helix-forming alanine. It is well known that CNGA1 channels do not inactivate[21], that is, no time-dependent inactivation in the cGMP-activated current is observed, neither in the presence of small permeant cations such as Na^+ nor in the presence of larger organic cations such as ethylammonium (EA^+). In the mutant channel P293A (Fig. 5c), the cGMP-activated current inactivated depending on the voltage

in the presence of EA^+ (green traces); however, in the presence of Na^+ (black traces) there was no inactivation of the current both at positive and negative voltage, indicating that mutations in the S4–S5 linker affect ionic permeation and therefore, validating the notion that in the open state, the S4–S5 linker is mechanically coupled to the pore region. To better analyse the role of this proline, we performed SMFS experiments with the mutant channel P293A as well (Fig. 5d,e). In the closed state, the force peak with Lc around 159 nm is not present in the majority (about 80%) of F–D curves as evident from the comparison of F–D curves (Fig. 5d) and the histograms (Fig. 5e) of the CNGA1 channels (red) and mutant channels P293A (green). The absence of the force peak at 159 nm in the mutant channel P293A strongly
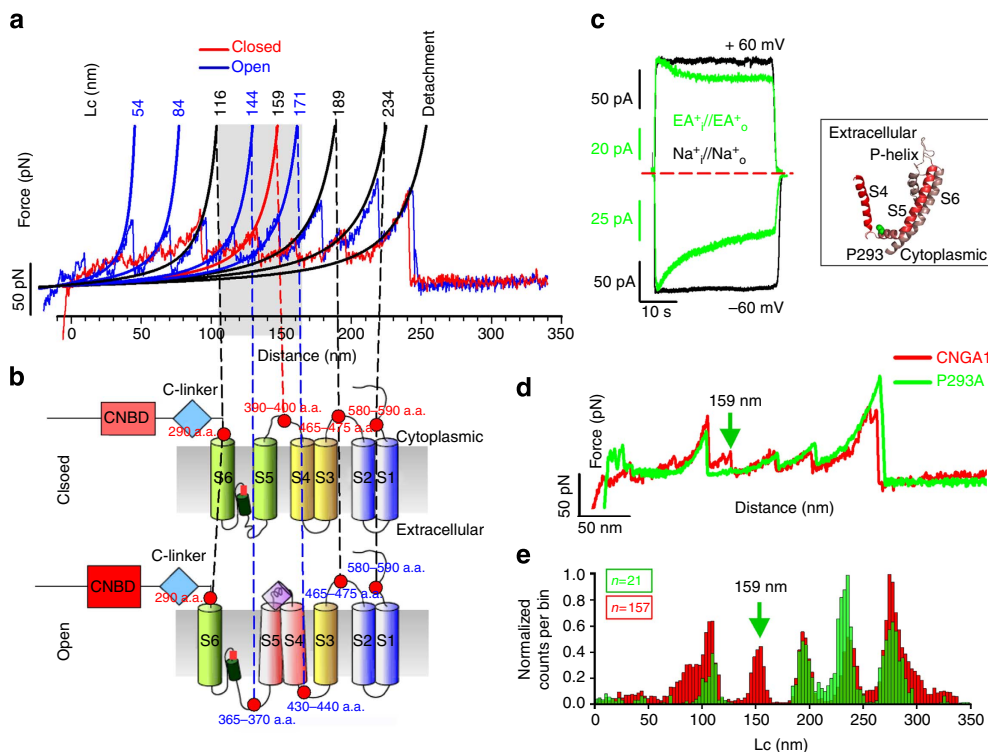
Figure 5 | Conformational changes in the transmembrane domain during the gating of CNGA1 channels. (**a**) Superposition of two representative *F–D* curves of CNGA1 channels in the closed (red) and open (blue) states. Continuous black lines obtained from the fitting with WLC model. Numbers indicate the corresponding values of Lc. (**b**) Schematic representation of hypothesized interactions between the transmembrane helices in the closed and open states. Red dots indicate the approximate location of the force peaks and the numbers of the corresponding a.a. (**c**) Electrophysiological recordings from mutant channel P293A in the presence of Na$^+$ (black) and ethylammonium (EA$^+$) (green) at ± 60 mV. In the black box, the homology model of the S4 and S6 transmembrane domains of the CNGA1 channel based on the molecular structure of the Kv1.2 channel; the conserved P293 is indicated in green. (**d**) Superposition of two representative *F–D* curves for the CNGA1 channel (red) and for the P293A (green), both in the closed state. The green arrow, corresponding to the value of Lc = 159 nm, indicates the differences between the two constructs. (**e**) Superimposition of histograms of normalized counts/bin against Lc from the 157 *F–D* curves of CNGA1 (red, the same as in Fig. 1h) and 21 *F–D* curves from mutant channel P293A in the closed state (green), both in the closed state. Arrow as in **d**.

suggests that S6, S5, S4 and S3 in this mutant channel, in the closed state, are mechanically coupled and unfold together, validating the notion that P293 is an α-helix breaker.

The determination of the exact value of Lc for a given force peak is limited by the shift (< ± 5 nm) used to align different *F–D* curves (Figs 1 and 2). This limitation is circumvented when the increase in contour length (ΔLc) is measured. ΔLc is a structural parameter determined by the number of a.a. residues involved in the folded structure[58], providing information on the kinetic barriers for the unfolding as well[10]. We have analysed the variability of the ΔLc between the force peaks with Lc values around 159–189 nm, corresponding to the unfolding of S4 and S3 in the closed state (ΔLc$_{closed(3/4)}$) and the variability of the ΔLc between the force peaks with Lc values around 171–189 nm, corresponding to the unfolding of S3 in the open state (ΔLc$_{open(3)}$). We have also computed the sum of ΔLc corresponding to the unfolding of all the transmembrane domains from S6 to S1 in the closed (ΣΔLc$_{closed(TM)}$) and open (ΣΔLc$_{open(TM)}$) state.

The distribution of ΔLc$_{closed(3/4)}$ has three distinct peaks, corresponding to the stretching of a different number of a.a. (Fig. 6a–c) that have a similar unfolding force (that is, same mechanical stability). The unfolding with a ΔLc of 26 nm occurs with a low probability (14%) and corresponds to the unfolding of S3 and S4 from approximately P293 up to E230 (Fig. 5d). The most probable (77%) unfolding of S3 and S4 occurs with a longer ΔLc of 34 nm from approximately P293 up to R218. In this case,

residues from E230 to R218 are mechanically coupled to S3, possibly being part of the α-helix-forming S3 (Fig. 6e). The unfolding with a ΔLc of 50 nm occurs with a lowest probability (9%) and corresponds presumably to the unfolding of S2 and S4 from approximately P293 up to T170 (Fig. 6f). In this case, S2 appears to be mechanically coupled to S4 and S3, suggesting that the connecting loop between S2 and S3 acts as a rigid handle and possibly forms a short α-helix. The distribution of ΣΔLc$_{closed(TM)}$ has several peaks at about 113, 123 and 131 nm (Fig. 6g,h), indicating a significant variability of the unfolding of the entire transmembrane domain. This variability is likely to originate from the unfolding of folded and partially folded α-helices forming the transmembrane domain[58]. Similar results were obtained when we analysed *F–D* curves obtained in the open state (Fig. 7) of CNGA1 channels. The distribution of ΔLc$_{open(3/4)}$ has distinct peaks, corresponding to the stretching of a different number of a.a. (Fig. 7a,b) and the unfolding with the two different ΔLc (Fig. 7c,d) occurs with a probability of 61% and 34%, respectively. The distribution of ΣΔLc$_{open(TM)}$ has two peaks (Fig. 7e,f), indicating a variability of the unfolding of the entire transmembrane domain. These results (Figs 5–7) show that the transmembrane α-helices S2, S3, S4 and S5 have a variable mechanical coupling, and that this coupling differs in the closed and open states.

In the open state the force necessary to unfold the transmembrane domain varies between 65 and 85 pN, whereas in the close state this force varies between 50 and 60 pN (Figs 1
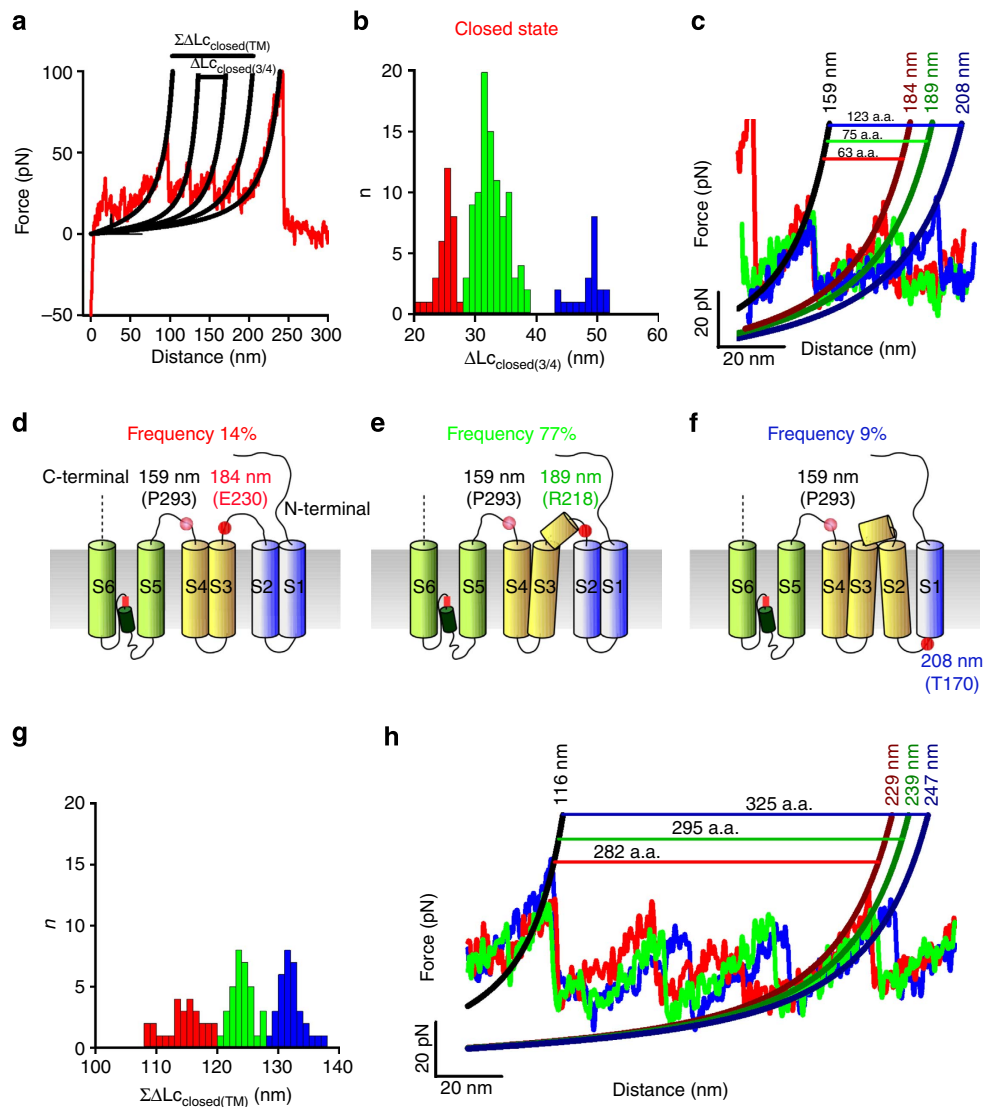
Figure 6 | Variability of the unfolding of the transmembrane segments in the closed state. (**a**) A representative *F–D* curve in the closed state (the same as in Fig. 5a). Continuous black lines obtained from the fitting with WLC model. Horizontal lines indicate the corresponding values of ΔLc and $\Sigma\Delta Lc$. (**b**) Histogram of $\Delta Lc_{closed(3/4)}$ (bin 2 nm) in the closed state between the force peaks with Lc values around 159 to 189 nm. Colours correspond to different clusters of *F–D* curves with values of $\Delta Lc_{closed(3/4)}$ around 26, 34 and 50 nm. (**c**) Superposition of representative *F–D* curves of the three clusters of **b** and the relative number of stretched a.a. (**d–f**) Schematic representation of the corresponding unfolding pathways. Small red dots or circles indicate the position of the force peaks, and the number is the corresponding value of Lc. The a.a. that presumably corresponds to the force peak is also indicated. (**g**) $\Sigma\Delta Lc_{closed(TM)}$ histogram (bin 1 nm) in the closed state for the force peaks as in **a** with values around 113, 123 and 131 nm. (**h**) Superposition of representative *F–D* curves of the three clusters of **g** and the relative number of stretched a.a.

and 2, and Supplementary Fig. 7). This difference in the unfolding force was observed when CNGA1 channels were fused with the N2B fingerprint and in the CNGA1–CNGA1 tandem construct. The force necessary to unfold the transmembrane segments of other membrane proteins increases upon the binding of the appropriate ligands[13], and the observed increase in the unfolding force is comparable to the force observed in CNGA1 channels. In β2-adrenergic receptors, ligand binding is thought to change the conformational and mechanical properties of the transmembrane segments of the receptor itself[13]. The breaking of a single H-bond requires a force of ~4 pN (refs 8,59), whereas the breaking of a single hydrophobic bond requires ~30 pN (refs 8,53) and breaking a single noncovalent bond requires a larger force of ~160 pN (refs 8,53). Therefore, the observed increase in the force necessary to unfold the transmembrane domain in the open state can be accounted for by the establishment of some H-bonds and/

or of one or two additional hydrophobic interactions. Another possibility is that in the open state, more residues are folded as α-helices, such as the residues in the loop connecting S4 and S5.

Discussion

We have performed SMFS experiments to recover structural information about CNGA1 channels in a physiological-like environment, thus avoiding purification and reconstitution into lipid bilayers. *F–D* curves obtained from the unfolding of CNGA1 channels expressed in *X. laevis* oocytes were identified using bioinformatics analysis validated by the N2B and I27 fingerprints, and were corroborated by experiments with CNGA1–CNGA1 tandem constructs and with the mutant channel F380C. Presented results provide new insights on the function of CNGA1 channels and show that S4 in the closed state is mechanically
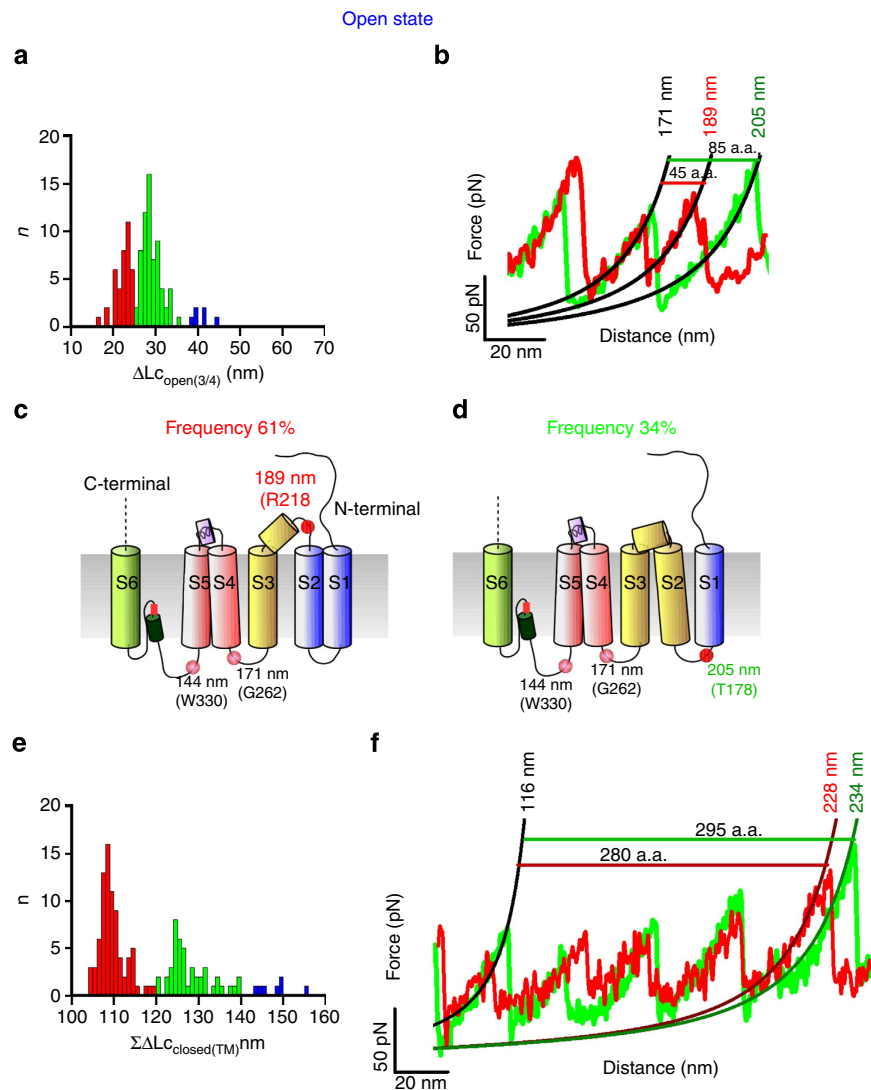
Figure 7 | Variability of the unfolding of the transmembrane segments in the open state. (**a**) Histogram of $\Delta Lc_{open(3/4)}$ (bin 2 nm) in the open state. (**b**) Superposition of representative F–D curves of the two clusters of **a** and the related number of stretched a.a. (**c,d**) Schematic representation of the corresponding unfolding pathways. Small red dots or circles indicate the position of the force peaks and the number is the corresponding value of Lc. The a.a. that presumably corresponds to the force peak is also indicated. (**e**) $\Sigma\Delta Lc_{open(TM)}$ histogram (bin 1 nm) in the open state. (**f**) Superposition of representative F–D curves of the two clusters of **e** and the related number of stretched a.a.

coupled to S3, but in the open state is mechanically coupled to S5. P293 in the S4–S5 linker and G262 in the loop connecting S3 and S4 could be the hinges regulating the mechanical coupling between these α-helices.

SMFS experiments also reveal a significant variability in the unfolding of the transmembrane domains (Fig. 6). This variability can originate from the existence of multiple unfolding pathways[10,14,58] and/or from the existence of different initial conformations[10,14,58]. The variability of $\Sigma\Delta Lc_{(TM)}$ (see Fig. 6) can be explained if the α-helices of the transmembrane domain can be properly folded but also partially folded, suggesting that these α-helices are highly dynamic and do not have a fixed mechanical stability and folding[10,14,58].

SMFS experiments can detect changes in the interactions of proteins that are not necessarily associated with changes in the secondary structure[60,61], and for a proper interpretation of the changes in the portion of the F–D curves (Fig. 3) corresponding to the cytoplasmic domain, we have used additional experimental insight from nuclear magnetic resonance and X-ray approaches

(Fig. 4). The unfolding of the cytoplasmic segment up to an Lc of 80 nm in the closed state requires forces below 25–35 pN, consistent with the notion that these domains do not have a well-defined conformation[30]. If the cytoplasmic domain of CNG channels does not have a well-defined 3D structure, it will be difficult to crystallize[31,35–37], in agreement with the recent AFM imaging of the CNB domain of the of MlotiK1 potassium channels, which has a tetrameric well-defined structure only in the presence of cyclic nucleotides[32]. The 3D structure of the CNB domain of HCN channels has been determined in the presence of cAMP by X-ray crystallography[31,37] and in the absence of cyclic nucleotide by nuclear magnetic resonance spectroscopy[36]. The comparison of these structures shows that in the absence of cyclic nucleotides some α-helices are either not folded or only partially folded. Therefore, the force peak with an Lc of 54 ± 3 nm (mean ± s.d., $n = 41$) (∼135 a.a.) present in the open state (Figs 2 and 5) with a force larger than that seen in the closed state could correspond to the unfolding of α-helices in the CNB domain of CNGA1 channels, possibly the C (23 a.a.) and B (10 a.a.) helices,

not folded in the absence of cGMP[30]. The force peak seen only in the open state with an Lc of 84 ± 3 nm (mean ± s.d., $n = 86$; Figs 2 and 4) could correspond to some other conformational change associated to tetramerization of the CNB domain[37]. However, these experiments do not allow us to distinguish between a tetramer and a dimer of dimers. The force peak at 116 nm (Figs 1, 2 and 5) corresponding to ~290 a.a. corresponds to the complete unfolding of C-termini till the end of S6 (a.a. 400).

In the closed state, some F–D curves terminate with a force peak with an Lc of 234 nm, but other F–D curves have an additional force peak with an Lc of ~276 nm (Fig. 1f), which exactly correspond to 690 a.a. (276 nm/0.4 nm = 690 a.a., that is, the total length of CNGA1 channels). Nonetheless, all these F–D curves are very similar before the force peak with an Lc of ~234 nm. If the N-terminal does not interact with the C-terminal of a neighbouring subunit or with other domains of the same subunit, detachment of the cantilever tip can occur simultaneously with the unfolding of S1; however, without N-terminal interactions, an additional pull is required for the final detachment. Some of the F–D curves obtained in the open state were longer (Fig. 2a,b) and the force peaks appeared to be replicated, suggesting that these curves do not correspond to the unfolding of a single CNGA1 subunit but instead represent the unfolding of two interacting subunits. Indeed, in the open state, the N-terminal of one subunit strongly interacts with the C-terminal of a neighbouring subunit[49,50]; thus, two neighbouring subunits are almost linked together. Under these conditions, when the cantilever tip unfolds one CNGA1 subunit, an additional subunit can subsequently be unfolded. Therefore, our results indicate a possible interaction between the N- and C-termini in the closed state and this interaction is clearly potentiated in the open state. In the open state, we never observed 'duplicated' F–D curves when pulling with the constructs CNGA1-N2B-HisTag, because in these constructs the added domains do not allow the N- and C-termini to interact as they do in the CNGA1 channels. The interaction between the C- and N-termini in the open state can also explain the lower success of SMFS at obtaining good and complete F–D curves (Fig. 5), because the cantilever tip has limited access to the C-terminal.

Which is the possible molecular mechanism underlying the gating of CNGA1 channels? The results presented here and previous experimental observations suggest a more accurate view of the molecular mechanism underlying gating. Upon the binding of cGMP to the CNB domain that is almost located at the C-terminal end of CNGA1 channels, several conformational changes occur in the cytoplasmic domain, the transmembrane domain, and the C- and N-termini. The structural information obtained in the present investigation and in similar ion channels, such as the K, HCN and MlotiK1 potassium channels[31,32], provides a better picture of the gating in CNG channels. Upon the binding of cGMP, the entire cytoplasmic domain acquires a more structured conformation[30], either as a dimer of dimers[30,35,62] or as a tetramer[63]. Similar to the observations in MlotiK1 potassium channels[64], the cytoplasmic domain of CNGA1 could move vertically towards the membrane and could induce rotations, vertical shifts and tilts of the S5 and S6 transmembrane domains[24,27], leading to widening of the filter region, where the gate is located[26,28].

The S4–S5 linker of CNGA1 channels is composed of 11 a.a., in which the α-helix breaker P293 is flanked on the right by predominantly hydrophobic residues and flanked on the left by predominantly hydrophilic residues[57], and the segment TNYP has a low propensity to be in an α-helical conformation[56]. Electrophysiological experiments with chimeric channels show that the C-linker interacts with the S4–S5 linker[57]. Therefore, we propose that in the closed state the cytoplasmic end of S4 is

unfolded, but in the open state it becomes an α-helix due to its interaction with the C-linker; this change increases the mechanical coupling between S5 and the voltage sensor in S4. As a consequence, CNGA1 channels acquire voltage gating in the open state, as recently shown when large cations such as Cs^+, methylammonium and dimethylammonium are the permeant ions[21]. A similar interaction between the cytoplasmic domain and the S4–S5 linker has been observed in CNG, Kv1.2 and hERG channels[57,65].

In summary, new insights on CNGA1 channels emerge from this analysis. The S4 domain is mechanically coupled to S3 in the closed state but to S5 in the open state (Fig. 5); moreover, there are multiple pathways for the unfolding of the transmembrane domain (Figs 6 and 7) and the degree of folding of α-helices forming the transmembrane domain varies (Fig. 6) possibly also assuming a 3_{10} helix conformation[66,67]. These experimental observations, obtained from SMFS, show that the transmembrane domain has a dynamical structure. Moreover, our results show that SMFS is a powerful tool for analysing ion channels, suggesting that the same approach combining SMFS with informatics, mutagenesis and fusion with known fingerprints can be used to study other ion channels and membrane proteins, and to detect their conformational changes at the single-molecule level and in a physiological-like environment.

Methods

Molecular biology and CNGA1 constructs. Eight different channel constructs (see Supplementary Fig. 1 and Supplementary Note 1) were cloned into the expression vector known as pGEM-HE[38]. The constructs are the CNGA1 channel cloned from bovine retinal rod photoreceptors, as previously described[17], which consists of 690 a.a. (here named the CNGA1 channel), the CNGA1 channel with a tag that is composed of six histidines (HisTag) at the C-terminal (CNGA1-HisTag), the CNGA1 with an N2B module (CNGA1-N2B-HisTag) and the CNGA1 with two I27 modules followed by the same tag [CNGA1-(I27)₂-HisTag]. The HisTag was used to increase the probability of a specific attachment between the protein and the functionalized cantilever tip, but because of the lower level of expression of the construct CNGA1-HisTag (Supplementary Fig. 1b), we used the construct CNGA1 without the HisTag. Nevertheless, the HisTag was used with the other constructs, because they had a higher level of expression (Supplementary Fig. 1). We used two fingerprints, the N2B module (the shortest titin isoform)[46–48] and two I27 modules (Ig module 27 of the I band of titin)[46,54], to differentiate the F–D curves that were obtained from the unfolding of the CNGA1 channels from those of native membrane proteins that were present in the oocyte plasma membrane. The N2B module is composed of 210 a.a. with the mechanical properties of a random coil unfolding that does not show any unfolding events[47,48]. The unfolding of the I27 modules (each 89 a.a. long) shows the characteristic sawtooth pattern, in which successive force peaks have an increase in contour length (ΔLc) of ~28 nm and amplitudes of ~200 pN. The CNGA1–CNGA1 tandem[51] construct was obtained using two identical CNGA1 subunits linked by a short 10 a.a. linker (GSGGTELGST) between the C-terminal end of the first subunit and the N-terminal end of the second subunit. The construct was generated by the insertion of one copy of the DNA coding for CNGA1 into a vector pGEMHE already containing another copy of DNA coding for CNGA1. The second subunit was made by replacing the ApaI restriction site (GGGCCC) at the end of CNGA1 without changing the a.a. (GGTCCC) and adding at the start codon a new ApaI restriction site followed by the linker, using a PCR reaction (Platinum Pfx DNA polymerase, Invitrogen). Subunits were linked after HindIII/ApaI cut using T4 DNA Ligase (Promega). We performed a point mutation in an exposed loop of the channel (P366C) (two constructs: P366C-HisTag and P366C-(I27)₂-HisTag), which is able to bind the gold surfaces used in our experiments. We also used two additional mutant channels: F380C and P293A. Single-residue mutagenesis was performed as described using the Quick Change Site-Directed Mutagenesis kit (Stratagene). Point mutations and cloning were confirmed by sequencing, using the sequencer LI-COR (4,000 l). The constructs CNGA1-N2B-HisTag and CNGA1-(I27)₂-HisTag were cloned by DNA2.0 (Menlo Park, CA) than subcloned in pGEMHE; in both cases the linker between the CNGA1 and the N2B or I27 was the same of the CNGA1–CNGA1 tandem and the restriction enzyme sites used for the cloning were HindIII/ApaI. Complementary DNAs were linearized with NheI and transcribed to RNA in vitro using the mMessage mMachine kit (Ambion, Austin, TX). All the restriction enzyme were from BioLabs (New England). The sequences for oligonucleotide primers and the sequences for the construct with N2B and I27 were included in the Supplementary Table 1.

Heterologous expression system and sample preparation. Purified RNA of the different constructs was injected into X. laevis oocytes ('Xenopus express' Ancienne

Ecole de Vernassal, Le Bourg 43270, Vernassal, Haute Loire, France). Oocytes were prepared as described[30]. *X. laevis* frogs were anaesthetized by immersion in a 0.2% aqueous solution of MS-222 (tricaine methanesulfonate) for ~20 min. The anaesthetized animal was put on its back on a box of ice and a small incision of about 1 cm was made with a scalpel, laterally on the abdomen. Once the skin and the underneath abdominal muscles were cut through, the ovarian lobes became visible. The follicle (oocytes and follicle cells) were surgically removed from the ovarian lobes and placed in a Barth solution containing the following (in mM): 88 NaCl, 1 KCl, 0.82 MgSO$_4$, 0.33 Ca(NO$_3$)$_2$, 0.41 CaCl$_2$, 2.4 NaHCO$_3$ and 5 TRIS-HCl (pH 7.4 buffered with NaOH). Follicles were separated in small groups and incubated for 1 h at 18 °C in a Barth solution without calcium, but supplemented with 1 mg ml^{-1} of collagenase. After this treatment, the residual follicle were removed manually with forceps. Selected oocytes were injected and maintained at 18 °C in a Barth solution that was supplemented with 0.05 mg ml^{-1} of gentamycin sulfate. Cells were incubated for 2–6 days. The vitelline membrane of oocytes was removed mechanically before the experiments. These oocytes were incubated on a freshly cleaved mica sheet (or on a gold surface) for 1–10 min in Standard solution (in mM) (110 NaCl, 10 HEPES and 0.2 EDTA; pH 7.4 buffered with NaOH) with or without 2 mM cGMP. We removed the cytoplasmic content (yolk and granules) using five to ten washings with the Standard solution after the membrane had been attached to the surface. The usual salts and reagents were purchased from Sigma-Aldrich (St Louis, MO, USA).

Electrophysiological recordings. The functionality of all constructs was verified by exposure to 2 mM cGMP (saturating concentration) and then recording the channel current using electrophysiological measurement in the excised patch configuration (see Supplementary Fig. 1a–g). cGMP-gated currents in a voltage-clamp condition were recorded using a patch-clamp amplifier (Axopatch 200, Axon Instruments Inc., Foster City, CA, USA) 2–6 days after RNA injection at room temperature (20–24 °C), using borosilicate glass pipettes with resistances of 2–5 MΩ. The perfusion system allowed a complete solution change in <1 s. During the experiments, oocytes were kept in Ringer's solution containing the following (in mM): 110 NaCl, 2.5 KCl, 1 CaCl$_2$, 1.6 MgCl$_2$ and 10 HEPES-NaOH (pH 7.4 buffered with NaOH). The Standard solution on both sides of the membrane consisted of (in mM) 110 NaCl, 10 HEPES and 0.2 EDTA (pH 7.4 buffered with NaOH). We used Clampex 10.0, Clampfit 10.1 and SigmaPlot 9.0 for data acquisition and analysis. Data are usually given as the mean ± s.e.m. We attempted SMFS only in oocytes in which the measured cGMP-activated current was larger than 1 nA at ± 100 mV.

AFM and cantilever functionalization. The NanoWizard 3 AFM system (JPK) and an inverted optical microscope (Olympus IX71) were used under liquid conditions in Standard solution with or without 2 mM cGMP. Rectangular silicon nitrite gold-coated cantilevers (HYDRA2R-50NGG from APPNANO) were functionalized and were used to localize plasma membrane patches and to perform SMFS experiments. For imaging of the membrane patch, the AFM system was operated in liquid using the tapping mode[44] with ~14 kHz as the operating frequency. The cantilever spring constant was ~0.08 N m^{-1} and was calculated before the start of each experiment by using the equipartition theorem. A 0.4 numerical aperture/ × 10 objective was used to localize the area of oocyte incubation. The scan rate for AFM imaging was kept between 1 and 0.5 Hz, depending on the image size (from 20 to 0.5 μm) and on the condition of each sample. AFM images were acquired with a resolution of 512 pixels. Cantilever tip functionalization was based on the thiol and nitrilotriacetic acid-Ni^{2+} specificity for gold and the HisTag, respectively[68,69]. Tips were first cleaned in ethanol for 15 min, dried under an N$_2$ flow and exposed to ultraviolet light for 15 min. The tips were further incubated for 5 min in chloroform and dried again under a N$_2$ flow. These three steps were repeated one more time to obtain cleaner tips. Cantilevers were then incubated for 30 min in 10 μM dithiobis-C$_2$-NTA (Dojingo Technologies, Japan), washed with ethanol and dried in a N$_2$ flow. The tips were then incubated for 20 min in 100 μM NiSO$_4$ and rinsed with MilliQ water before being dried in a N$_2$ flow. Finally, the functionalized tips were incubated for 20 min in 10 mM 6-mercapto-1-hexanol to avoid nonspecific adsorption and were dried under a N$_2$ flow. Salts and reagents were purchased from Sigma-Aldrich. To check the cantilever functionalization and activity of NTA, a control experiment was performed for each set of functionalized cantilevers. First, we performed an SMFS experiment on a polypeptide chain composed of eight modules of I27. The pulling efficiency was almost 10%, but in presence of 50, 100 and 200 mM imidazole the efficiency decreased to 1%, 0.5% and 0%, respectively (Supplementary Fig. 10).

SMFS experiments and data processing. SMFS experiments were performed using membrane extracted from injected oocytes expressing constructs at a high level (about 1,000–5,000 channels per μm^2) and in membrane extracted from uninjected oocytes as control. Oocytes were attached to a mica substrate or a gold surface (in case of cysteine mutant) and clean fragments of the membrane remained anchored to the substrate with the intracellular side exposed to the bathing medium and to the cantilever tip of the AFM. We used the AFM in liquid and in tapping mode[44] to image the membrane patches. We observed membrane patches that had a high or a low protrusion density in their surface patterns (Supplementary Fig. 1h,i). In both cases, as would be expected from a membrane

patch[44], structures emerging from the mica had a height of 4–6 nm. Membrane patches with a high protrusion level had additional peaks that were 2–3 nm in height (Supplementary Fig. 1i) and were taken as suitable samples for SMFS experiments.

After the localization of the membrane patch, we moved the AFM tip over the imaged area (usually 1–2 μm^2). Using the matrix scanning mode, the AFM tip was pushed into the surface with a contact force of 1 nN for 0.5 s, to give the protein a chance to adsorb on the stylus, and then retracted with a constant speed of 500 nm s^{-1}, while the force exerted between the tip and surface was recorded. In ~20% of the cases, the tip was able to adsorb a molecule, providing a sawtooth-like F–D curve, and if the magnitude of the force of these F–D curves was larger than 45 pN the curve was saved. In this manner, during an experimental session lasting up to 8–10 h, we collected ~10,000 F–D curves for each experimental session, and a total of ~200,000 and 300,000 F–D curves from membranes extracted from uninjected (control) oocytes in the presence and absence of cGMP, respectively; we also collected ~300,000 and 450,000 F–D curves from membranes extracted from oocytes injected with mRNA for the CNGA1 channels in the absence and presence of cGMP, respectively. Approximately 30% of these F–D curves had only nonspecific adhesion events and the remaining 70% showed very diverse unfolding pathways, which could originate from the unfolding of endogenous proteins or the partial unfolding of CNGA1 channels. Therefore, we had to identify the F–D curves from the unfolding of the full CNGA1 channel and we had to distinguish these curves from all other unfolding events. We set up an initial filtering to remove the F–D curves showing only nonspecific adhesions and all other invalid F–D curves (see next section). Next, the remaining F–D curves were fitted to the worm-like chain (WLC) model[1] with a persistence length (Lp) of 0.4 nm, and the corresponding contour length (Lc) was calculated using 0.4 nm as the length of a single a.a. All contour points for Lc were summarized in histograms and fitted using Gaussian model. In text and in the figures, maxima of the Gaussian fittings are expressed as the mean ± s.d.

Initial filtering of F–D curves. The F–D curves that were collected by the AFM JPK software were filtered to remove unsuitable cases. Filtering was based on the analysis of the pushing (red curves) and pulling (black curves). First, retraction curves were treated by median and variance filtering (if the number of peaks in the filtered pulling curve was <2, the curve was discarded; Supplementary Fig. 2a). Force offset between the retraction and extension curves was compared and if the offset was greater than a given threshold related to the type of experiment (at least 30 pN, but usually is greater) in the initial part of the curve, the curve was discarded (Supplementary Fig. 2b). We then compared crossings between the extension and retraction curves and if the force offset between two crossings was >20 pN, the curve was discarded (Supplementary Fig. 2c). Variance σ^2 of the extension curve was computed to estimate the motion of the baseline and if σ^2 was >10 pN^2, the curve was discarded (Supplementary Fig. 2d). Initial slope of the extension curve (Sp) and the retraction signal (Sr) was then compared and if $(1 - Sp/Sr)$ was >1, the curve was discarded (Supplementary Fig. 2d,e). The maximum pulling force (F) was calculated and if F was <30 pN, the curve was discarded (Supplementary Fig. 2f). The extension curve drift was calculated and if the maximum amplitude was >35 pN in the 'flat' region, the curve was discarded). Lengths of the TSS (distance or TSS) for the extension and retraction curves was compared and if the length difference was >10%, the curve was discarded. The (F,Lc) plot of the pulling curve was computed (the algorithm determines whether there is at least one peak, extracted as described in Methods, in the range between 80 and 300 nm and whether the last peak is in the range between 250 and 350 nm or a user-defined window; Supplementary Fig. 2a–f).

Bioinformatics analysis. We performed bioinformatics to identify F–D curves from single subunit of CNGA1 channels. These F–D curves must be found only in SMFS experiments from injected oocytes and we have modified the existing algorithms[45] for this purpose. The method had two steps. First, each F–D curve was mapped to a sequence of symbols that represented the location and amplitude of the force peaks (coding), and then these sequences were assembled in groups with similar properties (clustering). The coding step was based on the transformation of the F–D curves into a plot of force and contour lengths (F,Lc)[45] (Fig. 1a–e). We used the WLC model where Lp is the persistence length (0.4 nm), a parameter that represents the stiffness of the molecule.

For each tip-sample separation (D or TSS) value, the WLC model is used to compute the corresponding value of Lc that is obtained by solving the third order polynomial: $4\lambda^3 + \omega \ \lambda^2 - 1 = 0$, where $\lambda = 1 - D/Lc$ and $\omega = 4F(D,Lc)/\alpha - 3$ and $\alpha = k_b T/Lp$. This equation has three roots and the root of interest is the real root λ^* such that $0 < \lambda^* < 1$. In this manner, each point of the F–D curve (F,D) (for example, the curve in Fig. 1a) is transformed into a corresponding point (F,Lc), and each F–D curve is transformed into an (F,Lc) plot (see Fig. 1b). The three roots of the equation were obtained using a MATLAB routine. Owing to this transformation, each portion of the F–D curve that is fitted perfectly by the WLC model is mapped to a perfect vertical segment. The transformation of an F–D curve is therefore a relation (set of point) in the (F,Lc) plane rather than a function in the plane, and is also not a continuous curve.

Given a set of F–D curves, we computed the histogram of the normalized counts/bin of Lc values (normalized histogram of Lc values). The Lc axis of the

(F, Lc) plot is first divided into bins (in the range from 1 to 10 nm). All points with a value of F larger than 30 pN are counted in the corresponding bin and summed over all sets of the F–D curves, and the final histogram of counts/bin is normalized so that its maximal value is equal to 1. This histogram is used to quantify the occurrence of points in the F–D curves that correspond to a given value of Lc.

Given an (F,Lc) plot, it is possible to extract an (F,Lc) profile and to compute the local maxima (Histogram of Lc values at force peaks). The Lc axis is divided into fixed intervals of 1–10 nm (typically of 5 nm). We extract the maximum value of F in each interval to obtain the corresponding (F,Lc) profile (if all values of F in an interval are below 30 pN, the value of the force in that interval is set equal to 0 pN) and the local maxima of the (F,Lc) profile are computed.

At this point, it is possible to compute the final histogram from the local maxima of the (F,Lc) profile that is normalized by the total number of F–D curves that were considered; in this way, the histogram of the local maxima shows the probability of obtaining F–D curves that have a force peak with a given value of Lc.

Three different increasingly complex coding schemes were considered. The simplest coding scheme (Coding I) only codes the location of force peaks and only considers the value of Lc neglecting the corresponding value of F. If the F–D curve has n force peaks with values of Lc and F equal to Lc_i and F_i for $i = 1,..n$ and having selected a bin width ΔLc (varying between 1 and 10 nm), each F–D curve is converted into a sequence of symbols of the type (0,0,1,0,0,0,1,...). All symbols are set to 0 with the exception of some values of 1 located at position k corresponding to the integer value of $Lc_i/\Delta Lc$ (see red circles in Fig. 1c). This coding scheme is a binary code and was considered for its simplicity. For the next scheme, given a bin width ΔLc, such as 5 or 10 nm, each F–D curve is converted into a sequence of symbols (0,0,F1,0,0,0,F2,...), where Fi is the value of the k_{th} force peak, and if Lck is the corresponding value of Lc, the symbol Fk is located at the position that corresponds to the integer value of Lck/ΔLc (Coding II and red circles in Fig. 1d). A more complex coding scheme (Coding III) considers all points in the (F,Lc) profiles with values of F larger than 30 pN; for each interval between $k\Delta Lc$ and $(k + 1)$ ΔLc, this scheme selects the maximum value of the (F,Lc) plot in that interval (see red circles in Fig. 1e). In this case, the F–D curve is coded in the sequence of symbols $s_1, s_2, s_3,..s_n$, where s_k is the maximal value of F in the interval between $k\Delta Lc$ and $(k + 1)\Delta Lc$. Once the F–D curves are transformed into symbol sequences, a distance $D(x_i, x_j)$ between the two sequences x_i and x_j must be defined.

We then applied different clustering procedures with the rationale that clusters containing F–D curves that only originate from membranes extracted from injected oocytes are 'good' candidates to represent the unfolding of CNGA1 channels. For the clustering step (Supplementary Note 2), we consider all F–D curves with the last peak with a value of Lc larger than 220 nm, which are obtained from membranes extracted from injected and uninjected oocytes, and we look for a cluster of similar F–D curves that are only obtained from injected oocytes. We used clustering methods developed in Computer Science, to identify objects or patterns with similar features. At the end of the informatics analysis, we identified three major clusters of similar F–D curves that were obtained only from membranes extracted from injected oocytes. Other clusters were nondiscriminatory and were composed of F–D curves obtained from membranes extracted from injected and uninjected oocytes.

We then developed an algorithm for obtaining the F–D curves. Most of the available clustering algorithms require the number of subsets/clusters N to be given and N is the critical parameter controlling the quality of the clusterization (Supplementary Fig. 4). We compared the performance of many clustering algorithms (Supplementary Fig. 3) for their ability to provide clusters with F–D curves only from injected oocytes and they performed similarly. The critical step of the proposed algorithm is the choice of the value of N providing homogeneous clusters of F–D curves only from injected oocytes. The algorithm for obtaining the F–D curves shown in Fig. 1f,g is composed of the following steps. In step 1 (initial filtering), all the obtained F–D curves were first filtered as described in the previous section, to remove bad F–D curves (Supplementary Fig. 2). In step 2 (second filtering according to their length), F–D curves that passed the initial filtering were further filtered according to the largest value of Lc. We have restricted our analysis to those F–D curves that had a maximum Lc value larger than 220 nm and only ~1% of the F–D curves passed this filtering step. In step 3 (clustering), all F–D curves from injected ($S_{injected}$) and uninjected oocytes ($S_{uninjected}$) that passed step 1 and step 2 were merged in the same set S. S is composed by the union of $S_{injected}$ and $S_{uninjected}$. These F–D curves were coded as described before. The set S is broken in N subsets/clusters—with similar features—as described in details in the next section. In step 4 (choice of N), the value of N was progressively increased from 2 up to 300 and we searched for subsets/clusters containing only F–D curves from injected oocytes. The best value of N was chosen as the one generating the subset/cluster with the largest number of F–D curves containing only F–D curves from injected oocytes. The dependence of the clustering as a function of N is shown in Supplementary Fig. 4. Subsets/clusters of obtained F–D curves with similar features from injected oocytes are shown in Supplementary Fig. 5.

The same procedure was applied separately to F–D curves obtained in the absence of cGMP (Fig. 1) and in the presence of 2 mM cGMP (Fig. 2). In steps 1–4, F–D curves were not translated—or shifted—along the x axis—that is, the TSS.

In step 5, enrichment, F–D curves of the selected clusters C_i were taken as seeds of the 'good' F–D curves and enriched by comparison with all F–D curves belonging to $S_{injected}$, which passed steps 1 and 2. F–D curves that were similar— allowing a horizontal shift of 5 nm—to those in C_i were added to C_i.

Clustering of F–D curves.
Standard clustering procedures can be used after the F–D curves have been converted into symbol sequences $x_1, x_2,.....x_n$ and a similarity matrix $Sim(x,y)$ between the symbol sequences is available (see Supplementary Note 2). We have used and compared the average, centroid, complete, median, single, ward and weighted clustering algorithms (all these algorithms are agglomerative clustering algorithms in the MATLAB statistics toolbox http://www.mathworks.it/it/help/stats/clusterdata.html). For all these algorithms, the total number of clusters $N_{cluster}$ must be assigned and the choice of $N_{cluster}$ is crucial. We have circumvented this problem by mixing the F–D curves from membranes extracted from injected and uninjected oocytes, and we have varied the value of $N_{cluster}$. For values of $N_{cluster}$ that are <10, none of the tested clustering algorithms are able to distinguish between the F–D curves that were obtained from membranes extracted from injected and from uninjected oocytes. When $N_{cluster}$ is between 50 and 100, clusters of F–D curves can be observed from injected oocytes with probabilities of 0.8, 0.9 and 1, that is, in which 80%, 90% and 100% of curves are from membranes extracted from injected oocytes (Supplementary Fig. 4). We found that when we used the clustering algorithm 'complete' and when $N_{cluster}$ was larger than 100, several clusters from injected oocytes could be detected with a probability that was larger than 0.8. For the value of $N_{cluster}$, we selected the value for which we had the largest clusters of F–D curves from membranes extracted from injected oocytes with a probability of 1. Examples of the obtained clusters are shown in the Supplementary Fig. 5. There are several clusters with F–D curves (Supplementary Fig. 5d–f) obtained from both injected (red curves) and uninjected oocytes (cyan curves). These F–D curves presumably represent the unfolding of proteins or molecules that form the plasma membrane of X. laevis oocytes and therefore can be obtained from either membranes extracted from injected or uninjected oocytes. As shown in Supplementary Fig. 5a, we found one cluster (Cluster 1-CS) with 22 F–D curves that were only obtained from injected oocytes. These F–D curves represent the seed of putative F–D curves obtained from the unfolding of CNGA1 channels from their C-terminal. Cluster 2-CS had F–D curves similar to those present in Cluster 1-CS and F–D curves of Cluster 3-CS had different force peaks.

The Cluster 1-CS of 'good' F–D curves obtained from the bioinformatics analysis were enriched in the following way: F–D traces of the selected clusters Cluster 1-CS are taken as seeds and are enriched by comparison with all F–D traces belonging to injected oocyte plasma membrane, which passed Steps 1 and 2 (see previous section). F–D traces, which were similar—allowing a horizontal shift of <5 nm—to those in Cluster 1-CS, were added to Cluster 1-CS. The used similarity measure consisted in the following criteria: the added F–D curve does not increase the intracluster distance described in the next section.

Intracluster and intercluster similarity.
Given a cluster C1 and the corresponding similarity matrix $Sim(x,y)$ among the elements or sequences of C1, the intracluster difference IntraC$_1$ is defined[70] as: $IntraC_1 = (1/(n^2 - 1)) \sum_{i,j} Sim(x_i, x_j)$, where n is the total number of sequences in C1 and x_i, $i = 1,...n$, are the sequences in C1. Given two clusters C1 and C2, the intercluster difference InterC$_1$C$_2$ is defined[70] as: $InterC_1C_2 = (1/n\ m) \sum_j \sum_i Sim(x_i, y_j)$, where n and m are the total number of sequences in clusters C_1 and C_2, respectively, and x_i for $i = 1,...,n$ and y_j for $j = 1,...,m$ are the sequences present in C_1 and C_2, respectively. A cluster of fingerprints f_n FP identifies cluster C_i among a set of other clusters C_k, $k = ,...,N$, if InterFPC$_i$ <InterFPC$_k$ for all k different from i. A cluster of finger prints f_n FP identifies cluster C_i very well among a set of clusters C_k, $k = ,...,N$, if InterFPC$_i$ <InterFPC$_k$ for all k different from I and if InterFPC$_i$ is very similar (within 10%) to IntraC$_i$ and IntraFP. In Fig. 1f of the main text, the set of fingerprints with the N2B construct identifies cluster 1 among all clusters that were obtained as described below according to all considered codings and similarities, and identifies cluster 1 very well according to coding I. The F–D curves from the CNGA1-N2B-HisTag construct have slightly higher forces; thus, according to coding II and III, the value of InterFP clusters using the MAE method is higher for IntraFP clusters and approximately twice the value of Intra-clusters, whereas using the Hamming-force method, InterFP clusters is higher for IntraFP clusters and for Intra clusters (see Supplementary Table 2).

In Fig. 1f, clusters were obtained using Ncluster = 200 and by selecting those clusters in which at least 80% of the curves were obtained from membranes extracted from injected oocytes. Using this procedure, we identified 15 clusters and 3 were obtained only from membranes extracted from injected oocytes. F–D curves with the N2B fingerprint identified cluster I as obtained from the unfolding of CNGA1 channels. Supplementary Table 6 reports the Intracluster similarity for the three clusters and for the set of F–D curves (FP) with the N2B fingerprint, and also shows the Intercluster similarity between each cluster and FP.

References

1. Rief, M., Gautel, M., Oesterhelt, F., Fernandez, J. M. & Gaub, H. E. Reversible unfolding of individual titin immunoglobulin domains by AFM. *Science* **276**, 1109–1112 (1997).

2. Engel, A. & Gaub, H. E. Structure and mechanics of membrane proteins. *Annu. Rev. Biochem.* **77**, 127–148 (2008).

3. Müller, D. J., Wu, N. & Palczewski, K. Vertebrate membrane proteins: structure, function, and insights from biophysical approaches. *Pharmacol. Rev.* **60**, 43–78 (2008).

4. Hoffmann, T. & Dougan, L. Single molecule force spectroscopy using polyproteins. *Chem. Soc. Rev.* **41,** 4781–4796 (2012).

5. Valbuena, A. *et al.* On the remarkable mechanostability of scaffoldins and the mechanical clamp motif. *Proc. Natl Acad. Sci. USA* **106,** 13791–13796 (2009).

6. Oesterhelt, F. *et al.* Unfolding pathways of individual bacteriorhodopsins. *Science* **288,** 143–146 (2000).

7. Sapra, T. K. *et al.* Detecting molecular interactions that stabilize native bovine rhodopsin. *J. Mol. Biol.* **358,** 255–269 (2006).

8. Kawamura, S. *et al.* Kinetic, energetic, and mechanical differences between dark-state rhodopsin and opsin. *Structure* **21,** 426–437 (2013).

9. Kedrov, A., Ziegler, C. & Muller, D. J. Differentiating ligand and inhibitor interactions of a single antiporter. *J. Mol. Biol.* **362,** 925–932 (2006).

10. Peng, Q. & Li, H. Atomic force microscopy reveals parallel mechanical unfolding pathways of T4 lysozyme: evidence for a kinetic partitioning mechanism. *Proc. Natl Acad. Sci. USA* **105,** 1885–1890 (2008).

11. Ge, L., Perez, C., Waclawska, I., Ziegler, C. & Muller, D. J. Locating an extracellular K + -dependent interaction site that modulates betaine-binding of the Na + -coupled betaine symporter BetP. *Proc. Natl Acad. Sci. USA* **108,** E890–E898 (2011).

12. Bosshart, P. D. *et al.* The transmembrane protein KpOmpA anchoring the outer membrane of Klebsiella pneumoniae unfolds and refolds in response to tensile load. *Structure* **20,** 121–127 (2012).

13. Zocher, M., Zhang, C., Rasmussen, S. G., Kobilka, B. K. & Müller, D. J. Cholesterol increases kinetic, energetic, and mechanical stability of the human β2-adrenergic receptor. *Proc. Natl Acad. Sci. USA* **109,** E3463–E3472 (2012).

14. Kotamarthi, H. C., Sharma, R., Narayan, S., Ray, S. & Ainavarapu, S. R. Multiple unfolding pathways of leucine binding protein (LBP) probed by single-molecule force spectroscopy (SMFS). *J. Am. Chem. Soc.* **135,** 14768–14774 (2013).

15. Jan, L. Y. & Jan, Y. N. A superfamily of ion channels. *Nature* **345,** 672 (1990).

16. Yu, F. H., Yarov-Yarovoy, V., Gutman, G. A. & Catterall, W. A. Overview of molecular relationships in the voltage-gated ion channel superfamily. *Pharmacol. Rev.* **57,** 387–395 (2005).

17. Kaupp, U. B. *et al.* Primary structure and functional expression from complementary DNA of the rod photoreceptor cyclic GMP-gated channel. *Nature* **342,** 762–766 (1989).

18. Anderson, P. A. & Greenberg, R. M. Phylogeny of ion channels: clues to structure and function. *Comp. Biochem. Physiol. B Biochem. Mol. Biol.* **129,** 17–28 (2001).

19. Kaupp, U. B. & Seifert, R. Cyclic nucleotide-gated ion channels. *Physiol. Rev.* **82,** 769–824 (2002).

20. Matulef, K. & Zagotta, W. N. Multimerization of the ligand binding domains of cyclic nucleotide-gated channels. *Neuron* **36,** 93–103 (2002).

21. Marchesi, A., Mazzolini, M. & Torre, V. Gating of cyclic nucleotide-gated channels is voltage dependent. *Nat. Commun.* **3,** 973 (2012).

22. Tetreault, M. L., Henry, D., Horrigan, D. M., Matthews, G. & Zimmerman, A. L. Characterization of a novel cyclic nucleotide-gated channel from zebrafish brain. *Biochem. Biophys. Res. Commun.* **348,** 441–449 (2006).

23. Becchetti, A., Gamel, K. & Torre, V. Cyclic nucleotide-gated channels. Pore topology studied through the accessibility of reporter cysteines. *J. Gen. Physiol.* **114,** 377–392 (1999).

24. Flynn, G. E. & Zagotta, W. ,N. Conformational changes in S6 coupled to the opening of cyclic nucleotide-gated channels. *Neuron* **30,** 689–698 (2001).

25. Flynn, G. E. & Zagotta, W. N. A cysteine scan of the inner vestibule of cyclic nucleotide-gated channels reveals architecture and rearrangement of the pore. *J. Gen. Physiol.* **121,** 563–582 (2003).

26. Contreras, J. E., Srikumar, D. & Holmgren, M. Gating at the selectivity filter in cyclic nucleotide-gated channels. *Proc. Natl Acad. Sci. USA* **105,** 3310–3314 (2008).

27. Nair, A. V., Nguyen, C. H. & Mazzolini, M. Conformational rearrangements in the S6 domain and C-linker during gating in CNGA1 channels. *Eur. Biophys. J.* **38,** 993–1002 (2009).

28. Mazzolini, M., Anselmi, C. & Torre, V. The analysis of desensitizing CNGA1 channels reveals molecular interactions essential for normal gating. *J. Gen. Physiol.* **133,** 375–386 (2009).

29. Nair, A. V., Anselmi, C. & Mazzolini, M. Movements of native C505 during channel gating in CNGA1 channels. *Eur. Biophys. J.* **38,** 465–478 (2009).

30. Mazzolini, M., Punta, M. & Torre, V. Movement of the C-helix during the gating of cyclic nucleotide-gated channels. *Biophys. J.* **83,** 3283–3295 (2002).

31. Zagotta, W. N. *et al.* Structural basis for modulation and agonist specificity of HCN pacemaker channels. *Nature* **425,** 200–205 (2003).

32. Mari, S. A. *et al.* Gating of the MlotiK1 potassium channel involves large rearrangements of the cyclic nucleotide-binding domains. *Proc. Natl Acad. Sci. USA* **108,** 20802–20807 (2011).

33. Craven, K. B. & Zagotta, W. N. CNG and HCN channels: two peas, one pod. *Annu. Rev. Physiol.* **68,** 375–401 (2006).

34. Mazzolini, M., Marchesi, A., Giorgetti, A. & Torre, V. Gating in CNGA1 channels. *Pflugers. Arch.* **459,** 547–555 (2010).

35. Higgins, M. K., Weitz, D., Warne, T., Schertler, G. F. & Kaupp, U. B. Molecular architecture of a retinal cGMP-gated channel: the arrangement of the cytoplasmic domains. *EMBO J.* **21,** 2087–2094 (2002).

36. Schünke, S., Stoldt, M., Lecher, J., Kaupp, U. B. & Willbold, D. Structural insights into conformational changes of a cyclic nucleotide-binding domain in solution from *Mesorhizobium loti* K1 channel. *Proc. Natl Acad. Sci. USA* **108,** 6121–6126 (2011).

37. Lolicato, M. *et al.* Tetramerization dynamics of C-terminal domain underlies isoform-specific cAMP gating in hyperpolarization-activated cyclic nucleotide-gated channels. *J. Biol. Chem.* **286,** 44811–44820 (2011).

38. Shuart, N. G., Haitin, Y., Camp, S. S., Black, K. D. & Zagotta, W. N. Molecular mechanism for 3:1 subunit stoichiometry of rod cyclic nucleotide-gated ion channels. *Nat. Commun.* **2,** 457 (2011).

39. Derebe, M. G., Zeng, W., Li, Y., Alam, A. & Jiang, Y. Structural studies of ion permeation and Ca2+ blockage of a bacterial channel mimicking the cyclic nucleotide-gated channel pore. *Proc. Natl Acad. Sci. USA* **108,** 592–597 (2011).

40. Gorostiza, P. *et al.* Molecular handles for the mechanical manipulation of single-membrane proteins in living cells. *IEEE Trans. Nanobiosci.* **4,** 269–276 (2005).

41. Santacroce, M. *et al.* Imaging of *Xenopus laevis* oocyte plasma membrane in physiological-like conditions by atomic force microscopy. *Microsc. Microanal.* **19,** 1358–1363 (2013).

42. Orsini, F. *et al.* Atomic force microscopy characterization of *Xenopus laevis* oocyte plasma membrane. *Microsc. Res. Tech.* **69,** 826–834 (2006).

43. Santacroce, M. *et al.* Atomic force microscopy imaging of *Xenopus laevis* oocyte plasma membrane purified by ultracentrifugation. *Microsc. Res. Tech.* **71,** 397–402 (2008).

44. Orsini, F. *et al.* Intermittent contact mode AFM investigation of native plasma membrane of *Xenopus laevis* oocyte. *Eur. Biophys. J.* **38,** 903–910 (2009).

45. Bosshart, P. D., Frederix, P. L. & Engel, A. Reference-free alignment and sorting of single-molecule force spectroscopy data. *Biophys.* **102,** 2202–2211 (2012).

46. Li, H., Oberhauser, A. F., Fowler, S. B., Clarke, J. & Fernandez, J. M. Atomic force microscopy reveals the mechanical design of a modular protein. *Proc. Natl Acad. Sci. USA* **97,** 6527–6531 (2000).

47. Li, H. *et al.* Reverse engineering of the giant muscle protein titin. *Nature* **418,** 998–1002 (2002).

48. Watanabe, K. *et al.* Molecular mechanics of cardiac titin's PEVK and N2B spring elements. *J. Biol. Chem.* **277,** 11549–11558 (2002).

49. Gordon, S. E., Varnum, M. D. & Zagotta, W. N. Direct interaction between amino.and carboxyl-terminal domains of cyclic nucleotide-gated channels. *Neuron* **19,** 431–441 (1997).

50. Rosenbaum, T. & Gordon, S. E. Dissecting intersubunit contacts in cyclic nucleotide-gated ion channels. *Neuron* **33,** 703–713 (2002).

51. Mazzolini, M., Nair, A. & Torre, V. A comparison of electrophysiological properties of the CNGA1, CNGA1tandem and CNGA1cys-free channels. *Eur. Biophys. J.* **37,** 947–959 (2008).

52. Nair, A. V., Mazzolini, M., Codega, P., Giorgetti, A. & Torre, V. Locking CNGA1 channels in the open and closed state. *Biophys. J.* **90,** 3599–3607 (2006).

53. Grandbois, M., Beyer, M., Rief, M., Clausen-Schaumann, H. & Gaub, H. E. How strong is a covalent bond? *Science* **283,** 1727–1730 (1999).

54. Carrion-Vazquez, M. *et al.* Mechanical and chemical unfolding of a single protein: a comparison. *Proc. Natl Acad. Sci. USA* **96,** 3694–3699 (1999).

55. Andreopoulos, B. & Labudde, D. Efficient unfolding pattern recognition in single molecule force spectroscopy data. *Algorithms Mol. Biol.* **6,** 16 (2011).

56. Anselmi, C., Carloni, P. & Torre, V. Origin of functional diversity among tetrameric voltage-gated channels. *Proteins* **66,** 136–146 (2007).

57. Kusch, J. *et al.* Role of the S4-S5 linker in CNG channel activation. *Biophys. J.* **99,** 2488–2496 (2010).

58. Peng, Q., Fang, J., Wang, M. & Li, H. Kinetic partitioning mechanism governs the folding of the third FnIII domain of tenascin-C: evidence at the single-molecule level. *J. Mol. Biol.* **412,** 698–709 (2011).

59. Kedrov, A., Janovjak, H., Sapra, K. T. & Müller, D. J. Deciphering molecular interactions of native membrane proteins by single-molecule force spectroscopy. *Annu. Rev. Biophys. Biomol. Struct.* **36,** 233–260 (2007).

60. Dietz, H. & Rief, M. Exploring the energy landscape of GFP by single-molecule mechanical experiments. *Proc. Natl Acad. Sci USA* **101,** 16192–16197 (2004).

61. Dietz, H. & Rief, M. Protein structure by mechanical triangulation. *Proc. Natl Acad. Sci USA* **103,** 1244–1247 (2006).

62. Liu, D. T., Tibbs, G. R., Paoletti, P. & Siegelbaum, S. A. Constraining ligand-binding site stoichiometry suggests that a cyclic nucleotide-gated channel is composed of two functional dimers. *Neuron* **21,** 235–248 (1998).

63. Matulef, K. & Zagotta, W. N. Multimerization of the ligand binding domains of cyclic nucleotide-gated channels. *Neuron* **36,** 93–103 (2002).

64. Kowal, J. *et al.* Ligand-induced structural changes in the cyclic nucleotide-modulated potassium channel MloK1. *Nat. Commun.* **5,** 3106 (2014).

65. Ng, C. A. *et al.* The S4-S5 linker acts as a signal integrator for HERG K+ channel activation and deactivation gating. *PLoS One* **7**, e31640 (2012).

66. Clayton, G. M., Altieri, S., Heginbotham, L., Unger, V. M. & Morais-Cabral, J. H. Structure of the transmembrane regions of a bacterial cyclic nucleotide-regulated channel. *Proc. Natl Acad. Sci. USA* **105**, 1511–1515 (2008).

67. Yarov-Yarovoy, V. *et al.* Structural basis for gating charge movement in the voltage sensor of a sodium channel. *Proc. Natl Acad. Sci. USA* **109**, E93–102 (2012).

68. Murata, M. Novel biosensor for the rapid measurement of estrogen based on a ligand-receptor interaction. *Anal. Sci.* **17**, 387–390 (2001).

69. Verbelen, C., Gruber, H. J. & Dufrêne, Y. F. The NTA-His6 bond is strong enough for AFM single-molecular recognition studies. *J. Mol. Recognit.* **20**, 490–494 (2007).

70. Daliri, M. R. & Torre, V. Shape and texture clustering: the best estimate for the cluster numbers. *Image Vis. Comput.* **27**, 1603–1614 (2009).

Acknowledgements

Author contributions

S.M. performed SMFS experiments and data analysis; M.M. and M.A. performed electrophysiology and mutagenesis; P.F. and V.T. performed bioinformatics; S.M., M.M., A.V. and V.T. designed the experiments; S.M., M.M. and V.T. participated in interpreting results; S.M., M.M., M.L. and V.T. contributed to writing the paper; V.T. supervised the project.

Additional information

Supplementary Information accompanies this paper at http://www.nature.com/naturecommunications

Competing financial interests: The authors declare no competing financial interests.

Reprints and permission information is available online at http://npg.nature.com/reprintsandpermissions/

How to cite this article: Maity, S. *et al.* Conformational rearrangements in the transmembrane domain of CNGA1 channels revealed by single-molecule force spectroscopy. *Nat. Commun.* 6:7093 doi: 10.1038/ncomms8093 (2015).

4

A structural, functional, and computational analysis suggests pore flexibility as the base for the poor selectivity of CNG channels.

Luisa Maria Rosaria Napolitano, Ina Bisha, Matteo De March, Arin Marchesi, Manuel Arcangeletti, Nicola Demitri, Monica Mazzolini, Alex Rodriguez, Alessandra Magistrato, Silvia Onesti, Alessandro Laio, and Vincent Torre.

A structural, functional, and computational analysis suggests pore flexibility as the base for the poor selectivity of CNG channels

Luisa Maria Rosaria Napolitano[a], Ina Bisha[b], Matteo De March[a], Arin Marchesi[b], Manuel Arcangeletti[b], Nicola Demitri[a], Monica Mazzolini[b], Alex Rodriguez[b], Alessandra Magistrato[b,c], Silvia Onesti[a,1], Alessandro Laio[b,1], and Vincent Torre[b,1]

[a]Structural Biology Laboratory, Elettra-Sincrotrone Trieste S.C.p.A., Basovizza, Trieste 34149, Italy; [b]International School for Advanced Studies, Trieste 34136, Italy; and [c]National Research Council-Institute of Materials (CNR-IOM)-Democritos National Simulation Center c/o International School for Advanced Studies, Trieste 34136, Italy

Cyclic nucleotide-gated (CNG) ion channels, despite a significant homology with the highly selective K^+ channels, do not discriminate among monovalent alkali cations and are permeable also to several organic cations. We combined electrophysiology, molecular dynamics (MD) simulations, and X-ray crystallography to demonstrate that the pore of CNG channels is highly flexible. When a CNG mimic is crystallized in the presence of a variety of monovalent cations, including Na^+, Cs^+, and dimethylammonium (DMA^+), the side chain of Glu66 in the selectivity filter shows multiple conformations and the diameter of the pore changes significantly. MD simulations indicate that Glu66 and the prolines in the outer vestibule undergo large fluctuations, which are modulated by the ionic species and the voltage. This flexibility underlies the coupling between gating and permeation and the poor ionic selectivity of CNG channels.

CNG channels | pore flexibility | X-ray crystallography | MD simulations

In K^+ selective channels, the opening and closing of the ion channel pore (gating) and the translocation of ions through the pore (permeation) are considered independent processes with distinct structural basis (1). Gating is controlled by the bundle crossing at the intracellular side, whereas permeation reflects ion–ion and ion–pore interactions within the selectivity filter (1–5). Based on these experimental observations, the current paradigm assumes that the 3D structure of the selectivity filter is relatively rigid during ion translocation and the mechanisms of ionic permeation can be deduced in essence from its crystal structure. This paradigm has been successfully applied to several K^+ channels (4, 6, 7). Cyclic nucleotide-gated (CNG) channels underlie sensory transduction in the retina and olfactory epithelium and share a high degree of homology with K^+ channels (8–10). In contrast to K^+ channels, CNG channels' primary gate is located at the selectivity filter (11), suggesting that the same protein region controls ion permeation and gating. In CNG channels the ionic species present inside the pore influences channel gating; however, the nature of this coupling is not well understood (12–16). In the presence of large cations, such as Rb^+ and Cs^+, channel conductance and gating are also controlled by membrane voltage, and current–voltage relationships activated by 1 mM cGMP depend on the radius of the permeating ion (17, 18) (Fig. S1).

Structural information on CNG channels is limited to a low-resolution electron microscopy map (19), partial crystal structures of the intracellular cyclic nucleotide-binding domains (20–22), and the crystal structure of a chimeric channel in which the CNG selectivity-filter sequence is engineered into a bacterial NaK channel, creating a CNG mimic (NaK2CNG; Fig. 1 A and B) that shares several properties of CNG channels (23). This CNG mimic provides a suitable model for understanding the properties of the pore underlying the low ionic selectivity and the coupling between gating and permeation, which is common to all CNG channels.

To investigate the molecular basis of the effects of permeant ions and voltage on gating and conductance, we combined electrophysiology, X-ray crystallography, and large-scale molecular dynamics (MD) simulations in the presence of different alkali and monovalent organic cations using this CNG mimic as a model system. We demonstrate that the extracellular entrance of the selectivity filter and the filter itself exhibit a dynamic structure capable of structural rearrangements, which can be partially captured by X-ray crystallography and are best visualized and understood through MD simulations. Our results indicate that the pore of CNG channels is highly flexible, with a liquidlike energy landscape (24, 25). This flexibility underlies the poor selectivity of CNG channels and their strong coupling between gating and permeation.

Results

Influence of Permeant Ions and Voltage on Gating and Conductance of CNG Channels and Its Mimics. A crystal structure for the pore of CNG channels is currently unavailable. A CNG channel mimic has been constructed based on the bacterial NaK channel, in which the selectivity filter has been modified to reflect the CNG characteristic sequence ETPP (23), and has been crystallized in

---

Significance

Cyclic nucleotide-gated (CNG) channels underlie sensory transduction in photoreceptors and olfactory epithelium and share a high degree of homology with K^+ channels. However, these channels conduct Na^+ and K^+ differently: although K^+ channels discriminate with high accuracy Na^+ from K^+, CNG channels do not discriminate among different cations. By combining electrophysiology, molecular dynamics simulations, and X-ray crystallography we found that the pore region exhibits a dynamic structure. We show that (i) the selectivity filter can adapt to large and small ions with a different geometry and (ii) the pore diameter critically depends on the ion within. We conclude that the pore of CNG channels is highly flexible and that this flexibility is at the basis of their poor ionic selectivity.

the presence of Na⁺, K⁺, and Ca²⁺ ions (Fig. 1 *A* and *B*). The CNG mimic lacks both the voltage sensing and the cyclic nucleotide-binding domain and is therefore a model for only the channel core. We overexpressed and purified the corresponding protein (*Materials and Methods*) and recorded single-channel
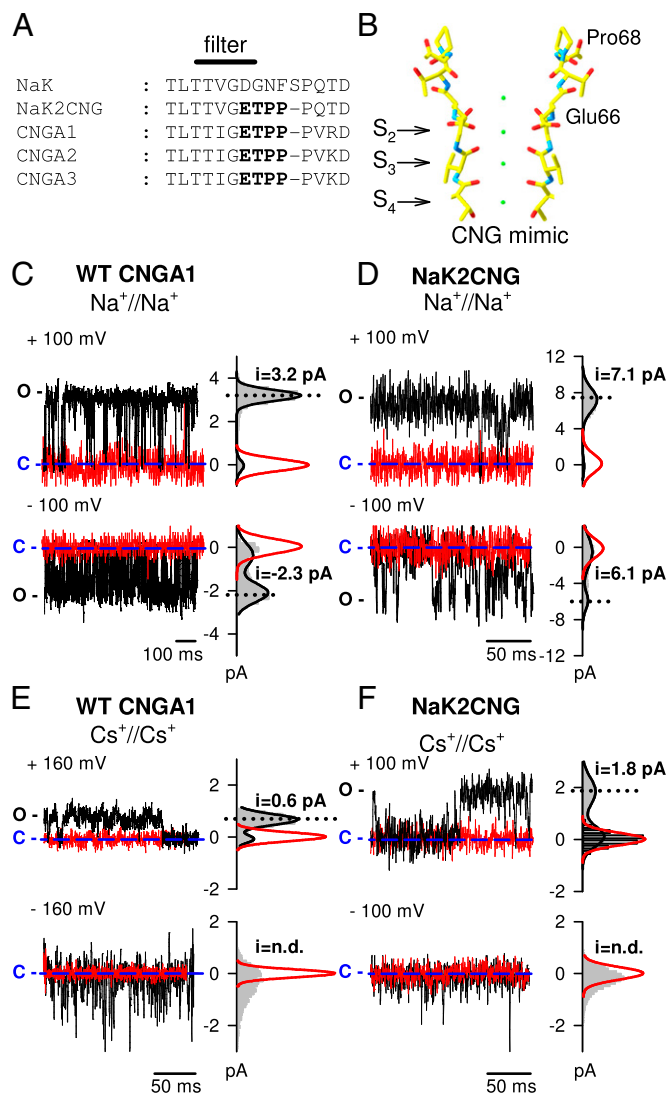

Fig. 1. Single-channel recordings in the presence of Na⁺ and Cs⁺ in the NaK2CNG and CNGA1 channels. (*A*) Sequence alignment of the selectivity filter of the bacterial NaK channel, the CNG-mimicking NaK chimera (NaK2CNG) and the bovine subunits CNGA1–CNGA3. The ETPP motif in the CNG signature is marked in bold. (*B*) Structure of the selectivity filter of the CNG-mimicking NaK channel in complex with K⁺ ions (PDB ID: 3K0D). (*C*) Current recordings from a single WT CNGA1 channel at +100 mV (*Upper*) and −100 mV (*Lower*) in the presence (black traces) and absence (red traces) of 1 mM cGMP in symmetrical 110 mM Na⁺ solution. (*D*) Current recordings from a single CNG-mimicking NaK chimeric channel at +100 mV (*Upper*) and −100 mV (*Lower*) in the absence (black traces) and presence (red traces) of 30 μM TPeA in symmetrical 110 mM Na⁺ solution. (*E*) As in *C* but in symmetrical 110 mM Cs⁺ solution and at ±160 mV. (*F*) As in *D* but in symmetrical 110 mM Cs⁺ solution. Amplitude histograms for recordings in the presence of 1 mM cGMP and in the absence of 30 μM TPeA for the WT and the mimic channel, respectively, are shown on the right (gray area). Black lines represent a two-term Gaussian fit to the histograms. Red lines represent a one-term Gaussian fit to the histograms for recordings in the absence of 1 mM cGMP and in the presence of 30 μM TPeA for the WT and the mimic channel, respectively. Blue dashed lines indicate the 0 current level. C and O refer to the closed and open states, respectively.

activity in the presence of Na⁺ and Cs⁺ ions at +100 mV and −100 mV in giant liposomes (23) to verify whether the mimic recapitulates the effects of permeant ions and voltage on gating and conductance observed in the CNGA1 channel (18); this coupling is best observed by comparing the behavior of symmetrical Na⁺ and Cs⁺ conditions (17, 18) (Fig. 1). Indeed, in the presence of Na⁺ ions, CNGA1 channels show clear openings with single-channel conductances of 32 and 23 pS at +100 and −100 mV, respectively (Fig. 1*C*). Under these conditions both single-channel conductance and open probability did not depend significantly on voltage (17, 18). In contrast, in the presence of Cs⁺ ions, single-channel openings with an amplitude of ~0.6 pA can be detected at +160 mV (at +100 mV, single-channel transitions were obscured by instrumental noise); however, at −160 mV, only brief current transients up to 3–4 pA are measured (Fig. 1*E*). Open probability was estimated to reduce more than threefold, from ~0.9 at +160 mV to ~0.25 at −160 mV (17, 18). A comparison with single-channel recordings from NaK2CNG channel mimic under identical ionic conditions (Fig. 1 *D* and *F*) indicates a similar behavior: in the presence of Na⁺, single-channel recordings have openings of 7.1 and 6.1 pA at +100 and −100 mV, respectively (Fig. 1*D*). In contrast, clear voltage-dependent asymmetries are observed in the presence of Cs⁺: the channel has flickering openings at −100 mV, with values ranging from 0.5 up to 2.5 pA and long-lasting well-defined channel openings of 1.8 pA at +100 mV (Fig. 1*F*). Moreover, channel activity is suppressed by the addition of the intracellular blocker tetrapentylammonium (TPeA; red traces in Fig. 1 *D* and *F*). Therefore, the bacterial CNG mimic is a suitable model for dissecting the molecular determinants of the coupling between gating, permeation, and voltage in the CNG channel pore.

Monovalent Cation Binding Sites in the NaK2CNG Channel Mimic. Previous experimental and theoretical studies have established a connection between a particular number of consecutive binding sites for cations and channel selectivity. Four binding sites were observed in the filter in K⁺ selective channel, whereas two or three binding sites were visualized in nonselective channel (23, 26). Therefore, we performed a comprehensive crystallographic structural analysis of monovalent alkali cations (Li⁺, Na⁺, Rb⁺, and Cs⁺) and organic compounds (MA⁺ and DMA⁺) bound to the NaK2CNG channel (Figs. 2 and 3*A*) to identify structural changes in the presence of different permeant ionic species.

The NaK2CNG channel was purified in the presence of 100 mM KCl, as previously described (23). Due to difficulties in crystal reproducibility, a variety of crystallization conditions were explored (Table S1); 25–100 mM glycine was added to produce well-diffracting crystals. The crystals were grown in 100 mM K⁺, followed by incubation in stabilization solutions containing 100 mM Na⁺, Rb⁺, or Cs⁺. Incubation of the crystals in stabilization solutions containing MA⁺ or DMA⁺ did not result in cation binding, most likely due to the large size of the organic compounds. Therefore, we purified the NaK2CNG channel in the presence of 100 mM MA⁺ or DMA⁺ and successfully obtained crystals (Table S1). Similarly, to obtain NaK2CNG in complex with Li⁺ ions, we purified and crystallized the protein in the presence of 100 mM LiCl.

We determined the corresponding crystal structures by molecular replacement using the coordinates determined in the presence of K⁺ (PDB ID: 3K0D; ref. 23) as a search model and refined the models to resolutions ranging from 2.3 to 2.85 Å. Data collection and refinement statistics are summarized in Table S2. During the final round of refinement, the ions and water molecules within the pore were omitted; following additional refinement cycles, omit maps were calculated to obtain an unbiased snapshot of the electron density within the pore.

The asymmetric unit contains two independent molecules; for each complex, only one of the two molecules is discussed, unless
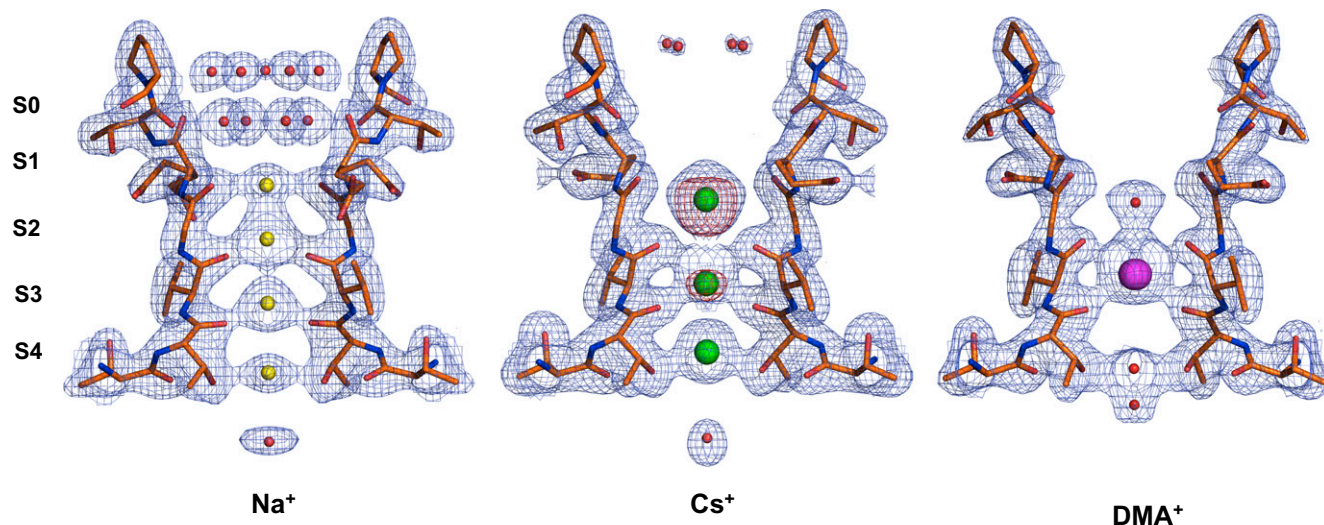
Fig. 2. Electron density maps for the pore region in the presence of a subset of monovalent cations. $2F_o–F_c$ electron density maps of Na^+, Cs^+, and DMA^+ at the filter region. The maps are contoured at 1.5σ for the Na^+ and DMA^+ structures and at 1.3σ for the Cs^+ structure. For the Cs^+ structure, the anomalous difference map contoured at 3σ is shown as a purple semitransparent surface.

significant differences among the two are present. The putative ion sites are named from 1 to 4, beginning from the extracellular side (7) (Fig. 2). A different pattern of electron density peaks within the selectivity filter can be observed in the presence of each ion, confirming that the channel is able to accommodate and to subtly adjust to a variety of chemical species. For simplicity, our detailed analysis is primarily focused on three complexes (Na^+, Cs^+, and DMA^+; Fig. 2) to provide a direct comparison with the electrophysiology and MD simulation results. Data for the remaining ion complexes are reported in Table S2.

The diffraction data collected in the presence of Na^+ ions exhibits some anisotropy; upon anisotropy correction (27) of the

data we obtained an electron density map that clearly shows metal binding sites. The electron density within the pore reveals some differences between the two crystallographically independent molecules. One of the two molecules can be better interpreted as containing three bound ions (Fig. S2), whereas the other appears to contain four (Fig. 2). On the basis of previous reports (6), we can speculate that the four or three sites are a balance mixture of an alternating arrangement of Na^+ and water molecules. The observed electron density is indeed an average image of all accessible ion-binding states represented within the crystal and it is impossible to distinguish between the contribution of Na^+ (11 electrons) and water molecules (10 electrons) to the electron density in the selectivity filter.
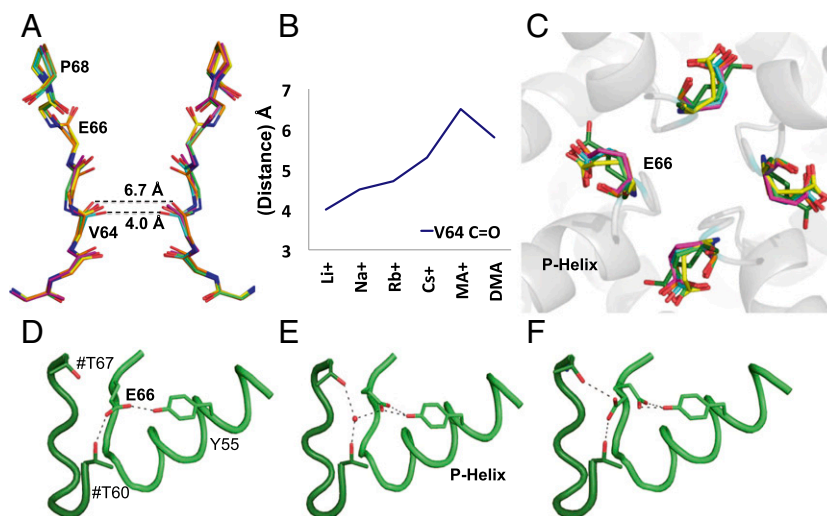

Fig. 3. Flexibility of the NaK2CNG channel pore. (*A*) The tetrameric structures of Li^+, Na^+, Rb^+, Cs^+, MA^+, and DMA^+ complexes are superposed, and the main chains of residues 62–68 are shown for two opposite subunits in the tetramer, viewed along the fourfold axis. The complexes are color coded as follows: Li^+ (cyan), Na^+ (yellow), Rb^+ (forest green), Cs^+ (green), MA^+ (orange), and DMA^+ (magenta). Changes in the pore size and the orientation of Glu66 carbonyls can be observed. (*B*) A plot of the distances for the carbonyl oxygens of two Val64 residues on opposite subunits against the various ions. (*C*) An overview of the changes in the relative orientation of the Glu66 side chains as viewed down the tetrameric channel axis from the extracellular side. (*D–F*) A sample of the different relative orientations and hydrogen-bonding patterns of Glu66. The neighboring molecule is shown in dark green; side-chain residues involved in the interactions are shown; and residues from an adjacent subunit are labeled with a hash.

When crystals grown in KCl are incubated in a solution of CsCl, three binding sites are observed (Figs. 2 and S2) with a more intense peak corresponding to site 2. X-ray anomalous signal could be collected at a wavelength of 1.2 Å and an anomalous difference map shows a strong peak at site 2, followed by a less intense peak at site 3, confirming the presence of Cs^+ ions and identifying the most populated Cs^+ sites within the filter (Fig. 2). Our data clearly show that Cs^+ predominantly binds at site 2 and 3, whereas the density at site 4 can be better interpreted as either a water molecule or a Cs^+ at lower occupancy (Fig. S2).

Our analysis was then extended to the organic compound DMA^+ to visualize the pore region in the presence of one of the largest permeant cations through CNG channels (28). The electron density map reveals a single strong peak at site 3, and weaker electron density peaks on the channel axis were interpreted as water molecules (Fig. 2).

Therefore, the NaK2CNG channel can accommodate a variety of cations indicating a degree of flexibility of the pore, which is further discussed below. In agreement with previous models (23, 26), Cs^+ and DMA^+ complex structures present less than four binding sites in the filter, consistent with the nonselective nature of the CNG channel.

Filter Conformational Change Underlying Ion Binding. The differences in position, ion occupancy, and ion size in the Li^+, Na^+, Rb^+, Cs^+, MA^+, and DMA^+ complexes also result in small but significant structural changes in the polypeptide backbone lining the pore lumen. A significant variation in the size of the pore is observed: an expansion of the lumen is detected with increasing cation size, particularly in the presence of the larger organic compounds (Fig. 3A). This trend can be monitored by measuring the distance between the carbonyl oxygens of Val64 on opposite subunits: this distance varies from 4 Å for the complex with Li^+ to 6.7 Å for the MA^+ complex (Fig. 3 A and B). The enlargement arises from both a small lateral displacement of the backbone polypeptide chain and a reorientation of main-chain carbonyls (Fig. 3A). These distances are generally consistent in the two crystallographically independent tetramers and indicate that the diameter of the pore region increases with the size of the bound cation.

Smaller structural variations are observed for Pro68 at the external vestibule. A comparison of the Na^+ and Cs^+ structures reveals a small lateral displacement of the backbone polypeptide chain in this region (Fig. 3A), resulting in a 0.7 Å widening of the funnel. Although this change is small and close to the level of the experimental error, it is consistent with the mobility observed by MD simulations (see the following section). A similar variation for the main chain of Glu66 is observed within the selectivity filter: in the presence of DMA^+, the main-chain carbonyl of Glu66 rotates by up to 60° away from the permeation pathway (Fig. 3 A and C). This movement is similar to that observed when this glutamate was mutated to aspartic acid or asparagine (23), stressing the conformational flexibility of this segment.

Significant structural differences are also observed in the region surrounding the selectivity filter. In the published NaK2CNG structure, in the presence of either K^+ or Na^+, the side-chain carboxylate of Glu66 (corresponding to Glu363 of the CNGA1 channel) forms a hydrogen bond with Thr60 of a neighboring subunit and with Tyr55 of the same subunit (23). However, in the structures reported herein, we observe a variety of conformations for the Glu66 side chain (Figs. 3C and S3), ranging from one similar to that previously described (Fig. 3D), to a distinct conformation in which the Glu66 carboxylate is engaged in a bifurcated intrasubunit hydrogen bond with Tyr55 and in an intersubunit interaction with Thr60 and Thr67 that is mediated by a water molecule (Fig. 3E). In some molecules, the electron density suggests the coexistence of two alternative conformations with approximately equal occupancies (Fig. 3F).

This variation is not directly caused by the different cations, as there are systematic differences in the two molecules present in the crystal, and simply reflects a large degree of mobility of this side chain. In summary, crystallographic data clearly indicate a higher degree of flexibility, in both the pore size and the conformation of the selectivity filter, than normally observed in NaK channel.

Filter Conformational Dynamics from Molecular Dynamics Simulations. Electrophysiological recordings reveal a significant voltage dependence of gating in the presence of Cs^+, but not in the presence of Na^+ (Fig. 1), and the crystal structures in the presence of a variety of monovalent cations (Fig. 3) suggest that the pore is rather flexible and that Glu66 in the vestibule can assume an array of different conformations. To elucidate the interplay between the selectivity filter dynamics and the permeation process, we used classical MD to model the CNG mimic embedded in a lipid membrane and surrounded by water molecules, using the crystal structure determined by Derebe et al. (PDB ID: 3K0G) (23) to build our model. We first performed 100 ns of MD at 300 K in the presence of either two Na^+ or two Cs^+ ions within the selectivity filter. Visual inspection of these trajectories reveals a significantly higher flexibility for the system in the presence of the Cs^+ ions (Movies S1 and S2). We used a recently developed clustering algorithm (*SI Materials and Methods*) (29) that is capable of identifying the metastable states of the system from its MD trajectory. Remarkably, we observed 38 metastable states for the Cs^+ system and only 3 for the Na^+ system (Fig. S4). The metastable states observed in the presence of Cs^+ primarily differ in the position of the Glu66 side chains, which adopt a large array of conformations, ranging from the crystallographic position to a reorientation toward the external vestibule and, finally, toward the pore, where they often coordinate the ion (Fig. 4). When the crystallographic structures presented in this paper are compared with the published structures (23), the overall RMSD of alpha-carbon per residues is very small (Fig. S5). Indeed the largest deviations coincide with the Glu66–Pro68 region and the conformation of the glutamate side chains, consistent with the observed mobility (Fig. S5).

Although these 100 ns of MD are sufficient to reveal that the presence of Na^+ or Cs^+ triggers a qualitatively different behavior of the channel, they cannot provide a quantitative picture of the free energy landscape that underlies this difference. Therefore, we used bias-exchange metadynamics (BE-META), which allows the computation of the free energy landscape in complex biomolecules as a function of several putative reaction coordinates (30–32), hereafter called collective variables (CVs). Because the electrophysiological experiments revealed a strong voltage dependence in the presence of Cs^+, the z component of the dipole of the selectivity filter was selected as a CV. To account for the long-range movement of the glutamate side chains, we selected as additional CVs the four distances between the carboxylate and carbonyl groups of Glu66 on opposite monomers within the tetramer (Fig. 4 and *Materials and Methods*). When the glutamates move, their side chain shifts from the crystallographic position, away from the pore axis (Fig. 3C), upward and toward the pore, getting closer to the opposite carbonyl. To depict the complex collective motion of the four Glu66 we also built a variable, hereafter referred as Glu66-Coordination, counting the number of carboxylate and carbonyl groups of Glu66 in opposite monomers with distances larger than 8 Å. When the value of this variable is high, the side chain of Glu66 is close to the crystallographic position. We then obtained the free energy as a function of the dipole of the selectivity filter and of the Glu66-Coordination variable (Fig. 4). Whereas in the presence of Na^+ (Fig. 4B), the landscape is characterized by a deep broad minimum, in the presence of Cs^+ (Fig. 4C), the landscape is flatter, with some local minima within a range of 1 kcal/mol from the global free energy minimum. This finding is consistent with that
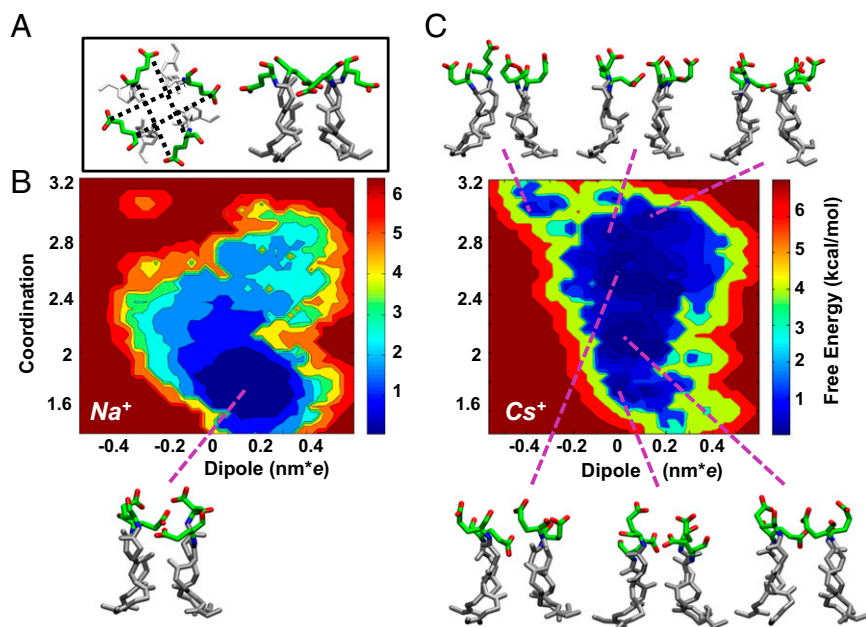
Fig. 4. Free energy of the Na$^+$ and Cs$^+$ systems. (A) Top and side views of the selectivity filter in the crystal structure are shown (Glu66 in green sticks; oxygen atoms are colored red). In the top view (*Left*), the distances between the carbonyl and carboxylic group of Glu66 in different monomers are shown as black dotted lines. (B, C) The free energy as a function of the *z* dipole [nanometers for electron charge (nm*e)] and of the Glu66-Coordination variable for the Na$^+$ (B) and Cs$^+$ system (C). The variable Glu66-Coordination is explicitly defined in the *SI Materials and Methods* and counts the number of carboxylate and carbonyl groups of Glu66 in opposite monomers whose distance is larger than 8 Å. Possible conformations of Glu66 residues corresponding to different minima are shown for both the Na$^+$ and the Cs$^+$ systems. Although minima are separated by rather small free energy barriers (0.5 kcal/mol), this is likely to be an effect of the 2D projection of the free energy surface, as these states are stable for more than 1 ns in the MD simulations. The crystal structure used as the initial model (PDB ID: 3K0G) falls at the coordinates (0.69 nm*e; 3.62).

observed by classical MD: the Cs$^+$ system is more ragged with several metastable states that significantly differ in the value of their dipole and in the conformations of Glu66.

To extrapolate the difference in the voltage dependence in the presence of Na$^+$ and Cs$^+$, we computed the 2D projection of the free energy as a function of the dipole and other geometrical observables, which describe the position of the ions in the selectivity filter, the position of the Glu66 residues, and the position of the Pro68 residues. In particular, we have chosen the RMSD of Pro68 (calculated on heavy atoms) as a CV because
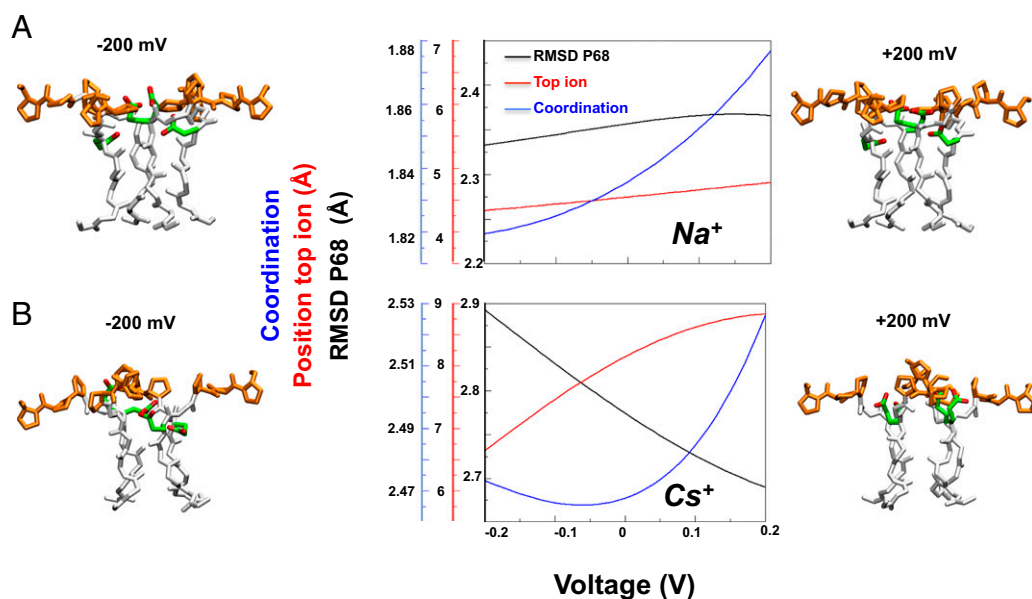

Fig. 5. Dependence on the external potential of selected structural observables. (A, B) The RMSD of Pro68 (calculated on heavy atoms) with respect to the crystal structure (black line), the position of the top ion measured as the distance (only along the *z* axis) of the ion from the center of the mass of the heavy atom of the four Gly65 residues (red line), and the Coordination variable (blue line) for the Na$^+$ (A) and Cs$^+$ systems (B). Structures of the selectivity filter in sticks (white), Glu66 (green with oxygens in red), and Pro68-70 (orange), corresponding to different voltages, are shown on the two sides of the plots.

the backbone of this residue changes conformation more significantly with V. From these projections of the free energy, it is possible to derive the dependence of the selected geometric variables on V. We estimate how geometric variables change with the voltage using Eq. 2. This equation is based on the assumption that the free energy of a microstate is modified by V according to its dipole. In this manner we model the response to the potential without performing simulations at different V (Fig. S6). The dependence on V is remarkably different in the presence of Na^+ and Cs^+ (Fig. 5). Namely, the average distance of the top Na^+ ion from the selectivity filter (i.e., the distance of the ion from the center of the mass the four Gly65 along the z direction) changes by only 0.2 Å when V is changed between −0.2 and 0.2 V (red line, Fig. 5A), whereas the distance of the top Cs^+ changes by more than 2 Å (red line, Fig. 5B). The coordination between Glu66 of opposite monomers grows linearly and regularly with V in the presence of Na^+ (blue line, Fig. 5A), whereas this value first decreases and then sharply increases in the presence of Cs^+ (blue line, Fig. 5B). Finally, the RMSD of Pro68 exhibits a strong voltage dependence in the presence of Cs^+ (black line, Fig. 5A), but not in the presence of Na^+ (Fig. 5B, black line).

We next investigated the difference between the transport mechanism in the presence of Na^+ and Cs^+, and we searched for structural signatures at the transition states that account for the coupling between permeation and gating. Therefore, we projected the free energy along the vertical position of the two ions in the selectivity filter (Fig. 6). Different minima in this landscape correspond to states in which the position of at least one of the two ions has changed. Although this landscape does not provide a complete description of the permeation process, it reveals important differences between the Na^+ and Cs^+ systems. In the presence of Na^+, the bottom ion can move between the two local minima without influencing the location of the top ion. In contrast, in the presence of Cs^+, the position of the two ions is coupled, and when the bottom ion moves upward, the top ion

must move toward the outer vestibule, clearly due to the larger size of the Cs^+ ion.

Moreover, we also extrapolated the dependence of this free energy profile on V. In the presence of Na^+, the free energy between the two minima does not change with V (Fig. S7); whereas, in the case of Cs^+, the free energy of the two minima is identical only for positive voltage. Decreasing the voltage causes the first minimum to become progressively favored (Fig. S7). The energy landscape associated to Cs^+ ions' movements within the pore seems to be affected by membrane voltage, thus voltage-dependent asymmetries in current flow are expected in this condition (Fig. S1).

The free energy landscape (Fig. 6B) suggests that for the Cs^+ system, the rate-limiting step of the permeation process, relative to the part of the free energy surface (FES) we have explored, is associated with the concerted movement of the two ions. We then analyzed the structure of the transition state between the two minima (white cross in Fig. 6B), and we identified the average structure of Pro68 at the transition state (blue sticks, Fig. 6C). This structure clearly indicates that at the transition state Pro68 is in a significantly distorted configuration with respect to the main minimum and is not compatible with thermal fluctuations, demonstrating that the permeation process of Cs^+ is coupled with the movement of Pro68 from its equilibrium position. Thus, because the external potential V dramatically affects the conformation of Pro68 only in the presence of Cs^+, V influences only the Cs^+ permeation process (Fig. 5B).

All these results point to the importance of the role played by Pro68. Indeed, the position of the top Cs^+ as well as the RMSD of Pro68 is strongly affected by changes of V (Fig. 5). At the same time, the transition between the two minima in Fig. 6, namely a crucial step in the permeation process, is coupled with a rearrangement of the Pro68 at the transition state (Fig. 6). Therefore, these findings suggest that by varying V one simultaneously controls the gating and affects the transition state of
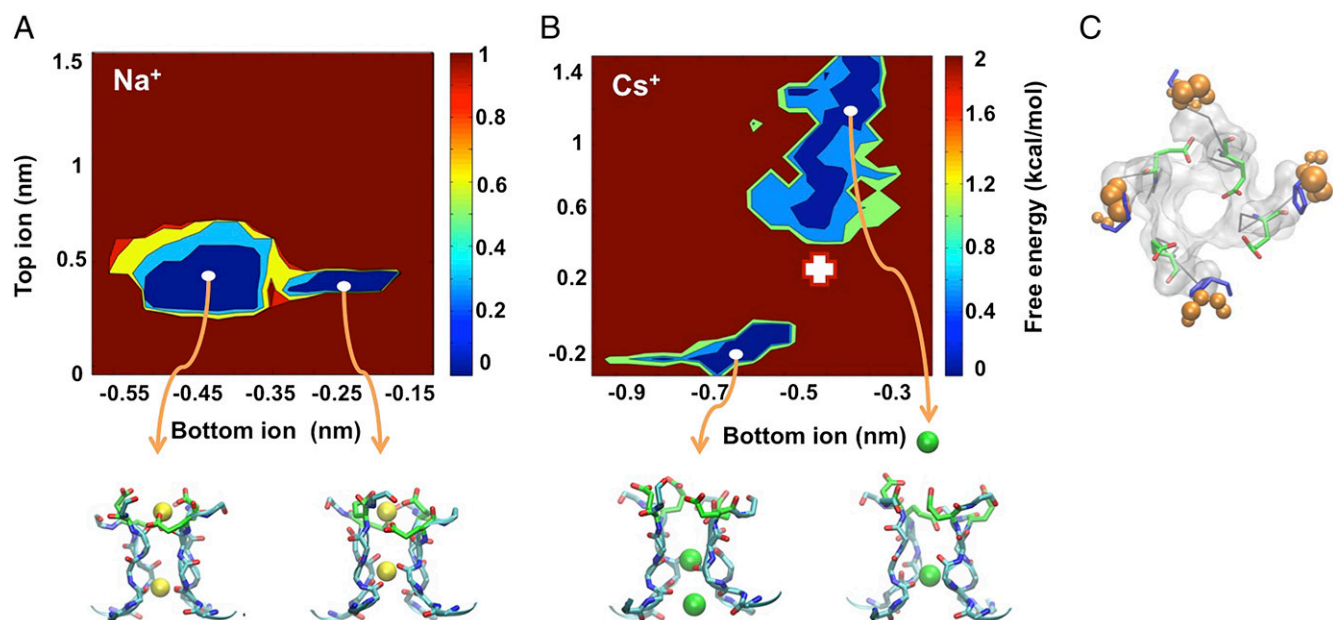

Fig. 6. Free energies of the Na^+ and Cs^+ systems. (A, B) Projection of the free energy (kcal/mol) as a function of the distances of the ions from the center of the mass of the heavy atom of the four Gly65 residues using only the z direction for the Na^+ (A) and Cs^+ (B) systems. (Lower) Representative structures of the minima: the selectivity filter is shown in cyan sticks and Glu66 in green sticks, whereas the ions are shown as yellow (Na^+) or green (Cs^+) spheres. (C) The transition state between the two free energy minima in the Cs^+ system is indicated by a white cross in B. Pro68 is shown in blue sticks. This has been identified by a cluster analysis of structures sampled by the BE simulations with respect to the two CVs on which the free energy is projected, and selecting the structure corresponding to a saddle point. Glu66 residues are shown in green sticks with their oxygens in red. For reference, the structure of Pro68 corresponding to the lower-left free energy minimum is shown as orange spheres centered on each nonhydrogen heavy atom, whose radius is equal to their fluctuation in the minimum.
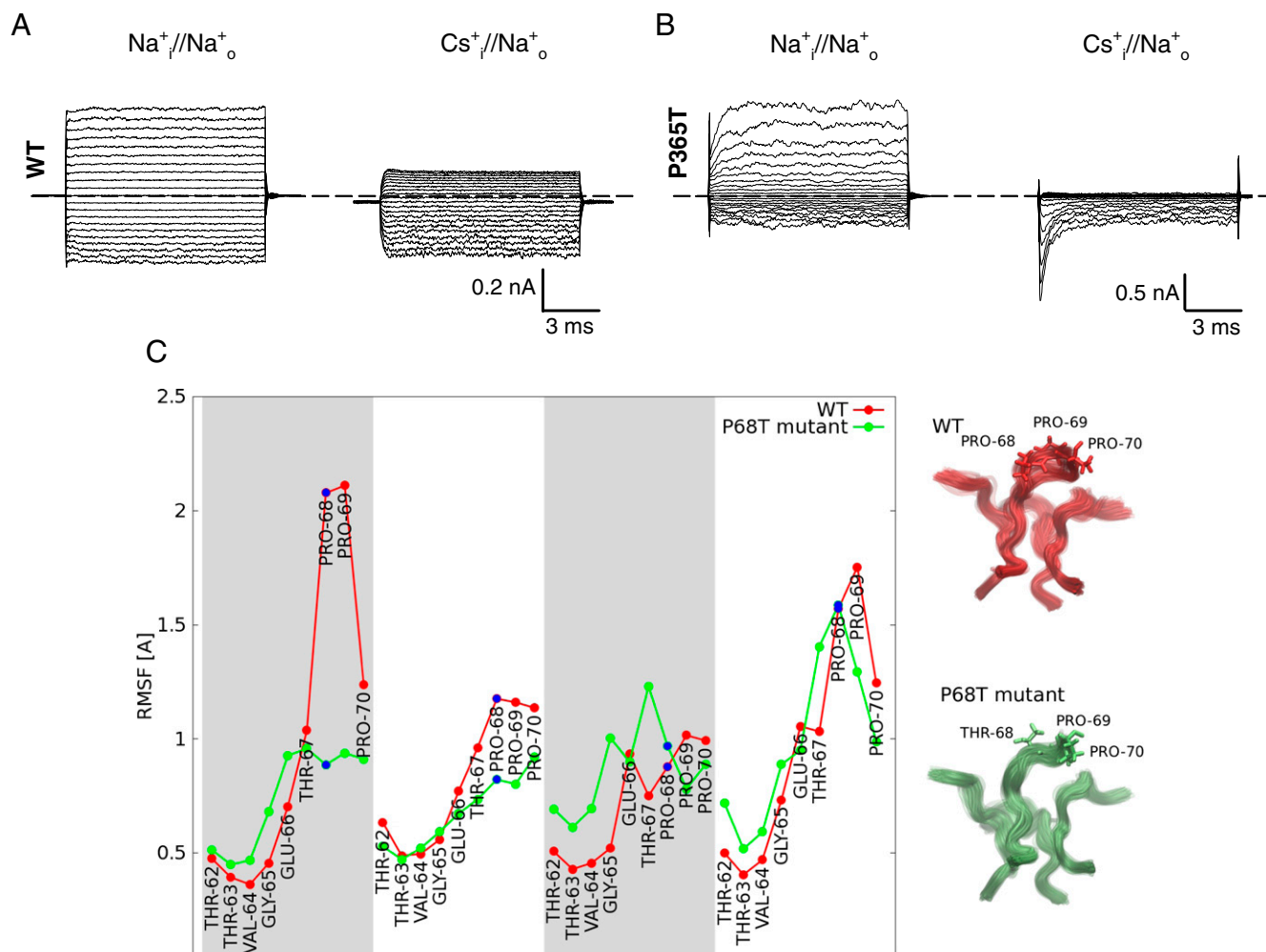
Fig. 7. Flexibility of the WT and Pro68Thr mutant. (*A*) Macroscopic currents recorded from the WT CNGA1 channel in the presence of 110 mM intracellular Na$^+$ (*Left*) and Cs$^+$ (*Right*) with 1 mM cGMP on the cytoplasmic side. The patch pipette was filled with 110 mM Na$^+$. Voltage steps from −200 to +200 mV (ΔV = 20 mV). (*B*) Macroscopic currents recorded from the mutant Pro365Thr CNGA1 channel. Ionic conditions and voltage protocol were the same as in *A*. It is notable that the presence of intracellular Cs$^+$ appears to slow down the deactivation kinetics as large Na$^+$ transients are observed at hyperpolarized membrane potentials only in the presence of Cs$^+$ (*B, Right*). (*C, Left*) Root mean square fluctuations per residue of the selectivity filter (red and green lines for the WT and the Pro68Thr mutant, respectively) calculated along 100-ns-long MD simulations. The four monomers are indicated by alternate white and gray areas. (*C, Right*) The fluctuations of the selectivity filter are shown for the wild type (red) and the mutant (green). Residues 68–70 are shown in sticks.

the permeation process. Indeed, previous electrical recordings from CNGA1 channels confirmed the involvement of this proline in Cs$^+$ permeation (14). When Pro365, which is equivalent to Pro68 in the mimic, is replaced with a threonine, differently from what is observed in the WT channel (Fig. 7*A*), Cs$^+$ permeation is nearly abolished (Fig. 7*B*). A 100-ns-long MD simulation of the Pro68Thr in the presence of Cs$^+$ shows indeed that in the mutant the flexibility of the filter is significantly modified (Fig. 7*C*). Thus, the mutation does not alter the structure of the channel, but its flexibility.

Discussion

By combining electrophysiology, molecular dynamics simulations, and X-ray crystallography we have found that the pore region exhibits a dynamic structure capable of conformational changes. MD simulations indicate that the flexibility critically depends on the ion present within the pore and influences ionic conduction, underlying the coupling between gating and permeation.

When comparing various crystal structures, the pore appears to adapt to the different ions by increasing its size, whereas the side chain of the critical residue Glu66 assumes a variety of conformations (Fig. 3). MD simulations confirm and extend these

observations by showing that the high degree of flexibility of the Glu66 side chains, together with the mobility of Pro68 in the outer vestibule, are likely to play an important role in the permeation of larger alkali cations such as Cs$^+$. Although high-resolution structures of CNG mimics are already available (23) and the mechanisms of ion conduction and selectivity studied since these X-ray structures were determined (26, 33), in this paper we have demonstrated such flexibility and we have discussed its implication in ionic permeation. Previous crystallographic titration experiments in the presence of different Na$^+$ and K$^+$ mole fractions suggested that the selectivity filter architecture does not depend significantly on the ion occupancy (34). Likewise, earlier MD simulations did not reveal conformational changes coupled to ionic permeation in the presence of different ions in this channel (26, 33).

A simple explanation of the selectivity of ionic channels, based on the thermodynamics of ion hydration and geometrical factors, suggested that the poor selectivity of CNG channels could result from a larger flexibility of the pore (35). Our results demonstrate that the filter of CNG-like channels is rather flexible and dynamic, which, according to this model, is consistent with its promiscuous nature. Also the KcsA selectivity filter and adjacent

regions show considerable conformational flexibility, as revealed from a comparison of existing KcsA structures in high and low K^+ and in partial and fully open states (7, 36, 37). These structural snapshots have been proposed to reflect the molecular events leading to the slow mechanism of gating at the selectivity filter known as C-type inactivation in K^+ channels (36, 37).

In K^+ channels, a 2-Å pinching of the permeation pathway at Gly77 appears as the structural signature of the supposed inactivated state (36, 38). In contrast, in the present manuscript, we observed a pore dilation when the channel was loaded with large organic cations. It is interesting to note that, based on electrophysiological experiments, a dilated state of the selectivity filter was previously postulated to occur also in K^+ channel following C-type inactivation: a transient permeation to Na^+ and large organic cation tetramethylammonium was observed upon K^+ ion depletion (39). If the period in K^+-free solutions is prolonged (greater or equal to 200 s), the channels enter a slowly reversible nonconducting or "defunct" state (39, 40). In our experiments we have never observed a loss of conduction in the presence of larger alkali cation Cs^+ and organic compounds: the dilated conformations of the filter reported in Fig. 3 do not appear to be connected to a nonphysiological "defunct" state as in K^+ channels. Moreover, the mobility herein described and the C-type inactivation process seem to have different timescales. Although structural fluctuations in CNG channels occur on nanosecond timescales and are coupled to ionic translocation from one binding site to the next, transitions between conductive and inactivated states of the selectivity filter are associated with high energy barriers in K^+ channels (15–20 kcal mol^{-1}) and occur in a millisecond timescale that are not easily observed in MD simulations (41). This means that throughout simulations, the selectivity filter stayed near the crystallographic conformation which is in contrast with the liquidlike energy landscape herein observed (Fig. 4) and with the mobility of Glu66 side chain and Pro68 observed during our MD trajectories (Movies S1 and S2).

What is the structural basis for the different behaviors of K^+ and CNG channels? In K^+ channels, two key interactions involving the tyrosine residue in the selectivity filter and the charged aspartate immediately following the signature sequence play a major role in maintaining the conductive conformation of the filter and are necessary for K^+ selectivity (42, 43). The ring of bulky tyrosine residues known as the "aromatic girdle" (4, 7) is conserved in most K^+ channels and is thought to provide the putative rigidity and the network of hydrogen bonds necessary to stabilize the structure of the selectivity filter (4, 43, 44). Moreover, the aspartate immediately following the filter has been shown to participate in a multipoint hydrogen bond network defining the energetic profile of C-type inactivation in KcsA channels (42, 45, 46). In CNG channels, the aromatic girdle is replaced by a ring of glutamate residues (Glu363/Glu66), whereas the aspartate immediately following the filter is substituted by Pro365 (Fig. 6). Therefore, these two key structural pillars, which anchor the K^+ channel selectivity filter in its conductive configuration, are lost in CNG channels. Pro365 is the first of a string of three consecutive prolines (Pro365-368) at the extracellular entrance of the selectivity filter. The analysis of the backbone dihedral angles reveals that these residues are arranged in a polyproline II helix, a secondary structure that, in contrast to the more common α-helix, is not stabilized by a regular pattern of main chain hydrogen bonds and is therefore more flexible (47). It is therefore not surprising that our MD simulations and our crystallographic results identify the mobility of Glu66 and Pro68 as the major molecular mechanism underlying the coupling between gating and permeation that is best observed in the presence of symmetrical Na^+ and Cs^+ conditions.

The rotameric change in conformation of the Glu66 side chains herein observed is reminiscent of the mobility recently reported for Na^+ bacterial channels, where the conformational isomerization of a ring of four glutamate side chains lining the

selectivity filter is coupled to ionic coordination (24, 25, 48). We propose that this flexibility, together with the number of equivalent and contiguous ion binding sites in the filter (26, 34, 49), underscores the poor ionic selectivity of CNG channels and reveals a conduction mode that differs substantially from that of classical K^+ channels, which are highly selective and have a fairly rigid molecular structure. This flexibility is likely shared by other nonselective ionic channels, such as transient receptor potential (TRP) and chloride channels, in which a significant coupling among gating and permeation is also known to occur (50–53).

Materials and Methods

Protein Expression and Purification. Expression plasmids for the NaK2CNG chimeric channels (NaK2CNG WT and Phe92Ala mutant) were kindly provided by Prof. Youxing Jiang, University of Texas Southwestern Medical Center, Dallas. Protein expression and purification were performed as previously described (23). In brief, the plasmid encoding the NaK2CNG chimera containing a C-terminal hexahistidine tag was transformed into *Escherichia coli* XL1B cells. Following expression at 25 °C, the proteins were extracted in 50 mM Tris·HCl, pH 8, in the presence of 100 mM KCl, LiCl, or DMA·HCl, and 40 mM n-decyl-β-D-maltoside (DM) (Anagrade) and purified by affinity chromatography using Talon resin, followed by size exclusion chromatography using a Superdex 200 gel filtration column (GE Healthcare) in 20 mM Tris·HCl, pH 8.0, 5 mM DM and the corresponding salt (100 mM LiCl, KCl or DMA·HCl).

Electrophysiology. For single-channel recordings of the NaK2CNG channel, a protein/lipid (POPE/POPG 3:1) ratio of 0.05–0.1 μg mg^{-1} was used to reconstitute the proteoliposomes. The NaK2CNG channel used for functional characterization contains an extra Phe to Ala mutation at a position equivalent to Phe92 of NaK to enhance the single-channel conductance (23). Giant liposomes were obtained by air drying 2–3 μL of liposome sample on a clean coverslip overnight at 4 °C, followed by rehydration in a bath solution at room temperature. Patch pipettes were pulled from borosilicate glass to a resistance of 8–12 MΩ. Solutions on both sides of the membrane consisted of 110 mM XCl, 10 mM Hepes, and 0.2 mM EDTA (pH 7.4), where X is the indicated alkali or organic cation. Voltage control and current acquisition were achieved using a Digidata 1322A board (Molecular Devices), an Axopatch 200 patch clamp amplifier (Molecular Devices), and Clampex Software (Molecular Devices). Currents were low-pass filtered at 5 kHz and sampled at 20 kHz.

Electrical recordings from bovine rod CNGA1 channels and its mutants (P365T) were obtained as previously described (18). In brief, WT and mutant cRNAs were injected into *Xenopus laevis* oocytes ("*Xenopus* express"; Ancienne Ecole de Vernassal), and cGMP-gated currents from excised patches were recorded 2–6 d after RNA injection at room temperature (20–24 °C). Leak and capacitive components from macroscopic currents were removed by subtracting recordings obtained in response to an identical voltage protocol but without cGMP from the cGMP-activated current. Single-channel currents (i_{sc}) were estimated from patches containing only one CNGA1 channel, fitting normalized all-point histograms with two-component Gaussian functions as previously described (18).

Protein Crystallization. Purified NaK2CNG was concentrated to 20 mg/mL and crystallized using the sitting drop vapor diffusion method at 20 °C by mixing equal volumes of protein and reservoir solution (crystallization conditions are provided in Table S1). Crystals of the protein purified in KCl were used in soaking experiments to obtain the structure in complex with various other cations (Na^+, Rb^+, and Cs^+). The crystals were incubated overnight at 20 °C in stabilization solutions containing 70% MPD, 10 mM DM, 100 mM Hepes, pH 7.5, and 100 mM salt (NaCl, RbCl, or CsCl), as previously described (23). For the Li^+, MA^+, and DMA^+ complexes, the protein was purified in the presence of the relevant salt. Crystallization conditions for all of the complexes are summarized in Table S1.

All of the crystals belonged to the tetragonal space group *I*4, with unit cell dimensions a = b = 68 Å and c = 83–90 Å, whereas the protein purified in MACl or DMACl crystallized in the related orthorhombic space group *P*222$_1$. All crystals were flash frozen in liquid nitrogen, and X-ray diffraction data were collected at 100 K at either the European Synchrotron Radiation Facility (ESRF) ID-29 (Na^+, Rb^+, and Cs^+ complex) or Elettra XRD1 beamline (Li^+, MA^+, and DMA^+ complex). Anomalous data were collected for the Cs^+ complex.

Structure Determination. Data reduction was performed using iMOSFLM (54) or XDS (55, 56) and the CCP4i suite (57). The resolution cutoff was chosen following I/σI criterion (58). Most of the datasets exhibited merohedral

twinning (59) and/or anisotropy. The anisotropic data were corrected by applying Sawaya's method (27). The structures were determined by molecular replacement using the published K^+ complex structure (PDB ID: 3K0D) (23), with the selectivity filter region omitted, as a search model. Repeated cycles of refinement using REFMAC5 (60) and model building using Coot were performed (61). Twin refinement was applied when necessary. Refinement statistics are listed in Table S2. All structural figures were prepared using PyMOL (www.pymol.org) software after aligning the tetramers using TM-align (62). PDB_REDO (63) has been used to check the quality of the crystallographic structure here reported.

Models and Simulations. The tetrameric model of the NaK2CNG chimera was based on chain B (residues 19–113) of the Na^+ complex (PDB ID: 3K0G), previously determined by Derebe et al. (23) The His residues, which are all exposed to the intracellular solvent, were protonated in the ε position. The Asp and Glu residues were considered deprotonated, whereas the Arg and Lys residues were considered protonated. The final tetrameric structure contained 95 residues (Ala2 to Arg96). The protein was embedded in a pure, preequilibrated 1-palmitoyl-2 oleylphosphatidylcholine (POPC) lipid model (kindly provided by T. A. Martinek) (64) using the gmembed tool of GROMACS and was oriented following the Orientation of Proteins in Membranes (OPM) database model. Subsequently, the system was neutralized and solvated with TIP3P model water molecules (76,305 total atoms in a box size of 92.8′ 91.9′ 87.5 Å^3). Two systems were prepared with different permeant ions. First, two sodium ions alternated by a water molecule were placed in the three Na^+ binding sites identified in the crystal structure. The simulations were performed in periodic boundary conditions at 300 K using the Nose–Hoover thermostat and Parrinello–Rahman barostat with a semisotropic pressure coupling type and a time step of 2 fs. Position restraints of atoms were fixed with a force constant (K) equal to 1,000 kJ mol^{-1} nm^{-2} were applied during the equilibration. We used the GROMACS4 package with the Amber03 force field for the protein and general amber force field (GAFF) for the membrane. This computational setup has been successfully used in the study of other membrane proteins (65–67). The equilibration was performed in three stages: (*i*) The system was heated for 2.5 ns with the protein backbone and ions fixed, whereas side chains were free to move. (*ii*) A time of 5.2 ns was run using position restraints only for the selectivity filter and the ions. In the first stage, we used the isobaric-isothermal ensemble (NPT) ensemble, whereas in the second stage, a surface tension equal to 600.0 bar·nm^2 was added. (*iii*) For the next 1 ns, the membrane area was held constant, performing constant area isothermal (NAT) simulations.

A configuration obtained from this step was used as a starting point for an MD simulation of ∼100 ns. Moreover, from this configuration, the two Na^+ ions were substituted by two Cs^+ ions, and the new system was relaxed for ∼100-ns-long MD. In the productive MD and subsequent biased simulations of the two systems the tetramer is fully free to relax. The same simulation protocol was used to perform 100-ns-long MD simulation of the Pro68Thr in presence of the Cs^+ ion.

Bias-Exchange Metadynamics. To explore the free energy surface of the conformational states of the channel and better characterize its variability in the two systems, we performed two bias-exchange metadynamics (BE-META) simulations in constant volume isothermal ensemble (NVT) of 384 ns (48 ns * 8 walkers) (for the system with two Na^+ ions in the selectivity filter) and 320 ns (40 ns * 8 walkers) (for the system with two Cs^+ ions in the selectivity filter).

The collective variables used are:

i) The dipole of the selectivity filter, only heavy atoms (164 atoms, 6 residues for each monomer, 2 walkers), defined as:

$$D_t = \sum_i q_i \left(z_{it} - \overline{z_t} \right),\qquad [1]$$

where for each atom i, the charge q is multiplied by the distance of its z coordinate at time t from the average of the z coordinates of all atoms at time t;

ii) the distance between the Cα of Glu66 and the C of the carboxylic group (Cδ) of Glu66 in the opposite monomer (four variables; see Fig. 4C);

iii) the coordination number of the ions with the two oxygens of the carboxylic group of Glu66 (where $n = 6$ and $m = 12$ for both systems; $r_0 = 0:3$ nm for Na^+ and $r_0 = 0:43$ for Cs^+); and

iv) the coordination pairs of the native contacts between carbonyl oxygens (O) of Glu66 residues and the hydroxyl group of Y55 and between carboxylic oxygens (Oδ) of Glu66 residues and the hydroxyl group of T60 ($n = 6$, $m = 12$ and $r_0 = 0:25$).

During the simulation time, the free energy converged for nearly all CVs in both the Na^+ and the Cs^+ systems. In particular, for the analysis of the Na^+ system, we used the two walkers biased on the dipole and the four distances [for a total time of 108 ns (18 ns * 6 walkers)], whereas for the Cs^+ system, we used one dipole, the four distances and the coordination number of the ions (for a total time of 90 ns, namely, 15 ns * 6 walkers). To understand and quantify the differences between the two systems, and, in particular, explain the voltage dependence observed in the electrophysiological experiments, we measured certain observables and we calculated their linear dependence on the external field. The dependence of an observable O on the external voltage V was calculated as follows:

$$o(V) = \frac{\sum_\alpha O_\alpha e^{-\frac{1}{kT}(F_\alpha - fVd_\alpha)}}{\sum_\alpha e^{-\frac{1}{kT}(F_\alpha - fVd_\alpha)}},\qquad [2]$$

where F_α is the free energy of microstate α, d_α is its dipole, f is the Faraday constant (96485.34 C/mol), and O_α is the value of the observable in microstate α. In this manner we did not apply any external voltage in the simulations, but we extrapolated the dependence on V of selected relevant observables using Eq. 2. We considered the following three observables:

i) the RMSD of the heavy atoms Pro68 of each monomer with respect to the crystal structure;

ii) the distance of the center of mass of the four Cδ of Glu66 residues from the center of the pore (measured as the center of mass of the four G65 residues); and

iii) the position of the top ion, measured as the distance of the ion from the center of the mass of the heavy atom of the four G65 residues, using only the z direction.

With the four distances used as CVs in BE-META, we built a variable termed Coordination, which approximately describes the location of the four Glu66 residues. This term is defined as the sum of four switching functions, with each from 0 to 1. The higher the value of this variable, the closer to the crystallographic position of Glu66, as follows:

$$\text{Coordination} = \sum_{i=1}^{4} 1 - \frac{\left(1 - \frac{r_i^{\alpha\delta}}{0.8}\right)^6}{\left(1 - \frac{r_i^{\alpha\delta}}{0.8}\right)^{12}},\qquad [3]$$

where $r_i^{\alpha\delta}$ is the distance between the Cα of Glu66 and the Cδ of Glu66 in the opposite monomer. The sum includes the four pairs of Cα–Cδ.

The free energy as a function of the voltage is estimated as follows:

$$F = -kT\ln\frac{\sum_\alpha e^{-\frac{1}{kT}(F_\alpha - fVd_\alpha)}}{N_\alpha},\qquad [4]$$

where N_α is the number of configurations assigned to microstate α.

1. Hille B (1992) *Ionic Channels of Excitable Membranes* (Sinauer Associates, Sunderland, MA), 2nd Ed.

2. Holmgren M, Shin KS, Yellen G (1998) The activation gate of a voltage-gated K+ channel can be trapped in the open state by an intersubunit metal bridge. *Neuron* 21(3):617–621.

3. Liu Y, Holmgren M, Jurman ME, Yellen G (1997) Gated access to the pore of a voltage-dependent K+ channel. *Neuron* 19(1):175–184.

4. Doyle DA, et al. (1998) The structure of the potassium channel: Molecular basis of K+ conduction and selectivity. *Science* 280(5360):69–77.

5. Jiang Y, et al. (2002) The open pore conformation of potassium channels. *Nature* 417(6888):523–526.

6. Morais-Cabral JH, Zhou Y, MacKinnon R (2001) Energetic optimization of ion conduction rate by the K+ selectivity filter. *Nature* 414(6859):37–42.

7. Zhou Y, Morais-Cabral JH, Kaufman A, MacKinnon R (2001) Chemistry of ion coordination and hydration revealed by a K+ channel-Fab complex at 2.0 A resolution. *Nature* 414(6859):43–48.

8. Mazzolini M, Marchesi A, Giorgetti A, Torre V (2010) Gating in CNGA1 channels. *Pflüg. Arch Eur J Physiol* 459(4):547–555.

9. Craven KB, Zagotta WN (2006) CNG and HCN channels: Two peas, one pod. *Annu Rev Physiol* 68:375–401.
10. Kaupp UB, Seifert R (2002) Cyclic nucleotide-gated ion channels. *Physiol Rev* 82(3):769–824.
11. Contreras JE, Srikumar D, Holmgren M (2008) Gating at the selectivity filter in cyclic nucleotide-gated channels. *Proc Natl Acad Sci USA* 105(9):3310–3314.
12. Hackos DH, Korenbrot JI (1999) Divalent cation selectivity is a function of gating in native and recombinant cyclic nucleotide-gated ion channels from retinal photoreceptors. *J Gen Physiol* 113(6):799–818.
13. Ruiz ML, Karpen JW (1997) Single cyclic nucleotide-gated channels locked in different ligand-bound states. *Nature* 389(6649):389–392.
14. Gamel K, Torre V (2000) The interaction of Na(+) and K(+) in the pore of cyclic nucleotide-gated channels. *Biophys J* 79(5):2475–2493.
15. Holmgren M (2003) Influence of permeant ions on gating in cyclic nucleotide-gated channels. *J Gen Physiol* 121(1):61–72.
16. Kusch J, Nache V, Benndorf K (2004) Effects of permeating ions and cGMP on gating and conductance of rod-type cyclic nucleotide-gated (CNGA1) channels. *J Physiol* 560(Pt 3):605–616.
17. Arcangeletti M, Marchesi A, Mazzolini M, Torre V (2013) Multiple mechanisms underlying rectification in retinal cyclic nucleotide-gated (CNGA1) channels. *Physiol Rep* 1(6):e00148.
18. Marchesi A, Mazzolini M, Torre V (2012) Gating of cyclic nucleotide-gated channels is voltage dependent. *Nat Commun* 3:973.
19. Higgins MK, Weitz D, Warne T, Schertler GFX, Kaupp UB (2002) Molecular architecture of a retinal cGMP-gated channel: The arrangement of the cytoplasmic domains. *EMBO J* 21(9):2087–2094.
20. Zagotta WN, et al. (2003) Structural basis for modulation and agonist specificity of HCN pacemaker channels. *Nature* 425(6954):200–205.
21. Lolicato M, et al. (2011) Tetramerization dynamics of C-terminal domain underlies isoform-specific cAMP gating in hyperpolarization-activated cyclic nucleotide-gated channels. *J Biol Chem* 286(52):44811–44820.
22. Shuart NG, Haitin Y, Camp SS, Black KD, Zagotta WN (2011) Molecular mechanism for 3:1 subunit stoichiometry of rod cyclic nucleotide-gated ion channels. *Nat Commun* 2:457.
23. Derebe MG, Zeng W, Li Y, Alam A, Jiang Y (2011) Structural studies of ion permeation and Ca2+ blockage of a bacterial channel mimicking the cyclic nucleotide-gated channel pore. *Proc Natl Acad Sci USA* 108(2):592–597.
24. Chakrabarti N, et al. (2013) Catalysis of Na+ permeation in the bacterial sodium channel Na(V)Ab. *Proc Natl Acad Sci USA* 110(28):11331–11336.
25. Boiteux C, Vorobyov I, Allen TW (2014) Ion conduction and conformational flexibility of a bacterial voltage-gated sodium channel. *Proc Natl Acad Sci USA* 111(9):3454–3459.
26. Furini S, Domene C (2012) Nonselective conduction in a mutated NaK channel with three cation-binding sites. *Biophys J* 103(10):2106–2114.
27. Strong M, et al. (2006) Toward the structural genomics of complexes: Crystal structure of a PE/PPE protein complex from Mycobacterium tuberculosis. *Proc Natl Acad Sci USA* 103(21):8060–8065.
28. Picco C, Menini A (1993) The permeability of the cGMP-activated channel to organic cations in retinal rods of the tiger salamander. *J Physiol* 460:741–758.
29. Rodriguez A, Laio A (2014) Machine learning. Clustering by fast search and find of density peaks. *Science* 344(6191):1492–1496.
30. Baftizadeh F, Biarnes X, Pietrucci F, Affinito F, Laio A (2012) Multidimensional view of amyloid fibril nucleation in atomistic detail. *J Am Chem Soc* 134(8):3886–3894.
31. Piana S, Laio A (2007) A bias-exchange approach to protein folding. *J Phys Chem B* 111(17):4553–4559.
32. Granata D, Camilloni C, Vendruscolo M, Laio A (2013) Characterization of the free-energy landscapes of proteins by NMR-guided metadynamics. *Proc Natl Acad Sci USA* 110(17):6817–6822.
33. Furini S, Domene C (2011) Gating at the selectivity filter of ion channels that conduct Na+ and K+ ions. *Biophys J* 101(7):1623–1631.
34. Sauer DB, Zeng W, Canty J, Lam Y, Jiang Y (2013) Sodium and potassium competition in potassium-selective and non-selective channels. *Nat Commun* 4:2721.
35. Laio A, Torre V (1999) Physical origin of selectivity in ionic channels of biological membranes. *Biophys J* 76(1 Pt 1):129–148.
36. Cuello LG, et al. (2010) Structural basis for the coupling between activation and inactivation gates in K(+) channels. *Nature* 466(7303):272–275.
37. Cuello LG, Jogini V, Cortes DM, Perozo E (2010) Structural mechanism of C-type inactivation in K(+) channels. *Nature* 466(7303):203–208.
38. Cordero-Morales JF, et al. (2006) Molecular determinants of gating at the potassium-channel selectivity filter. *Nat Struct Mol Biol* 13(4):311–318.
39. Loboda A, Melishchuk A, Armstrong C (2001) Dilated and defunct K channels in the absence of K+. *Biophys J* 80(6):2704–2714.
40. Hoshi T, Armstrong CM (2013) C-type inactivation of voltage-gated K+ channels: Pore constriction or dilation? *J Gen Physiol* 141(2):151–160.
41. Ostmeyer J, Chakrapani S, Pan AC, Perozo E, Roux B (2013) Recovery from slow inactivation in K+ channels is controlled by water molecules. *Nature* 501(7465):121–124.
42. Cheng WW, McCoy JG, Thompson AN, Nichols CG, Nimigean CM (2011) Mechanism for selectivity-inactivation coupling in KcsA potassium channels. *Proc Natl Acad Sci USA* 108(13):5272–5277.
43. Sauer DB, Zeng W, Raghunathan S, Jiang Y (2011) Protein interactions central to stabilizing the K+ channel selectivity filter in a four-sited configuration for selective K+ permeation. *Proc Natl Acad Sci USA* 108(40):16634–16639.
44. Bernèche S, Roux B (2005) A gate in the selectivity filter of potassium channels. *Structure* 13(4):591–600.
45. Cordero-Morales JF, et al. (2007) Molecular driving forces determining potassium channel slow inactivation. *Nat Struct Mol Biol* 14(11):1062–1069.
46. Cordero-Morales JF, Jogini V, Chakrapani S, Perozo E (2011) A multipoint hydrogen-bond network underlying KcsA C-type inactivation. *Biophys J* 100(10):2387–2393.
47. Adzhubei AA, Sternberg MJE, Makarov AA (2013) Polyproline-II helix in proteins: Structure and function. *J Mol Biol* 425(12):2100–2132.
48. Furini S, Domene C (2012) On conduction in a bacterial sodium channel. *PLOS Comput Biol* 8(4):e1002476.
49. Derebe MG, et al. (2011) Tuning the ion selectivity of tetrameric cation channels by changing the number of ion binding sites. *Proc Natl Acad Sci USA* 108(2):598–602.
50. Betto G, et al. (2014) Interactions between permeation and gating in the TMEM16B/anoctamin2 calcium-activated chloride channel. *J Gen Physiol* 143(6):703–718.
51. Chung MK, Güler AD, Caterina MJ (2008) TRPV1 shows dynamic ionic selectivity during agonist stimulation. *Nat Neurosci* 11(5):555–564.
52. Banke TG, Chaplan SR, Wickenden AD (2010) Dynamic changes in the TRPA1 selectivity filter lead to progressive but reversible pore dilation. *Am J Physiol Cell Physiol* 298(6):C1457–C1468.
53. Darré L, Furini S, Domene C (2015) Permeation and dynamics of an open-activated TRPV1 channel. *J Mol Biol* 427(2):537–549.
54. Leslie AGW (2006) The integration of macromolecular diffraction data. *Acta Crystallogr D Biol Crystallogr* 62(Pt 1):48–57.
55. Kabsch W (2010) Integration, scaling, space-group assignment and post-refinement. *Acta Crystallogr D Biol Crystallogr* 66(Pt 2):133–144.
56. Kabsch W (2010) XDS. *Acta Crystallogr D Biol Crystallogr* 66(Pt 2):125–132.
57. Collaborative Computational Project, Number 4 (1994) The CCP4 suite: Programs for protein crystallography. *Acta Crystallogr D Biol Crystallogr* 50(Pt 5):760–763.
58. Karplus PA, Diederichs K (2012) Linking crystallographic model and data quality. *Science* 336(6084):1030–1033.
59. Yeates TO (1997) Detecting and overcoming crystal twinning. *Methods Enzymol* 276:344–358.
60. Murshudov GN, et al. (2011) REFMAC5 for the refinement of macromolecular crystal structures. *Acta Crystallogr D Biol Crystallogr* 67(Pt 4):355–367.
61. Emsley P, Lohkamp B, Scott WG, Cowtan K (2010) Features and development of Coot. *Acta Crystallogr D Biol Crystallogr* 66(Pt 4):486–501.
62. Zhang Y, Skolnick J (2005) TM-align: A protein structure alignment algorithm based on the TM-score. *Nucleic Acids Res* 33(7):2302–2309.
63. Joosten RP, Joosten K, Murshudov GN, Perrakis A (2012) PDB_REDO: Constructive validation, more than just looking for errors. *Acta Crystallogr D Biol Crystallogr* 68(Pt 4):484–496.
64. Jójárt B, Martinek TA (2007) Performance of the general amber force field in modeling aqueous POPC membrane bilayers. *J Comput Chem* 28(12):2051–2058.
65. Schulz R, Vargiu AV, Collu F, Kleinekathöfer U, Ruggerone P (2010) Functional rotation of the transporter AcrB: Insights into drug extrusion from simulations. *PLOS Comput Biol* 6(6):e1000806.
66. Jójárt B, Kiss R, Viskolcz B, Keseru GM (2008) Activation mechanism of the human histamine H4 receptor—An explicit membrane molecular dynamics simulation study. *J Chem Inf Model* 48(6):1199–1210.
67. Bisha I, Rodriguez A, Laio A, Magistrato A (2014) Metadynamics simulations reveal a Na+ independent exiting path of galactose for the inward-facing conformation of vSGLT. *PLOS Comput Biol* 10(12):e1004017.

92

Interactions between the C-linker and the S4-S5 linker mediate gating in CNGA1 channels

Manuel Arcangeletti[1], Monica Mazzolini[1], Claudio Anselmi[2], Debora Grosa[1], Sourav Maity[1], Arin Marchesi[3], Luisa Napolitano[1-4] and Vincent Torre[1]

In preparation

Interactions between the C-linker and the S4-S5 linker mediate gating in CNGA1 channels

Manuel Arcangeletti[1], Monica Mazzolini[1], Claudio Anselmi[2], Debora Grosa[1], Sourav Maity[1], Arin Marchesi[3], Luisa Napolitano[1-4] and Vincent Torre[1]

[1] International School for Advanced Studies, Trieste 34136, Italy;

[2] National Heart, Lung and Blood Institute, National Institutes of Health, Bethesda, Maryland 20892, USA;

[3] French Institute of Health and Medical Research Paris, Bio-AFM Lab, Marseille, France;

[4] Structural Biology Laboratory, Elettra-Sincrotrone Trieste S.C.p.A., Basovizza, Trieste 34149, Italy;

Abstract

Cyclic Nucleotide Gated (CNG) channels underlie sensory transduction in photoreceptors and olfactory epithelium. They belong to the family of voltage-gated ion channels, but open following binding of cyclic nucleotides (CNs). While electrophysiology combined with mutagenesis have identified the channel pore and the binding domain for CNs, conformational changes associated with gating have remained elusive. In this study we combine electrophysiology, site-directed mutagenesis, homology modelling and single molecule force spectroscopy (SMFS) to determine the molecular mechanisms underlying gating. Gating is mediated by electrostatic interactions between aspartate D413 in the C-linker and arginine R297 in the S4-S5 linker. Indeed when residues in position 413 and 297 are cross-linked, the mutant channels are locked in the open state. These electrostatic interactions induce an upward motion combined with a small rotation of the transmembrane α-helix S5 leading to conformational rearrangements of residues flanking the pore so that the lumen of the pore widens and the channel opens. Therefore gating of CNG channels is not mediated by a motion of the transmembrane α-helix S6 as in usual voltage gated Na^+, K^+ and Ca^{2+} channels, but by interactions between the cytoplasmic domain and the S4-S5 linker, possibly shared also by HCN channels.

Introduction

Ion channels are membrane proteins playing a major functional role in all cells. They can open in response to voltage and/or ligands (gating), and when open, they allow the passage of specific molecules and ions (permeation) (Hille, 2001). Ion channels are divided into families; cyclic nucleotide-gated (CNG) channels, together with K^+, Na^+, Ca^{2+} and transient receptor potential channels are members of the superfamily of voltage-gated ion channels, whose gating (transitions between the open and closed conformation) depends on the membrane (del Camino et al., 2000; Doyle et al., 1998; Hille, 2001; Hodgkin and Huxley, 1952; Holmgren et al., 1998; Jan, 1990; Mazzolini et al., 2010; Payandeh et al.), but their conductance is thought to be independent from the membrane potential, and their gating regulated by the binding of cytosolic cyclic nucleotides (CNs) to the cyclic nucleotide-binding (CNB) domain (Kaupp and Seifert, 2002; Kaupp et al., 1989; Matulef and Zagotta, 2002). CNG channels are expressed in vertebrate photoreceptors and olfactory sensory neurons, and mediate sensory transduction (Kaupp and Seifert, 2002; Mazzolini et al., 2010). Native CNG channels are heterotetramers composed of A (CNGA1-A5) and B (CNGB1 and B3) subunits (Kaupp and Seifert, 2002; Mazzolini et al., 2010; Tetreault et al., 2006). CNGA1 channels, when expressed in a heterologous system, can form functional channels with properties similar, but not identical, to native CNG channels (Colamartino et al., 1991; Kaupp and Seifert, 2002; Picco and Menini, 1993; Sesti et al., 1995; Tetreault et al., 2006).

In K^+ and Na^+ channels, gating is controlled by a 'bundle crossing' at the intracellular side, which controls the opening and closing of the pore (del Camino et al., 2000; Doyle et al., 1998; Holmgren et al., 1998; Long et al., 2005) while in CNG channels, the gate is located in the selectivity filter (Contreras et al., 2008; Mazzolini et al., 2010). A single subunit of bovine CNGA1 channels are constituted by 690 amino acid residues (a.a.) with six transmembrane α-helices (S1 to S6) linked by nonspanning loops, which are either extracellular or intracellular with both the amino- and carboxy-terminal ends in the cytoplasmic side (Kaupp et al., 1989).

The functional properties of CNG channels have been broadly investigated (Craven and Zagotta, 2006; Kaupp and Seifert, 2002; Mazzolini et al., 2010) but only few structural information are available (Derebe et al., 2011; Higgins et al., 2002; Lolicato et al., 2011; Napolitano et al., 2015; Schünke et al., 2011; Shuart et al., 2011; Zagotta et al., 2003); additionally, the full-length channel has never been crystallized and the gating mechanism is still not understood. The molecular mechanism by which the binding of CNs to the CNB domain is triggered to the opening of the channel (gating) has been the subject of many investigations (Craven and Zagotta, 2006;

Cukkemane et al., 2011; Gofman et al., 2014; Karpen and Ruiz, 2002; Maity et al., 2015; Mazzolini et al., 2010; Richards and Gordon, 2000). Conformational changes of S6 - such as a rotation, tilting and a translation - have been proposed to act as the main gate of CNGA1 channels (Flynn and Zagotta, 2001).

In the present manuscript, we show that gating in CNGA1 involves molecular mechanisms different from those previously proposed: first, gating is mediated primarily by electrostatic interactions between the C-linker and the S4-S5 linker; second, as a consequence of these interactions, the linker S4-S5 changes its rigidity. Third, although if a more thorough analysis with investigation of additional mutants in the upper region of S5 is certainly required, on the basis of our preliminary results, we hypothesize that there is a small upward motion of S5 inducing the widening of the pore lumen opening the pore. Therefore, the movements of S6, underlying gating in voltage dependent K^+ and Na^+ channels, are not pivotal in CNGA1 channels in which, instead, the motion of S5 is the crucial event. Thus, a gating mechanism based on electrostatic interactions between an Arginine and an Aspartate located in the S4-S5 and C-linker, respectively, could be a molecular mechanism common to CNG and HCN channels.

Methods

Modelling of CNGA1.

Template structures were searched for in the Protein Data Bank by using HHpred (Söding, 2005) with three multiple sequence alignment (MSA) generation iterations and HHblits (Remmert et al., 2012) as MSA generation method. The bovine CNGA1 sequence accession number was Q00194 from the UniProtKB database (Consortium, 2014). The best resulting template was the paddle chimera channel Kv1.2-Kv2.1 (PDB id. 2R9R) (Long et al., 2007) with ~12% of sequence identity. The initial alignment was performed with HHalign (Söding, 2005) and then it was refined following an iterative procedure. First of all, we analyzed the predicted secondary structure and transmembrane topology of CNGA1 to avoid gaps in secondary structure regions. Then we ensured that less conserved residues point toward the protein surface, while more conserved residues participate to the protein core. Finally regions with lower sequence identity were refined by building structural models with different shifted alignments and assessing the likelihood of those models by calculating the local ProQM score (Ray et al., 2010). The secondary structure

prediction was performed with PSIPRED v3.3 (Buchan et al., 2013), while the transmembrane topology prediction has been performed with the TOPCONS web server (Bernsel et al., 2009). The conservation patterns were calculated with the ConSurf server (Ashkenazy et al., 2010). All structural models were generated as tetramers by homology modeling with MODELLER v. 9.10 (Šali, 1995). In order to improve the modeling of the pore region, we introduced a second template, the CNG-mimicking NaK mutant (PDB id. 3K04) (Derebe et al., 2011). Thus the NaK mutant pore region from residues 52 to 86 was structurally aligned to that of the chimera channel Kv1.2-Kv2.1 with STAMP (Russell and Barton, 1992). The final alignment used for homology modeling is reported in (see Supplementary Fig. SI1A). The best model with the lowest MODELLER probability distribution function score out of a set of 100 models was further refined following the fast relax protocol of ROSETTA version 2014wk05 (Leaver-Fay et al., 2011), with 5 relaxation cycles and using the high-resolution energy function for proteins in the membrane environment (Barth et al., 2007; Yarov-Yarovoy et al., 2006). Four-fold symmetry was imposed by using ROSETTA symmetric mode. The final model was that with the lowest ROSETTA score out of a set of 100 models. Finally the helices A' of the C-linker (residues 407-420) were added to the best ROSETTA model by extending the helices S6 with MODELLER. Supplementary Fig. SI1B shows the ProQM profiles of the best structural models obtained with initial and final alignment and after the ROSETTA relax. Thanks to the refinement procedure, the total ProQM scores of the best models improve from 0.60 for the initial alignment, to 0.61 for the final alignment to 0.65 for the final ROSETTA model. In addition, it is known that the addition of the mild oxidizing agent copper phenanthroline (CuP) locks the F380C mutant either in the open or closed state suggesting that the cysteine in position 380 can form a disulfide bridge with the endogenous C314 (Nair et al., 2006) and, consequently, that this two residues can access conformations where they are close in space. In the initial model the Cα-Cα distance between F380 and C314 is extremely large, equal to 21.4 Å, but it lowers to 13.4 Å in the final model. Even if this distance is actually larger than in a normal disulfide bridge, it should be considered that the expected accuracy of the model is ~3.5 Å RMSD on Cα atoms due to the low sequence identity (~12%) (Forrest et al., 2006). In addition cysteine bridging often captures conformations that are not the equilibrium ones due to the irreversible S-S bonding.

Evaluating the structural rigidity of the hinge between S4 and S4-S5 by free-energy calculations.

We planned to evaluate the structural rigidity of the hinge between S4 and S4-S5, approximately corresponding to residues 291-293, for the WT CNGA1 channel and the mutants P293A, P293G and P293F by means of molecular dynamics (MD) and free-energy calculations. However, the low accuracy of the CNGA1 model (~3.5 Å RMSD on Cα atoms), consequence of the ~12% sequence identity (Forrest et al., 2006), prevented us from running free-energy MD simulations on the whole channel. We therefore decided to tackle the problem in a simpler way. We built α-helical models of the 19 amino acid tracts from F283 to L301 for the wt and the mutants and evaluated the energy of helix unfolding at residues 291-293. Initially an α-helix was built for the P293A mutant with UCSF Chimera v. 1.8.1 (Yang et al., 2012), as alanine can stabilize the secondary structure. The helix was inserted in a cubic box with edge length of 60 Å containing ~6,700 TIP3P water molecules. Na^+ and Cl^- ions were introduced to achieve the system electroneutrality and guarantee 100 mM electrolyte concentration. The final molecular model amounts to ~20,000 atoms. As regards for equilibration, we used conventional MD simulations with gradually weaker positional constraints applied to the protein followed by 10 ns of simulation. The molecular models of the WT and the other mutants were generated from the last snapshot of the P293A simulation by alchemically converting the alanine residue into the desired amino acid in a continuous way over 1 ns MD run. The CHARMM36 force field for proteins (Best et al., 2012) was used in all the calculations. All molecular dynamics (MD) simulations were carried out with NAMD 2.9 (Phillips et al., 2005) at constant pressure (1 atm) and temperature (298 K) and with periodic boundary conditions. The pressure was maintained using a Nose-Hoover Langevin piston barostat (Feller et al., 1995). Temperature control was performed by using Langevin dynamics. Electrostatic interactions were calculated using Particle-Mesh Ewald (PME) (Darden et al., 1993) with a real space cutoff of 12 Å. The same cut-off was also used for treating the van-der-Waals interactions by means of a shifted Lennard-Jones potential. Numerical integration of the equations of motion used a time step of 2 fs. Free energy calculations were carried out with the adaptive biasing force (ABF) method (Hénin et al., 2010). The chosen coordinate of reaction (COR) was the distance between the centers of mass of the Cα atoms of the four amino acids preceding N291 and following P293, discretized in small bins of width 0.01 Å. The biasing force was applied just after 500 determinations of the instantaneous force acting along the COR for each bin. X short ABF simulations (X ns) were performed for each system until the convergence of the free-energy profiles was reached (see Supplementary Fig. SI3A).

Ethical approval

All studies were approved by the SISSA's Ethics Committee according to the Italian and European guidelines for animal care (d.l. 116/92; 86/609/C.E.). Oocytes were harvested from female *Xenopus laevis* frogs using an aseptic technique. All *X. laevis* surgeries were performed under general anaesthesia, obtained by immersion in a 0.2% solution of tricaine methane sulfonate (MS-222) adjusted to pH 7.4 for 15–20 min. Depth of anaesthesia was assessed by loss of the righting reflex and loss of withdrawal reflex to a toe pinch. After surgery animals were singly housed for 48 h. Frogs were monitored daily for 1 week post-operatively to ensure the absence of any surgery-related stress. Post-operative analgesics were not routinely used. Considering the simplicity of the procedure, the lack of complications, the effectiveness of anaesthetic regimens and reductions in the number of animals likely to occur compared to the number that would be required if only one surgery were permitted, multiple surgeries on a single animal were performed. Individual donors were used up to five times, conditional upon the relative health of an individual animal. Recovery time between oocyte collection from the same animal was maximized by rotation of the frogs being used. A minimum recovery period of 1 month was ensured between ovarian lobe resection from the same animal to avoid distress. Evidence of surgery-related stress resulted in an extended rest period based on recommendations from the veterinary staff. After the fifth terminal surgery frogs were humanely killed through anaesthesia overdose via 2 h of immersion in a 5 g l−1 MS-222 solution adjusted to pH 7.4.

Molecular biology

The CNGA1 channel from bovine rods consisting of 690 amino acids was used (Kaupp et al., 1989). Selected residues were replaced as described (Becchetti et al., 1999) using the Quick Change Site-Directed Mutagenesis kit (Stratagene, La Jolla, CA, USA). Point mutations were confirmed by sequencing, using a LI-COR sequencer (4000 l; LI-COR Biosciences, Lincoln, NE, USA). cDNAs were linearized and were transcribed to cRNA in vitro using themMessage mMachine kit (Ambion, Austin, TX, USA).

Oocyte preparation and chemicals

Mutant channel cRNAs were injected into X. laevis oocytes ('Xenopus express' Ancienne Ecole de Vernassal, Le Bourg 43270, Vernassal,Haute-Loire, France). Oocytes were prepared as described (Nizzari et al., 1993). Injected eggs were maintained at 18°C in a Barth solution supplemented with

50 µg ml–1 gentamycin sulfate and containing (in mM): 88 NaCl, 1 KCl, 0.82 MgSO4, 0.33 Ca(NO3)2, 0.41 CaCl2, 2.4 NaHCO3 and 5 Tris-HCl, pH 7.4 (buffered with NaOH). During the experiments, oocytes were kept in a Ringer solution containing (in mM): 110 NaCl, 2.5 KCl, 1 CaCl2, 1.6MgCl2 and 10 Hepes, pH 7.4 (buffered with NaOH). Usual salts and reagents were purchased from Sigma Chemicals (St Louis, MO, USA), and MTS compounds were purchased from TRC (Toronto Research Chemicals, Canada). MTSET link covalently to only one cysteine. Cross-linker compounds such as M–2–M (1,2-Ethanediyl bismethanethiosulfonate) and M–4–M (1,4-Butanediyl bismethanethiosulfonate) had different maximum cross-linking span—i.e., the longest distance between the S atoms of the cross-linker reacting with the S atoms of cysteine and forming S–S bonds (Loo and Clarke, 2001). These compounds, in contrast, can link to two cysteines. The cross-linker M–2–M has a cross-linking span of 5.2 Å and an actual volume of 139 $Å^3$. When M–2–M reacts with an S atom it loses one SO_2CH_3 group and when it cross-links with two S atoms its effective volume becomes 73.8 $Å^3$. The different effect of reagents able to link to one cysteine - such as MTSET, MTSPT, MTSPtrEA - and those able to link to two cysteines - M-X-M cross-linkers - with the same size and volume is used to discriminate whether blockage is caused by bridging two cysteines by the binding of the compound to one end only.

Recording apparatus

cGMP-gated currents from excised patches (Hamill et al., 1981) were recorded with a patch-clamp amplifier (Axopatch 200; Axon Instruments Inc., Foster City, CA, USA), 2–6 days after RNA injection, at room temperature (20–24°C). The perfusion system was as described (Sesti et al., 1995) and allowed a complete solution change in less than 0.1 s. Macroscopic and single-channel current recordings were obtained with borosilicate glass pipettes which had resistances of 2–5Min symmetrical standard solution. The standard solution on both sides of the membrane consisted of (in mM) 110 NaCl, 10 Hepes and 0.2 EDTA (pH 7.4). Solutions were buffered with tetramethylammonium hydroxide at the desired pH. When the cation X^+ was used as the charge carrier, NaCl in the standard solution on both sides of the membrane patch was replaced by an equimolar amount of the cation X^+. We used Clampex version 10.0 for data acquisition. Recordings to perform noise analysis were low-pass filtered at 10 kHz. Current signals were sampled with a 16-bit A/D converter (Digidata 1440A; Axon Instruments), using a sampling rate of 50 kHz. All other macroscopic current recordings were low-pass filtered at 1 kHz and sampled at 2.5 kHz if not otherwise indicated.

Data analysis

Statistical significance for parametric analysis was determined using unpaired two-tailed t-test or single-variable ANOVA, as indicated. For pairwise comparisons, a Holm–Sidak test was used as post hoc test. $P < 0.01$ or $P < 0.05$ were considered significant, as indicated. Data analysis and figures were made with Clampfit version 10.1 (Molecular Devices, Sunnyvale, CA, USA) and Sigmaplot 12.5 (Systat Software, Chicago, IL, USA). Kinetic models were generated and evaluated using MatLab 7.9.0 (MathWorks, Natick, MA, USA).

SMFS experiments and data processing

See Maity et al., 2015 for methods.

Results

We carried out an extensive site-directed alanine or cysteine scanning mutagenesis in the S4-S5, S5, P-helix, S6 and C-linker domains of the CNGA1 channel and the effect on channel activity of sulfhydryl-specific cross-linkers and reagents, in excised inside-out patches, in the presence and in the absence of a saturating concentration of cGMP, was examined. The mutant and WT constructs were expressed in Xenopus laevis oocytes. Each residue was mutated either into an Alanine and/or into a Cysteine (A/C); residues when mutated into alanine become almost unreactive but when mutated into a cysteine can react with the thiol group of the cysteine of a variety of agents (DeLano, 2002).

Mutation of specific residues alters gating of CNGA1 channels
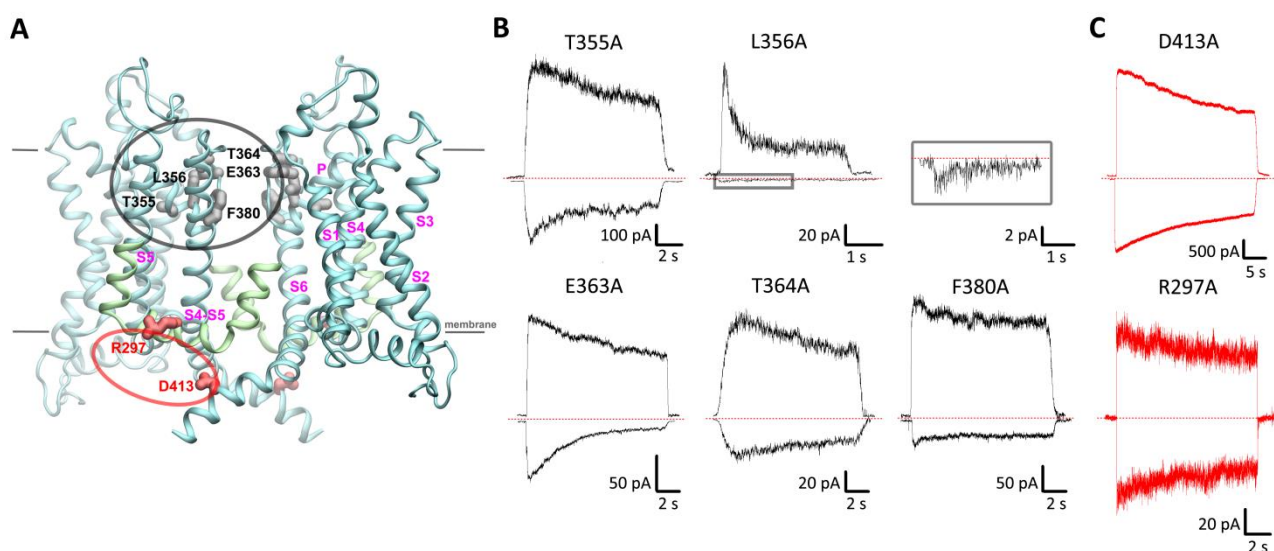
Figure 1: Inactivation of mutant channels. A: cartoon representation of two opposite subunits of the homology model of the tetrameric bovine CNGA1 channel. Key residues are highlighted in stick representation. Mutant channels that inactivate in a voltage dependent manner (black circle); mutant channels that inactivate in a non-voltage dependent manner (red circle) **B-C:** cGMP-activated currents in symmetrical Na$^+$ solution in the presence of 1 mM cGMP at ±60 mV for mutant channels that inactivate in a voltage dependent manner T355A, L356A, E363A, T364A, F380A (**B**) and for mutant channels that inactivate in a non-voltage dependent manner: D413A and R297A (**C**). Dashed red lines indicate the closed state of the channels.

We mutated into cysteine and/or alanine each residue from L583 to N610, that correspond to the C-helix of the CNB domain (Giorgetti et al., 2005; Mazzolini et al., 2002, 2010), residues from R345 to S371 in the pore region (Becchetti et al., 1999), from F375 to S399 in the S6 TM domain

(Giorgetti et al., 2005; Mazzolini et al., 2010; Nair et al., 2009), from N400 to V424 in the C-linker (Giorgetti et al., 2005; Nair et al., 2009), from R289 to R297 in the S4-S5 linker and from I298 to I308 and S320 to D328 in S5 TM domain. Voltage pulses at + and - 60 mV and lasting 10-30 s were applied, while changing the medium bathing the intracellular side of the membrane patch. Out of all these 125 mutant channels we found only 7 (T355A, L356A, E363A, T364A, F380A, D413A and R297A) that, in symmetrical Na^+ condition, exhibited inactivation, i.e. a decline in time of the cGMP-activated current.

Gating and inactivation was voltage dependent (**Fig.1B**) in 5 of these mutant channels (T355A, L356A, E363A, T364A and F380A) and the inactivation was more pronounced at negative than that at positive voltages (**Fig.1B, D**). Unexpectedly we found two mutant channels D413A (as well as D413C) and R297A (as well as R297C) which inactivated in a non-voltage dependent way and the amplitude of the cGMP activated current was very weakly voltage dependent (**Fig.1C, D**).

Homology modelling (**Fig.1A**) shows that D413 is located in the A' helix of C-linker – i.e. in the cytoplasmic domain - and R297 in the intracellular loop connecting S4 and S5 – i.e. the S4-S5 linker. In contrast, mutant channels inactivating in a voltage dependent way, are located closer to the pore region. Voltage independent inactivation in mutant D413A and R297A and their distant location from the pore suggest that they could play an important role in gating, i.e. in the coupling of conformational changes occurring in the CNB domain and those in the transmembrane (TM) domain. Indeed the ionic bonds between the side chain of the positively charged R297 and of the negatively charged D413 could be the molecular mechanism relaying events occurring in the CNB domain to those occurring in the TM domain leading to the widening of the pore lumen, as in HCN2 channels where electrostatic interaction between R339 of the S4-S5 linker and D443 of the C-linker is necessary to stabilize the closed state (Decher et al., 2004).

The double mutant channel R297C_D413C can be locked in the open state

In order to verify the involvement of the interaction between D413 and R297 in the coupling between gating and voltage sensing in the CNGA1 channel, we constructed a double mutant (D413C_R297C) having both the residues mutated into cysteines.
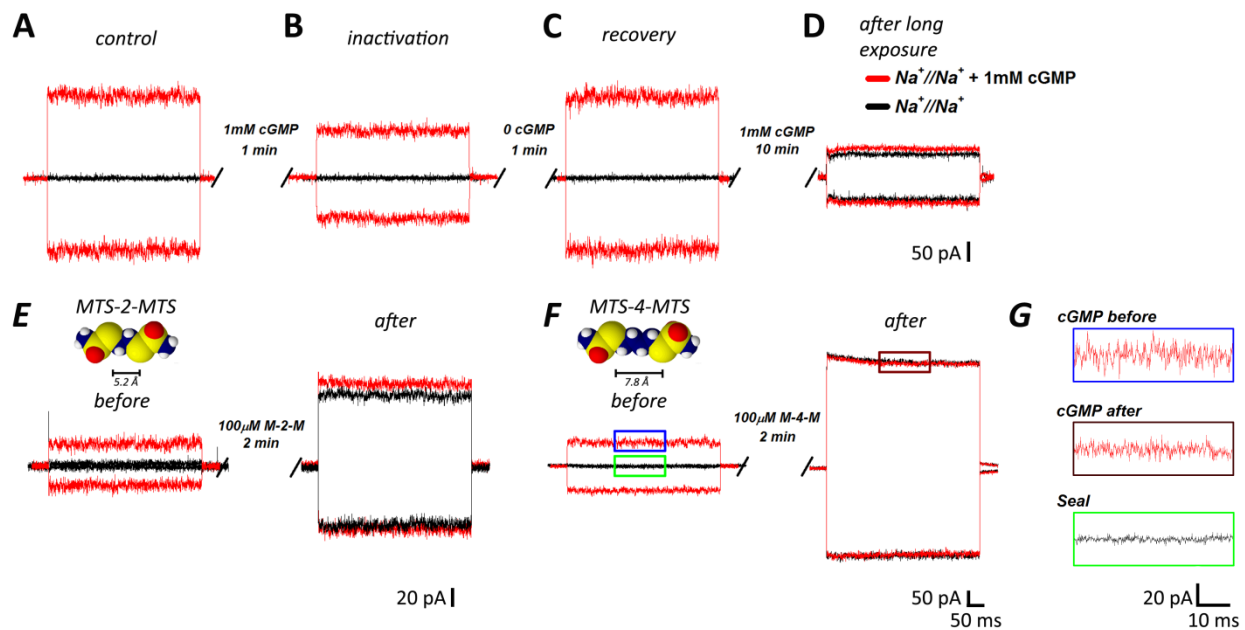
Figure 2: Interaction between S4-S5 linker and C-linker. A-D: inactivation and locking effect in the double mutant channel D413C&R297C. cGMP-activated currents in symmetrical Na$^+$ solution in the presence of 1 mM cGMP at ±60 mV immediately after the membrane patch excision (**A**) and after 1 minute (**B**) showing the inactivation of the current in the open state. The recovery (**C**) of the current is after 1 minute in the closed state (i.e. maintaining the patch in the absence of cGMP). Irreversible lock of the current in the open state (**D**) after a longer exposure of cGMP (10 minutes) as shows comparing the red and black traces. **E:** Locking effect in presence of 100 μm MTS-2-MTS at ±60 mV immediately after the membrane patch excision (left panel) and after 2 minutes in the open state (right panel). The molecular structure of M-2-M is shown. **F:** The same as in **E** but in presence of 100 μm M-4-M. Red and black lines represent the current evoked by 1 mM and 0 cGMP. **G:** enlargements of boxes depicted in **F,** showing the difference in the noise fluctuations before and after application of MTS-4-MTS.

We applied brief voltage pulses at + and - 60 mV, while changing the intracellular solution. The double mutant channel D413C_R297C rapidly inactivates following the application of 1 mM cGMP and within 1-2 minutes the cGMP activated current was reduced by about 50 % (**Fig.2A,B**) but it recovered completely its original amplitude after cGMP removal for 1-3 minutes (**Fig.2C**). Unexpectedly, we found that a longer exposure (~ 10 minutes) to cGMP irreversibly lock the channel in the open state (**Fig.2D**). We therefore evaluated the effect of specific cross-linkers acting between the two exogenous cysteines. In these conditions, the double mutant channel D413C_R297C was irreversibly locked in the open state by the simultaneous exposure to 1 mM cGMP and the cross-linkers MTS-2-MTS and MTS-4-MTS (**Fig.2E and F**) - bearing two thiol reagent groups at a distance of 5.2 and 7.8 Å respectively - within less than 2 minutes. The double mutant channels, once locked in the open state, does not inactivate any more. Furthermore this locking in

the open state is associated to a potentiation and a strong reduction of the current noise. Noise analysis suggests that fluctuations with a Lorentzian component with a cut-off frequency of about 100 Hz are abolished when the double mutant channel is locked in the open state (see Supplementary Fig.SI2 and **Fig.2G**). As a further validation, SMFS experiments with the double mutant channel D413C_R297C confirmed that the addition of MTS-4-MTS cross-linker in the open state introduced a strong bond between the two exogenous cysteine. These experiments suggest that, during opening of CNGA1 channels, the C-linker becomes close enough to the S4-S5 linker of the same, or of a neighboring subunit, to permit molecular interactions triggering the gating mechanism. The next question is how these interactions can lead to the widening of the pore lumen?

SMFS experiments on CNGA1 channel revealed conformational changes upon gating
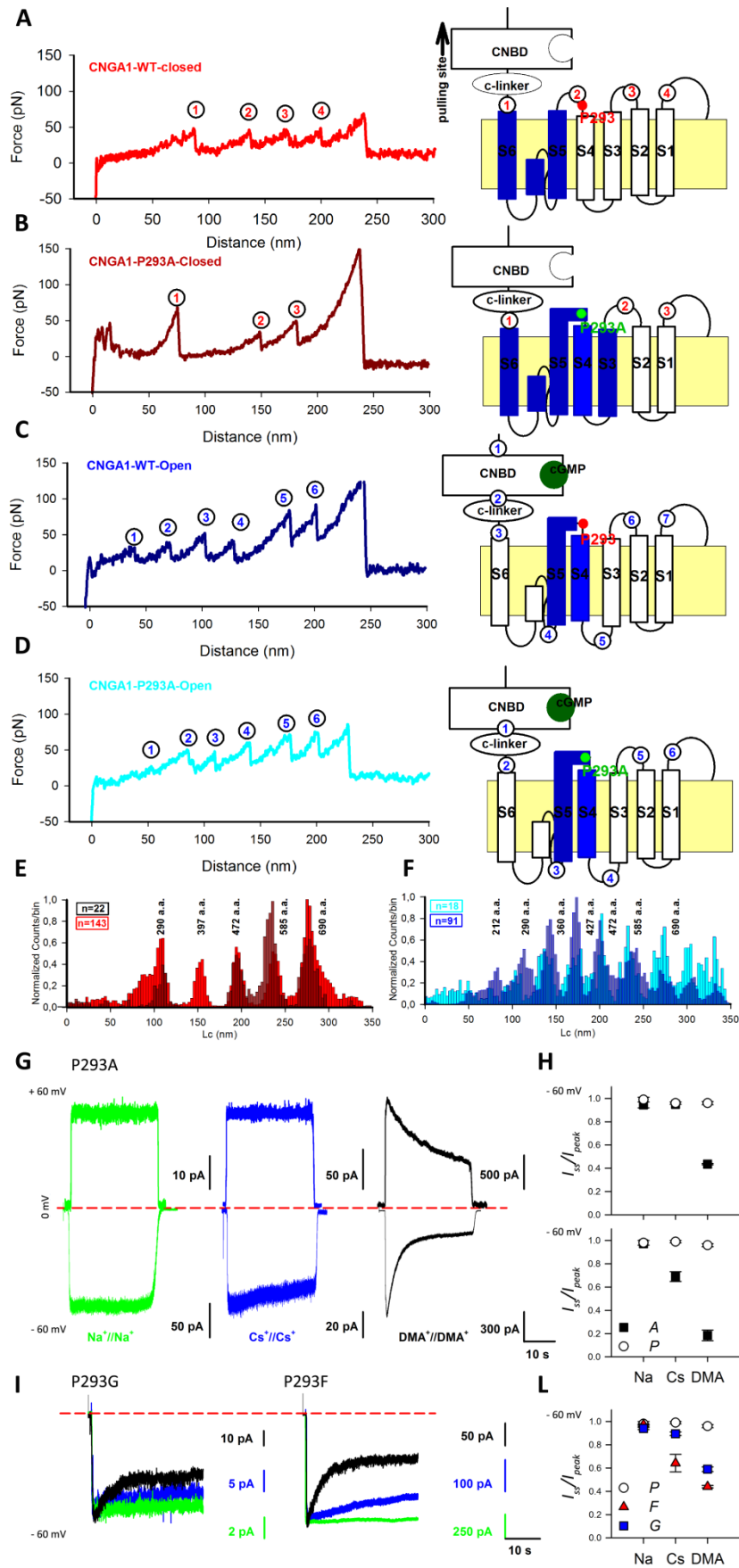
Figure 3: Role of the residue P293 located in the S4-S5 linker. A-D: example of representative *F–D* curves for the CNGA1 channel (**A** and **C**) and for the P293A (**B** and **D**), for the closed (red traces) and open state (blue traces). Schematic representation of the unfolding sequence for the WT and the mutant channel P293A are also represented. **E,F:** superimposition of histograms of normalized counts/bin against Lc from CNGA1 (see also Maity et al., 2015) and mutant channel P293A, both in the closed (**E**) and open state (**F**). **G:** cGMP-activated currents for the mutant channel P293A in the presence of 1 mM cGMP at ±60 mV in presence of different symmetrical ion solutions (Na$^+$-green, Cs$^+$-blue, DMA$^+$-black). **H:** plot representing the residual current after inactivation, versus the ion species. **I:** the same as in **G**, for mutant channels P293G and P293F, at -60 mV. **L:** the same as in **I**, for mutant channels P293G and P293F and only at -60 mV. Helix-propensity energy profiles (Kcal/mol): proline 3.16; glycine 1.00; phenylalanine 0.54; alanine 0.00 (Pace and Scholtz, 1998).

A clue to this question comes from recent SMFS experiments performed on the wild type CNGA1 channels in closed and open state (Maity et al 2015): in the closed state S5 is mechanically coupled to S6 but in the open state S5 is mechanically coupled to S4, suggesting a pivotal role of the S4-S5 linker in the gating of CNG channels. The S4-S5 linker is composed by a stretch of aas TRTNY<u>P</u>NIFRI (see Supplementary Fig.SI1) where P293, an aa with a low propensity to form α-helices (Anselmi et al., 2007; Tendulkar and Wangikar, 2011), could act as an hinge as in K$^+$ channels (Labro and Snyders, 2012; Labro et al., 2003). Therefore we constructed the mutant channel P293A expected to have a more stable α-helix conformation (**Fig.3**) and we investigated its properties both in SMFS and electrophysiological experiments.

SMFS experiments show that in the closed state in the WT CNGA1 channel there is a force peak with a value of Lc at about 157 nm (**Fig.3A**) corresponding to the unfolding of S5-P-helix-S6, but in the mutant channel P293A this force peak is absent (**Fig.3C**), presumably because the hinge in position 293 - in the middle of the S4-S5 linker - is absent leading to a stronger mechanical coupling between S4 and S5. However, the unfolding of the TM domain in the open state in mutant channel P293A is similar to what observed in WT CNGA1 channels (**Fig.3B** and **D**), suggesting that in mutant channel P293A the conformation of the S4-S5 linker is very similar in the open and closed.

Electrophysiological experiments in mutant channels P293A show an unusual gating: mutant channels P293A do not inactivate in the presence of symmetrical Na$^+$ conditions (**Fig.3E, F**) but unexpectedly inactivate slightly in a voltage dependent way in the presence of larger permeant cations such as Cs$^+$ (**Fig.3E, F**) and, to a greater extent, in the presence of DMA$^+$ (**Fig.3E, F**) and EA$^+$ (Maity et al., 2015). When P293 is mutated into a Glycine and/or a Phenylalanine the degree of

inactivation correlates with the α-helical propensity of the aa located in position 293, supporting the idea that the rigidity of the linker S4-S5 is, in turn, associated to gating. (**Fig.3G, H** and Supplementary Fig.SI 4A, B). Mutant channels P293A have also altered tail currents (see Supplementary Fig. SI4) providing further support to the role of the S4-S5 linker in the gating of CGA1 channels.

These experiments suggest that the S4-S5 linker, during gating - as a consequence of the interaction with the C-linker - becomes more rigid and is mechanically coupled to S5. In this view the binding of cGMP to the CNB domain affects the state of the pore lumen, not through S6, as believed for a long time (Flynn and Zagotta, 2001), but through the motion of S5.

S5 transfers the gating movements to the pore widening
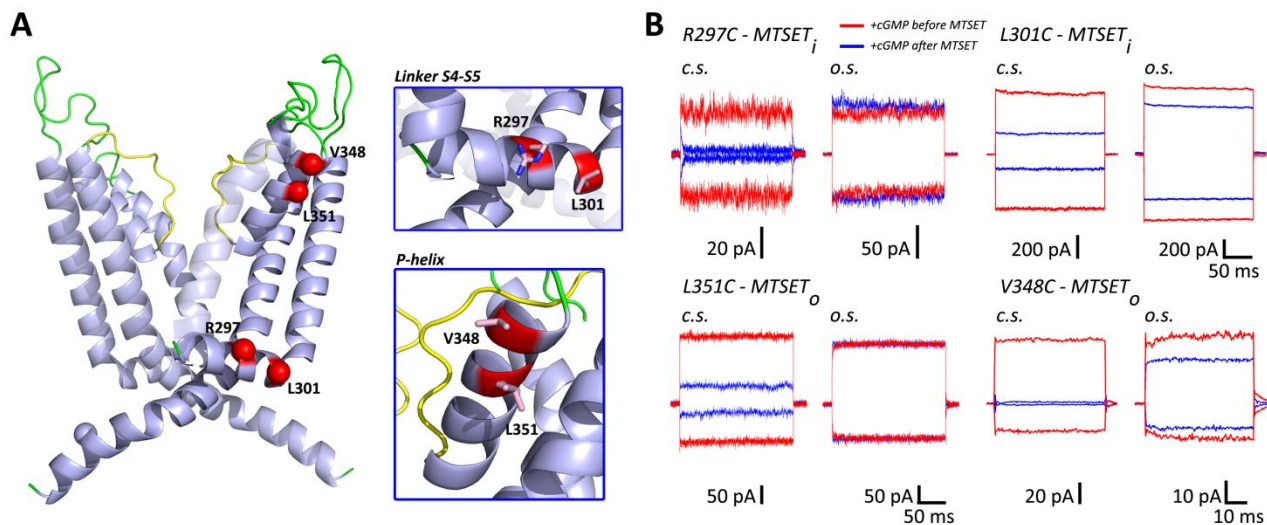
Figure 4: Interaction between S4-S5 linker and C-linker. A-B: cartoon representation of two opposite subunits of the homology model of the tetrameric bovine CNGA1 channel. Key residues are highlighted in stick representation. Comparison between the cGMP-activated currents for the mutant channels R297C (left-upper panel), L301C (right-upper panel), L351C (left-lowest panel), V348C (right-lowest panel) in the open and closed states before (red lines) and after (blue lines) 3 minutes application of 2.5 mM MTSET in the intracellular side. For the mutant channel L351C and V348C the MTSET has been applied by filling the patch pipette i.e. the extracellular side.

We then analyzed the motion of S5 and the P-helix by Cysteine scanning mutagenesis of residues in its lower (from R297 to I308) and upper portion (from S320 to D328) of S5 and residues in the P-helix from R345 to T360 (see also Becchetti et al., 1999) comparing blockage by MTSET in the closed and open state. The idea was to attach a huge and bulky molecule to a specific residue trying to tether the motion of S5. In the lower portion of S5, out of all the mutant channels, we found two (R297C and L301C) (**Fig.4A**) that were blocked, within 3-10 minutes, by the application of 2.5 mM MTSET in the closed state. MTSET blockage in mutant channel R297C was complete but not in mutant channel L301C, which was ~ 70% (n=2). According to the predicted structure of the CNGA1 channel, the side chains of residues R297 and L301 are oriented in the same direction (**Fig.4A**) and are accessible to reagents added into the intracellular medium, such as MTSET. When MTSET was added in the open state mutant channel R297C was not blocked but mutant channels L301C were partially blocked (~ 30% n=2) (**Fig.4B - upper panel**).

Mutant channels 298C, 299C, 300C, 302C, 303C, 304C, 305C, 306C, 307C and 308C were not blocked by MTSET neither in the open not in the closed state. Blockage of these mutant channels was not observed also when MTSET was present in the patch pipette, i.e. at the extracellular side

of the membrane. These results suggest that residues from 302 to 308 are not accessible to reagents added to the intracellular and extracellular side presumably because they are embedded in the membrane both in the closed and open state.

If the change of accessibility observed for R297C is connected to the motion of S5 there should be an homologous change of accessibility for one or a for a number of residues in the upper portion of S5. Preliminary results of cysteine scanning in the upper portion of S5 have shown that mutant channels G326 can be locked in the open state by the application of 2.5 mM MTSET but not in the closed state.

These results are consistent with an upward motion of S5 during gating approximately corresponding to about or less than 1 turn of an α-helix, i.e. 5 Å. If this motion is associated to channel gating, there should be corresponding rearrangements in the filter region and in particular in the P-helix. In agreement with previous observations (Becchetti et al., 1999) we found that V348 and L351 in the P-helix change their accessibility during gating: by filling the patch pipette with 2.5 mM MTSET i.e. the extracellular side of the membrane, we found that mutant channels V348C and L351C were not blocked by extracellular MTSET in the open state but at some extent in the closed state (**Fig.4 - lower panel**). Cysteine scanning mutagenesis of residues in S6 TM domain from F375 to S399 (Giorgetti et al., 2005; Mazzolini et al., 2010; Nair et al., 2009) shows less significant changes of accessibility during gating. The analysis of Cd^{2+} and MTS compounds blockage suggests that during gating these residues do not undergo the large displacement occurring in K^+ channels. In fact the effect of thiol reagent on mutant channels from F375C to S399C is very similar in the open and in the closed state indicating negligible conformational rearrangements. In contrast, residues from A400C to N409C have more significant spatial rearrangements during channel gating, observing a block of mutant channels in the closed but not in the open state.

Different consideration can be made for the mutant channel D413C in which there is a blockage of the same extent in both the open and the closed state suggesting that the sulfhydryl compounds may act disrupting putative interactions of this residue with different regions of the channel.

Discussion

More than 35 years have passed since the first CNGA1 channel has been cloned; in this study, by combining a large amount of electrophysiological experiments with site-directed mutagenesis, SMFS and bioinformatic tools, such as homology modelling with known molecular structures of related ionic channels, we were able to identify the molecular steps underling channel gating. We studied gating rearrangements of cyclic nucleotide-modulated channels in different domain of the channel through alanine or cysteine scanning mutagenesis and electrophysiology experiments. We uncovered several key residues that could play an important role in the gating process in CNG channels. We found two mutant channels, R297A and D413A, located in the C-linker and in the S4-S5 linker, respectively, which inactivated in a non-voltage dependent way. This, in addition with their distant position from the pore suggest that they could play an important role in coupling conformational changes occurring in the CNB domain and those in the transmembrane (TM) domain, as previously demonstrated for HCN channels (Decher et al., 2004).

Through electrophysiology and SMFS experiments we proved the existence of an interaction between these two residues, indeed we demonstrate that the double mutant channel D413C_R297C can be irreversibly locked in the open state by a brief exposure to sulfhydryl cross-linkers and unexpectedly by a longer exposure to cGMP.

These experiments suggest that, only in the open state, the C-linker of the CNG channel is close enough to the S4-S5 linker of the same, or of a neighboring subunit, to permit molecular interactions leading to the gating. On the basis of recent SMFS experiments (Maity et al., 2015), homology modelling and electrophysiology experiments, we identified a proline in the linker S4-S5 (P293) determinant for the secondary structure of the linker itself and we proposed a possible mechanism by which the S4-S5 linker can couple the gating to S5. In this view the binding of cGMP to the CNB domain affects the state of the pore lumen, not through S6, as believed for a long time (Flynn and Zagotta, 2001), but through the motion of S5. We therefore examined the effect of restricting normal channel movements through tethering and we found two couple of residues - R297 and L301 at the bottom of S5 and V348 and L351 in the N-terminal part of the P-helix- that display a change of accessibility during gating probably related to the motion of S5. Moreover, our preliminary results of cysteine scanning mutagenesis in the upper part of S5 reveal the presence of a glycine in position 326 that is locked in the open state by MTSET only in the open state. We believe that V348 and L351 pointing toward S5, could interact with a hydrophobic residue in S5 so that the motion of S5 could be driven to the pore through the P-helix.

These results show that during gating the accessibility of residues in S5 and in N-terminal end of the P-helix changes more than those in S6 (Giorgetti et al., 2005; Mazzolini et al., 2010; Nair et al., 2009).
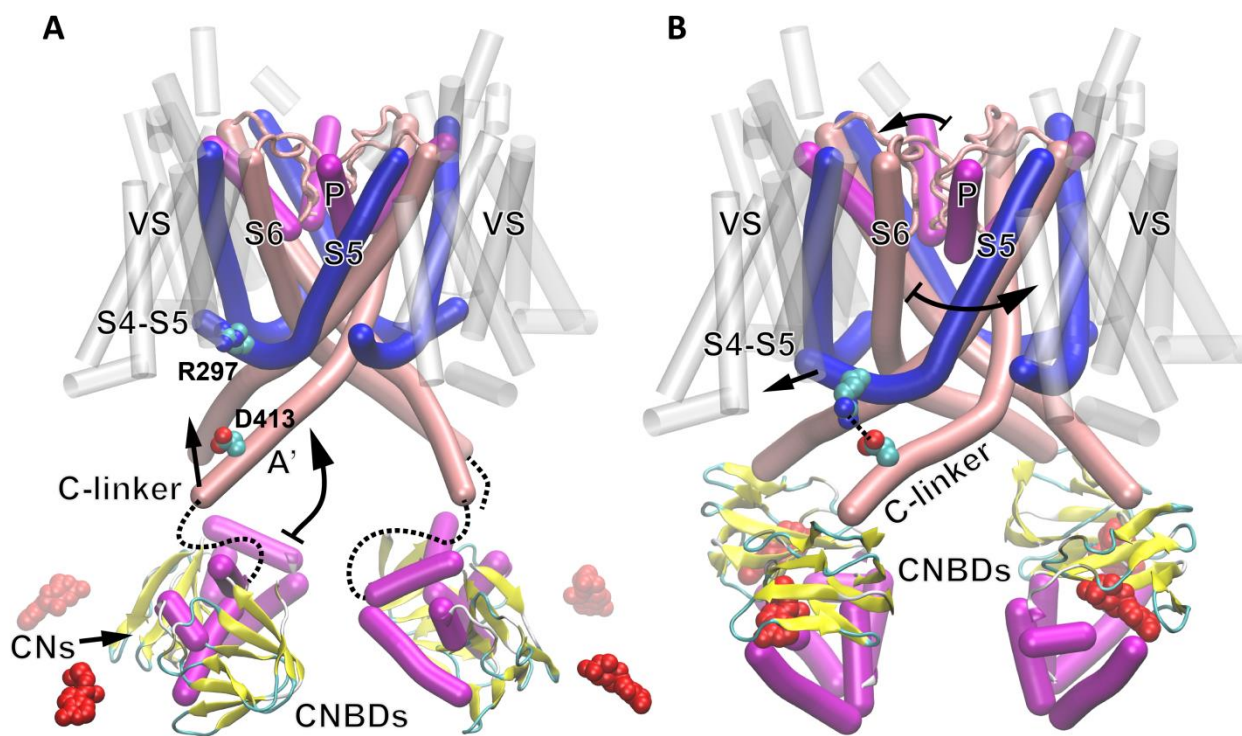

Figure 5: Pictorial representation of the proposed gating mechanism of CNGA1 from the closed state to the open state. **A:** after the binding of cyclic nucleotides (CNs), the cyclic nucleotide binding domains (CNBDs) change their conformation and eventually move toward the transmembrane domain, similarly to what it is observed in MlotK1 (Kowal et al., 2014). **B:** as a consequence, helix A' of the C-linker is pushed toward the channel core. Here the interaction between R297 in S4-S5 and D413 in A' cause the rotation of S4-S5 and S5 toward the outside, eventually opening the gate at the selectivity filter. VS indicates the voltage sensor domain from S1 to S4, here in transparent white cylinders. Sequence tracts from S4-S5 to S5 are colored in blue, those from S6 to A' in pink, P helices are colored in magenta. Helices were rendered with the plugin Bendix (Dahl et al., 2012) implemented in VMD v. 1.9.2 (Humphrey et al., 1996).

In agreement with what observed in the bacterial K$^+$ channels gated by CNs, in the absence of CNs the CNB domain is not properly folded (Chiu et al., 2007; Kowal et al., 2014) but becomes properly folded after binding of CNs and moves upwards towards the membrane (Fig.5a) as recently shown to occur in the Mlotk1 channel (Kowal et al., 2014). Following this upward motion D413 and R297 are attracted by electrostatic interactions and as a consequence of the interaction between the C-linker and the S4-S5 linker the complex S4-S5 and S5 stiffens and moves. The motion of S5, possibly a rotation combined to an upward motion widen the lumen of the pore (**Fig.5A, B**).

References

Sali, A. (1995). Comparative protein modeling by satisfaction of spatial restraints. Mol. Med. Today *1*, 270–277.

Anselmi, C., Carloni, P., and Torre, V. (2007). Origin of functional diversity among tetrameric voltage-gated channels. Proteins *66*, 136–146.

Ashkenazy, H., Erez, E., Martz, E., Pupko, T., and Ben-Tal, N. (2010). ConSurf 2010: calculating evolutionary conservation in sequence and structure of proteins and nucleic acids. Nucleic Acids Res. *38*, W529–W533.

Barth, P., Schonbrun, J., and Baker, D. (2007). Toward high-resolution prediction and design of transmembrane helical protein structures. Proc. Natl. Acad. Sci. U. S. A. *104*, 15682–15687.

Becchetti, A., Gamel, K., and Torre, V. (1999). Cyclic nucleotide-gated channels. Pore topology studied through the accessibility of reporter cysteines. J. Gen. Physiol. *114*, 377–392.

Bernsel, A., Viklund, H., Hennerdal, A., and Elofsson, A. (2009). TOPCONS: consensus prediction of membrane protein topology. Nucleic Acids Res. *37*, W465–W468.

Best, R.B., Zhu, X., Shim, J., Lopes, P.E.M., Mittal, J., Feig, M., and MacKerell, A.D. (2012). Optimization of the additive CHARMM all-atom protein force field targeting improved sampling of the backbone ϕ, ψ and side-chain χ1 and χ2 dihedral angles. J. Chem. Theory Comput. *8*, 3257–3273.

Buchan, D.W.A., Minneci, F., Nugent, T.C.O., Bryson, K., and Jones, D.T. (2013). Scalable web services for the PSIPRED Protein Analysis Workbench. Nucleic Acids Res. *41*, W349–W357.

del Camino, D., Holmgren, M., Liu, Y., and Yellen, G. (2000). Blocker protection in the pore of a voltage-gated K+ channel and its structural implications. Nature *403*, 321–325.

Chiu, P.-L., Pagel, M., Evans, J., Chou, H.-T., Zeng, X., Gipson, B., Stahlberg, H., and Nimigean, C. (2007). The structure of the prokaryotic cyclic nucleotide-modulated potassium channel MloK1 at 16Å resolution. Struct. Lond. Engl. 1993 *15*, 1053–1064.

Colamartino, G., Menini, A., and Torre, V. (1991). Blockage and permeation of divalent cations through the cyclic GMP-activated channel from tiger salamander retinal rods. J. Physiol. *440*, 189.

Consortium, T.U. (2014). UniProt: a hub for protein information. Nucleic Acids Res. gku989.

Contreras, J.E., Srikumar, D., and Holmgren, M. (2008). Gating at the selectivity filter in cyclic nucleotide-gated channels. Proc. Natl. Acad. Sci. *105*, 3310–3314.

Craven, K.B., and Zagotta, W.N. (2006). CNG AND HCN CHANNELS: Two Peas, One Pod. Annu. Rev. Physiol. *68*, 375–401.

Cukkemane, A., Seifert, R., and Kaupp, U.B. (2011). Cooperative and uncooperative cyclic-nucleotide-gated ion channels. Trends Biochem. Sci. *36*, 55–64.

Dahl, A.C.E., Chavent, M., and Sansom, M.S.P. (2012). Bendix: intuitive helix geometry analysis and abstraction. Bioinforma. Oxf. Engl. *28*, 2193–2194.

Darden, T., York, D., and Pedersen, L. (1993). Particle mesh Ewald: An N·log(N) method for Ewald sums in large systems. J. Chem. Phys. *98*, 10089–10092.

Decher, N., Chen, J., and Sanguinetti, M.C. (2004). Voltage-dependent Gating of Hyperpolarization-activated, Cyclic Nucleotide-gated Pacemaker Channels MOLECULAR COUPLING BETWEEN THE S4–S5 AND C-LINKERS. J. Biol. Chem. *279*, 13859–13865.

DeLano, W.L. (2002). Unraveling hot spots in binding interfaces: progress and challenges. Curr. Opin. Struct. Biol. *12*, 14–20.

Derebe, M.G., Zeng, W., Li, Y., Alam, A., and Jiang, Y. (2011). Structural studies of ion permeation and Ca2+ blockage of a bacterial channel mimicking the cyclic nucleotide-gated channel pore. Proc. Natl. Acad. Sci. *108*, 592–597.

Doyle, D.A., Cabral, J.M., Pfuetzner, R.A., Kuo, A., Gulbis, J.M., Cohen, S.L., Chait, B.T., and MacKinnon, R. (1998). The Structure of the Potassium Channel: Molecular Basis of K+ Conduction and Selectivity. Science *280*, 69–77.

Feller, S.E., Zhang, Y., Pastor, R.W., and Brooks, B.R. (1995). Constant pressure molecular dynamics simulation: The Langevin piston method. J. Chem. Phys. *103*, 4613–4621.

Flynn, G.E., and Zagotta, W.N. (2001). Conformational changes in S6 coupled to the opening of cyclic nucleotide-gated channels. Neuron *30*, 689–698.

Forrest, L.R., Tang, C.L., and Honig, B. (2006). On the Accuracy of Homology Modeling and Sequence Alignment Methods Applied to Membrane Proteins. Biophys. J. *91*, 508–517.

Giorgetti, A., Nair, A.V., Codega, P., Torre, V., and Carloni, P. (2005). Structural basis of gating of CNG channels. FEBS Lett. *579*, 1968–1972.

Gofman, Y., Schärfe, C., Marks, D.S., Haliloglu, T., and Ben-Tal, N. (2014). Structure, Dynamics and Implied Gating Mechanism of a Human Cyclic Nucleotide-Gated Channel. PLoS Comput. Biol. *10*.

Hamill, O.P., Marty, A., Neher, E., Sakmann, B., and Sigworth, F.J. (1981). Improved patch-clamp techniques for high-resolution current recording from cells and cell-free membrane patches. Pflüg. Arch. Eur. J. Physiol. *391*, 85–100.

Hénin, J., Fiorin, G., Chipot, C., and Klein, M.L. (2010). Exploring Multidimensional Free Energy Landscapes Using Time-Dependent Biases on Collective Variables. J. Chem. Theory Comput. *6*, 35–47.

Higgins, M.K., Weitz, D., Warne, T., Schertler, G.F.X., and Kaupp, U.B. (2002). Molecular architecture of a retinal cGMP-gated channel: the arrangement of the cytoplasmic domains. EMBO J. *21*, 2087–2094.

Hille, B. (2001). Ion Channels of Excitable Membranes (Mass.).

Hodgkin, A.L., and Huxley, A.F. (1952). A quantitative description of membrane current and its application to conduction and excitation in nerve. J. Physiol. *117*, 500–544.

Holmgren, M., Shin, K.S., and Yellen, G. (1998). The Activation Gate of a Voltage-Gated K+ Channel Can Be Trapped in the Open State by an Intersubunit Metal Bridge. Neuron *21*, 617–621.

Humphrey, W., Dalke, A., and Schulten, K. (1996). VMD: visual molecular dynamics. J. Mol. Graph. *14*, 33–38, 27–28.

Jan, L.Y. (1990). A superfamily of ion channels. Nature *345*, 672–672.

Karpen, J.W., and Ruiz, M. (2002). Ion channels: does each subunit do something on its own? Trends Biochem. Sci. *27*, 402–409.

Kaupp, U.B., and Seifert, R. (2002). Cyclic nucleotide-gated ion channels. Physiol. Rev. *82*, 769–824.

Kaupp, U.B., Niidome, T., Tanabe, T., Terada, S., Bönigk, W., Stühmer, W., Cook, N.J., Kangawa, K., Matsuo, H., Hirose, T., et al. (1989). Primary structure and functional expression from complementary DNA of the rod photoreceptor cyclic GMP-gated channel. Nature *342*, 762–766.

Kowal, J., Chami, M., Baumgartner, P., Arheit, M., Chiu, P.-L., Rangl, M., Scheuring, S., Schröder, G.F., Nimigean, C.M., and Stahlberg, H. (2014). Ligand-induced structural changes in the cyclic nucleotide-modulated potassium channel MloK1. Nat. Commun. *5*, 3106.

Labro, A.J., and Snyders, D.J. (2012). Being flexible: the voltage-controllable activation gate of kv channels. Front. Pharmacol. *3*, 168.

Labro, A.J., Raes, A.L., Bellens, I., Ottschytsch, N., and Snyders, D.J. (2003). Gating of shaker-type channels requires the flexibility of S6 caused by prolines. J. Biol. Chem. *278*, 50724–50731.

Leaver-Fay, A., Tyka, M., Lewis, S.M., Lange, O.F., Thompson, J., Jacak, R., Kaufman, K., Renfrew, P.D., Smith, C.A., Sheffler, W., et al. (2011). Rosetta3: An Object-Oriented Software Suite for the Simulation and Design of Macromolecules. Methods Enzymol. *487*, 545–574.

Liu, Y., Schmidt, B., and Maskell, D.L. (2010). MSAProbs: multiple sequence alignment based on pair hidden Markov models and partition function posterior probabilities. Bioinforma. Oxf. Engl. *26*, 1958–1964.

Lolicato, M., Nardini, M., Gazzarrini, S., Möller, S., Bertinetti, D., Herberg, F.W., Bolognesi, M., Martin, H., Fasolini, M., Bertrand, J.A., et al. (2011). Tetramerization Dynamics of C-terminal Domain Underlies Isoform-specific cAMP Gating in Hyperpolarization-activated Cyclic Nucleotide-gated Channels. J. Biol. Chem. *286*, 44811–44820.

Long, S.B., Campbell, E.B., and Mackinnon, R. (2005). Voltage sensor of Kv1.2: structural basis of electromechanical coupling. Science *309*, 903–908.

Long, S.B., Tao, X., Campbell, E.B., and MacKinnon, R. (2007). Atomic structure of a voltage-dependent K+ channel in a lipid membrane-like environment. Nature *450*, 376–382.

Loo, T.W., and Clarke, D.M. (2001). Determining the Dimensions of the Drug-binding Domain of Human P-glycoprotein Using Thiol Cross-linking Compounds as Molecular Rulers. J. Biol. Chem. *276*, 36877–36880.

Maity, S., Mazzolini, M., Arcangeletti, M., Valbuena, A., Fabris, P., Lazzarino, M., and Torre, V. (2015). Conformational rearrangements in the transmembrane domain of CNGA1 channels revealed by single-molecule force spectroscopy. Nat. Commun. *6*, 7093.

Matulef, K., and Zagotta, W.N. (2002). Multimerization of the Ligand Binding Domains of Cyclic Nucleotide-Gated Channels. Neuron *36*, 93–103.

Mazzolini, M., Punta, M., and Torre, V. (2002). Movement of the C-helix during the gating of cyclic nucleotide-gated channels. Biophys. J. *83*, 3283–3295.

Mazzolini, M., Marchesi, A., Giorgetti, A., and Torre, V. (2010). Gating in CNGA1 channels. Pflüg. Arch. Eur. J. Physiol. *459*, 547–555.

Nair, A.V., Mazzolini, M., Codega, P., Giorgetti, A., and Torre, V. (2006). Locking CNGA1 Channels in the Open and Closed State. Biophys. J. *90*, 3599–3607.

Nair, A.V., Nguyen, C.H.H., and Mazzolini, M. (2009). Conformational rearrangements in the S6 domain and C-linker during gating in CNGA1 channels. Eur. Biophys. J. EBJ *38*, 993–1002.

Napolitano, L.M.R., Bisha, I., De March, M., Marchesi, A., Arcangeletti, M., Demitri, N., Mazzolini, M., Rodriguez, A., Magistrato, A., Onesti, S., et al. (2015). A structural, functional, and computational analysis suggests pore flexibility as the base for the poor selectivity of CNG channels. Proc. Natl. Acad. Sci. U. S. A. *112*, E3619–E3628.

Nizzari, M., Sesti, F., Giraudo, M.T., Virginio, C., Cattaneo, A., and Torre, V. (1993). Single-channel properties of cloned cGMP-activated channels from retinal rods. Proc. Biol. Sci. *254*, 69–74.

Pace, C.N., and Scholtz, J.M. (1998). A helix propensity scale based on experimental studies of peptides and proteins. Biophys. J. *75*, 422–427.

Payandeh, J., El-Din, T.M.G., Scheuer, T., Zheng, N., and Catterall, W.A. Crystal structure of a voltage-gated sodium channel in two potentially inactivated states. Nature *486*, 135.

Phillips, J.C., Braun, R., Wang, W., Gumbart, J., Tajkhorshid, E., Villa, E., Chipot, C., Skeel, R.D., Kalé, L., and Schulten, K. (2005). Scalable Molecular Dynamics with NAMD. J. Comput. Chem. *26*, 1781–1802.

Picco, C., and Menini, A. (1993). The permeability of the cGMP-activated channel to organic cations in retinal rods of the tiger salamander. J. Physiol. *460*, 741.

Ray, A., Lindahl, E., and Wallner, B. (2010). Model quality assessment for membrane proteins. Bioinformatics *26*, 3067–3074.

Remmert, M., Biegert, A., Hauser, A., and Söding, J. (2012). HHblits: lightning-fast iterative protein sequence searching by HMM-HMM alignment. Nat. Methods *9*, 173–175.

Richards, M.J., and Gordon, S.E. (2000). Cooperativity and cooperation in cyclic nucleotide-gated ion channels. Biochemistry (Mosc.) *39*, 14003–14011.

Russell, R.B., and Barton, G.J. (1992). Multiple protein sequence alignment from tertiary structure comparison: assignment of global and residue confidence levels. Proteins *14*, 309–323.

Schünke, S., Stoldt, M., Lecher, J., Kaupp, U.B., and Willbold, D. (2011). Structural insights into conformational changes of a cyclic nucleotide-binding domain in solution from Mesorhizobium loti K1 channel. Proc. Natl. Acad. Sci. U. S. A. *108*, 6121–6126.

Sesti, F., Straforini, M., Lamb, T.D., and Torre, V. (1994). Gating, selectivity and blockage of single channels activated by cyclic GMP in retinal rods of the tiger salamander. J. Physiol. *474*, 203.

Sesti, F., Eismann, E., Kaupp, U.B., Nizzari, M., and Torre, V. (1995). The multi-ion nature of the cGMP-gated channel from vertebrate rods. J. Physiol. *487*, 17.

Shuart, N.G., Haitin, Y., Camp, S.S., Black, K.D., and Zagotta, W.N. (2011). Molecular mechanism for 3:1 subunit stoichiometry of rod cyclic nucleotide-gated ion channels. Nat. Commun. *2*, 457.

Söding, J. (2005). Protein homology detection by HMM–HMM comparison. Bioinformatics *21*, 951–960.

Tendulkar, A.V., and Wangikar, P.P. (2011). Characterization and sequence prediction of structural variations in α-helix. BMC Bioinformatics *12 Suppl 1*, S20.

Tetreault, M.L., Henry, D., Horrigan, D.M., Matthews, G., and Zimmerman, A.L. (2006). Characterization of a novel cyclic nucleotide-gated channel from zebrafish brain. Biochem. Biophys. Res. Commun. *348*, 441–449.

Yang, Z., Lasker, K., Schneidman-Duhovny, D., Webb, B., Huang, C.C., Pettersen, E.F., Goddard, T.D., Meng, E.C., Sali, A., and Ferrin, T.E. (2012). UCSF Chimera, MODELLER, and IMP: an Integrated Modeling System. J. Struct. Biol. *179*, 269–278.

Yarov-Yarovoy, V., Schonbrun, J., and Baker, D. (2006). Multipass Membrane Protein Structure Prediction Using Rosetta. Proteins *62*, 1010–1025.

Zagotta, W.N., Olivier, N.B., Black, K.D., Young, E.C., Olson, R., and Gouaux, E. (2003). Structural basis for modulation and agonist specificity of HCN pacemaker channels. Nature *425*, 200–205.

Supplementary Informations

Figure SI1
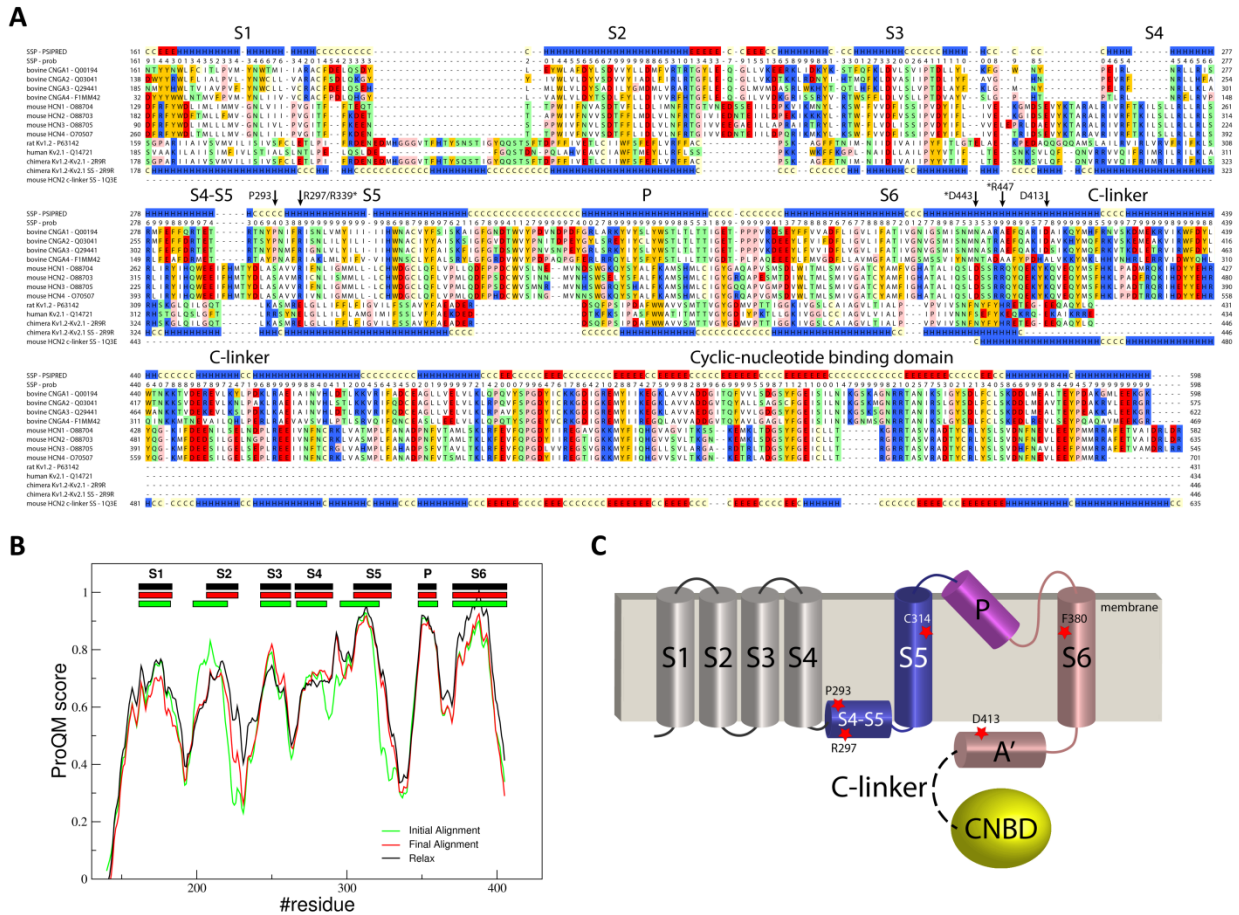
A: sequence alignment between CNGA and HCN channels in the region from the putative helix S1 to the cyclic nucleotide binding domain (CNBD) and the core regions of Kv1.2 and the chimera Kv1.2-Kv2.1 channels used for modeling. The predicted secondary structure of the bovine CNGA1 (SSP-PSIPRED), the prediction confidence (SSP-prob) and the known secondary structure (SS) of the chimera Kv1.2-Kv2.1 and the C-linker from murine HCN2 are shown above and below the sequences. Key residues of bovine CNGA1 and murine HCN2 (indicated with a *) are reported. Sequences were aligned by using MSAProbs (Liu et al., 2010). **B:** ProQM profiles of the best structural models obtained from the initial alignment from HHalign, from the final refined alignment, and after the ROSETTA relax procedure. Thanks to the refinement procedure, the total ProQM of the best model improves from 0.60 for the initial alignment, to 0.61 for the final alignment to 0.65 for the final ROSETTA model. The transmembrane helix boundaries of the different models are shown above the profiles. **C:** overview of the topology and fold of bovine CNGA1 as evinced from the predicted secondary structure and transmembrane topology and from the template, the chimera channel Kv1.2-Kv2.1 X-ray structure (PDB id. 2R9R). Locations of key residues are indicated as red stars. Color coding is as in **Fig. 5**.

Figure SI2
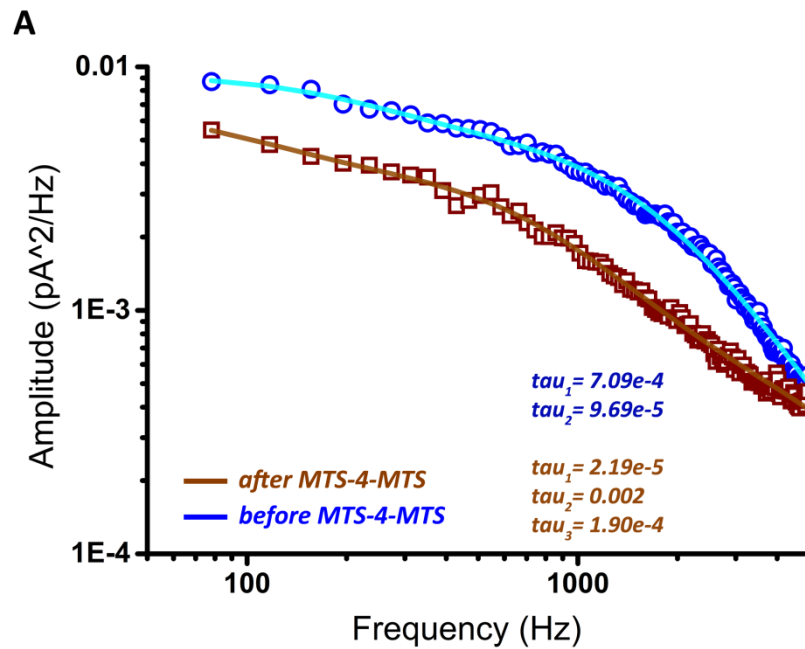
A: power spectrum of current fluctuations in the presence of 1 mM cGMP, before (empty blue circles) and after (empty brown squares) of the application of 100 µM MTS-4-MTS, at +40 mV. Current recordings were filtered at 20 kHz and sampled at 60 kHz. Power spectra were computed as described by Sesti et al., 1994.

Figure SI3
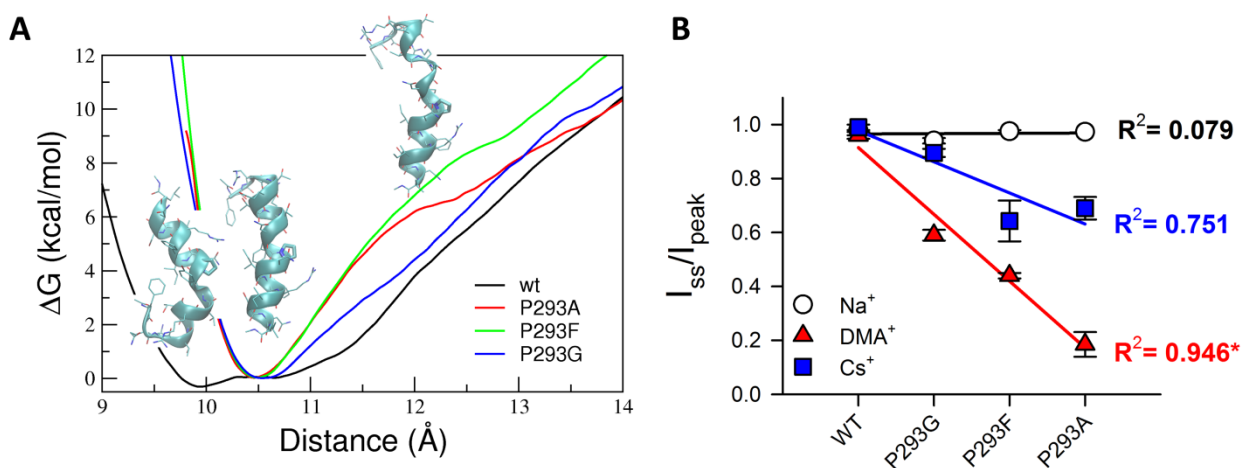
A: free energy profiles delineating the reversible unfolding at residue positions 290-293 as a function of the coordinate of reaction COR. COR was chosen as the distance between the centers of mass of the Cα atoms of amino acids 287-290 and 294-297. **B:** rate of inactivation plotted versus

the helical propensity in the presence of all cations; analysis of the linear regression for each ion was performed. * indicates a statistical significance with p < 0.05.

Figure SI4
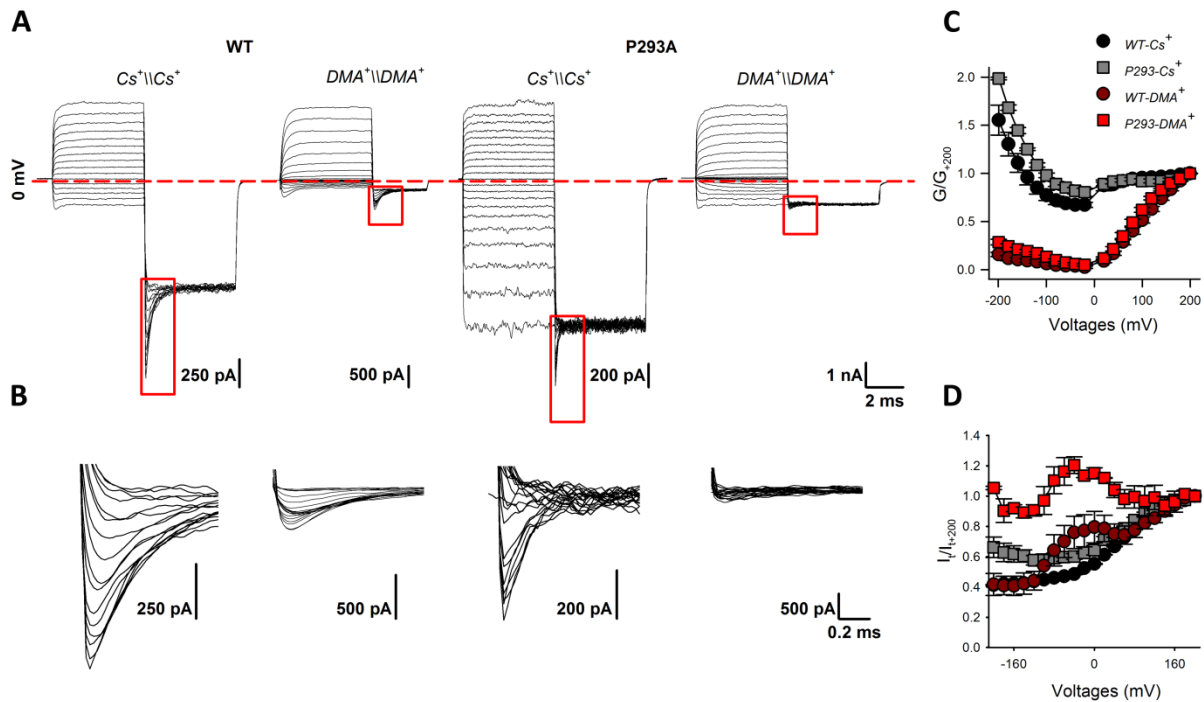
A: macroscopic currents recorded from excised patches in symmetrical solutions of Cs^+ and DMA^+ for WT and P293A mutant channels with 1 mM cGMP in the intracellular medium. Leak and capacitative components were removed subtracting from the cGMP-activated current those records obtained in response to the same voltage protocol but without cGMP. The voltage commands were stepped from a holding potential of 0 mV to prepulses varying between −100 and +200 mV in 20 mV steps. At the end, the voltage command was moved to −200 mV for 5 msec in order to elicit tail currents It(V). Red broken line indicates 0 current level. **B:** enlargement of tail currents (boxed areas in **A**). Current recordings were filtered at 10 kHz and sampled at 50 kHz to resolve rapid transients. **C:** Dependence of G/G_{+200} on V in symmetrical solutions of Cs^+ (black and grey) and DMA^+ (red and dark red) for WT (circles) and P293A (squares) mutant channels. **D:** Estimation of P_o/P_{o_max} from tail currents. P_o/P_{o_max} was estimated as I_t/I_{t+200} symbols and colors are the same as in **C**.

CONCLUSIONS AND PERSPECTIVES

During these years, my work has been directed in investigating some structural and functional features of the CNGA1 channels. Up to now, only few information about the structure are available and unfortunately a complete structure of the channel is still lacking. We kept advantage of different techniques, like single molecule force spectroscopy, molecular dynamic simulation, X-ray crystallography, molecular biology techniques (site-directed mutagenesis) and electrophysiological tools (patch-clamp current recordings) in order to characterize these aspects of the channel.

As mentioned before, voltage gating in CNGA1 channels strictly depends on the permeating ion: in presence of small monovalent alkali cations, such as Li^+, Na^+, and K^+, gating is weakly voltage dependent, but gradually more for larger alkali cations, such as Rb^+ and Cs^+ and for organic cations such as ethylammonium$^+$ (EA$^+$) and dimethylammonium$^+$ (DMA$^+$). The results described in this work are summarized below:

1. We demonstrated the existence of two voltage-dependent transitions in the WT CNGA1 channel. The first is likely associated with conformational rearrangements in the S4-type voltage sensor whereas the second might reflect an intrinsic pore voltage sensitivity that can be modulated by the permeant ion. We showed, furthermore, that only the first voltage-dependent transition is sensible to mutation of charged residues in the S4 helix. In the presence of physiological ions, such as Na^+ and K^+, a reduced motion of the S4 transmembrane segment in addition to an inefficient coupling between the voltage-sensing domain and the channel gate which is modulated by the permeant ion, is at the basis of the reduced voltage sensitivity. In the presence of larger monovalent alkali cations and of a variety of organic cations, gating of CNG channels becomes voltage dependent, however, the permeation of Rb^+ and Cs^+ unveils the action of a pore voltage sensor whose mechanism is at the basis of the inward rectification.

2. CNG channel activity is also regulated by protons, indeed, when the external pH is decreased from 7.4 to 6 or lower, WT CNGA1 channels inactivate with a current decline that is reminiscent of the usual C-type inactivation observed in K_v channels. We also described some key features of the reported current decline, such as the time course of inactivation, its pH dependency, the instantaneous and steady-state rectification and the fractional

current blockage observed at low pH_o, with a general kinetic scheme in which two non-equivalent and non-independent proton binding reactions were modelled. We argued a possible explanation for the proton blockage according to which it could arise from the high-affinity binding to the main chain carbonyl oxygens within the selectivity filter and from a second, low-affinity binding site for protons constituted by the Glu363 side chain, the titration of which results in a destabilization of the pore moiety, leading to a slow collapse toward a non-conductive, inactivated state. Since, as mentioned in the introduction, changes in extracellular hydrogen ion concentration (pH_o) occur in a variety of physiological and pathophysiological conditions and since pH changes could play also a very important role in adaptation of the retinal response to different light intensities, determining the effect of protons on CNG channel gating could have a great clinical and physiological significance.

3. The extracellular entrance of the selectivity filter and the filter itself, in CNG channels, exhibit a dynamic structure capable of structural rearrangements and this is thought to be mediated by two key interactions involving the "aromatic girdle" that is constituted by a ring of bulky tyrosine residues in the selectivity filter and a charged aspartate immediately following the signature sequence. In CNG channels these residues are replaced by a ring of glutamate (Glu363/Glu66) and by a string of three consecutive prolines (Pro365-368). These residues are arranged in a secondary structure that is more flexible; with the aid of MD simulations and X-ray crystallography, we identified, in these residues, the major molecular mechanism underlying the coupling between gating and permeation that is best observed in the presence of symmetrical Na^+ and Cs^+ conditions. We proposed then that this flexibility, together with the number of equivalent and contiguous ion binding sites in the filter, underscores the poor ionic selectivity of CNG channels and reveals a conduction mode that differs substantially from that of classical K^+ channels, which are highly selective and have a fairly rigid molecular structure.

4. With the help of single-molecule force spectroscopy (SMFS) we shed light on a putative yet undiscovered mechanical coupling between the voltage sensor and the gating mechanism; we proved the existence of an interaction between two residues: R297A located in the S4-S5 linker and D413A, in the C-linker; indeed we demonstrated that the double mutant channel D413C_R297C can be irreversibly locked in the open state by a brief exposure to sulfhydryl cross-linkers and unexpectedly by a longer exposure to cGMP. A similar

interaction has also been shown previously for HCN channels (Decher et al., 2004). This suggest that, only in the open state, the C-linker of the CNG channel is close enough to the S4-S5 linker of the same, or of a neighboring subunit, to permit molecular interactions leading to the gating. Moreover, on the basis of recent SMFS experiments (Maity et al., 2015) in which has been found that S4 in the closed state is mechanically coupled to S3, but in the open state to S5, homology modelling and electrophysiology experiments, we identified a proline in the linker S4-S5 (P293) determinant for the secondary structure of the linker itself and we proposed a possible mechanism by which the S4-S5 linker can couple the gating to S5. In this view the binding of cGMP to the CNB domain affects the state of the pore lumen, not through S6, as believed for a long time (Flynn and Zagotta, 2003), but through the motion of S5.

Certainly, more analysis and experiments are requested in order to validate the hypothesis of the motion of S5. We should examine with further mutagenesis the effect of restricting normal channel movements through tethering different portions of the channel in order to get more understandings about the gating mechanism of CNGA1 channels. Moreover, while electrophysiology has proven to be a very sensible tool for studying the function of ion channels, even at a single molecule level, in order to gain a complete understanding of the 3D structure of the channel and for a better identification of the mechanisms that are behind some critical channel operations, it seems necessary to carry on using techniques like molecular biology, X-ray crystallography, molecular dynamics simulations and SMFM combining to these other techniques, including imaging techniques, such as EPR spectroscopy, cryo-electron microscopy and optical spectroscopic methods.

ACKNOWLEDGEMENTS